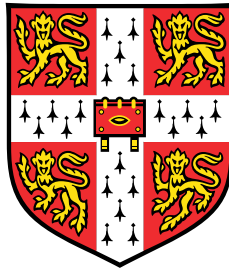


Eddy-resolving simulations of the flow around a vertical tail plane



Andrea Masi

Department of Engineering
University of Cambridge

This dissertation is submitted for the degree of
Doctor of Philosophy

To my family
Alla mia famiglia

Declaration

I hereby declare that, except where specific reference is made to the work of others, the contents of this dissertation are original and have not been submitted in whole or in part for consideration for any other degree or qualification in this, or any other university. This dissertation is my own work and contains nothing which is the outcome of work done in collaboration with others, except as specified in the text and Acknowledgements. This dissertation contains fewer than 65,000 words including appendices, bibliography, footnotes, tables and equations and has fewer than 150 figures.

Andrea Masi
October 2017

Acknowledgements

The PhD journey would not have been possible without the support of many people. I would like to acknowledge my supervisor, Professor Paul Tucker, who has always shown great enthusiasm towards my project. I would like to thank him for his invaluable technical advice, encouragement and support, and for being available at any time during the year. His extra financial assistance during the later stages of my thesis is also greatly appreciated. I would like to thank my industrial advisor, Mr Jerry Benton, who has guided me throughout my experience at Airbus, always keeping an eye open to my academic activities at Cambridge. Jerry's industrial expertise has no equals, and I consider myself privileged to have had such a supervisor.

The project is part of the ANADE (Advances in Numerical and Analytical tools for DEtached flow) consortium, with funding coming from the European Commission under the Marie Curie Actions. I am very grateful to the consortium, and notably to Professor Eusebio Valero, for their support. The consortium has given me the unique opportunity to work in close collaboration with other PhD students and researchers outside of the Cambridge environment. In particular, I would like to thank Maria Chiara Iorio, Andrea Resmini, Chris Hennekinne, Dirk Ekelschot, Bastien Jordi, and David Vallespin, not only for their professional collaboration but also for the great time spent together during the unforgettable 'ANADE trips', and the friendship that we have established. ANADE has also given me the opportunity to spend time at DLR in Germany. I would like to acknowledge Dr Axel Probst for his help and the interesting discussions we have had.

The Cambridge CFD group has been an exciting environment in which to learn and work towards the best results, and I would like to thank the whole research team for this. In particular, Jiahuan Cui and Ashley Scillitoe have been always very collaborative and I thank them for their insights into the research. I would also like to thank Hardeep Kalsi, Bryn Ubald, Ahmed Al-Shabab, Iffi Nakavi, James Tyacke, and Rao Vadlamani for the interesting discussions. People in the lab have certainly made the time in Cambridge more enjoyable. In particular, I am glad I have shared good moments with Girish Nivarti, Camille Bilger, and Carlo Quaglia, both in the lab and outside. They made my stay in Cambridge memorable, and I hope our lives will intersect again in the future. College life was also unforgettable. During

the last three years, I have met many people, from different countries, and with completely different backgrounds. Darwin College helped me develop personality and soft skills, giving me the chance to escape from the ‘Engineering bubble’. I would like to thank everyone who has contributed to this, during discussions, laughs, and drinks at ‘DarBar’. I much appreciate the friendship of Victoria Bartels and Charissa Varma, two incredible personalities who have always been available to listen, give advice and also spend fun times together.

Fifteen thousand miles! This is approximately the distance I have covered during the last three years, commuting from Cambridge to Bristol. At Airbus I have worked in a challenging and competitive industrial environment. I would like to thank the EGDCU team of Airbus, notably the PhD students and researchers. My colleague and friend Feng Zhu has always shown great interest in my research, and has given interesting inputs to the study. He has also hosted me many times during my visits to Bristol, and I will always be grateful for this. Many thanks also to Christian Agostinelli, Giuseppe Trapani, Giovanna Ferraro, Jean Demange, Simone Simeone, and Gabriele Mura for creating an enjoyable research environment. The first house-share experience in Bristol was memorable, especially due to the presence of my friends Jordi Bayer Alsina, Luisa Jolin Rubio, and Alessandro Saturni. Leaving Bristol was not easy after having spent a year with them. I am also grateful to Chris Curran and Sonia Richardson for their friendship and hospitality in Bristol. I would like to thank also Hansel Williams, the brightest light in the darkest period of my PhD. I thank him for his motivation and support. He taught me how to avoid procrastination and overcome drama.

Moreover, I would like to thank my friends Domenico De Fazio and Antonella Emili. Life and study circumstances have brought us to the same city again, and I am grateful to them for the great time spent together and for their encouragement and hospitality. They have always been ready to give me support when needed. Furthermore, I would like to thank those friends that are always there for me, and make life easier and better, notably Silvia Erario, Elena Monticelli, Rafael Narvaez Gracia, Kiliana Vink, Collegio Einaudi’s people, Valentina Corrado and ‘gli Storti’ of Toulouse.

The PhD course has been a great experience, despite some moments of discouragement that have been successfully overcome. This has been possible thanks especially to the endless support of my family. They keep saying that I am their pride, but they cannot express how important they have been throughout my studies. I will be grateful to them forever.

Andrea Masi
October 2017

Abstract

Enhancing the ability of engineers to predict the flow around the Vertical Tail Plane (VTP) of an aircraft generates important benefits to the aviation industry. For common multi-engine commercial airliners, the size of the VTP is driven by a particular flight condition - loss of an engine during take-off and low speed climb. Nowadays, Computational Fluid Dynamics (CFD) is the main tool used by engineers to assess VTP flows. However, due to uncertainties in the prediction of VTP effectiveness, aircraft designers keep to a conservative approach, which may risk oversizing of the tail plane, thus adding more resistance to the flight. Uncertainties emerge from difficulties in predicting the massive separation that occurs on the swept tail when it is approached by a flow at high incidence. Furthermore, the deployment of the control surface (the rudder) over the tail plane and the skewed flow along the span increase the CFD challenges. Improved predictive capabilities of the flow around VTPs would enable a more optimal design approach with potential resultant weight and drag savings.

The correct prediction of flow separation is the main driver of this study. Currently, the industry uses steady Reynolds-Averaged Navier-Stokes (RANS) simulations for or the assessment of VTPs flow. In order to assess RANS performance, the study of a flow detaching from a backward rounded ramp is performed in this thesis. The flow is skewed as it would be on the surface of a VTP. RANS simulations are compared to highly-resolved Large-Eddy Simulations (LES), also performed in this work. The analysis shows that, even though RANS may predict the onset of flow separation correctly, they completely miss the location of flow reattachment over the ramp, and this affects the whole flow solution. Moreover, in the LES the flow features a strong anisotropy at the onset of separation, difficult to be captured by RANS. The analysis shows that RANS cannot predict the same level of production of turbulent kinetic energy in the detached flow region, discouraging flow mixing, and delaying flow reattachment and recovery. A hybrid RANS/LES carried out on the same test case shows the benefits of using eddy-resolving simulations for detached flows. The prediction of the locations of the separation and reattachment points differs by only 1% from the highly-resolved simulation.

The VTP investigation carried out in this thesis uses a wind tunnel model tested at Airbus. The study starts with steady RANS approaches for different turbulence models. RANS simulations produce acceptable results for the flow at low incidence levels. On the contrary, at high incidence, when flow separation occurs RANS methods fail and it is not possible to assess the aerodynamic characteristics of the VTP. The second step of the research consists of using unsteady RANS (URANS) simulations for VTP flows at high sideslip angles. The introduction of time-accuracy brings important benefits. Nevertheless, the results still show some inaccuracies, especially in the local prediction of the pressure distribution over the surfaces of the model (around 20% error).

Finally, restarting from the flow solutions obtained by URANS simulations, higher fidelity hybrid RANS/LES techniques in the form of Delayed Detached-Eddy Simulations (DDES) are used to assess the characteristics of the separated flow around the tail plane. Results show a remarkable improvement of the flow solution. The pressure distribution matches experimental results favourably, and this translates into an improved prediction of the aerodynamic loads over the VTP (3-7% error with respect to experimental measurements). This leads towards a new strategy for the assessment of the flow over aircraft VTPs, amounting to an important contribution to the design of future aircraft.

Table of contents

List of figures	xv
List of tables	xxi
Nomenclature	xxiii
1 Introduction	1
1.1 A reasonable growth	1
1.2 Reduction of aircraft drag	2
1.3 The design of the vertical tail plane	4
1.3.1 Flow separation: a limiter of VTP efficiency	5
1.4 Use of Computational Fluid Dynamics in aeronautics	6
1.5 Structure of the thesis	10
2 Literature review	13
2.1 Introduction	13
2.2 Air-flow characteristics over vertical tail planes	14
2.3 CFD for VTP flow assessment	21
2.3.1 RANS simulations	23
2.3.2 LES	29
2.3.3 Hybrid RANS/LES	32
2.4 Conclusions and objectives of the thesis	39
3 Numerical methods	41
3.1 Introduction	41
3.2 Governing equations	42
3.3 Finite Volume Method	44
3.3.1 Central scheme for spatial discretization	45
3.4 Time discretization	47

3.4.1	Time-marching method for steady-state problems	47
3.4.2	Dual time-stepping for unsteady problems	49
3.5	Hybrid RANS/LES in TAU	50
3.6	Control of the artificial dissipation	52
3.7	Low-Mach number treatments	54
3.8	Data analysis	55
3.8.1	Monitoring of the residuals for steady-state simulations	55
3.8.2	Temporal-averaging for unsteady simulations	56
3.8.3	Visualising turbulence	56
3.8.4	Computation of the forces and moments over the aircraft model	57
3.9	Computer resources	59
4	Separation of a skewed boundary layer: an idealisation of VTP dynamics	61
4.1	Introduction	61
4.2	The test case	62
4.2.1	The mesh	63
4.2.2	Inflow and boundary conditions	64
4.3	Highly-resolved LES with crossflow	67
4.3.1	Overall view and major characteristics of skewed flow	67
4.3.2	Velocity and Reynolds-stress profiles	72
4.4	RANS with crossflow	76
4.4.1	Overall view and major characteristics	76
4.4.2	Velocity profiles	79
4.5	Production and dissipation of turbulent kinetic energy	82
4.6	Hybrid RANS/LES with crossflow	86
4.7	Conclusions	89
5	Steady and unsteady RANS simulations	91
5.1	Introduction	91
5.2	The VTP model	92
5.3	Steady RANS simulations	98
5.3.1	Steady results for VTP without rudder deflection	98
5.3.2	Steady results for the VTP with rudder deflection	101
5.4	Unsteady RANS simulations	104
5.4.1	Unsteady results for VTP without rudder deflection	105
5.4.2	Unsteady results for VTP with rudder deflection	108
5.4.3	Cost of the URANS simulations	111

5.5	Conclusions	111
6	Eddy-resolving simulations	115
6.1	Introduction	115
6.2	Mesh refinement	116
6.3	Flow and numerical parameters	118
6.4	Results	119
6.4.1	Overall flow characteristics	119
6.4.2	Predictions of the aerodynamic loads	125
6.4.3	Shape of the turbulence and validity of turbulence modelling	131
6.4.4	Assessment of the behaviour of the DDES delay function	133
6.5	Cost of the simulations and overall considerations	135
6.6	Conclusions	136
7	Concluding remarks and recommendations for future work	139
7.1	Conclusions	139
7.2	A strategy for the correct VTP flow assessment	140
7.3	Recommendations for future work	142
Appendix A	Reynolds-Averaged Navier-Stokes Equations	145
A.1	Navier-Stokes Equations	145
A.2	The Reynolds equations	148
A.2.1	The continuity equation in Reynolds form	149
A.2.2	Momentum equations in Reynolds form	150
A.2.3	The energy equation in Reynolds form	150
A.3	The problem of the closure	151
A.4	Filtering the equation for Large-Eddy simulations	151
Appendix B	Turbulence models	153
B.1	The Spalart-Allmaras turbulence model	153
B.2	The Menter-SST turbulence model	154
B.3	The SSG/LRR- ω turbulence model	156
Appendix C	Validation of LES on the backward ramp without crossflow	159
Appendix D	Grid convergence studies	165
D.1	Backward rounded step	165
D.2	VTP model	166

Appendix E	Wind tunnel measurements	171
E.1	Data acquisition	171
E.2	Aerodynamic corrections	172
References		175

List of figures

1.1	Trend of RPKs (in trillion US dollars) over the years. [8]	2
1.2	Rear fuselage of the Airbus A380 aircraft. Photo courtesy of Airbus.	3
1.3	Scheme of the forces and moments on the aircraft when an engine fails during take-off or climb.	5
1.4	Scheme of the forces and moments on the aircraft in the presence of cross-wind at landing.	6
1.5	CFD in aircraft design [117].	8
1.6	Turbulence modelling hierarchy [30].	10
2.1	Aircraft vertical tail plane (VTP).	16
2.2	Velocity distribution of a boundary layer in the presence of an adverse pressure gradient (image from www.thermopedia.com accessed on 12 August 2016).	17
2.3	Structure of three-dimensional boundary layer [31].	17
2.4	(a) Separation profile emanating from a separation point. (b) Separation surface emanating from a separation line [103].	18
2.5	(a) Reattachment profile emanating from a separation point. (b) Reattachment surface emanating from a separation line [103].	18
2.6	Flow visualization over a VTP at $\beta = 0^\circ$ and $\delta_r = 40^\circ$ [91].	19
2.7	Mid-span flow visualization over the rudder of a VTP at $\beta = 0^\circ$ and $\delta_r = 30^\circ$. Separation along the rudder surface. Photo courtesy of Airbus.	20
2.8	Flow visualization over a VTP at $\beta = 20^\circ$ and $\delta_r = 0^\circ$ [76].	20
2.9	Schematic of a section of the VTP	21
2.10	Use of CFD for the aerodynamic design of an Airbus A380 aircraft [2].	22
2.11	Surface pressure distribution on the NDF hump. Comparison of different turbulence models results with experimental data [67].	26
2.12	Skin-friction lines over an A330 wind tunnel model VTP at $\beta = 10^\circ$ [16].	28

2.13	Schematic representation of the main flow features of the cube, Iaccarino <i>et al.</i> [50].	29
2.14	Grid requirements against Reynolds numbers for a flow around a wing section of a span equal to the wing chord. Re-adapted from Tucker [109].	31
2.15	Sketch of flow regions around an aerofoil in rotor downwash during hover, Spalart [100].	33
2.16	Generic flight envelope of a civil transport aircraft, with examples of hybrid RANS/LES simulations, Deck <i>et al.</i> [30].	36
2.17	Visualization of the turbulent structures of the flow detaching from the spoilers over an aircraft wing [43].	36
2.18	Visualaization of the turbulent structures of the separated flow past the wing, Sartor <i>et al.</i> [90].	37
2.19	Time-averaged wing pressure distribution at six spanwise stations of the wing of the CRM, Waldmann <i>et al.</i> [119].	38
3.1	Contol volumes around points $P(j1)$ and $P(j2)$ [32].	45
3.2	Energy spectrum obtained by incompressible HYDRA LES without SGS model (readpated from Cui [27]). The experiment data is by Comte-Bellot [23].	53
3.3	Turbulent kinetic energy spectra for the DIT case. Experiment vs. TAU DDES.	53
3.4	Lumley triangle showing limits of invariants η and ξ , Hamilton <i>et al.</i> [45].	58
3.5	Pressure force acting on a boundary face (re-adapted from [32]).	59
4.1	Analogy between VTP and backward rounded step.	62
4.2	Duct with backward rounded step.	63
4.3	Grid spacing in wall units and aspect ratio $\Delta x/\Delta y$ along the bottom wall [13].	65
4.4	Flow-snapshots of the inflow for the backward rounded map test case, organized in a turbulent box. Inflow data was received from Lardeau [57].	65
4.5	Mean velocity in streamwise direction. Inflow data was received from Lardeau [57].	66
4.6	Turbulent boundary (characteristic displacement thickness $Re_\theta \approx 1190$) of the inflow [13]. Comparison with DNS data [54].	66
4.7	Source term in the z -momentum equation.	67
4.8	LES: Time-averaged flow along the duct.	68
4.9	Skin-friction lines on the wall of the backward ramp.	69
4.10	Skin-friction lines on the wall of the backward ramp. Zoom on separation and reattachment lines.	69

4.11	Instantaneous streamwise velocity.	70
4.12	Isosurface of the Q -criterion coloured by streamwise velocity.	70
4.13	Streamline contours of the time-averaged and spanwise-averaged flow field in the recirculation region.	71
4.14	Magnified streamlines.	71
4.15	Distributions of pressure and skin friction coefficients along the lower wall.	72
4.16	Mean velocity profiles	74
4.17	Reynolds stresses profiles.	75
4.18	Contour of the flatness parameter A	76
4.19	Lumley triangles of the flow in the recirculation region, with $y/H < 1.5$	76
4.20	RANS: flow along the duct.	77
4.21	Pressure coefficient over the lower wall of the duct computed by LES and RANS.	78
4.22	RANS: mean velocity profiles	80
4.23	Reynolds stresses profiles: LES vs. RSM-RANS.	81
4.24	Production of turbulent kinetic energy contours.	83
4.25	Dissipation rate of turbulent kinetic energy contours.	84
4.26	Production and dissipation of TKE for $x/H = 1.5$	85
4.27	TKE profiles along the ramp.	85
4.28	Hybrid RANS/LES: flow along the duct.	86
4.29	Hybrid RANS/LES: flow recirculation region.	86
4.30	Pressure coefficient over the lower wall of the duct computed by LES and hybrid RANS/LES.	87
4.31	Hybrid RANS/LES: mean velocity profiles	88
4.32	Hybrid RANS/LES: production of turbulent kinetic energy contours.	89
5.1	Assembly of the model in the wind tunnel. Photo courtesy of Airbus.	93
5.2	Sections of cuts of the VTP.	94
5.3	The computational domain.	94
5.4	2D sections of the VTP with a plane $z = const$	95
5.5	Aerodynamic loads generated by the VTP.	96
5.6	Surface mesh of the wind tunnel model.	97
5.7	RANS - Convergence of density residuals and sideforce: $\delta_r = 0^\circ$, $\beta =$ $0^\circ, \dots, 20^\circ$	98
5.8	RANS - Flow visualizations for $\delta_r = 0^\circ$. Top: suction side. Bottom: pressure side. Streamlines on C_p contours (RSM turbulence model).	99

5.9	RANS - Pressure coefficient for four sections of cut obtained for $\delta_r = 0^\circ$ and $\beta = 0.17^\circ$ (RSM turbulence model).	100
5.10	RANS - Convergence of density residuals and sideforce: $\delta_r = 30^\circ$, $\beta \approx 0^\circ, \dots, 20^\circ$	101
5.11	RANS - Flow visualizations for $\delta_r = 30^\circ$. Top: suction side. Bottom: pressure side. Streamlines on C_p contours (RSM turbulence model).	102
5.12	RANS - Pressure coefficient for four sections of cut obtained for $\delta_r = 30^\circ$ and $\beta = 0.17^\circ$ (RSM turbulence model).	103
5.13	URANS - Flow visualizations for $\delta_r = 0^\circ$ and $\beta = 14^\circ$ (averaged skin-friction lines, Menter SST turbulence model).	105
5.14	URANS - Pressure coefficient for four sections of cut obtained for $\delta_r = 0^\circ$ and $\beta = 14^\circ$	106
5.15	URANS - Instantaneous Mach number contours with time-averaged streamlines, for $\delta_r = 0^\circ$ and $\beta = 14^\circ$. Section A-A (Menter SST).	107
5.16	URANS - Flow visualizations for $\delta_r = 30^\circ$ and $\beta = 10^\circ$ (averaged skin-friction lines, Menter SST turbulence model).	109
5.17	URANS - Pressure coefficient for four sections of cut obtained for $\delta_r = 30^\circ$ and $\beta = 10^\circ$	110
5.18	URANS - Mach number contours with time-averaged streamlines for $\delta_r = 30^\circ$ and $\beta = 10^\circ$. Menter-SST turbulence model. Section A-A.	111
5.19	URANS - Isosurface of the Q criterion for $\delta_r = 30^\circ$ and $\beta = 10^\circ$. Menter-SST turbulence model.	112
6.1	Schematics of a section of VTP at high sideslip angle.	116
6.2	Surface contours showing Δy^+ for wall cell height.	117
6.3	Schematic of the grid refinement procedure [32].	118
6.4	Mesh refinement in the target zone.	118
6.5	Flow visualizations for $\delta_r = 0^\circ$ and $\beta = 14^\circ$ for the averaged flow, showing skin-friction lines and C_p colour contours. Comparison SST-URANS vs. SST-DDES.	120
6.6	DDES - Instantaneous Mach number contours with time-averaged streamlines, for $\delta_r = 0^\circ$ and $\beta = 14^\circ$. Section A-A $\eta = 0.7$	121
6.7	DDES - Instantaneous isosurface of the Q -criterion for $\delta_r = 0^\circ$ and $\beta = 14^\circ$ coloured by streamwise velocity.	121
6.8	Flow visualizations for $\delta_r = 30^\circ$ and $\beta = 10^\circ$ for the averaged flow, showing skin-friction lines and C_p colour contours. Comparison SST-URANS vs. SST-DDES.	122

6.9	DDES - Instantaneous Mach number contours with time-averaged streamlines for $\delta_r = 30^\circ$ and $\beta = 10^\circ$. Section A-A ($\eta = 0.7$).	123
6.10	Comparison of URANS and DDES turbulent structures for $\delta_r = 30^\circ$ and $\beta = 10^\circ$.	124
6.11	DDES - Pressure coefficient for four sections of cut obtained for $\delta_r = 0^\circ$ and $\beta = 14^\circ$.	126
6.12	DDES - Evolution of the side force coefficient with time, $\delta_r = 0^\circ$ and $\beta = 14^\circ$.	127
6.13	DDES - Evolution of the yaw moment coefficient with time, $\delta_r = 0^\circ$ and $\beta = 14^\circ$.	127
6.14	Comparison of the accuracy of the three CFD methods ($\delta_r = 0^\circ$ and $\beta = 14^\circ$).	128
6.15	DDES - Pressure coefficient for four sections of cut obtained for $\delta_r = 30^\circ$ and $\beta = 10^\circ$.	129
6.16	Comparison of the accuracy of the three CFD methods ($\delta_r = 30^\circ$).	130
6.17	Fourier Transform of the side force coefficient with respect to the Strouhal number.	131
6.18	Three snapshots of the flow solution for $\eta = 0.8$.	131
6.19	Flatness parameter for a section of the flow field.	132
6.20	Lag between shear stresses and strains for a section of the flow field.	133
6.21	Isosurfaces of the Q criterion coloured by the delay function f_d .	134
6.22	Contour map of the delay function f_d for $\eta = 0.7$.	135
7.1	Suggested strategy for VTP flow assessment.	141
A.1	Control volume fixed in space, with the fluid flow moving through it [10].	145
A.2	Reynolds decomposition.	148
B.1	SSG/LRR- ω Reynolds stress scheme.	156
C.1	Pressure coefficient C_p obtained by LES without crossflow and comparison with reference data by Bentaleb <i>et al.</i> [13].	160
C.2	Validation velocity profiles.	161
C.3	Validation velocity profiles.	163
D.1	Grid independence study on RANS mesh for the backward rounded ramp. u velocity contours and streamlines.	166
D.2	Comparison of the flow velocity profiles obtained on the baseline and refined grids.	167
D.3	Density residual for the refined mesh for $\beta = 0^\circ$.	168

D.4	Flow visualization for the refined mesh for $\beta = 0^\circ$	168
D.5	Grid convergence study: baseline mesh vs. refined mesh, $\delta_r = 0^\circ$ and $\beta = 0^\circ$	169
E.1	Wind tunnel constraints. Picture courtesy of Airbus.	173
E.2	Wind tunnel support corrections. Picture courtesy of Airbus.	174

List of tables

2.1	Reattachment point of the flow downstream a cube. Analysis of results from Iaccarino <i>et al.</i> [50].	29
2.2	Landing gear study: wheel drag coefficient. Analysis of results from Hedges <i>et al.</i> [46].	34
3.1	Smoothing coefficient used in the thesis.	47
3.2	Features of the clusters used for VTP simulations.	60
4.1	Grid sizes for LES, RANS and hybrid RANS/LES of the backward ramp.	64
4.2	Comparison of separation and reattachment locations.	77
4.3	Comparison of separation and reattachment locations.	87
5.1	VTP geometry.	92
5.2	Sections of cut of the VTP.	92
5.3	RANS mesh details.	97
5.4	Loading on the VTP at $\beta = 0.17^\circ$ and $\delta_r = 30^\circ$	104
5.5	Loading on the VTP for $\delta_r = 0^\circ$ at $\beta = 14^\circ$	107
5.6	Comparison between period and turbulent timescales in the SST and RSM URANS simulations.	108
5.7	Loading on the VTP at $\beta = 10^\circ$ and $\delta_r = 30^\circ$	111
5.8	Accuracy vs. costs of URANS.	111
6.1	DDES mesh details.	118
6.2	DDES test cases.	119
6.3	Loading on the VTP at $\beta = 14^\circ$ and $\delta_r = 0^\circ$	127
6.4	Loading on the VTP at $\beta = 10^\circ$ and $\delta_r = 30^\circ$	128
6.5	Accuracy vs. costs of URANS and DDES.	136
B.1	Constants for the SA turbulence model.	154
B.2	Constants for the SSG/LRR- ω RSM turbulence model ($C_2^{(LRR)} = 0.5556$).	158

C.1 Comparison of separation and reattachment locations. 160

D.1 Backward rounded ramp grids comparison (no. of grid points). 165

D.2 VTP grid comparison. 166

Nomenclature

Roman Symbols

A	First invariant (flatness parameter)
A_2	Second invariant
A_3	Third invariant
C_L	Lift coefficient
C_{D_0}	Zero-lift coefficient
C_{D_i}	Induced drag coefficient
C_{DES}	DES coefficient
C_{f_y}	Side-force coefficient
CFL	Courant number
Cm_z	Yaw moment coefficient
C_p	Pressure coefficient
E^+	Normalised turbulent kinetic energy
f	Frequency OR Body force (source term) in Navier-Stokes equations
f_d	DDES delay function
F_y	Force in y -direction (side-force)
IQ	Quality index
k	Turbulent kinetic energy

k^+	Normalised wavenumber
kL	Wavenumber multiplied by the integral length scale
l_{hyb}	Hybrid RANS/LES length scale
l_{LES}	LES length scale
l_{RANS}	RANS length scale
M_∞	Free stream Mach number
M_z	Moment in z -direction (yaw moment)
P_k	Production of turbulent kinetic energy
Q	Second scalar invariant of the velocity derivative tensor
Re	Reynolds number
St	Strouhal number
t_i	Turbulent timescale
t_p	Unsteadiness period
u	x -velocity
v	y -velocity
V_∞	Free stream velocity
w	z velocity
y^+	Dimensionless wall distance
y_{wall}	Wall coordinate
CFD	Computational Fluid Dynamics
CPU	Computer Power Unit
DDES	Delayed Detached-Eddy Simulation
DES	Detached-Eddy Simulation
DR	Departure Region

ER	Euler Region
FR	Focus Region
HPC	High-Performance Computing
IDDES	Improved Delayed Detached-Eddy Simulation
LES	Large-Eddy Simulation
MAC	Mean Aerodynamic Chord
MPI	Message Passing Interface
NS	Navier-Stokes
RANS	Reynolds-Averaged Navier-Stokes
RPK	Revenue Passenger Kilometres
RSM	Reynolds Stress Model
SA	Spalart-Allmaras turbulence model
SST	Menter Shear-Stress Transport model
TKE	Turbulent kinetic energy
URANS	Unsteady Reynolds-Averaged Navier-Stokes
VTP	Vertical Tail Plane

Greek Symbols

α_{MA}	Stress-strain misalignment angle
β	Sideslip angle
δ_r	Rudder deflection angle
η	Normalised spanwise coordinate

Chapter 1

Introduction

1.1 A reasonable growth

Aviation has changed society dramatically in the last century, introducing new, efficient, and fast ways of transporting people and goods. The growth of air traffic in the last 50 years has been impressive and projections by the Advisory Council for Aeronautics Research in Europe (ACARE) show that this trend is likely to continue in the future [3]. Air traffic is already well-established in developed countries, with many routes connecting North America with Europe. However, nowadays developing markets, such as China, India, and Brazil, are participating more and more in the world economy, and air traffic is reflecting this. The number of *mega-cities* will increase within the next 20 years and air traffic is likely to increase in proportion to connect these hubs of the global economy [8]. Airbus, for example, has reported an analysis by the ICAO (International Civil Aviation Organization), showing that, since air transport began, Revenue Passenger Kilometres¹ (RPKs) have doubled every 15 years, despite the economic crisis of 2008. Figure 1.1 shows that, In 2012, global RPKs were equal to 6.5 trillion US dollars, whereas in 2032 this amount will reach around 14 trillion US dollars. As a consequence, the global aircraft fleet will need to grow.

This forecast is promising not only for the world economy, but also for research and technological development. In fact, the aviation industry involves a lot of sectors which will see the benefits of common technological development. However, there are many challenges in terms of sustainability. The amount of greenhouse gas emissions will increase worryingly if aircraft manufactures do not try to reduce them through the use of advanced technologies. In addition, attention needs to be paid to acoustic pollution: airports will be busier and busier; new hubs will appear, and more people will be affected by aircraft noise. Furthermore,

¹RPKs = Number of revenue-paying passengers multiplied by the distance travelled.

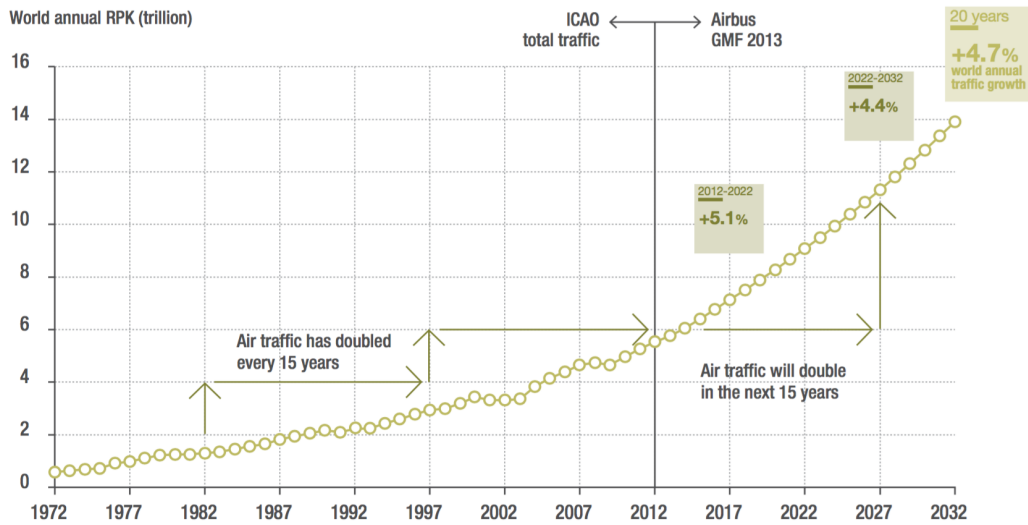


Fig. 1.1 Trend of RPKs (in trillion US dollars) over the years. [8]

governments already impose high charges on air traffic, which could increase in the near future, possibly causing a shift of passengers towards cheaper transport systems over short distances, such as the train. The aviation industry must act now to achieve improvements in aircraft performance, therefore sustain reasonable growth.

1.2 Reduction of aircraft drag

Aircraft design is highly advanced. Thanks to research and development in the last century, manufacturers constantly try to improve the aircraft design, in order to sell competitive products. Fuel consumption is one of the most critical parameters of aircraft performance. Reducing the consumption of kerosene gives rise to two main advantages: a reduction in the emission of pollutant gases (NO_x and CO_2), and a cut in the operating costs. The aviation engine industry works hard to design efficient engines, but to reduce fuel consumption, first of all it is necessary to optimize the aerodynamic shape of the aircraft. Engines have to generate the thrust to sustain the aircraft in the air. The higher the resistance the aircraft generates in flight, the higher the thrust generated by the engines needs to be, and the higher the fuel consumption. For this reason, reducing aircraft drag, the force that opposes the motion of the aircraft through the air, is a top priority of the aviation industry.

Aerodynamic drag is a mechanical force generated by the interaction and contact of a solid body (the aircraft) with a fluid in motion (the air). In aircraft subsonic aerodynamics, drag comprises two contributions: the zero-lift drag and lift induced drag. The former is due to frictional resistance of the body passing through the air. The latter is caused by

the generation of lift. It is also called ‘drag due to lift’ because it only occurs on finite, lifting wings. For a lifting wing, there is a pressure difference between the upper and lower surfaces of the wing. Vortices are formed at the wing tips, which produce a swirling flow that is very strong near the wing tips and decreases towards the wing root. The wing’s local angle of attack is increased by the induced flow of the tip vortex, giving an additional, downstream-facing component to the aerodynamic force acting on the wing. The force is called ‘induced drag’ because it has been ‘induced’ by the action of the tip vortices.

In cruise conditions, drag contributions are almost equally divided among wing, fuselage, and nacelles (30% each), and 10% at the tail planes, equally split into 5% for the horizontal tail and 5% for the vertical tail [77]. This thesis studies a particular aircraft component - the Vertical Tail Plane (VTP), or vertical stabilizer. The installation of the VTP on the rear part of the fuselage requires high assembly complexity and significant mass. Figure 1.2 shows the rear part of the Airbus A380, the biggest passenger aircraft in the world. The VTP span is about 15 metres long and the geometric mean chord is approximately equal to seven metres. The photo gives a sense of how big these dimensions are compared to the human size. Therefore, one can imagine that this component generates a large drag. Being a crucial element for the manoeuvrability of the aircraft, the VTP has to be efficient and has to ensure safety, and no design errors are allowed. A smaller fin would help designers to accrue benefits in aircraft performance. To achieve this, it is necessary to improve current aerodynamic design capabilities.



Fig. 1.2 Rear fuselage of the Airbus A380 aircraft. Photo courtesy of Airbus.

1.3 The design of the vertical tail plane

In order to ensure manoeuvrability and control, aircraft are equipped with a flight control system. The flight control system consists of primary and secondary controls. Primary controls include the ailerons, the elevators, and the rudder and are mounted respectively on the wing, the horizontal, and the vertical tail planes. The ailerons control the roll of the aircraft, the elevators control the pitch, and the rudder governs the yaw. However, there are also coupled effects that the controls can generate by their activation. The throttle is also a primary control which acts on the thrust generated by the engine or engines. Secondary controls generally give the pilot finer control and can alleviate their workload. Some of the secondary controls are the elevator trim, the flaps, and the slats. This thesis focuses upon the vertical tail plane, which consists of two parts: one is fixed (the fin), and the other (the rudder) can rotate around a hinge axis. The conventional tail configuration for commercial airliners consists of fuselage-mounted tail planes, and both the horizontal and the vertical tails are anchored to the rear fuselage. This configuration shows high efficiency and increased manoeuvrability capabilities compared to other shapes.

The criteria that drive the design of the VTP are given in FAR Part 23.149 and FAR Part 25.149 (Federal Aviation Regulations) and have been summarized in several books of aircraft design. Torenbeek [104] identifies four requirements for the VTP:

- a. the vertical tail plane must not stall as a result of an oscillation after deflection of the rudder or sudden engine failure;
- b. after failure of the critical engine, multi-engined aircraft must remain controllable to ensure steady flight;
- c. it should be possible to land transport aircraft in crosswinds up to 30 knots (55 km/h), and
- d. the aircraft must possess positive directional and lateral static stability and short-period lateral/directional oscillation (Dutch roll) must be damped.

The condition of engine failure is the most critical if the VTP is to maintain control over the aircraft. The failure of an engine is most critical during take-off and climb, due to the low speed of the aircraft. In four engine configurations, such as the A380, the case of two-engine-failure is the most restrictive design condition. As Figure 1.3 shows, the failure of an engine causes a yawing moment which must be balanced through deflection of the rudder on the VTP. Due to the coupling of aerodynamic effects on the aircraft's longitudinal and lateral planes, a minor effect of engine failure consists of a rolling moment, which must

be controlled by use of the wing ailerons. This particular flight condition determines the size of the VTP and the rudder efficiency; it might also affect the size of the ailerons on the wing.

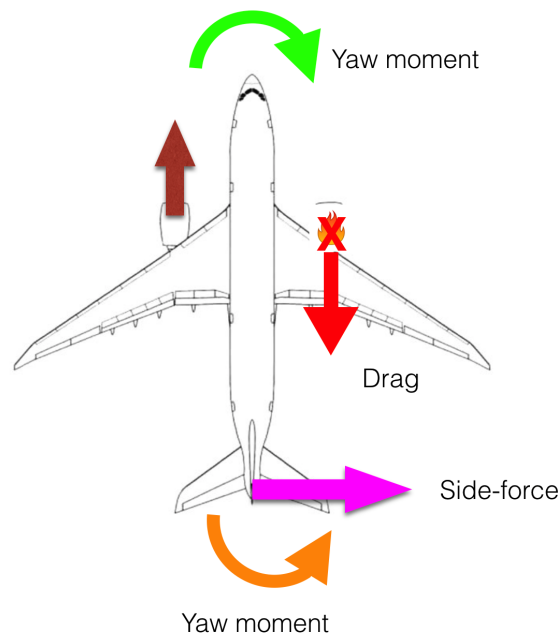


Fig. 1.3 Scheme of the forces and moments on the aircraft when an engine fails during take-off or climb.

Crosswind landing is another particular flight condition that drives the size of the VTP. As sketched in Figure 1.4, a crosswind unbalances the aircraft, so the rudder must be used to balance the forces on the aircraft.

Finally, in order to have a symmetric flight in normal flight conditions, the section of the aerofoil of the VTP must be symmetrical.

1.3.1 Flow separation: a limiter of VTP efficiency

The flow around the aircraft generates forces and moments that sustain and control the aircraft. If the flow detaches from the aircraft surfaces, these forces and moments are generally reduced. The worst case consists of the stall of that flying surface, which then loses its efficiency. This is commonly known for the most important component of an aircraft, the wing. However, flow separation can also affect the vertical tail surfaces. For this reason, it is important to design all of the components of the aircraft in order to delay flow separation as much as possible. Moreover, it is necessary to understand when flow separation occurs, where the onset of detachment is, and how far the efficiency of the flying surfaces is

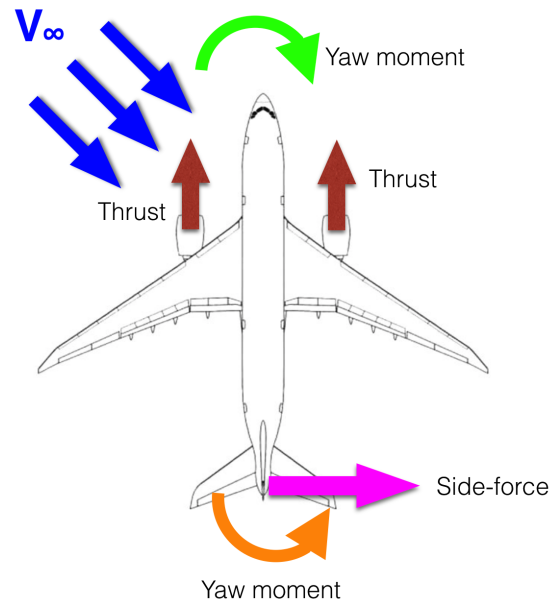


Fig. 1.4 Scheme of the forces and moments on the aircraft in the presence of crosswind at landing.

affected. At present the problem is that, due to current uncertainties in aerodynamic design and lack of experimental data at operative Reynolds numbers, aircraft designers tend to use a conservative approach in sizing the VTP. This is to ensure that, even if flow separation occurs earlier than predicted by design, it is possible to maintain the efficiency of the rudder control. If prediction methods can be improved, weight and drag savings could be achieved through the use of smaller VTPs. The objective of this thesis is to assess the flow around a VTP, validating computational methods that can provide an accurate answer to the problem of flow separation. The objective will be explained further in Chapter 2.

1.4 Use of Computational Fluid Dynamics in aeronautics

The criteria that must be followed to design a VTP define particular flow conditions, which include low speed (compared to general aircraft cruise speed), turbulence, and flow separation. Therefore, the assessment of VTPs flow is challenging and research is currently investing a lot of resources to address this task. This thesis suggests ways and opportunities to improve the design of tail surfaces through the use of novel numerical techniques in Computational Fluid Dynamics (CFD). Spalart and Bogue [96] observe that CFD is used not only in design conditions, but also in off-design conditions. Tucker [107] explains that CFD

is used in external aerodynamics, in cabin ventilation flows, and also in avionics, electronics, and fire management. CFD is a powerful tool in aerodynamic design and is widely used in the aviation industry. As we see in Figure 1.5, it takes its proper place in the design process. The ‘CFD Environment’ includes:

1. Geometry and CAD modelling: every test case that needs to be studied has to be represented via computed-aided design (CAD) software on a machine;
2. Grid generation: the geometry needs a mesh, which is a grid consisting of points that define subdomains of the flow;
3. Solver computation: the mesh is given to a solver, which implements some algorithms to compute the flow. The task of the solver is to *resolve* or *model* the Navier-Stokes equation, which will be presented later in the thesis, and
4. Post-processing: Once the solution has been obtained, it needs to be analysed and visualized.

Grid generation is considered as the bottleneck of CFD for many reasons, as explained by Vos *et al.* [117]. First of all, meshing is usually a time-consuming task, which needs good precision. Often the process is not automated, and requires constant inputs from the user. For the VTP, challenging meshing areas are the intersection between the fuselage and the tails, and also the gap between VTP and fuselage in the case of rudder deflection. Secondly, the quality of the mesh needs to be constantly tested and the user must make sure that the results are not grid-dependent.

The computation performed by the solver needs to represent the physics of the flow around the VTP in design conditions. But why is this flow challenging for CFD simulations? The main challenge resides in the presence of flow separation. In fact, when the flow reaches the vertical tail surfaces with a high angle of attack, flow detachment can occur along the fin. Eventually, as the angle of attack increases, the tail surface can also stall, leading to loss of VTP efficiency. A massively detached flow is extremely unsteady and turbulent, and results in being very difficult to study with current industrial tools. Another location of flow separation for the VTP is the deflected rudder, and the flow tends to separate around the hinge axis. Hence, for this configuration, the tail plane has two different locations of flow separation, and CFD simulations are even more challenging.

Challenges also include the turbulent character of the flow. Most aerospace flows involve high Reynolds numbers and will typically have turbulent boundary layers over all surfaces. In 1964 physicist and philosopher Richard Feynman stated: “Turbulence is the last great unsolved problem in classical physics”. And, although many studies have been done on this

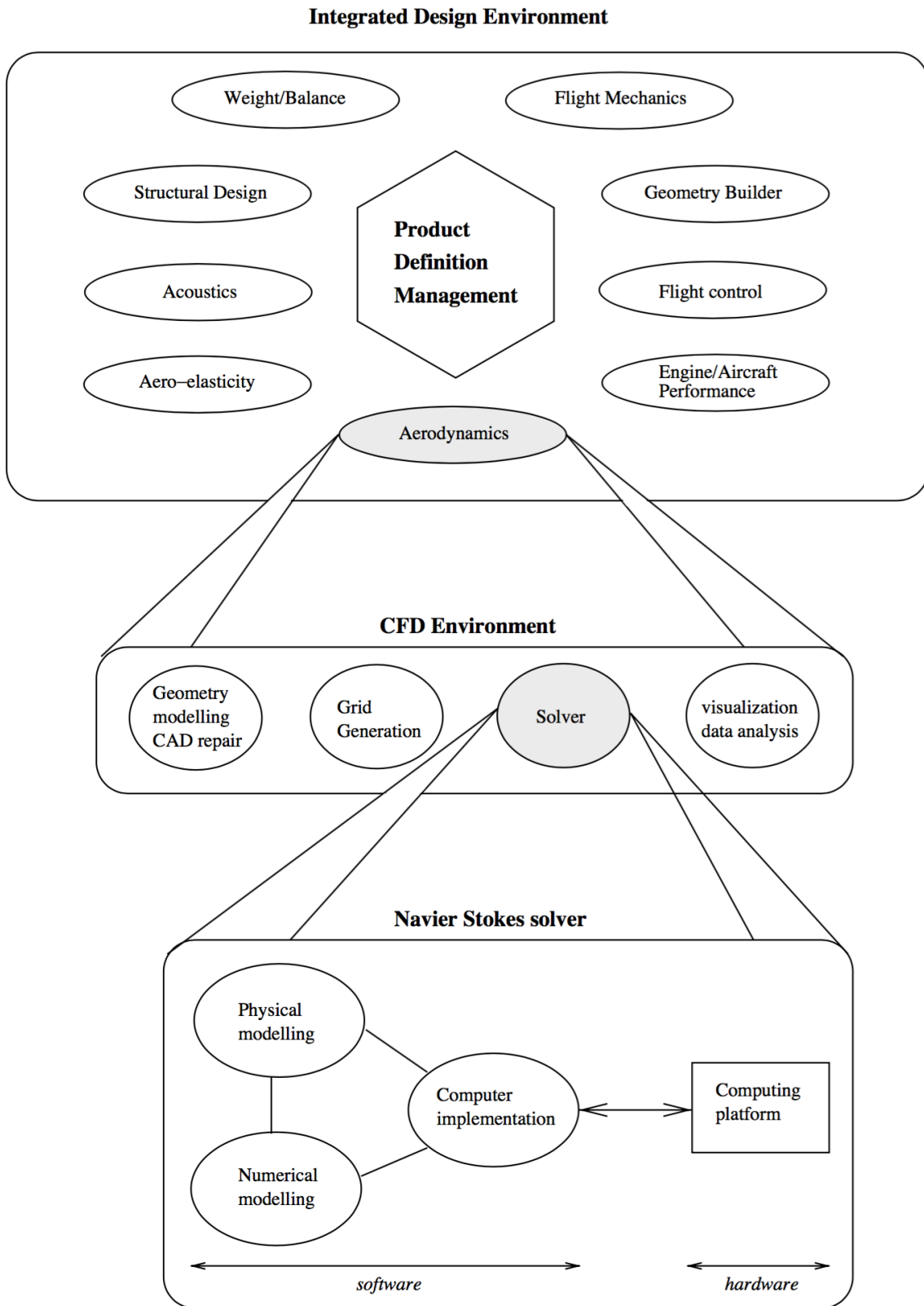


Fig. 1.5 CFD in aircraft design [117].

subject, the problem of characterizing turbulence is still open. In 1510, Leonardo made the first attempt to study fluid motion. Observing water, he wrote²:

*”Observe the motion of the water surface,
which resembles that of hair, that has two motions:
one due to the weight of the shaft,
the other to the shape of the curls;
thus, water has eddying motions,
one part of which is due to the principal current,
the other to the random and reverse motion.”*

Leonardo understood that the motion of a fluid can be divided into a mean part and a fluctuating part. The lack of mathematical tools did not enable him to formulate this principle, and several centuries had to pass before Reynolds would introduce the decomposition that bears his name (see Appendix A). Introducing the Reynolds decomposition in the Navier-Stokes equations and time-averaging leads the way towards the formulation of the Reynolds-Averaged Navier-Stokes (RANS) equations, which are the industry tool most widely used nowadays for computational aerodynamic design (see Appendix A). In the RANS equations, new unknowns appear - the ‘Reynolds stresses’ - and modelling of the turbulence is necessary for the closure of the system of the equations.

Another technique used in CFD is Large-Eddy Simulation (LES). Its formulation derives from another kind of mathematical decomposition (see Appendix A). The main idea behind LES consists of *resolving* the large scales of turbulence within a flow, and modelling the small scales of turbulence. As will be discussed in Chapter 2, using LES for whole aircraft geometries is still computationally prohibitive.

Between RANS and LES, hybrid methods settle. Their scope is to combine the accuracy of LES for those flows which RANS cannot capture correctly with the simplicity of the RANS technique in regions where a more accurate simulation is not needed.

Figure 1.6 shows the classification of the CFD methods cited above in a pyramid organized with respect to the accuracy of the CFD technique. Steady and unsteady RANS methods are less accurate and more turbulence model-dependent, therefore they are at the bottom of the pyramid. However, relative to the other methods, their cost is low, hence the industry uses them as design tools. Hybrid RANS/LES and LES then follow. At the top of the pyramid, Direct Numerical Simulation (DNS) is found. This is the only CFD approach that does not need any sort of modelling, but its application on industrial cases is currently prohibitive, due to the level of grid and time refinement that is necessary.

²Translated by Piomelli [80].

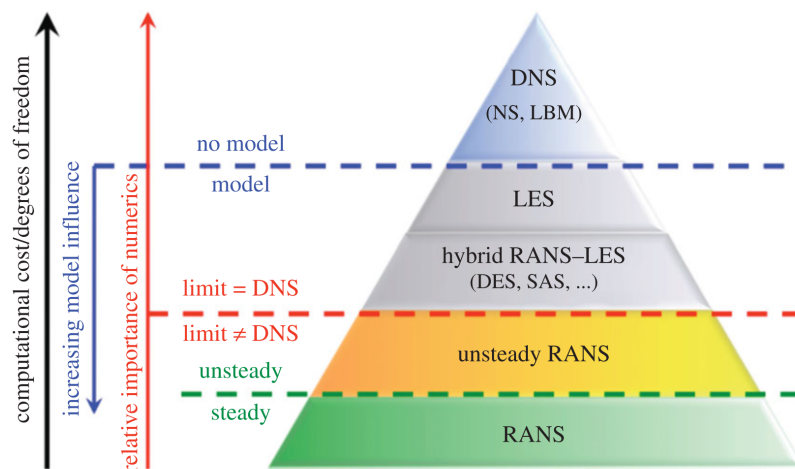


Fig. 1.6 Turbulence modelling hierarchy [30].

In this thesis attention is paid to RANS, URANS, hybrid RANS/LES, and LES approaches, with the aim of understanding how the aerodynamic prediction of the flow around a vertical tail plane can be improved.

1.5 Structure of the thesis

Chapter 2 presents a literature survey, which aims to understand the physics of the flow around aircraft stabilizers and which CFD methodologies may be successful (or not successful) for predicting VTP air-flow characteristics. This will help define the objectives of the thesis, together with a strategy for the assessment of VTP flows.

Chapter 3 illustrates the methodology used for the CFD analysis performed in this thesis, with special attention to eddy-resolving methods.

Chapter 4 presents the study of a three-dimensional boundary layer separating from a backward rounded ramp. Since the correct prediction of flow separation is key important for the assessment of the flow around a VTP, the test case studied in Chapter 4 highlights the reasons why industrial CFD methods, based on RANS approaches, fail to predict a detached flow. Eddy-resolving simulations will be also investigated.

Chapters 5 and 6 address the problem of CFD simulations over an aircraft VTP for different sideslip angles and two configurations of the rudder control (zero deflection and 30° deflection). Chapter 5 presents steady and unsteady RANS simulations, and highlights their accuracies and their limits with VTP flows at high incidence. In Chapter 6, the use of eddy-resolving simulations will be investigated.

Using the insights gained from the results chapter, in the final chapter a strategy for the correct VTP flow assessment is suggested.

Chapter 2

Literature review

2.1 Introduction

In the public literature, few CFD studies of vertical tail planes are available, although many studies of aircraft wing-body configurations have been published. However, the flow topology around the VTP is quite different from that observed around a wing. This is due to the fact that wings and vertical fins have to satisfy different design criteria and performance requirements. Generally, for a commercial two-engine (or four-engine) aircraft, the VTP consists of a low-aspect-ratio wing, which is equipped with a movable control surface (the rudder), that is deflected when needed. Most wing-body CFD studies cover test cases at cruise speed ($M_\infty \approx 0.8$), involving transonic flows and eventually the presence of shock waves. By contrast, as discussed in the introduction, in VTP design there is growing interest in CFD for low-velocity regimes (take-off or landing speeds), high sideslip angles, and deflected rudders.

This literature survey aims to understand the physics of the flow around aircraft stabilizers and which CFD methodologies may be successful (or not successful) for predicting VTP air-flow characteristics. Since VTP design conditions involve flows at high sideslip angles and/or high rudder deflections, the problem of flow separation is the main driver of this study, and we need to investigate how CFD tackles this problem in the current state of the art. To achieve this, the literature review covers RANS, LES and hybrid RANS/LES studies, discussing the applications that are relevant to this thesis. This will lead to the definition of the objectives of this work and the research strategy will be drawn.

A better understanding of the behaviour of the flow around a VTP can bring important improvements to aerodynamic design. First of all, the prediction of the pressure distribution, hence of the aerodynamic loads, can come closer to the measurements, and this would impact directly the sizing of the VTP. Moreover, a deep understanding of the separation mechanisms

on the VTP can lead to the design of more efficient active flow control devices¹. In fact, today the industry is interested in the possibility of delaying or suppressing flow separation from aircraft surfaces, including the vertical fin and the rudder, through the use of passive and active flow control technologies, as explained by Abbas *et al.* [1, 2]. Hence a correct prediction of VTP flow is important for a useful outcome in the design of such systems. Furthermore, it would also be beneficial for the improvement of rapid-CFD methods, which are used in the preliminary conceptual design of an aircraft. Therefore, this research may open new scenarios for future work.

When can a CFD flow solution be considered good enough for VTP design? There is no straight answer to this question. In 1998, in a report from AIAA² it was stated that “validation is the process of determining the degree to which a [CFD] model is an accurate representation of the real world from the perspective of the intended uses of the model” [5]. Unfortunately it is not possible to give a definite answer about the maximum allowable error from a CFD simulation with respect to experimental data. Aircraft manufacturers generally assess the validity and the accuracy of a CFD simulation based on the following criteria:

- examination of the iterative convergence of the numerical simulation;
- examination of the consistency of the CFD solution, in terms of comparison with previous or similar studies;
- examination of the convergence with respect to the mesh refinement of the computational domain (if possible);
- comparison with experimental data, and
- examination of model uncertainties.

Therefore, these steps need to be followed in order to assess the validity of the flow solutions presented in this thesis.

2.2 Air-flow characteristics over vertical tail planes

Today, the most common VTP geometry chosen for civil aircraft consists of fuselage-mounted tail planes, which ensure a better response in controllability and manoeuvrability of the aircraft with respect to other configurations. The VTP, also known as stabilizer, is divided into two main components, that is, the fin, which does not move, and the rudder,

¹Flow control devices prevent or delay flow separation over a flying surface.

²American Institute of Aeronautics and Astronautics.

which can rotate around the hinge line (see Figure 2.1a). The root of the VTP is connected to the fuselage (omitted in the picture); usually the tail is tapered, which means that the tip has a smaller chord with respect to the root. The sweep angle suggests a decomposition of the free stream flow velocity V_∞ into two components (Figures 2.1b): V_\perp perpendicular to the leading edge, and V_\parallel which is parallel to the leading edge. Therefore the flow is characterized by marked three-dimensionality, with a component of the velocity that runs along the span of the tail (spanwise).

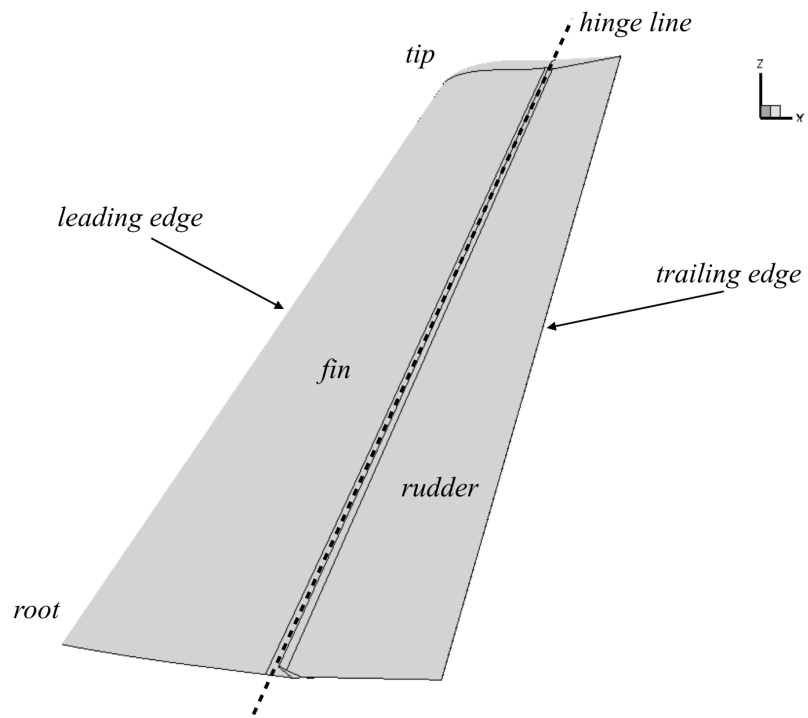
As explained earlier, the design conditions of flow around VTPs involve high incidences, which may lead to flow separation. The problem of flow separation was firstly studied by Prandtl, in the formulation of the theory of boundary layers. As reported by Chang [74], Prandtl states flow separation occurs under two conditions:

- adverse pressure gradient along the flow path, and
- viscosity effects.

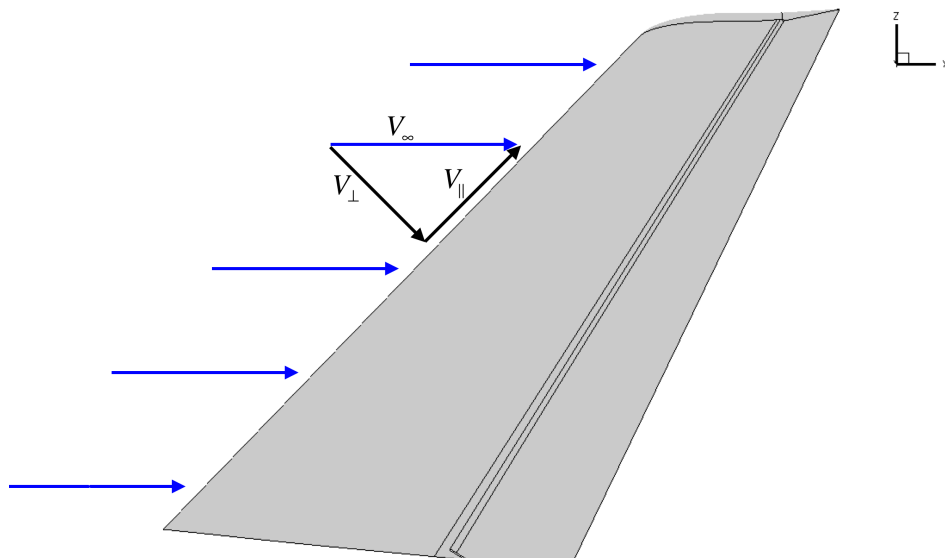
Flow separation cannot occur without viscosity. Prandtl proved this by looking at the flow in a channel; in the diverging part (where the adverse pressure gradient is present) the boundary layer tends to separate. The scientist did the same experiment by sucking away the boundary layer from the walls of the channel, showing that flow did not separate.

Figure 2.2 shows what happens in the boundary layer in the presence of an adverse (positive) pressure gradient, that is, the pressure increases in the flow direction. The adverse pressure gradient causes fluid particles in the boundary-layer to slow down at a greater rate than that is due to boundary-layer friction alone. The flow loses energy and the velocity distribution changes gradually from sections 1 to 4. In section 3, a point of inflection in the velocity profile appears. This stage, denoted by S, is the onset of separation. The flow evolves further and reverses, as shown in section 4. The dashed line *a-a* denotes the locus of the points where the velocity is null. The separation generates reverse flows and swirls.

For industrial geometries, flow separation is more complex due to the presence of three-dimensional boundary layers, as shown in Figure 2.3. The picture shows that the velocity distribution is given by two contributions: the streamwise profile and the crossflow profile. Flow separation over aircraft surfaces can be detected by looking at the skin-friction lines, as explained by Delery [31] and Surana *et al.* [103]. When flow separation occurs, skin-friction lines show a mathematical singularity over the surface, converging or tending to converge towards a single line. By contrast, when the flow reattaches to the surface, the skin-friction lines diverge, redistributing sensibly on the surface. This is shown in figures 2.4 and 2.5 respectively. Skin-friction lines can also show the presence of vortical structures downstream



(a) VTP components.



(b) Flow decomposition over a VTP.

Fig. 2.1 Aircraft vertical tail plane (VTP).

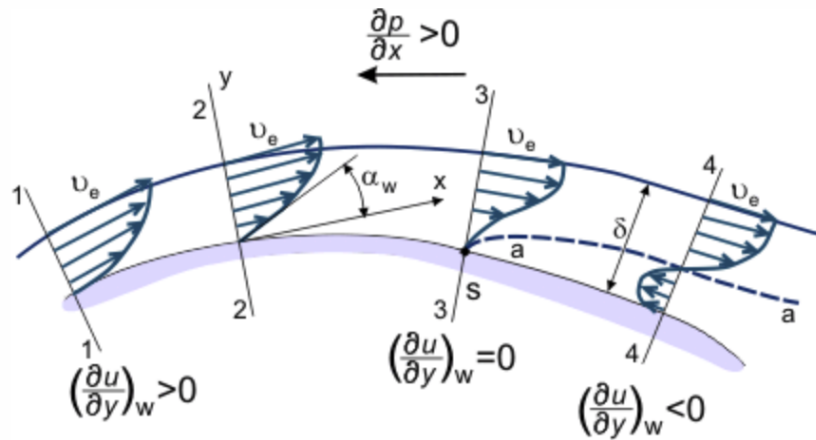


Fig. 2.2 Velocity distribution of a boundary layer in the presence of an adverse pressure gradient (image from www.thermopedia.com accessed on 12 August 2016).

of the separation. For these reasons, the use of skin-friction line plots from numerical computations is a method that can satisfactorily show the presence of separated flows.

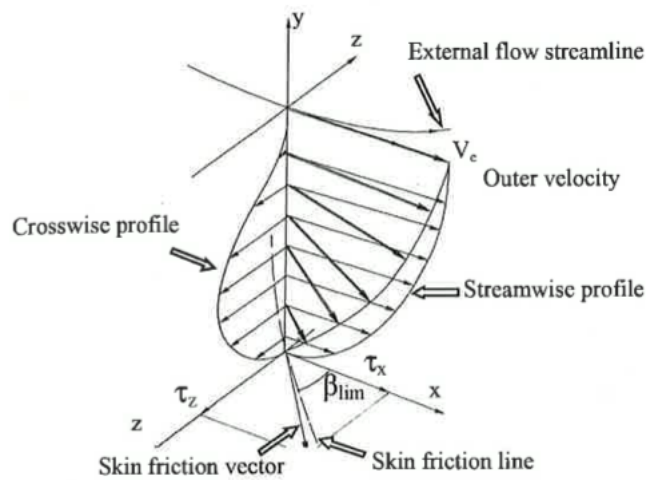


Fig. 2.3 Structure of three-dimensional boundary layer [31].

Experimental observations and CFD simulations have shown that aircraft VTPs feature flow separation in the presence of a high sideslip angle of the flow and/or when the rudder control surface is deflected. For example, Seele *et al.* [91] have recently performed a test campaign at the CalTech³ Wind Tunnel, in which they assess the performance enhancement of a vertical stabilizer equipped with flow control devices. In the baseline experiment (without flow control devices), the authors present flow visualizations for a VTP at zero sideslip angle

³California Institute of Technology.

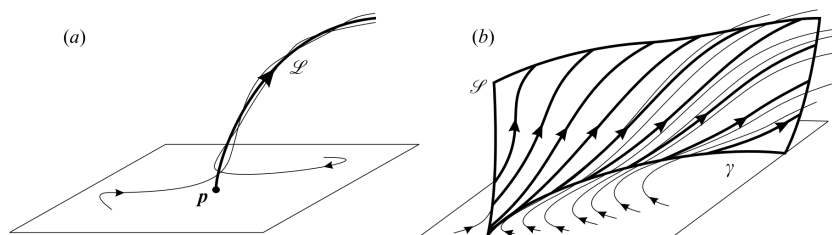


Fig. 2.4 (a) Separation profile emanating from a separation point. (b) Separation surface emanating from a separation line [103].

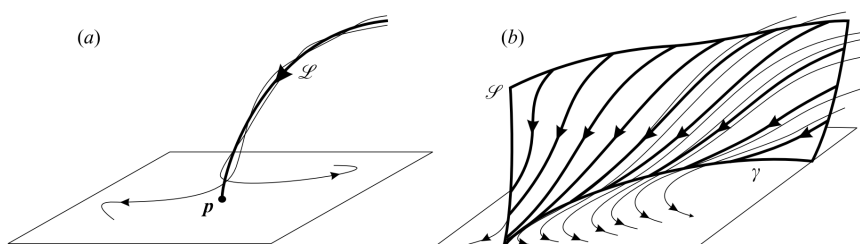


Fig. 2.5 (a) Reattachment profile emanating from a separation point. (b) Reattachment surface emanating from a separation line [103].

and at different angles of deflection of the rudder. The flow is visualized through the use of tufts, which are small lengths of string attached to the surface at one end and frayed at the other. The tufts adhere to the tested surface if the flow is attached, whereas they detach from the surface if the flow is separated. Figure 2.6 shows that for about 40° of rudder deflection (80% of its maximum extension), the flow topology over the fin is quite different from the one over the rudder. In fact, on the fin the flow is attached and the streamlines are parallel to the free-stream flow. Aft of the hinge, the tuft deflections show unevenness, which would suggest more disturbed flow due to separation. A similar study has been performed at Airbus, through the use of surface oil visualizations. Figure 2.7 shows the streamlines over a VTP at zero sideslip angle and 30° rudder deflection. The streamlines reach the hinge-line and change direction feeding the vortex tip. A separation line is located along the rudder, running upwards along the span.

Varying the sideslip angle of the free-stream flow modifies the flow topology over the VTP, as derived from a wind tunnel test by Nicolosi *et al.* [76]. The authors study the flow around a vertical stabilizer at Reynolds number equal to $4.6 \cdot 10^5$ (based on the mean chord), and sideslip angle $\beta = 20^\circ$. The flow speed is equal to 50 m/s. Figure 2.8 shows the VTP configuration with tufts on the suction side surfaces. The flow is completely separated, as depicted by recirculation of the tufts.

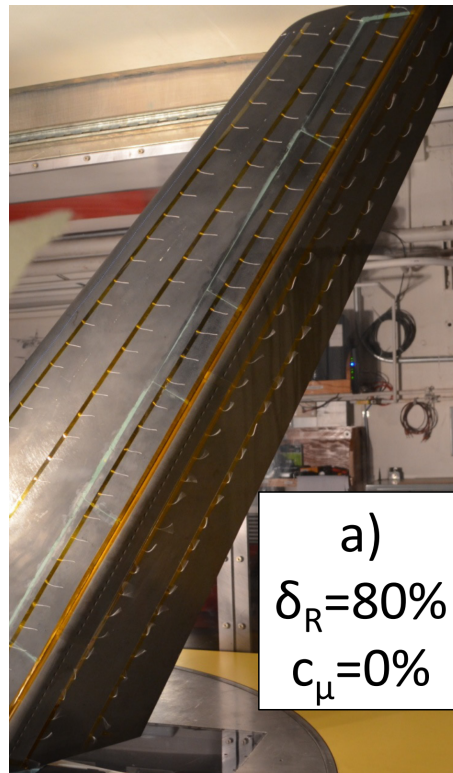


Fig. 2.6 Flow visualization over a VTP at $\beta = 0^\circ$ and $\delta_r = 40^\circ$ [91].

From these experiments, we can identify two regions of flow separation on aircraft VTPs, that is, flow separation along the leading edge of the fin, and flow separation along the hinge line of the rudder. The former may occur when the free-stream flow reaches the fin at high sideslip angle, whereas the latter may occur when the rudder is deflected. For simplicity, Figure 2.9 shows a schematic of a 2D section of a VTP. The flow that reaches the VTP at incidence β splits into two parts. One passes over the pressure side down to the rudder, and the other one contours around the leading edge of the fin and reaches the suction side. At high sideslip angles, the flow separates massively from the leading edge of the fin. If the flow reattaches on the tail, it convects down to the rudder, which is the second location of flow separation. On the VTP, the separation lines tend to be skewed along the span, toward the tip of the tail.

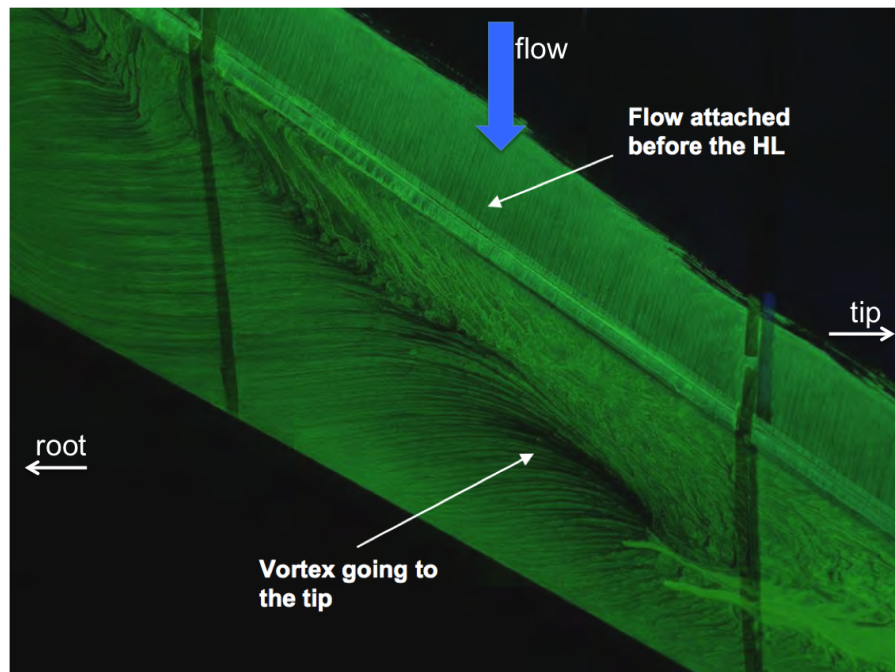


Fig. 2.7 Mid-span flow visualization over the rudder of a VTP at $\beta = 0^\circ$ and $\delta_r = 30^\circ$. Separation along the rudder surface. Photo courtesy of Airbus.



Fig. 2.8 Flow visualization over a VTP at $\beta = 20^\circ$ and $\delta_r = 0^\circ$ [76].

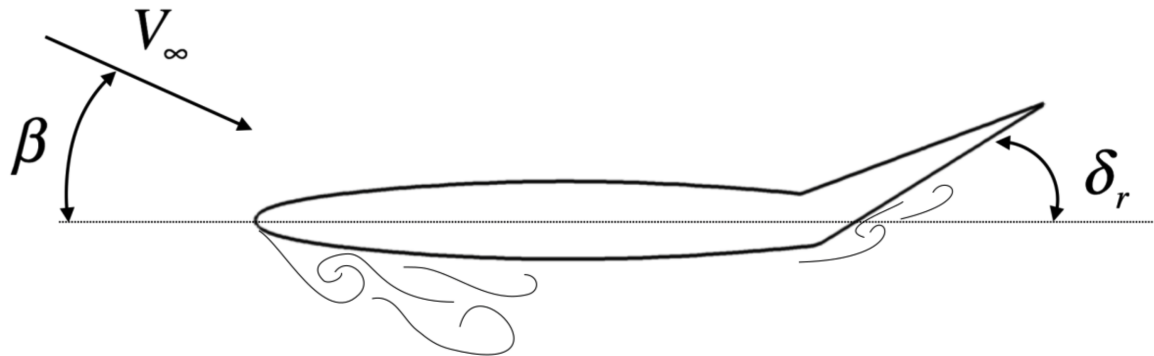


Fig. 2.9 Schematic of a section of the VTP

2.3 CFD for VTP flow assessment

Having assessed the flow characteristics over aircraft VTPs, it is important to understand now how CFD can tackle the problem of separated flows on such industrial applications. However, the literature lacks test cases involving the combination of high sideslip angles and rudder deflection, hence information must be gathered from related literature in order to use the transferable knowledge from previous and current research. CFD is widely used in the aerospace industry, with a vast number of applications, extending from traditional design conditions to the off-design flow over peripheral components, as explained by Tucker [108]. Abbas *et al.* [2] describe the state of the art of numerical simulations for aerodynamic design at Airbus, one of the world's major aircraft manufacturers. Figure 2.10 shows that CFD is used to design most aircraft components, including the tails. Moreover, aircraft designers are also becoming more interested in using CFD also for increasing the comfort of passengers, reducing engine noise, and improving cabin ventilation. This interest is growing significantly, consequently numerical simulations incur new challenges. A similar scenario is present at the other major aircraft manufacturer, Boeing, as described by Spalart and Venkatatarishnan [99] in a more recent publication.

RANS simulations can deliver results with a good compromise between accuracy and cost, at least in design conditions at cruise speeds. However, the same level of reliability is not achieved in off-design conditions involving, for instance, the deflection of the rudder on the VTP at low speeds. In the industry, priority to resolve these flows is given to steady RANS approaches, and generally 2-equations eddy-viscosity turbulence models are used for this task. Increased demand for accuracy has recently pushed CFD practitioners to investigate



Fig. 2.10 Use of CFD for the aerodynamic design of an Airbus A380 aircraft [2].

also Reynolds Stress Models (RSM, see Appendix B). The objective consists of trying to predict all local flow phenomena correctly, and the introduction of six transport equations (one for each Reynolds stress) in the turbulence model is thought to be beneficial for this task. Nevertheless, the computer time needed to resolve this set of equations increases considerably, with respect to simpler two-equation models. Hence, in the literature and in industrial practice, this has not yet been demonstrated for the flow around a VTP. Does the complexity of the turbulence model really add something more to the solution obtained by, for instance, a Menter-SST simulation? If so, at what cost? These questions are addressed in this thesis.

In aircraft design CFD is usually complimented by wind tunnel experiments, and vice-versa. Measurements continue to be a major means of providing aerodynamic information, and comparison (when possible) is still an important means of validating the numerical simulation. However, as explained by Tucker [111], wind tunnel tests for real industrial applications present many challenges. The main difficulty consists of reaching the Reynolds numbers typical of aircraft speeds and geometries, therefore experimentalists adopt geometry scaling and/or flow conditions scaling. Other limitations associated with wind tunnel experiments consist of the blockage effect of the wind tunnel, due to the presence of the walls, the presence of the structure that holds the model, the deformation of the model, due to

high pressures used to achieve high Reynolds numbers, the elevated cost of the models and experiments, and other factors that are presented in Appendix E. For these reasons, nowadays, CFD simulations, whatever their limitations, are becoming the favourite tool for aerodynamic design.

2.3.1 RANS simulations

Agarwal [4] reviewed CFD methods for whole-body aircraft simulations, focusing especially upon steady RANS studies. At the end of the last century, Reynolds-averaged numerical simulations were cost-prohibitive. In less than 20 years, computer power has increased exponentially, reducing simulation costs significantly. The flow around an aircraft at cruise speed is reasonably well-predicted by RANS, which nowadays constitute the main design tool in industry. However, for some flow topologies, the gain in accuracy of steady RANS simulations has not been satisfactory, as explained by Spalart [94]. For instance, flow separation due to high incidence of the flow is still an open issue, and this is crucial for the correct prediction of the flow over VTPs.

Details of turbulence modelling for CFD can be found in references by Pope [81] and Wilcox [123]. A comprehensive review of turbulence models was performed by Leschziner and Drikakis [64]. In order to predict correctly the separated flow over a surface, it is necessary to model the near-wall shear-stresses and normal stresses correctly, as explained by Leschziner [63]. For 3D boundary layers, like on the VTP surface, all components of the shear-stress have to be detected. This influences locations of flow separation and reattachment dramatically.

Generally, turbulence models are grouped in the following branches:

- Linear Eddy-Viscosity Models (LEVM), which make use of the Boussinesq approximation in order to close the system of equations. The Boussinesq hypothesis (see Section A.3) proportionally links the flow Reynolds stresses and the flow shear stresses gradients through the eddy-viscosity [15, 81]. The models are usefully classified according to the number of transport equations they use, as discussed hereby:
 - Algebraic models: the simplest models, designed for canonical flows not involving much separation. Algebraic models tend to predict excessive levels of eddy-viscosity, which results in difficulty in predicting the onset of flow separation.
 - One-equation models. The Spalart-Allmaras (SA) model [95] is the most investigated model of this category. It tends to delay the onset of flow separation. Tucker

[107] explains that the SA model is not designed for streamline curvature and turbulence anisotropy. This is due to the fact that the transport equation, which is written for a pseudo-turbulent viscosity, does not have enough information for the treatment of a separated flow. Moreover, Leschziner [63] states that SA relies heavily on model calibration. Studies from Oriji [78] show also another problem of SA model for predicting separating flows; this consists of flow laminarisation in the presence of streamline curvature and acceleration. A subsequent interaction with an adverse pressure gradient affects the separation and reattachment points importantly. Kalsi [55] demonstrates this using the SA model in a study of the flow separating from the NASA hump.

- Two-equation turbulence models, of which there are several versions. The most popular are: $k - \varepsilon$ [60], $k - \omega$ [122], and Menter Shear Stress Transport (SST) [70], which is a blend of the other two with the addition of shear-stress limiting terms. In its vast number of applications, the $k - \varepsilon$ model has shown weak receptivity of the adverse pressure gradient, resulting in the inhibition or delay to capture the onset of flow separation. In fact, as explained by Rodi and Scheuerer [87], the $k - \varepsilon$ model tends to over-predict the skin friction coefficient of decelerating boundary layers. This is due to the fact that the model predicts a too steep increase of turbulent kinetic energy k near the wall. This results in the prediction of a smaller separation region. Moreover, the model needs extreme grid refinement near the wall, due to the fact that, within the boundary layer, the changes of k and ε are rapid. The $k - \omega$ model gives a superior representation of the boundary layer separation, according to Leschziner [63], but it is very sensitive to free-stream/inlet conditions, as explained by Menter [69]. The SST model is widely used in industry, having been the main turbulence model for CFD design [71]. This model does not include this free-stream flow issue of the $k - \omega$ model, since it performs $k - \varepsilon$ in these regions. Conversely, at the wall, it does not suffer the rapid changes of ε instead. Furthermore, the SST model introduces a shear-stress limiter in accordance with Bradshaw's hypothesis, which states that the shear-stress is proportional to the turbulent kinetic energy in attached zero-pressure gradient boundary layer. The limiter is used, however, even for regions of adverse and favourable pressure-gradient. This results in a good prediction of the onset of flow separation, as shown in the results achieved by Batten *et al.* [12] on the flow separating around a fin. However, in this study, even though the SST model is capable of predicting the separation line correctly, it does not resolve the complex structure of the vortex, resulting in delayed

flow reattachment. This is due to the fact that the limiter introduces an inverse proportionality between the eddy-viscosity and the strain rate; by contrast, in a separated flow region, the strain rate increases, whereas the turbulent viscosity decreases. The SST model contains also another limiter in the production of turbulent kinetic energy. This might result in a lack of accuracy in the prediction of turbulent kinetic energy in a detached flow, discouraging flow mixing and delaying reattachment. Improvements to the SST model were obtained by Evans *et al.* [38] who performed a recalibration of the shear-stress limiter, which works well for high-speed flows.

- Non-linear eddy-viscosity models (NLEVM), which extend the Boussinesq approximation with the addition of quadratic or cubic terms (as reported by Speziale [101] and Craft *et al.* [25]). These models are computationally expensive, but they can potentially capture anisotropy and stream-line curvature, at least partially, and can deal with problems at stagnation points. However, as reported by Tucker [111], numerical convergence of NLVM is more difficult to secure, and their accuracy can be worse than simpler models.
- Reynolds Stress Models discard the Boussinesq hypothesis, and write instead six transport equations for the six Reynolds stresses. Moreover, one more equation is needed for the closure of the system, this being for the turbulence length scale or dissipation rate. In this thesis, the SSG/LRR- ω [36] Reynolds stress model is used (see Appendix B). As Leschziner and Drikakis [64] highlight the amount of information on the performance of advanced anisotropy-resolving models - like RSM models - is quite limited, partly because only a few groups were able to undertake computations with these models for complex flows. In fact, RSM models are quite demanding in terms of cost of the computation, since there are more equations to resolve, and robustness of the solver is difficult to achieve. However, since 2002 computing power has increased significantly and today there are more codes with good implementations of RSM available. RSM models are generally shown to give a superior representation of complex flow features, especially those involving effects of curvature or rotation on turbulence. However, prediction of flow separation and reattachment is a challenging task for RSM closure. In fact, as explained by Leschziner [63], the pressure-strain term introduced within the second-moment closure redistributes the turbulence energy among the normal stresses. This drives the turbulence towards an isotropic state, whereby flow separation is characterised by a marked anisotropy of the boundary layer.

Hence it is interesting to investigate how the RSM turbulence model performs for a VTP.

The literature includes plenty of studies of separation due to adverse pressure gradients on different test cases. For instance, two-dimensional humps have been widely used to assess the capabilities of eddy-viscosity models to predict flow separation. Certainly, the study by Madugundi *et al.* [67] is a comprehensive example. The paper studies the flow over the NDF (National Diagnostic Facility) and NASA humps. Figure 2.11 shows the results for the NDF hump in a free-stream flow. The pressure distribution is plotted against the position along the hump. The surface pressure distribution matches well in the flow acceleration zone, but the peak of the C_p is not well determined by the turbulence models. All of them over-predict the negative peak of C_p , which is also shifted along the chord of the ramp. The figure also shows that SST is the closest to experimental data, followed by the SA turbulence model. Analogous information can be gathered from the NASA hump and from simulations over 3D hills, as shown in references [41, 79].

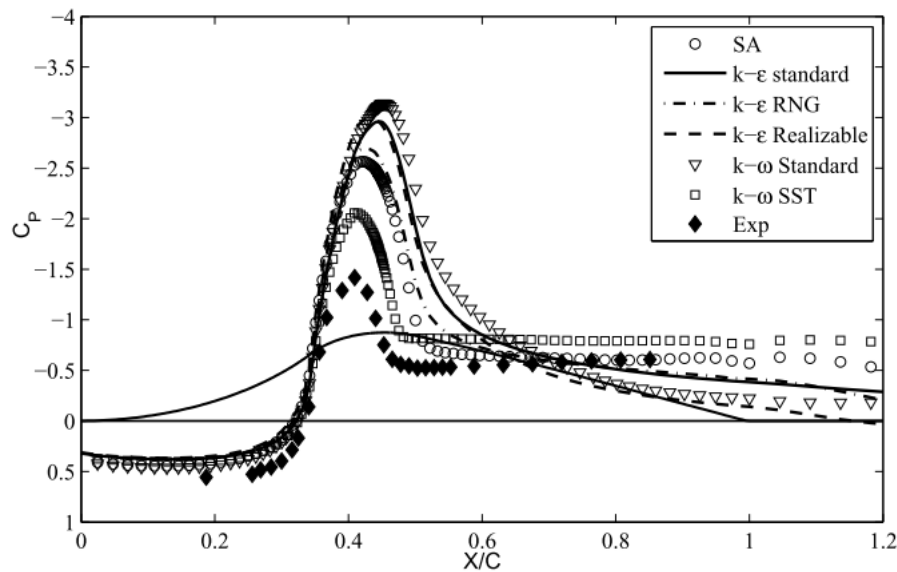


Fig. 2.11 Surface pressure distribution on the NDF hump. Comparison of different turbulence models results with experimental data [67].

When it comes to the use of Reynolds Stress Models, a study of separated turbulent flow over three dimensional bodies was performed by Alpman and Long [9], who used unstructured grids around a 6:1 prolate spheroid and around a sphere. The former was tested at a low Mach number, equal to 0.13, and at a free stream flow at 30° of incidence. The Reynolds number (based on the length) was equal to $6.5 \cdot 10^6$. The numerical investigation

was compared to experimental data, showing overall a good agreement in the pressure coefficient distribution, with an error contained below 20%, except for the aft end of the spheroid where the error in the C_p computation is about 100%-200%.

Hills, humps, and prolate spheroids are quite different from a vertical stabilizer. Certainly, a wing is closer to the shape of a VTP, and separated flows over wings are quite challenging for steady CFD. This leads to contrasting results and the assessment of the performance of turbulence models cannot be unique. Catalano and Amato [18] performed steady RANS studied on an A310⁴ wing at high incidence. The authors used various eddy-viscosity models, but only the Menter-SST could predict the sudden variation of the aerodynamic coefficients over the wing in the presence of massively separated flow (stall condition). However, the accuracy of the simulation was not satisfactory: even though the separation onset was well-predicted, the unsteadiness of the flow is not captured by the RANS solution. Efforts with the use of RSM models are found in the study from Einfeld *et al.* [35], who studied the flow separating from the LANN⁵ wing. The simulated Mach number was equal to 0.82 and the Reynolds number was equal to 7.17×10^6 , based on the mean aerodynamic chord. The RSM and the SST models predict the location of flow separation effectively, but then, in the separation region, SST loses accuracy dramatically, under-predicting the pressure coefficient by about 100%. In the same conditions, the RSM shows more accuracy in the prediction the pressure distribution in the separated region. An analogous performance of the two turbulence models was found by Cecora *et al.* [19] in the study of the ONERA M6 wing⁶.

An analysis of a VTP flow at high sideslip angles was conducted after the aircraft accident that occurred on November 12, 2001 in New York [6]. The authorities determined that the most probable cause of the accident was the in-flight separation of the VTP from the main body of the aircraft as a result of excessive aerodynamic loads over the tail plane caused by the activation of the rudder control by the pilot. At the moment of the accident, the airliner was subject to the wake of a Boeing 747 that had taken off few minutes before, provoking high sideslip angles⁷ that the pilot attempted to compensate with a command from the rudder pedals. Bower and O'Callaghan [16] studied the flow conditions of the accident using steady RANS. The resultant skin-friction lines are plotted in Figure 2.12. On the left figure, the suction side of the VTP is presented, whereas the pressure side is shown on the right hand side. On the former, the flow is reversed over the tail surface, and a singularity line is present close to the tip, indicating a further flow separation. The RANS study shows weakness in the

⁴Airbus A310 aircraft.

⁵The LANN wing is a moderate-aspect-ratio wing designed used for research purposes.

⁶Low aspect ratio wing design at ONERA, the French Aerospace Research Centre.

⁷The wake encounter was fairly modest, but the high sideslip angles that eventually followed were due to multiple reversals of large rudder control inputs by the pilot.

prediction of the pressure over the tail. The higher the sideslip angle, the more significant the mismatch between measurements and CFD. Also, this mismatch is more marked closer to the tip. CFD over-predicts the side-force by approximately 33% and this is excessive for use of CFD in design.

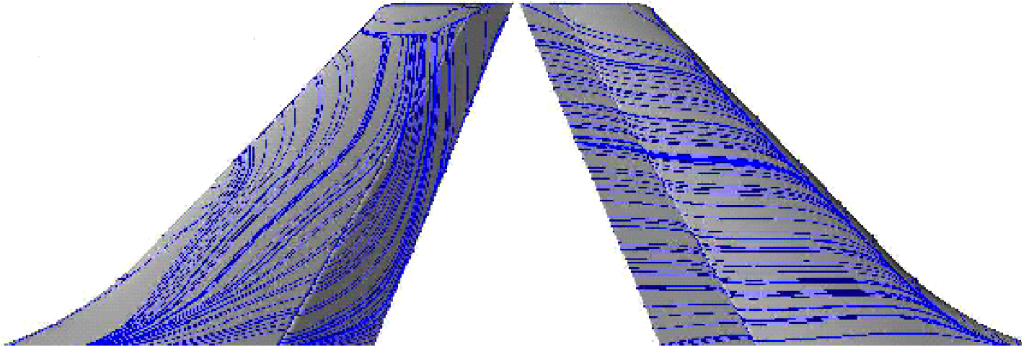


Fig. 2.12 Skin-friction lines over an A330 wind tunnel model VTP at $\beta = 10^\circ$ [16].

The difficulty of predicting flows at high sideslip angles is also shown in a study by Nicolosi *et al.* [77]. The authors performed RANS studies on a VTP for two different Reynolds numbers. The simulations fail to compute the yawing moment at high sideslip angle, presenting a mismatch of about 27% for high sideslip angles with respect to experimental data.

These results give rise to many uncertainties linked to the CFD methods used to study the flow around a VTP at high sideslip angles, especially because nowadays most of the aerodynamic design of a VTP is performed by steady RANS. To what extent can aircraft designers trust this kind of CFD result? Is the topology of the flow detachment correct, or is it misleading? Does the flow stay attached at the root of the VTP, and then separate outboard? How good is the prediction of aerodynamic loads? These are still open questions that are addressed in this thesis.

Flow separation over aircraft tails is a highly unsteady phenomenon, therefore it is necessary to investigate time-dependent CFD approaches. As explained by Iaccarino *et al.* [50], massively separated flows have an intrinsically unsteady nature, thus it is sensible to evaluate how unsteady approaches describe this phenomenon. Iaccarino *et al.* study the more basic flow developing along a flat plate and then encountering a cube. Figure 2.13 shows that the flow separates massively downstream of the cube. The authors compare the different reattachment points of the separation bubble downstream the cube computed with different CFD approaches, as reported in Table 2.1. Steady RANS predicts that the reattachment point is too far downstream, over 2.5 times with respect to the experiment. Unsteady RANS and LES feature 5% and -4% error respectively, demonstrating that the introduction of a time

accuracy in the CFD method is important for the correct prediction of the flow topology. Iaccarino *et al.* explain that steady RANS simulations omit an important component of the averaged flow field, that is the periodic vortex shedding downstream the cube. On the contrary, unsteady RANS can reproduce this phenomenon hence predict essential physics of this 3D massively separated flow better.

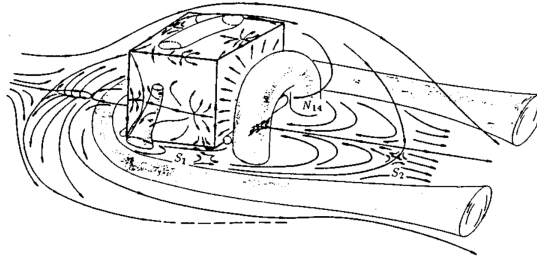


Fig. 2.13 Schematic representation of the main flow features of the cube, Iaccarino *et al.* [50].

Table 2.1 Reattachment point of the flow downstream a cube. Analysis of results from Iaccarino *et al.* [50].

	x_R/h	Error
Steady RANS	4.81	+248%
Unsteady RANS	1.45	+ 5%
LES	1.32	-4%
Experiment	1.38	-

The literature is rich in URANS simulations of rotating flows (such as engine or helicopter flows), or to assess aircraft in manoeuvre, such as in Hitzel *et al.* [47]. However, no unsteady simulations are publicly available for VTP flows. Nevertheless, the parallel development of hybrid RANS-LES methods has encouraged researchers to shift development effort towards these innovative and promising methods, as reported by Frohlich and Von Terzi [40]. These methods will be discussed in Section 2.3.3.

2.3.2 LES

Large-Eddy Simulation “relies on a decomposition of the aerodynamic field between the large scales (responsible for turbulent production) and the small scales of the flow, the former being directly resolved while the effect of the latter is taken into account through the use of a model”, quoting Sagaut [89]. In the LES approach the larger scales of the turbulence

within even thin attached boundary layers will be resolved. A subgrid model handles the effects of the dissipative small scales throughout the turbulent field, that cannot be resolved on the computational mesh. In addition some form of near-wall model would be added to avoid the need to resolve the very small scales that occur near the base of the boundary layer, which the subgrid model is not designed to handle on its own in the absence of resolved turbulence. Despite these modelled elements, the level of resolution needed in LES makes it computationally very expensive.

LES is a mature technique, having been introduced almost 50 years ago. However, it is still impossible to resolve the flow around a complete aircraft entirely using LES, since in the boundary layer the grid and time resolution has to be extremely fine in order to resolve the turbulent structures. Figure 2.14 is adapted from Tucker [109], and plots the LES grid requirements with respect to the Reynolds number of the flow. VTP chord Reynolds numbers for real geometries range between $20 \cdot 10^6$ and $80 \cdot 10^6$. Hence LES would need about $2 \cdot 10^8$ grid points just for a section of the span equal to the mean chord. This is essentially due to the excessive computer resources needed in terms of grid and time refinement, which implies long simulation times and huge computer memory and disk space for data storage. Only some components, such as turbine and compressor blades, pipes, combustion chambers, and four-valve combustion engines, have been treated with LES, as reported by Mary [68].

In 2014 Larsson and Wang [58] discussed the current challenges of using large-eddy simulations in engineering design. In industry, turn-around time is very important and CFD engineers constantly seek time-efficient methods. Hence, rather than moving towards high-fidelity CFD, rapid methods are sought. The problem is that these methods rely upon RANS, which can be misleading. So why do CFD experts predict that: “in the near future, LES will be a real alternative to RANS” [113]? Piomelli [80] considers it fair to assume that, between the increases of computational power and the development of novel algorithms, LES will be used in more complex configurations for engineering analysis, and perhaps also design. Highly resolved LES, where smaller scales are resolved such that only a simple very-near-wall model is needed, can also be seen as a tool complementary to experiments, and the information gleaned from this simulation can help improve current models for industrial applications. Whilst by 2030 the whole aircraft will still be beyond reach for pure LES, smaller problems, in which the turbulence physics are quite complete, will still be a target for LES.

Moreover, LES can give insights to understand the limits of industrial CFD methodologies to predict flow separation. Notably, it is useful to compare highly-resolved simulation with RANS studies, when possible. In the literature, many LES have been performed on flows detaching from gently curved surfaces, such as backward rounded ramps. References

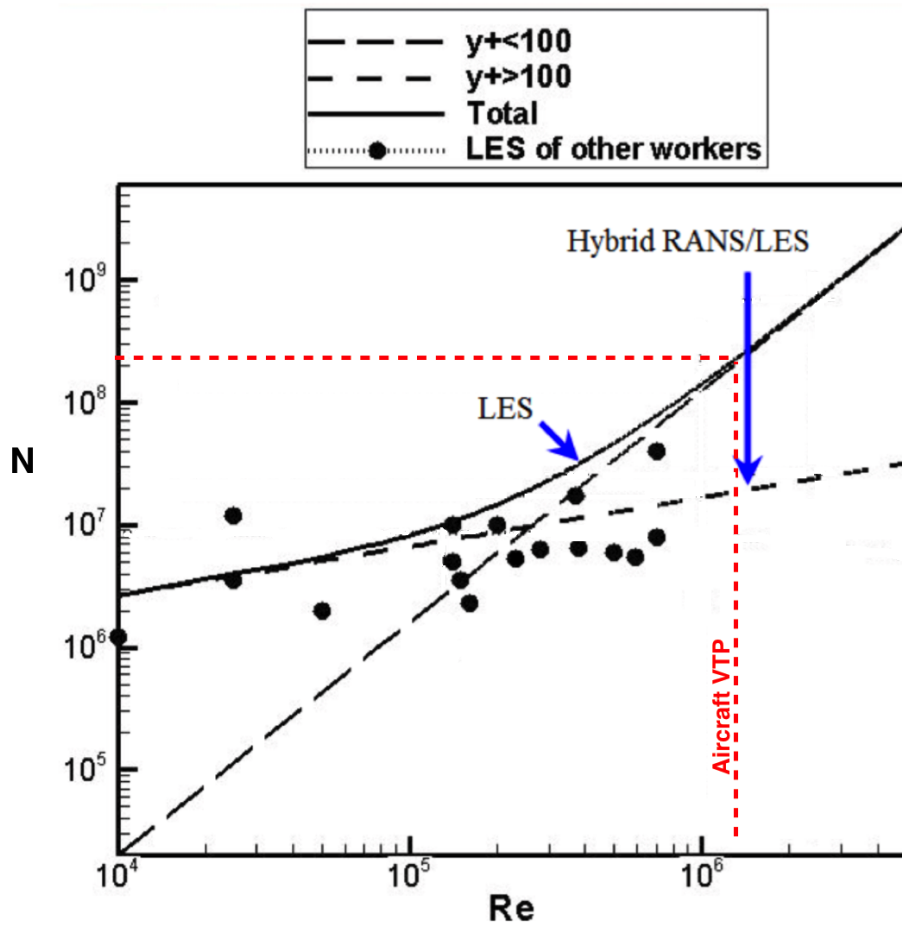


Fig. 2.14 Grid requirements against Reynolds numbers for a flow around a wing section of a span equal to the wing chord. Re-adapted from Tucker [109].

[13, 37, 42, 57] are just some examples. However, none of the cited test cases involve a skewed flow, as on the surface of a VTP. For these reasons, in this work a skewed boundary layer separating from a gently curved ramp is studied through the use of LES, and results will be compared to those obtained by steady RANS.

LES has influenced the aerodynamic community for decades, as Chapman [20] forecast in the late 1970s. Today it is possible to use hybrid RANS/LES in industrial applications, as discussed in the next section, and be enlightened by highly-resolved LES on more fundamental applications. Perhaps this is what it is needed in order to achieve another golden age in aeronautics, as suggested by Lele and Nichols [62].

2.3.3 Hybrid RANS/LES

In the previous section, the impossibility of using LES for full industrial applications has been highlighted. Nevertheless, nowadays CFD is experiencing a transient era, in which the applicability of RANS simulations is combined with the accuracy of LES through hybrid RANS/LES methods. The main idea behind hybrid simulations consists of the RANS treatment of the boundary layer, whereas the regions of detached flow are treated in LES mode. This saves costs in terms of grid density in the boundary layer, making hybrid RANS/LES affordable for industrial applications. In fact, considering Figure 2.14, we notice that the number of grid points required for a hybrid RANS/LES simulation for a VTP flow is almost two order of magnitudes lower than LES requirements.

The first formulation of hybrid RANS/LES for CFD dates back to 1997, when Spalart *et al.* [98] introduced DES (also known as DES97). Since the early 2000s, following the publication of the paper “*Young person’s guide to Detached-Eddy Simulation Grids*” [100], the interest in hybrid RANS/LES methods has been substantial. The paper is very useful for hybrid RANS/LES applications because it explains how important it is to have a well-designed grid. In fact, in hybrid approaches the flow field is filtered with a length scale proportional to the grid spacing; the turbulent structures larger than the grid spacing will be *resolved* by the solver, whereas the others will be *modelled*. For a VTP at high incidence, it is useful to look at how Spalart defines the different flow regions in his DES guide. Though drawn for a different application, Figure 2.15 shows that three macro-areas can be distinguished:

- the Euler Region (ER), which is never entered by turbulence. It contains a small share of the grid points;
- the RANS Region (RR), which includes the boundary layer, including the initial separation;
- the Focus Region (FR), which is the region close to the body where the turbulence is resolved, and
- the Departure Region (DR), where the resolution of the grid is lower than in the FR. The grid spacing smoothly converges towards the one of the ER.

These design guidelines will be followed for the definition of the VTP grid used for eddy-resolving simulations.

After few studies with DES97, Spalart diagnosed some weaknesses associated with the hybrid approach. The weaknesses concern the grid-driven switch from RANS to LES: when

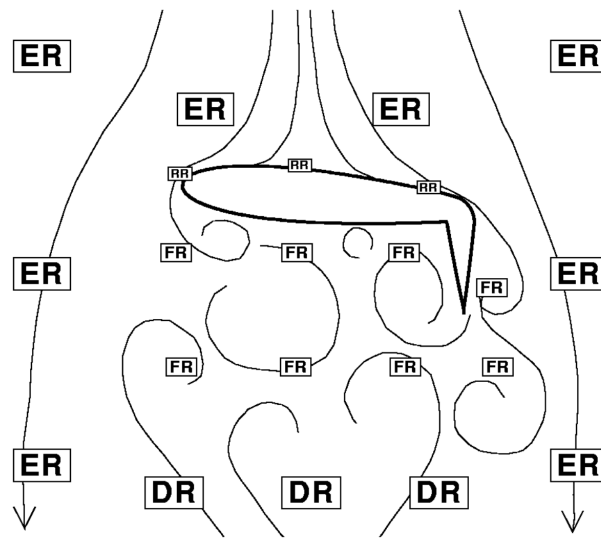


Fig. 2.15 Sketch of flow regions around an aerofoil in rotor downwash during hover, Spalart [100].

it happens in the attached boundary layer, the grid is not fine enough to support the velocity fluctuations (i.e. the LES content), resulting in a weakened eddy viscosity, but not weak enough to allow LES eddies to form, which yields lower Reynolds stress levels compared to those provided by the RANS model. To fix this issue, two main approaches are proposed in the literature:

1. Delayed Detached-Eddy Simulations (DDES) by Spalart [97], which enable us to delay the switch to LES mode outside of the boundary layer⁸.
2. Zonal-DES (ZDES) by Deck [29], where the user defines the RANS and LES zones, and fully attached boundary-layer regions are treated in RANS mode regardless of the grid resolution.

Hence both the approaches zonalise the flow domain; the first approach is automatic, whereas the second is manual. As Deck [29] explains, Z-DES are used for cases of flow separation which are clearly geometrically defined (such as the flow past a deflected spoiler or around high-lift devices). In the case of a VTP at high incidence, it is not possible to define this *a priori*, therefore the first approach is more suitable.

As Hedges *et al.* [46] reported, many academic test cases have been studied with hybrid approaches, involving flows over cylinders [105], spheres [24], and aerofoils [92]. For

⁸This method will be explained numerically in Chapter 3.

instance, Im *et al.* [51] performed DDES on a NACA0012 at incidence $\alpha = 60^\circ$, which gave a much better response compared to URANS, both qualitatively and quantitatively. In the study, URANS calculated the lift coefficient with an error of 28% compared to measurements, whereas DDES resulted in an error of about 7%.

Massive flow separation has been studied through hybrid approaches also on industrial applications. Simulations on multiple bluff bodies, such as cylinders in tandem or triple cylinders (Xiao *et al.* [124]), led to successful results on aircraft landing gears. Hedges *et al.* [46] studied the flow separating from a 4-wheel landing gear configuration at Mach number equal to 0.1. Table 2.2 reports the results obtained with SA-URANS and SA-DES, compared with wind tunnel measurements. Both the CFD approaches under-estimate the drag coefficient, but the DES results are better than the URANS ones. In fact, for the front wheel DES have a 16% error, against 30% error from the unsteady RANS simulation; for the rear wheel, which is more difficult to study since it is in the wake of a separated flow, the error is much more significant: 35% for DES against 45% for URANS. Therefore, despite not being perfect, the DES approach showed already an improvement in the computation of a massively separated flow.

Table 2.2 Landing gear study: wheel drag coefficient. Analysis of results from Hedges *et al.* [46].

	Front wheel C_D	Error	Rear wheel C_D	Error
DES	0.127	-16%	0.105	-35%
URANS	0.105	-30%	0.089	-45%
Experiment	0.151	-	0.161	-

The literature is rich in studies on flow separating from military aircraft wings at high incidence. In fact, the first DES application on a full aircraft was performed by Morton *et al.* [75] and Fortysthe *et al.* [39], who compared SA-URANS and SA-DES results on an F15-E at high incidence ($\alpha = 65^\circ$) at Mach number $M = 0.3$ and mean chord Reynolds number $Re = 13.6 \cdot 10^6$. CFD results were compared against the Boeing database. DES results showed an error in the prediction of the lift coefficient ranging between 4,25% and 2.81%, whereas URANS compute the lift coefficient with about 10% error. Hence DES showed better performance, although the authors seem surprised also by the accuracy shown by URANS. In fact, the force and moments integration can allow error cancellation across the surfaces. A spuriously accurate C_L can be the outcome of a prediction with entirely wrong flow topology. Thus for CFD validation it is always important to compare local flow details, such as at least pressure distribution, to gain insight into the extent to which the flow topology is captured. For large 3D separation involving influential vortical structures, it is going to

be important to have confidence in the ability of the CFD to capture those topologies also, with reasonable accuracy. The study by Morton *et al.* is useful to this thesis also for learning more about grid generation techniques. In fact, to obtain the DES grid, the authors increased the resolution of the URANS one by a factor of 2 for each spatial direction. An unstructured grid was used, with a predominance of tetrahedra outside the boundary layer. The authors explain that the advantage of using tetrahedra consists of having a nearly isotropic mesh; this quality is important for resolving the small eddies of the flow, since the orientation of small turbulent structures are not known *a priori*. A good example which shows the potential of the DDES formulation is found in a study by Jeans *et al.* [53], who performed the study of the flow separating from the delta wing of a fighter at $\alpha = 30^\circ$ incidence and Mach number equal to 0.4. The DDES predicts the unsteady aerodynamic behaviour of the flow, with an excellent agreement with experiments.

Hybrid RANS/LES have been performed over several civil aircraft installations. An example of hybrid simulations on aircraft is presented in Figure 2.16 by Deck *et al.* [30]. The figure shows the typical flight envelope of a generic transport aircraft, linking the corresponding flow conditions that have been treated with eddy-resolving approaches in the literature. It does not show any hybrid RANS/LES applications on aircraft tails, and this is a gap in the literature. In fact, the take-off/landing branches should also contemplate the presence of the flow detaching from the fin at high incidence and from the deflected rudder. Whilst this is an off-design condition for the whole aircraft, the possibility of engine failure on take-off and/or crosswind landings are instead the most critical situation that the vertical stabilizer has to face, therefore it requires study.

Cases involving flow separation include multi-element wings, with the deployment of high-lift devices (flaps and slat, such as in the study by Deck [29]), or the activation of the spoiler control. The latter application was studied in the emergency dive flight condition by Gand [43]. The author performed Z-DES on a wing-body configuration with deflected spoilers. Figure 2.17 shows the resolved turbulent structures detaching from the spoilers. The qualitative accuracy in the description of the flow topology finds only a marginal quantitative improvement in the computation of the global lift coefficient (C_L) and yaw moment coefficient (C_n) generated by the aircraft. In fact, the prediction of the C_L improves by only 2.3%, whereas the C_n coefficient varies of about 15% with respect to RANS, but it is still far from the experimental data. The main reason for these discrepancies might be the fact that the mesh used for the study is too coarse to predict the finest turbulent structures on the spoiler area.

Sartor *et al* [90] have recently used the DLR-TAU code to perform DDES and URANS simulations of the flow separating from the wing of a transonic aircraft (both run with the

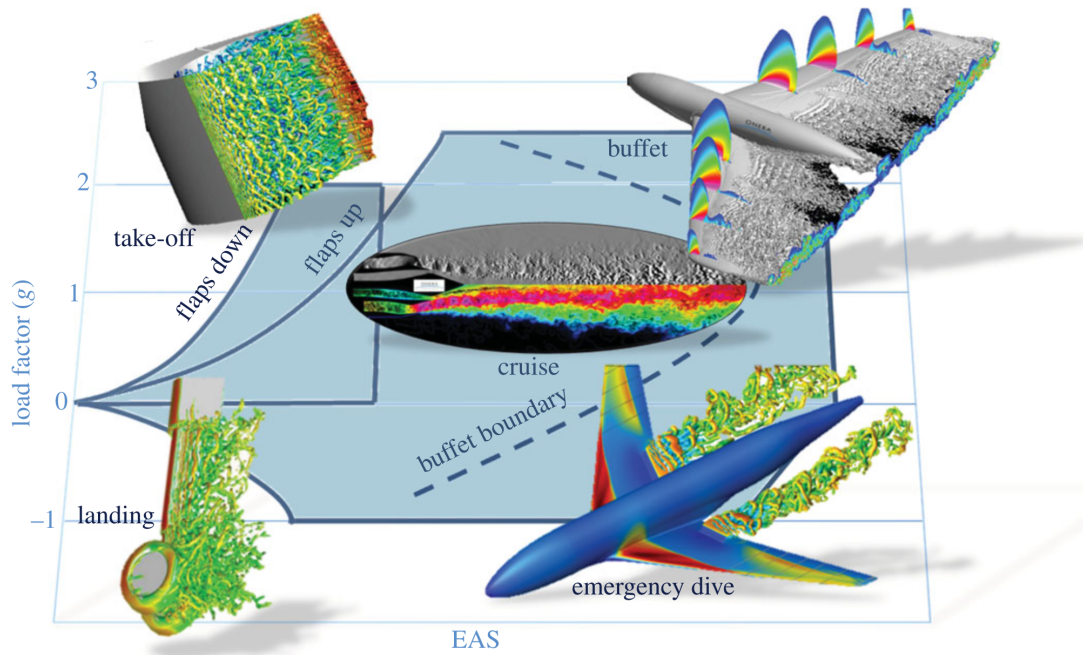


Fig. 2.16 Generic flight envelope of a civil transport aircraft, with examples of hybrid RANS/LES simulations, Deck *et al.* [30].

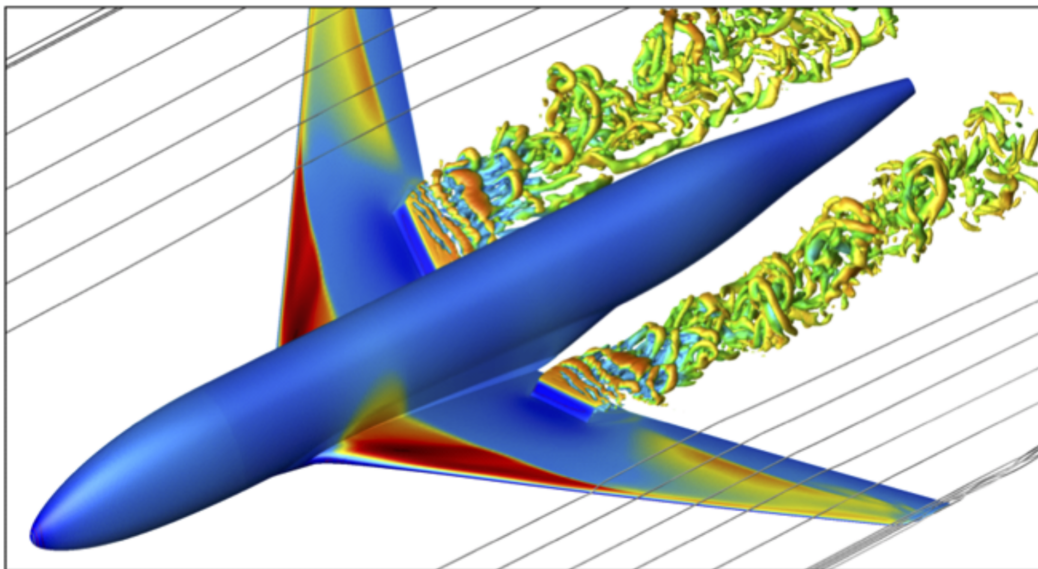


Fig. 2.17 Visualization of the turbulent structures of the flow detaching from the spoilers over an aircraft wing [43].

SA turbulence model). The flow has a Mach number $M = 0.8$ and reaches the wing with an incidence $\alpha = 3.8^\circ$. The mean chord Reynolds number is equal to $3.75 \cdot 10^6$. Although the

study lacks a deep comparison with experimental observations, the DDES provides a more careful description of the flow physics involved in the separated flow (as shown in Figure 2.18, which contrasts turbulent structures of the separated flow over the wing computed by URANS and DDES.). However, the authors point out that the URANS approach is capable of retrieving the main features of the flow.

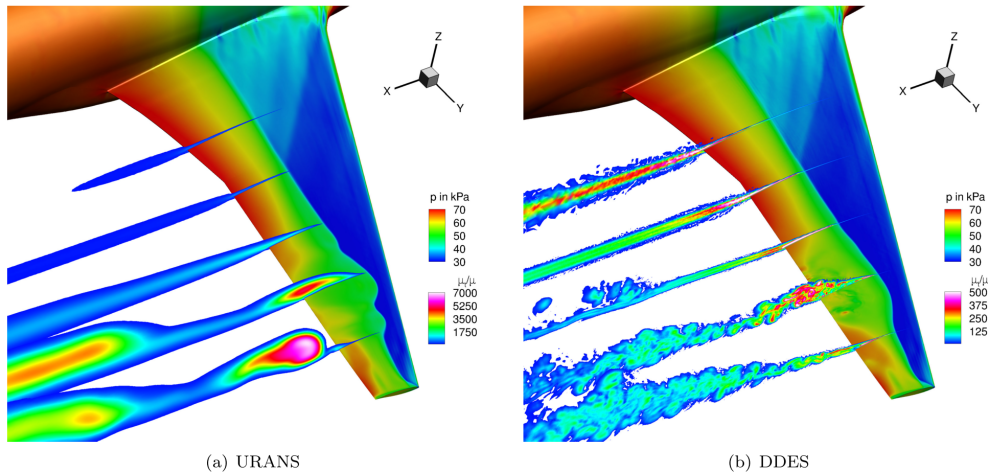


Fig. 2.18 Visualization of the turbulent structures of the separated flow past the wing, Sartor *et al.* [90].

Another interesting example of SA-DDES using the TAU code can be found in the study by Waldmann *et al.* [119], who studied the NASA Common Research Model (CRM), which consists of a wing-body configuration without the vertical stabilizer (further information about the geometry is given by Vassberg *et al.* [115]). The CRM was simulated at Mach number equal to 0.25, for a Reynolds number $Re = 11.6 \cdot 10^6$, and an incidence angle $\alpha = 18^\circ$. At such incidence, the wing stalls and the flow separates massively. Figure 2.19 shows averaged pressure distributions obtained by DDES and URANS simulations compared to wind tunnel data (labelled “ETW” in the picture, indicating the European Transonic Wind Tunnel). The C_p are averaged over 100 convective time steps⁹. The plots are shown for different locations η along the span of the wing. It is interesting to look at what happens on the suction side of the wing (for negative C_p values). In the most inboard section ($\eta = 13.1\%$), the CFD results do not agree with experimental data. At this location, the flow is still attached, as suggested by the distribution of measured points, whereas the trend predicted by URANS is completely flat, indicating detached flow. DDES show a trend that is somewhere in between experiment and URANS. We learn that the flow at this spanwise location is difficult to capture by DDES

⁹The convective time step is the time the flow takes to travel the aerodynamic mean chord of the wing of the CRM.

properly. This is a sort of “grey area”, in which there is the onset of flow separation and it is likely that the flow is intermittently attached and detached. Moving outwards along the span of the wing, to $\eta=28.3\%$, the flow is completely detached. The agreement between DDES and experimental data is excellent, whereas URANS tend to over-predict or under-predict the pressure coefficient with 25% error. Further outboard, both DDES and URANS return good predictions, with DDES slightly better. It is interesting to learn whether this happens also for the simulation over the VTP.

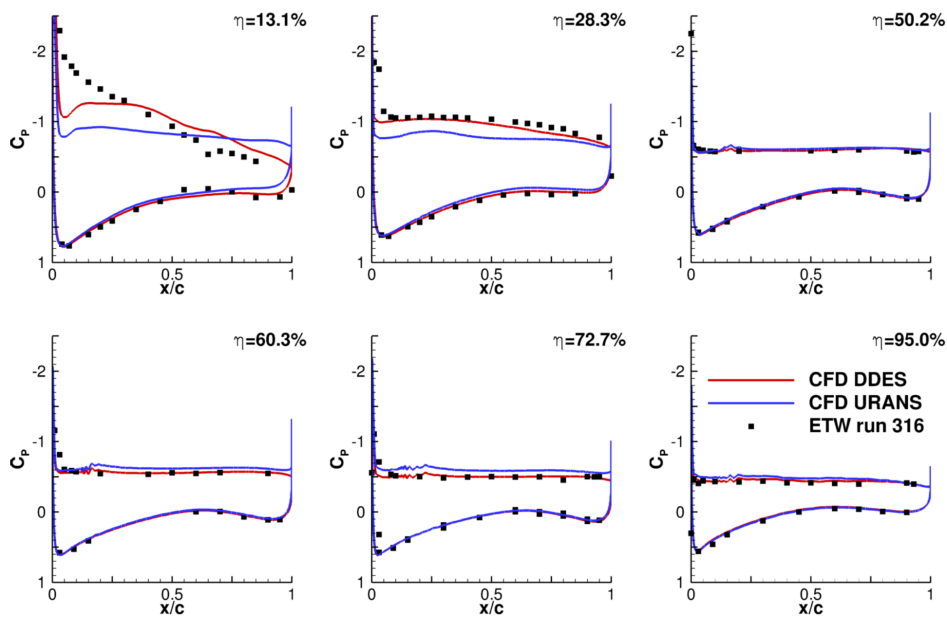


Fig. 2.19 Time-averaged wing pressure distribution at six spanwise stations of the wing of the CRM, Waldmann *et al.* [119].

A DDES of a full vertical stabilizer was performed by Childs *et al.* [21] only recently, in 2016. The simulated flow reaches the tail plane at Mach number equal to 0.15; the rudder is deflected of 30° . The mean chord Reynolds number of the flow is equal to $1 \cdot 10^6$. Results are performed for both RANS, using the Menter-SST turbulence model, and SST-DDES. It is important to highlight that the flow studied in this paper does not present a sideslip angle. The authors report also the results obtained by a RANS simulation. Despite the fact that the flow separates along the hinge line of the deflected rudder, both SST-RANS and SST-DDES agree with experiment along the span of the VTP. According to this study, using hybrid RANS/LES for no sideslip angle conditions does not bring a significant improvement to the RANS solution. However, a flow at high sideslip angle would have been worth investigating, since this is the relevant test case used for VTP design.

2.4 Conclusions and objectives of the thesis

The literature review has shown that the air-flow conditions around aircraft stabilizers can involve flow separation. This happens when the the flow has a sideslip angle and/or when the rudder is deflected. RANS methods do not perform well with such kind of flows, and they cannot achieve manufacturer's accuracy requirements. This has been shown through examples that involve flow physics similar to those that characterise a VTP. However, extensive studies of VTP flows are lacking in the public literature.

Due to the fact that LES is not yet a viable technique for use in industry, there is interest in understanding how hybrid RANS/LES techniques perform with VTP flows. Studies on similar industrial test cases have shown that DDES in particular can be effective and efficient for highly separated flows, therefore this is a technique that has to be investigated.

The objective of this work is to assess the flow around a vertical tail plane, validating methods that can offer greater accuracy and thus confidence in the design process. Application of current industry standard steady RANS methods forms a baseline for the study. It is proposed to evaluate alternative, more advanced, turbulence models, and also unsteady formulations of RANS. The study is then extended to hybrid methods in the form of DDES.

The first step of this research consists of assessing current industrial RANS techniques to predict a flow that detaches from and reattaches to a surface. To achieve this, the flow separating from a backward rounded ramp is studied. The flow is skewed, to induce a spanwise component of flow, as it would have on the surface of a VTP. The results from RANS methods are compared to highly-resolved LES (quasi-DNS) results. This LES is used as a reference flow here, in place of experimental data. The objective of this consists of understanding how RANS performs and what may be the cause of any differences from the LES.

The study of the VTP involves the following stages::

- Assessment of the state of the art of current industrial CFD methods, based on RANS with eddy-viscosity models (notable the SA and the SST models). Moreover, also RSM modelling will be tested, in order to investigate whether this more sophisticated modelling is also more accurate for this type of flow. The advantages and limitations of the steady RANS approach will be highlighted.
- Assessment of URANS methods for the flow around the VTP at high sideslip angle and with deflected rudder. Different turbulence models will be tested with the scope of understanding their performance and preparing the route towards eddy-resolving simulations.

- Restarting from the best URANS solution, DDES simulations will be performed on the VTP model. The objective of this investigations consists of understanding whether using DDES provides a better description of the flow topology around the tail plane and a reliable prediction of pressure distributions and aerodynamic loading. Moreover, the cost of the simulation will be assessed in order to learn whether DDES can be performed in the demanding design environment of the aeronautical industry.

Chapter 3

Numerical methods

3.1 Introduction

In this chapter the CFD methodologies used in this thesis will be described. A CFD process consists of three major steps: preprocessing, flow solution, and post-processing. In the first one, the computational domain is meshed, and the domain is prepared for the computation. Details about grid generation and meshes are given in chapters 4, 5 and 6 for each test case used in this thesis. In this chapter the characteristics of the flow solvers are described.

Fluid dynamics is governed by the Navier-Stokes (NS) equations, which are reported in Appendix A. The NS equations describe the physics of the problem. For compressible three-dimensional flows, the exact solution of the NS equations is still unknown. Therefore, numerics has the crucial task of providing some methods that give the best approximated answer to the problem, and nowadays CFD can achieve successful results, especially when flow turbulence is resolved.

In this thesis, two flow solvers have been used: a highly-modified version of HYDRA, the Rolls-Royce in-house solver (see Moinier [73], Crumpton *et al.* [26]), and TAU, developed by DLR, the German Aerospace Research Centre (Gerhold *et al.* [44], Dwight [34]). The two solvers are similar to each other, being both finite volume codes, using cell-vertex metrics. They both allow for a parallel computation, based on domain decomposition and MPI (Message Passing Interface) communication protocols. Even if most features of HYDRA and TAU overlap, in this chapter the relevant differences related to the particular CFD methodologies will be highlighted. The need for two codes comes from the fact that the highly-modified version of HYDRA used in this thesis enables us to resolve the incompressible flow field studied in Chapter 4. In fact, even though the TAU code allows low-Mach number treatments (i.e. pre-conditioning, as explained in Section 3.7), for Mach

numbers tending to zero, pre-conditioning is not effective and a solution cannot be found. In this thesis, TAU has been used for the study of the compressible VTP flow using RANS, URANS and DDES.

This chapter is structured as follows. First of all, the governing equations are presented. Then, the features of the flow solvers are discussed, in terms of spatial discretization and temporal discretization. Notably, the focus is on time-dependent techniques for unsteady simulations. Hence, special attention is paid to hybrid RANS/LES simulations, with the control of the artificial dissipation. The treatment of the boundary conditions is left to the description of the study cases presented in the following chapters. Finally, some of the data analysis techniques used in this thesis are illustrated.

3.2 Governing equations

The Navier-Stokes equations (see Appendix A) can be written in integral form as:

$$\frac{\partial}{\partial t} \int \int \int_{\Omega} \mathbf{W} d\Omega = - \int \int_{\partial\Omega} \mathbf{Q} \cdot \mathbf{n} dS \quad (3.1)$$

where Ω is an arbitrary control volume with boundary $\partial\Omega$ and \mathbf{n} is the normal vector pointing from the inner domain to the outer domain. \mathbf{W} is the vector of conserved quantities:

$$\mathbf{W} = \begin{pmatrix} \rho \\ \rho u \\ \rho v \\ \rho w \\ \rho E \end{pmatrix}$$

and \mathbf{Q} is a matrix composed of the flux vectors (divided into convective c and viscous v contributions):

$$\mathbf{Q} = (\mathbf{F}_c + \mathbf{F}_v) \cdot \mathbf{e}_x + (\mathbf{G}_c + \mathbf{G}_v) \cdot \mathbf{e}_y + (\mathbf{H}_c + \mathbf{H}_v) \cdot \mathbf{e}_z, \quad (3.2)$$

where \mathbf{e} is unit vector in Cartesian directions x, y, z .

The convective fluxes are:

$$\mathbf{F}_c = \begin{pmatrix} \rho u \\ \rho u^2 + p \\ \rho uv \\ \rho uw \\ \rho Hu \end{pmatrix} \quad \mathbf{G}_c = \begin{pmatrix} \rho v \\ \rho uv \\ \rho v^2 + p \\ \rho vw \\ \rho Hv \end{pmatrix} \quad \mathbf{H}_c = \begin{pmatrix} \rho w \\ \rho uw \\ \rho vw \\ \rho w^2 + p \\ \rho Hw \end{pmatrix}$$

whereas the viscous fluxes are:

$$\mathbf{F}_v = - \begin{pmatrix} 0 \\ \tau_{xx} \\ \tau_{xy} \\ \tau_{xz} \\ u\tau_{xx} + v\tau_{xy} + w\tau_{xz} + q_x \end{pmatrix}$$

$$\mathbf{G}_v = - \begin{pmatrix} 0 \\ \tau_{xy} \\ \tau_{yy} \\ \tau_{yz} \\ u\tau_{xy} + v\tau_{yy} + w\tau_{yz} + q_y \end{pmatrix}$$

$$\mathbf{H}_v = - \begin{pmatrix} 0 \\ \tau_{xz} \\ \tau_{yz} \\ \tau_{zz} \\ u\tau_{xz} + v\tau_{yz} + w\tau_{zz} + q_z \end{pmatrix}.$$

The variable q_i is the rate of heat lost by conduction in i -direction (see Appendix A). The stresses can be expressed as the sum of the molecular and turbulent stresses. The molecular stresses are due to the viscosity μ of the fluid. The molecular viscosity depends on the temperature of the fluid given by the Sutherland's Law in Equation A.11 (Appendix A). The turbulent stresses appear as a consequence of Reynolds-Averaging of the NS equations (in the case of RANS approaches), or filtering of the NS equations (in the case of LES). Details can be found in Appendix A. Although the two processes have totally different physical meanings, analytically, Reynolds-averaging and filtering are two identical processes. The linear eddy-viscosity models considered in this thesis make use of the Boussinesq assumption (Equation 3.3) [15], which expresses the turbulent stresses τ'' as linear functions of mean flow gradients, paralleling the formulation of molecular stresses, with eddy viscosity μ_t playing the same role as molecular viscosity:

$$\tau''_{ij} = -\overline{\rho u''_i u''_j} = \mu_t \left(\frac{\partial \bar{u}_i}{\partial x_j} + \frac{\partial \bar{u}_j}{\partial x_i} - \frac{2}{3} \delta_{ij} \frac{\partial \bar{u}_k}{\partial x_k} \right) - \frac{2}{3} \delta_{ij} \bar{\rho} k \quad (3.3)$$

The expression for μ_t will depend on the turbulence model used (see Appendix B).

The same concept is used in LES, but with the use of a sub-grid dynamic viscosity μ_{sgs} and filtered flow gradients. Further details can be found in Wagner *et al.* [118]. Hence, the stress terms are given by the sum of molecular and turbulent stresses:

$$\tau_{ij} = (\mu + \mu_{t,sgs}) \left(\frac{\partial u_i}{\partial x_j} + \frac{\partial u_j}{\partial x_i} \right) - \frac{2}{3} \delta_{ij} (\mu + \mu_{t,sgs}) \frac{\partial u_k}{\partial x_k} \quad (3.4)$$

Moreover, for eddy-viscosity RANS models, the right hand side of the turbulent normal stresses includes also the term $-2/3\rho k$, where k is the turbulent kinetic energy.

For RANS, another way of formulating expressions for the turbulent stresses consists of discarding the Boussinesq hypothesis, and writing instead six separate transport equations for each of the six independent turbulent stresses. This is the case of Reynolds-Stress Models, described in Appendix B.

Moreover, the highly-resolved LES carried out in this thesis do not make use of a subgrid-scale model, but quasi-DNS simulations are used instead (Cui [27]). Hence $\mu_{sgs} = 0$. Here the numerical dissipation does the job that a an SGS model would do. To ensure stability, a minimal smoothing is added to the numerical equations.

Finally, the pressure is calculated thanks to the equation of state:

$$p = (\gamma - 1) \rho \left(E - \frac{u^2 + v^2 + w^2}{2} \right) \quad (3.5)$$

where E is the total energy (see Appendix A).

3.3 Finite Volume Method

HYDRA and TAU implement the Finite Volume Method (FVM) for representing and evaluating partial differential equations in the form of algebraic equations. Both HYDRA and TAU adopt a cell-vertex formulation of the FVM. The first step involves mesh generation in which the computational domain is divided into a number of small cells by use of meshing software tools, often requiring much manual intervention to obtain an acceptable distribution of cell sizes. These cells are connected in an unstructured way, and the topology of each cell must be one of the set of shapes that the flow solver can handle. Typically these would be tetrahedra, hexahedra, pyramids, and prisms. The vertices, or corner points, of the cells are viewed as the nominal centroids of control volumes which are created by connecting face-centroids, midpoints of edges and mesh cell centroids from the primary mesh. This forms a second mesh of multi-faceted control volumes, and is referred to as the dual mesh. The main physical principle behind the FVM is that the rate of change of the flow quantities

within the control volume must be equal to the flux of each through the boundaries of the control volume, as expressed in Equation 3.1.

From Equation 3.1, for a control volume fixed in space and in time, the temporal rate of change of the conservatives variables can be expressed as:

$$\frac{\partial}{\partial t} \mathbf{W} = - \frac{\int \int_{\partial\Omega} \mathbf{Q} \cdot \mathbf{n} dS}{\int \int \int_{\Omega} d\Omega}. \quad (3.6)$$

Performing the volume and surface integration. one obtains:

$$\frac{d}{dt} \mathbf{W} = - \frac{1}{\Omega} \cdot \mathbf{Q}^F, \quad (3.7)$$

where \mathbf{Q}^F represents the fluxes over the boundary faces of the control volume.

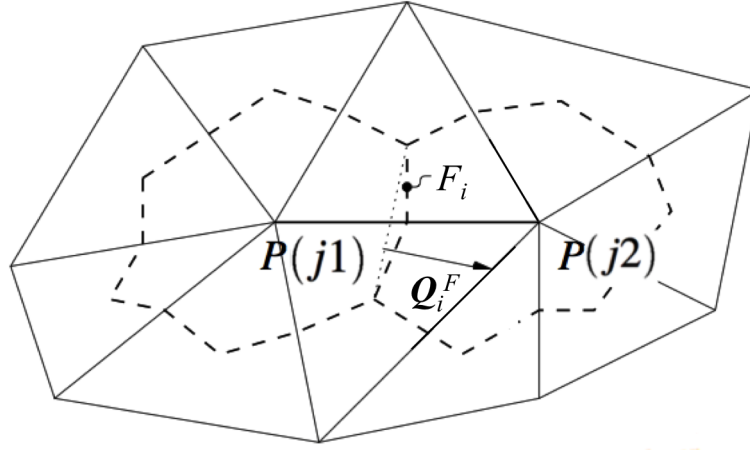


Fig. 3.1 Control volumes around points $P(j1)$ and $P(j2)$ [32].

The boundary is divided into n faces, as shown in Figure 3.1. \mathbf{Q}^F is then given by:

$$\mathbf{Q}^F = \sum_{i=1}^n \mathbf{Q}_i^F \quad (3.8)$$

where \mathbf{Q}_i^F denotes the fluxes over the respective face. These fluxes need to be determined using a discretization scheme. In this work the central scheme is used for this purpose.

3.3.1 Central scheme for spatial discretization

In this thesis, the central discretization scheme within both TAU and HYDRA solvers is used for all results presented. An outline of the scheme is given in the following.

The flux on face i Q_i^F can be split into convective and viscous parts, as in Equation 3.2:

$$\mathbf{Q}_i^F = \mathbf{Q}_i^{F,c} + \mathbf{Q}_i^{F,v} \quad (3.9)$$

In Figure 3.1, the point $P(j1)$ and $P(j2)$ are separated by the face F_i . Let $\mathbf{F}_i = (F_i^x; F_i^y; F_i^z)^T$ be the outward normal vector to the surface of the control volume around $P(j1)$. The inviscid central fluxes over the face can be computed as:

$$\mathbf{Q}_i^{F,c} = F_i^x \mathbf{F}_{c,i} + F_i^y \mathbf{G}_{c,i} + F_i^z \mathbf{H}_{c,i} \quad (3.10)$$

where $\mathbf{F}_{c,i}$, $\mathbf{G}_{c,i}$, $\mathbf{H}_{c,i}$ are the convective fluxes evaluated for face i by use of simple averages of the flow quantities at the two points $j1, j2$ either side of the face. Thus:

$$\mathbf{F}_{c,i} = \frac{1}{2} (\mathbf{F}_c(j1) + \mathbf{F}_c(j2)), \quad (3.11)$$

$$\mathbf{G}_{c,i} = \frac{1}{2} (\mathbf{G}_c(j1) + \mathbf{G}_c(j2)), \quad (3.12)$$

$$\mathbf{H}_{c,i} = \frac{1}{2} (\mathbf{H}_c(j1) + \mathbf{H}_c(j2)). \quad (3.13)$$

However, this simple second order scheme is not numerically stable, as explained by Jameson [52]. Therefore, it is necessary to add some artificial dissipation D_i , and the expression of the fluxes for the control volume enclosed by faces i and centred on the point $j1$, becomes:

$$\mathbf{Q}^F = \sum_{i=1}^n \left[\left(\mathbf{Q}_i^{F,c} - \frac{1}{2} \mathbf{D}_i \right) + \mathbf{Q}_i^{F,v} \right] \quad (3.14)$$

The artificial dissipation is treated very similarly by HYDRA and TAU. The dissipative flux across the dual face i corresponding to the edge connecting $j1$ and $j2$ is given by (Moinier [73]):

$$\mathbf{D}_i(j1, j2) = \varepsilon |\mathbf{A}| [L(\mathbf{W}(j1)) - L(\mathbf{W}(j2))] \quad (3.15)$$

The operator L represents the pseudo-Laplacian (Moinier [73]), and the Jacobian A at face i is given by:

$$\mathbf{A} = \frac{\partial \mathbf{Q}_i^{F,c}}{\partial \mathbf{W}}. \quad (3.16)$$

Particular attention should be paid to the smoothing coefficient ε when performing eddy-resolving simulations. Its value should be kept as small as possible in order to avoid non-physical dissipation of the resolved eddies. Table 3.1 reports that the smoothing coefficient used in HYDRA is equal to $\varepsilon = 0.1$, whereas in TAU it is equal to $\varepsilon = 1/64$ for (U)RANS

and $\varepsilon = 1/128$ for eddy-resolving simulations. In Section 3.6 the control of the artificial dissipation for eddy-resolving simulation will be discussed.

Table 3.1 Smoothing coefficient used in the thesis.

Solver	CFD method	Value of ε
HYDRA	LES and Hybrid RANS/LES	0.1
TAU	(U)RANS	1/64
TAU	DDES	1/128

The treatment of the viscous fluxes follows the standard approximation of the flux half-way along the edge and then the integration around each control volume, see Moinier [73].

3.4 Time discretization

3.4.1 Time-marching method for steady-state problems

Steady RANS simulations of the VTP flow are performed using the TAU solver, which implements a time-marching technique described in this section.

Equation 3.6 for a point $P(j1)$ can be written as:

$$\frac{d}{dt} \mathbf{W}(j1) + \mathbf{R}(j1) = 0 \quad (3.17)$$

where

$$\mathbf{R}(j1) = \frac{1}{\Omega(j1)} \cdot \mathbf{Q}^F(j1). \quad (3.18)$$

For steady-state problems, equation 3.17 becomes:

$$\mathbf{R}(j1) = 0 \quad (3.19)$$

and can be solved with a time marching method with the introduction of a fictitious time t^* :

$$\frac{d}{dt^*} \mathbf{W}(j1) + \mathbf{R}(j1) = 0. \quad (3.20)$$

For time-independent problems, the first order Backward Euler implicit scheme has been used. This is an implicit scheme, which is preferred in industrial applications (Zhu [127]).

Equation 3.20 is discretised with respect to the future time level¹

$$\frac{\mathbf{W}^{(n+1)} - \mathbf{W}^{(n)}}{\Delta t^*} = -\mathbf{R}(\mathbf{W}^{(n+1)}). \quad (3.21)$$

This is a non-linear algebraic system, which needs to be linearised around the time level $n + 1$ through a Taylor expansion:

$$\mathbf{R}(\mathbf{W}^{(n+1)}) = \mathbf{R}(\mathbf{W}^{(n)}) + \frac{\partial \mathbf{R}(\mathbf{W}^{(n)})}{\partial \mathbf{W}} \Delta \mathbf{W} + O((\Delta t^*)^2) \quad (3.22)$$

which gives:

$$\mathbf{R}(\mathbf{W}^{(n+1)}) = \mathbf{R}(\mathbf{W}^{(n)}) + \frac{\partial \mathbf{R}(\mathbf{W}^{(n)})}{\partial \mathbf{W}} \frac{\partial \mathbf{W}}{\partial t^*} \Delta t^* + O((\Delta t^*)^2), \quad (3.23)$$

where:

$$\frac{\partial \mathbf{W}}{\partial t^*} \Delta t^* = \Delta \mathbf{W} + O((\Delta t^*)^2) = \mathbf{W}^{(n+1)} - \mathbf{W}^{(n)}. \quad (3.24)$$

Applying Equation 3.24 into Equation 3.23, and substituting into Equation 3.21, the following linear algebraic system is obtained:

$$\mathbf{A}(\mathbf{W}) \Delta \mathbf{W} = -\mathbf{R}(\mathbf{W}^{(n)}) \quad (3.25)$$

where $\mathbf{A}(\mathbf{W})$ is a matrix expressed as:

$$\mathbf{A}(\mathbf{W}) = \left[\frac{1}{\Delta t^*} \mathbf{I} + \frac{\partial \mathbf{R}(\mathbf{W}^{(n)})}{\partial \mathbf{W}} \right] \quad (3.26)$$

where I is the identity matrix. The system is resolved with respect to $\Delta \mathbf{W}^{(n)}$, hence the solution $\mathbf{W}^{(n+1)} = \mathbf{W}^{(n)} + \Delta \mathbf{W}^{(n)}$ can be evaluated. To achieve this, TAU uses the Lower-Upper Symmetric-Gauss-Seidel (LU-SGS) method is used. The details of LU-SGS can be found in Yoon and Jameson [125] and in Dwight [34].

Choice of the time step

Now the question is how to choose the pseudo-time step size $\Delta t^*(j1)$ for the cell $j1$. For a grid with N_c dual cells, when *global time stepping* is adopted, the fictitious time step

¹The index $j1$ here is dropped.

$\Delta t^*(j1)$ is defined as:

$$\Delta t^*(j1) = \min_{j=j1}^{jN_c} [\Delta t(j)] \quad (3.27)$$

which means that the pseudo-time step width is given globally by the minimum time step over all N_c dual grid cells. For cell $j1$, $\Delta t(j1)$ is given by:

$$\Delta t(j1) = CFL \cdot \frac{1}{\lambda^c(j1)}, \quad (3.28)$$

where CFL is the Courant number and $\lambda^c(j1)$ denotes the maximum eigenvalue of the flux Jacobian. Notably, the eigenvalue can be determined in an integration over the surface of the control volume around point $P(j1)$ with $n - 1$ neighbouring points $P(j2), \dots, P(jn)$:

$$\lambda^c(j) = \sum_{i=1}^{n-1} |\mathbf{v}(i) \cdot \mathbf{F}(i)| + a(i) \cdot |\mathbf{F}(i)| \quad (3.29)$$

where $\mathbf{F}(i)$ represents the face vectors of the control volume face for the i -th neighbour of $P(j1)$, $a(i)$ is the speed of sound, and $\mathbf{v}(i)$ indicates the face velocity vector. Let face $F(i)$ be the interface between two control volumes around $P(j1)$ and $P(j2)$. The face velocities $\mathbf{v}(i)$ are computed by an arithmetic averaging of the respective point values:

$$\mathbf{v}(i) = \frac{1}{2} \cdot \left[\begin{pmatrix} u(j1) \\ v(j1) \\ w(j1) \end{pmatrix} + \begin{pmatrix} u(j2) \\ v(j2) \\ w(j2) \end{pmatrix} \right]. \quad (3.30)$$

For steady state problems, the solution of equation 3.20 remains unchanged if d/dt^* is replaced by $(1/A)d/dt^*$, where A is a local acceleration parameter parameter that enables the solver to converge more quickly:

$$\frac{1}{A(j1)} \frac{d}{dt^*} \mathbf{W}(j1) + \mathbf{R}(j1) = 0. \quad (3.31)$$

In local time stepping, $\Delta t^*(j1)$ is chosen equal to 1, and $A(j1) = \Delta t(j1)$, where $\Delta t(j1)$ denotes the local time step size from Equation 3.28.

3.4.2 Dual time-stepping for unsteady problems

HYDRA and TAU use second order backward differences for the time-accurate discretization of the unsteady governing equations, using global, physically real, time steps. Both the solvers use a dual time-stepping technique with the Runge-Kutta method [17] to perform

pseudo-time iterations within each real time step, until an adequately converged solution for the end of that time step is achieved.

Equation 3.17² writes:

$$\frac{d}{dt}\mathbf{W} + \mathbf{R} = 0.$$

In a first step a second order backward difference formula for discretizing the time derivative is employed:

$$\frac{3\mathbf{W}^{(n+1)} - 4\mathbf{W}^{(n)} + \mathbf{W}^{(n-1)}}{2\Delta t} = -\mathbf{R}^{(n+1)}, \quad (3.32)$$

Assuming that $\mathbf{W}^{(n)}$ and $\mathbf{W}^{(n-1)}$ have already been computed, the following equation for $\mathbf{W}^{(n+1)}$ can be written in fictitious pseudo-time t^* :

$$\frac{d}{dt^*}\mathbf{W}^{(n+1)} = -\mathbf{R}^{DTS}(\mathbf{W}^{(n+1)}) \quad (3.33)$$

with

$$\mathbf{R}^{DTS}(\mathbf{W}^{(n+1)}) = \mathbf{R}(\mathbf{W}^{(n+1)}) + \frac{3\mathbf{W}^{(n+1)} - 4\mathbf{W}^{(n)} + \mathbf{W}^{(n-1)}}{2\Delta t}. \quad (3.34)$$

This can be integrated with a Runge-Kutta scheme [17] until a steady state in the pseudo-time has been reached. The choice of the physical time step is discussed with respect to the test case studied.

3.5 Hybrid RANS/LES in TAU

In hybrid RANS/LES simulations, the basic idea is to replace the integral turbulent length scale in the dissipation term of the turbulence model with a suited, grid-dependent filter length l_{hyb} . This allows the model to locally operate in LES mode. In Delayed Detached-Eddy Simulations (DDES), the filter length is given by:

$$l_{hyb} = l_{RANS} - f_d \cdot \max(0, l_{RANS} - l_{LES}), \quad (3.35)$$

with:

$$l_{LES} = C_{DES}\Delta. \quad (3.36)$$

Δ is a representative edge length of a mesh cell element, typically either a maximum or some form of average of the cell edge lengths.

²The index $j1$ is dropped.

The entity f_d is called delay function. Its aim is to prevent the switch to LES mode taking place within an attached boundary layer. With $f_d = 1$ the original DES scheme is recovered. As explained in the Literature Review, it was found that on refined meshes there is a risk of switching to LES mode within an attached boundary layer. This causes premature reduction of the RANS length scale while also the LES eddies are insufficiently developed. This is referred to as modelled stress depletion, leading to one of the most notable defects of the DES scheme, categorized as grid-induced separation. The mechanism for this can be seen as follows. l_{RANS} can be assumed to be roughly proportional to the distance from the wall, and the LES Δ scale measures cell size as described above. To avoid the problem in DES it is necessary for the streamwise mesh spacing in a boundary layer to be large compared with the layer thickness. Then l_{LES} can remain larger than l_{RANS} until at least the edge of the boundary layer is reached, so l_{hyb} maintains the full l_{RANS} value. It can be seen that if the streamwise spacing is reduced, the reduction in l_{LES} can trigger reduction of l_{hyb} within the layer. Therefore in DDES f_d is formulated to achieve $f_d = 0$ within the boundary layer, delaying the reduction in l_{hyb} until close to the edge of the layer. In other regions, when $f_d = 1$, normal DES behaviour based on grid resolution is retained. The delay function depends upon the flow characteristics. It reads:

$$f_d = 1 - \tanh(8r_d^3) \quad (3.37)$$

with:

$$r_d = \frac{\mu + \mu_t}{\sqrt{S_{ij}S_{ij}}\kappa^2 d_w^2}. \quad (3.38)$$

When the Menter-SST model is used, l_{RANS} is given by:

$$l_{RANS,SST} = \frac{\sqrt{k}}{\beta^* \omega}, \quad (3.39)$$

where β^* is a constant (see Appendix B). The model has both the $k - \varepsilon$ and the $k - \omega$ branches. Notably, the $k - \omega$ branch is active in the near-wall region, whereas the $k - \varepsilon$ model is active in the regions away from the boundary layer. Thus the $k - \varepsilon$ branch is relevant in DDES applications. To consider the blending of the two turbulence models, the C_{DES} coefficient is defined by Travin *et al.* [106] as:

$$C_{DES} = (1 - F)C_{DES}^{k-\varepsilon} + FC_{DES}^{k-\omega}, \quad (3.40)$$

with $C_{DES}^{k-\varepsilon} = 0.61$ and $C_{DES}^{k-\omega} = 0.78$. F is defined in Appendix B.

3.6 Control of the artificial dissipation

As explained earlier, the artificial dissipation is introduced in the spatial discretization for the stability of the central scheme. However, for eddy-resolving simulations it is necessary to control the level of numerical smoothing that is used to assure the resolution of the turbulent length scales. To achieve this, a classic test consists of assessing the capability of the flow solver to compute the Homogeneous Decay of Turbulence (HDT). This was measured in an experiment by Comte-Bellot [23]. In this thesis, for the numerical simulation, the spatial decay of grid turbulence in a wind tunnel is transformed into a purely time-dependent decay of stationary turbulence within a cubic domain with a normalized edge length of 2π . The initialization of the flow follows the method explained by Probst *et al.* [82], who uses a transformation of the measured energy spectrum at an instant in time back to physical space, following the work of Kraichnan [56]. The computational domain was discretized with a structured grid of dimensions 64^3 .

Cui [27] tested the the HYDRA solver and results are reported for a smoothing coefficient $\varepsilon = 0.1$. Figure 3.2 shows the energy spectrum of the decay of turbulent kinetic energy E with respect to the normalized wave number k , extracted at $t = 2$ s. The spectrum compares favourably with the experiment by Comte-Bellot [23]. This means that HYDRA is capable to resolve the turbulent length scales of the flow, even for large wavenumbers. This means that the solver is a good candidate for highly-resolved LES.

In this thesis, the same approach is used to test TAU's capability to perform eddy-resolving simulations. Figure 3.3 shows the spectrum obtained for $t = 0.87$ s. The smoothing constant is set equal to $\varepsilon = 1/128$. The spectrum is in agreement with the experimental data up to $k \approx 12$, but then the decay of turbulent kinetic energy is too rapid. This means that the model succeeds in predicting the large eddies and turbulent structures, whereas it is too dissipative for the smallest structures of the flow. However, this is sufficient for the purpose of this thesis, since it intends to capture the large eddies of the VTP flow.

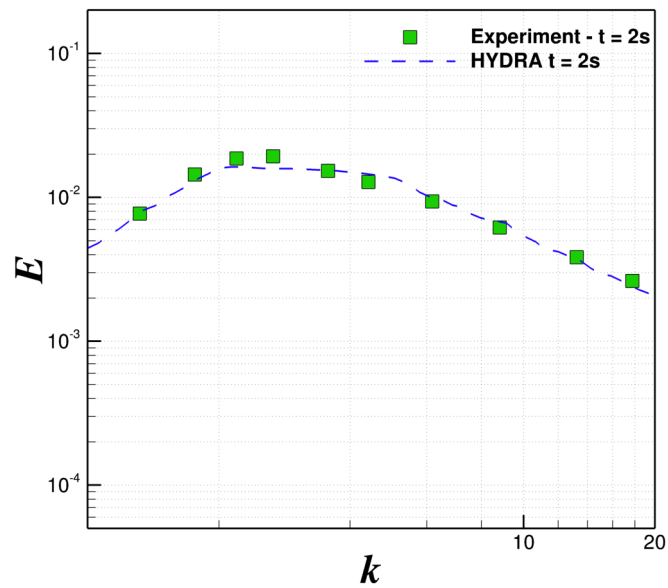


Fig. 3.2 Energy spectrum obtained by incompressible HYDRA LES without SGS model (readpated from Cui [27]). The experiment data is by Comte-Bellot [23].

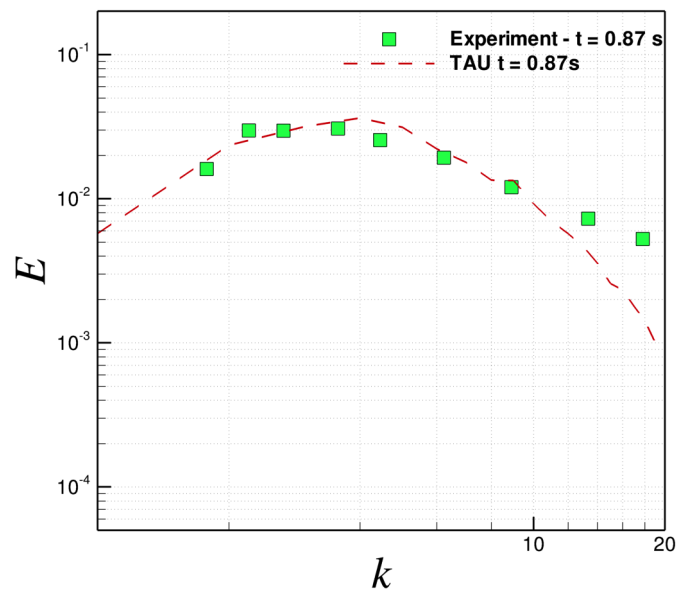


Fig. 3.3 Turbulent kinetic energy spectra for the DIT case. Experiment vs. TAU DDES.

3.7 Low-Mach number treatments

The flow regime around aircraft tail planes may involve low-Mach number regions, in which the flow shows very little effects of compressibility. The problem is that at low Mach numbers, compressible codes encounter degraded convergence speeds due to the wide disparity that exists between the flow motion and acoustic wave speeds [22]. This makes the system of equations stiff to be resolved [32]. Preconditioning is used in TAU in order to reduce this disparity. Further information can be found in Turkel [114] and Radespiel [84].

In TAU, preconditioning is introduced in the definition of the artificial dissipation (Probst *et al.* [83]):

$$\mathbf{D}_i(j1, j2) = \varepsilon |\mathbf{PA}| [L(\mathbf{W}(j1)) - L(\mathbf{W}(j2))] \quad (3.41)$$

where \mathbf{P} is the preconditioning matrix expressed as [84]:

$$\mathbf{P} = \begin{pmatrix} \frac{m^2 g}{a^2} & 0 & 0 & 0 & -m^2 \frac{\gamma p}{T} \delta \\ 0 & 1 & 0 & 0 & 0 \\ 0 & 0 & 1 & 0 & 0 \\ 0 & 0 & 0 & 1 & 0 \\ \frac{\gamma-1}{\gamma \rho} (m^2 g - 1) & 0 & 0 & 0 & 1 - (\gamma-1)m^2 \delta \end{pmatrix} \quad (3.42)$$

where $m^2 = \beta/a^2$, and $g = 1 + (\gamma-1)\delta$. The term a is the speed of sound, $\gamma = 1.4$, and δ is equal to 1 if $M^2 < 1$ or zero if $M^2 > 1$ (M is the Mach number). The parameter β is called ‘‘artificial speed of sound’’, and prevents singularities in the matrix \mathbf{P} . It is defined as:

$$\beta = \min [\max (|u^2 + v^2 + w^2|, K|u_\infty^2 + v_\infty^2 + w_\infty^2|), a^2] \quad (3.43)$$

where $K = 2.5$ is the cut-off value, and $u_\infty, v_\infty, w_\infty$ represent the components of the free-stream velocity.

For Mach numbers tending to zero, ultimately it is not possible to recover pressure from the density variation. Since in this thesis a test case with $M \rightarrow 0$ is studied (in Chapter 4), the incompressible version of HYDRA is used instead. This version was developed by Cui [27], who introduced the Rogers & Kwak scheme [88] within the HYDRA framework. The Rogers & Kwak scheme adopts an artificial density parameter which couples the pressure and the velocity fields. This enables us to use a density-based solver. The idea consists of introducing a pseudo-time derivative of the artificial density $\tilde{\rho}$ in the incompressible continuity equation, which in differential form becomes:

$$\frac{\partial \tilde{\rho}}{\partial t^*} + \frac{\partial u}{\partial x} + \frac{\partial v}{\partial y} + \frac{\partial w}{\partial z} = 0. \quad (3.44)$$

The artificial density given by $\tilde{\rho} = \beta^{-1} p$ and t^* is the pseudo-time. The parameter β is the tunable pseudo-compressibility constant. In this thesis, its value is $\beta = 10$. The governing equations become:

$$\Gamma_t \frac{\partial \mathbf{B}}{\partial t} \frac{\partial \mathbf{B}}{\partial t^*} + \frac{\partial(\mathbf{F}_c - \mathbf{F}_v)}{\partial x} + \frac{\partial(\mathbf{G}_c - \mathbf{G}_v)}{\partial y} + \frac{\partial(\mathbf{H}_c - \mathbf{H}_v)}{\partial z} = 0 \quad (3.45)$$

where

$$\mathbf{B} = \begin{pmatrix} p/\rho \\ u \\ v \\ w \end{pmatrix} \quad \mathbf{F}_i = \begin{pmatrix} \beta u \\ u^2 + p/\rho \\ uv \\ uw \end{pmatrix} \quad \mathbf{G}_i = \begin{pmatrix} \beta v \\ uv \\ v^2 + p/\rho \\ vw \end{pmatrix} \quad \mathbf{H}_i = \begin{pmatrix} \beta w \\ uw \\ vw \\ w^2 + p/\rho \end{pmatrix}.$$

and $\Gamma_t = \text{diag}[0, 1, 1, 1]$. Hence the shape of the residual fluxes has changed, but the numerical methods of HYDRA can stay the same. More details can be found in Cui's thesis [27].

3.8 Data analysis

3.8.1 Monitoring of the residuals for steady-state simulations

As previously described, fluxes for each cell are computed during each pseudo time step, and are used to update the flow solution by time integration. The fluxes thus define the time rate of change of the solution. This rate is most conveniently expressed as the magnitude of the flux residual \mathbf{R} . As the steady state is approached during the iterative stepping through pseudo time, the rate of change of the flow variables, and thus the residual, will tend towards zero. To check for steady conditions, both the decaying variation of the flow, and the reduction in residuals should be monitored throughout the computation. For convenience it is usual to monitor just one residual, typically the density residual associated with the continuity equation, and this is the practice adopted in this thesis. Clearly each cell will have a value of each residual, so a single global value is needed for monitoring. In this thesis the root mean square value is used, where the global density residual at a given time step n is given by:

$$\|res_\rho^n\| = \sqrt{\sum_{j=1}^N \frac{[res_\rho^n(j)]^2}{N}}, \quad (3.46)$$

where N denotes the number of points. In this thesis, a steady simulation is considered converged when the residual drops by at least 5-6 orders of magnitude.

3.8.2 Temporal-averaging for unsteady simulations

For unsteady simulations, the temporal time-averaging is performed in fly with the flow solution. The process is started after that the solver is allowed to develop the transient solution. This can vary for each test case, hence this is a process that needs to be monitored with respect to the simulation that is being performed.

The solver saves a certain number of *snapshots* of the flow solution. If \mathbf{W} is the vector containing the conserved variables w_i , given a number of iteration N_{iter} , the time-averaged primitive variable $w_{ave,i}$ is calculates as:

$$w_{ave,i} = \frac{w_{ave,i}(N_{iter} - 1) + w_i}{N_{iter}}. \quad (3.47)$$

The time-average of the Reynolds stresses is calculated differently. The time-averaged Reynolds stresses are expressed as: $\tau'_{ij} = \rho \overline{u'_i u'_j}$, for $i, j = 1, 2, 3$. u'_i represents the fluctuation of the u_i velocity component, expressed as $u'_i = u_i - \bar{u}_i$ (see Appendix A). Hence the expression for the averaged Reynolds-stresses becomes:

$$\tau'_{ij} = \rho (\overline{u_i u_j} - \bar{u}_i \bar{u}_j). \quad (3.48)$$

3.8.3 Visualising turbulence

In order to visualise the turbulent structures of the flows studied in this thesis, the following techniques are used.

Q criterion The Q -criterion is a way to visualise the vortices with a turbulent flow. It was introduced by Hunt *et al.*[49], who define the vortex as a spatial region where

$$Q = \frac{1}{2} [|\boldsymbol{\Omega}|^2 - |\mathbf{S}|^2] > 0. \quad (3.49)$$

The term $\boldsymbol{\Omega}$ represents the vorticity tensor, whereas \mathbf{S} denominates the rate of strain tensor. Hence a vortex can be identified as that region where the vorticity dominates the rate of strain. Isosurfaces of thw Q -criterion are used to visualize the vortices. Typically the isosurfaces are coloured by a physical quantity, such as the velocity of the flow.

Anisotropy maps The stress tensor τ_{ij} can be divided into its traceless deviator part τ'_{ij} , and its isotropic part τ_{ij}° (as discussed by Simonsen and Krogstad [93]):

$$\tau_{ij} = \tau'_{ij} + \tau_{ij}^\circ \quad (3.50)$$

where

$$\tau'_{ij} = \tau_{ij} - \frac{1}{3} \tau_{kk} \delta_{ij}. \quad (3.51)$$

If in the flow field turbulence was truly isotropic, then τ'_{ij} would be zero. Expressing these equations in terms of velocity fluctuations and turbulent kinetic energy, the non-dimensionalized deviatoric stress tensor can be defined as:

$$a_{ij} = \frac{\overline{u'_i u'_j}}{k} - \frac{2}{3} \delta_{ij}. \quad (3.52)$$

Resolving the characteristic equation for this symmetric tensor [93], three invariants (eigenvalues) can be found. They are expressed as:

$$A = 1 - \frac{9}{8} (A_2 - A_3), \quad A_2 = a_{ji} a_{ij}, \quad A_3 = a_{ij} a_{jk} a_{ki}. \quad (3.53)$$

Notably, A is called "flatness parameter". When $A = 1$ turbulence is isotropic, whereas when it is zero it indicates that turbulence is anisotropic. In this thesis, the invariants will be plotted with contour maps.

Lumley triangles From Equations 3.53, the following parameters are defined for the construction of the "Lumley triangles" [65], which help understand the "shape" of the turbulence. The parameter η is linked to the second invariant A_2 through [13]:

$$6\eta^2 = A_2/4, \quad (3.54)$$

whereas the parameter ξ is linked to the third invariant as [13]:

$$6\xi^3 = A_3/8. \quad (3.55)$$

In a turbulent flow, the values of η and ξ tend to be enclosed within a pseudo-triangle. Figure 3.4 shows the triangle and the "shapes" that the turbulent structures assume at its edges and vertices. The point (0,0) corresponds to isotropic turbulence, which is indicated with a sphere. The opposite edge represents 2-component turbulence, eddies tend to have a more elongated structure, until they collapse in 1-component turbulent structures at the top-right vertex.

3.8.4 Computation of the forces and moments over the aircraft model

In this thesis, TAU is used to compute the forces generated on the VTP geometry. The forces are subdivided into two contributions: pressure forces and viscous forces.

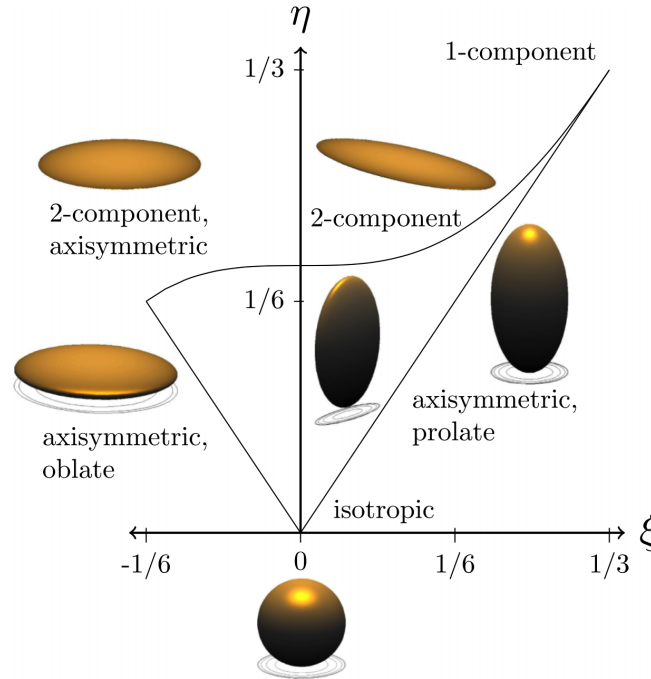


Fig. 3.4 Lumley triangle showing limits of invariants η and ξ , Hamilton *et al.* [45].

Pressure forces

Figure 3.5 shows the pressure $p(j)$ acting on a face j of the boundary b of the aircraft model. Let $S_b(j)$ be the surface of the face j and \mathbf{n} be the vector normal to the face. The pressure force vector is calculated at the vertex i of the grid as:

$$\mathbf{F}^p(b, i) = p(j)S_b(j)\mathbf{n}. \quad (3.56)$$

Viscous forces

In order to compute the viscous contributions for the global aerodynamic forces, the friction on the boundary has to be taken into account. For a surface point i of the grid, the viscous forces are calculated as:

$$\mathbf{F}^v(b, i) = \begin{pmatrix} \tau_{xx} & \tau_{xy} & \tau_{xz} \\ \tau_{xy} & \tau_{yy} & \tau_{yz} \\ \tau_{xz} & \tau_{yz} & \tau_{zz} \end{pmatrix} S_b(j)\mathbf{n} \quad (3.57)$$

where τ_{ij} is the tensor defining the viscous stresses.

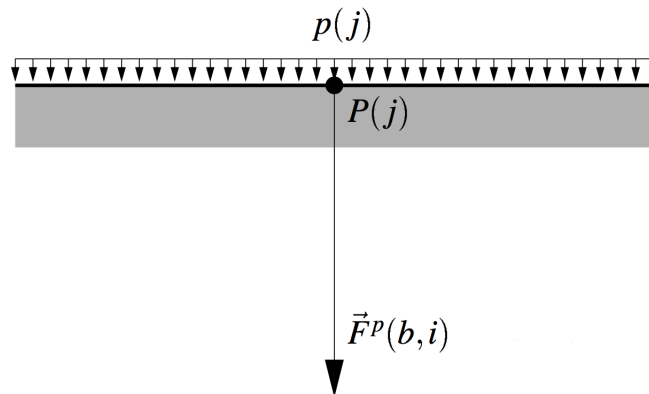


Fig. 3.5 Pressure force acting on a boundary face (re-adapted from [32]).

Therefore, the total force will be given by the sum of the pressure forces and viscous forces. TAU calculates also the force coefficients, as it will be explained in Chapter 5.

3.9 Computer resources

CFD studies on the VTP have been performed using Airbus HPC (High Performance Computing) facilities. The solvers perform a parallel computation, based on domain decomposition and the MPI (*Message Passing Interface*) communication protocol. The simulations inherent in this project have been run on machines based in Hamburg and Toulouse, whose features are reported in Table 3.2. Airbus HPC machines appear in the TOP500 list of the most powerful computers in the world. The Toulouse cluster was ranked at 167th position in November 2015. It is an HP POD, using Intel Xeon multi-core processors, with a LINPACK performance (Rmax) equal to 516.897 TFlop/s, and a theoretical peak (Rpeak) of 746.496 TFlop/s³.

LES simulations on the backward rounded step have been carried out on the Archer HPC, which is a British academic facility based around a Cray XC30. It has a total 4920 nodes, which corresponds to more than 118,000 cores⁴.

³<http://www.top500.org/>

⁴<http://www.archer.ac.uk/about-archer/hardware/>

Table 3.2 Features of the clusters used for VTP simulations.

HPC	Number of nodes	Number of cores	RAM per node (GB)
Hamburg 1	736	5888	24
Hamburg 2	232	1856	48
Toulouse 1	800	9600	36
Toulouse 2	208	2496	72
Toulouse 3	800	9600	36
Toulouse 4	208	2496	72

Chapter 4

Separation of a skewed boundary layer: an idealisation of VTP dynamics

4.1 Introduction

The Literature Review has described the flow characteristics over aircraft VTPs. The boundary layer developing along the VTP surface is three-dimensional, due to a velocity component aligned along the span of the VTP which skews the flow. When the 3D boundary layer meets the deflected rudder, and/or when the flow has a high incidence, flow separation occurs. RANS is the main methodology used in industry for the assessment of VTP flows. In order to assess its capabilities to predict separation and reattachment of a three-dimensional boundary layer, in this chapter a skewed flow along a backward rounded ramp is studied with three turbulence models (SA, SST and RSM). Results will be compared to a highly-resolved LES (quasi-DNS), also performed in the framework of this thesis. The LES will be used as the baseline study, with respect to which results from RANS and hybrid RANS/LES will be compared. The objective of this chapter is to assess RANS methodologies for the study of three-dimensional separated flow, and improve RANS through use of hybrid RANS/LES. This study prepares the field and the research strategy for the investigation of the same problem on the VTP.

To what extent can a flow on a backward step be connected to that on a swept VTP? Figure 4.1 shows a cut section on the VTP. A flow at zero incidence reaches the tail plane and the boundary layer grows along its surface. As explained in Chapter 2 (Figure 2.1b), due to the sweep angle of the VTP, the flow over the tail surface can be subdivided into two components: one running parallel to the free-stream velocity, and the other running along the span of the VTP (as shown in Figure 4.1). When the boundary layer reaches the hinge

line, the flow is subjected to a significant adverse pressure gradient and separates. The same phenomena occur on the backward rounded ramp plotted in Figure 4.1. A boundary layer having a spanwise flow component grows along the flat plate upstream of a gentle rounded step. This boundary layer is also subjected to an adverse pressure gradient, such that flow separation is expected. In order to recreate the effect of the sweep angle, the flow over the ramp is also skewed normally to the main flow direction. This is achieved with a body force added to the momentum equation, as explained in Section 4.2.2. Hence, even though the two geometries are quite different, the flow physics are similar. This is what justifies the analogy between the VTP and the backward ramp.

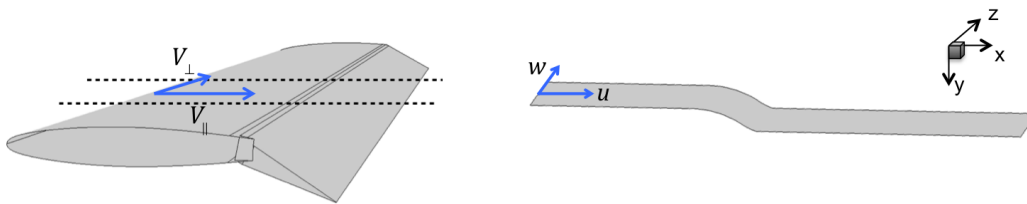


Fig. 4.1 Analogy between VTP and backward rounded step.

This chapter is structured as follows. First of all, the test case is presented, with information about the computational domain, the boundary conditions, and the grids used for the different CFD methodologies presented in the chapter. Then, the study of a highly-resolved LES (quasi-DNS) is illustrated. A detailed analysis of the overall flow features, velocity and Reynolds-stress profiles, and “shape” of the turbulence is carried out. The results from the LES will be used as reference data in order to assess how RANS models perform with predicting flow separation and reattachment of the three-dimensional boundary layer over the ramp. Finally, an improvement to one of the RANS models will be presented though use of a hybrid RANS/LES. The simulations used in this chapter are carried out with the HYDRA code, whose features were presented in Chapter 3.

4.2 The test case

The geometry chosen for the ramp is the same as used by Bentaleb *et al.* [13] in their study without skewed flow. Figure 4.2 shows the backward rounded step placed in a duct. The origin of the coordinates is placed at the upstream edge of the curved part, and notably x represents the directions parallel to the longest edge of the duct, y is the coordinate normal to the lower and upper walls, and z is the direction parallel to the span of the duct. The geometric entities are given with respect to the height of the step, which is equal to $H = 1$,

and are indicated in Figure 4.2. Notably, the length of the duct is equal to $15H$, its depth is equal to $3.7H$, and its height is equal to $8.52H$. The domain depth is the same as in the LES carried out by Bentaleb *et al.*. In the LES presented in this chapter, the width of the shear layer (which defines the integral length scale of the problem) is approximately similar to the one computed by Bentaleb *et al.*. Therefore, this box is sufficiently wide to capture all important structures in the simulation. The step shape is described by the following equations:

$$y_{wall} = \begin{cases} (1 - R_1) + \sqrt{R_1^2 - x^2}, & 0 < x/H < 2.3 \\ y_2 - \sqrt{\frac{R_1^2}{4} - (x_2 - x)^2}, & 2.3 < x/H < 2.835 \\ R_2 - \sqrt{R_2^2 - (3 - x)^2}, & 2.835 < x/H < 2.937 \end{cases} \quad (4.1)$$

where $R_1 = 4.03$, $R_2 = 0.333$, $x_2 = 3.449$ and $y_2 = 1.936$.

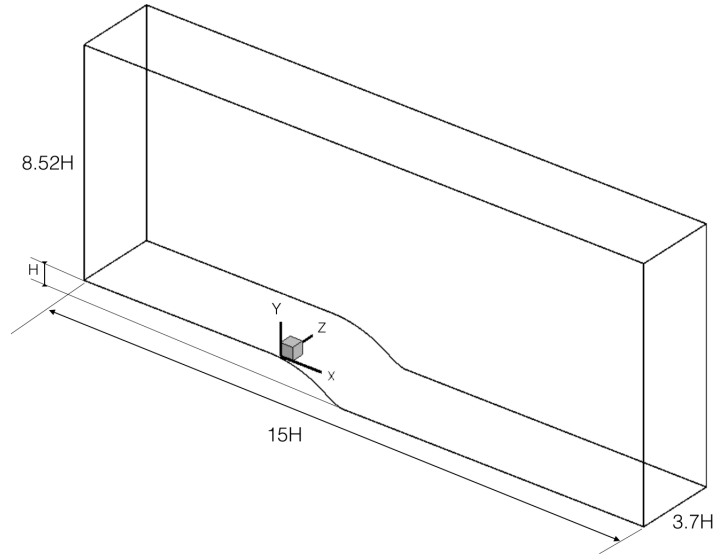


Fig. 4.2 Duct with backward rounded step.

4.2.1 The mesh

The domain is meshed with a structured grid. Table 4.1 reports the mesh sizes for the three methodologies used for this study. Notably, for LES, the grid has 768 grid-points in x -direction, 160 grid-points in y -direction, and 192 grid-points in z -direction. The same mesh size and the same mesh spacing were used by Bentaleb *et al.* [13] and tested for convergence,

therefore a grid sensitivity study has not been performed for LES. Appendix D shows that the RANS mesh is converged, which means that results are sufficiently grid-independent.

Table 4.1 Grid sizes for LES, RANS and hybrid RANS/LES of the backward ramp.

LES	RANS	Hybrid RANS/LES
$768 \times 160 \times 192$	$195 \times 160 \times 20$	$400 \times 160 \times 40$

It is convenient to define the grid spacing in wall units. For instance, for the y -direction, the Δy^+ distance is defined as [81]:

$$\Delta y^+ = \frac{u_\tau \Delta y}{\nu} \quad (4.2)$$

where u_τ is the friction velocity defined as $\sqrt{\tau_w/\rho}$, τ_w being the shear stress at the wall. ν and ρ are respectively the kinetic viscosity and the density of the flow.

Figure 4.3 shows the grid spacing in wall units and the aspect ratio $\Delta x/\Delta y$ along the bottom wall for the LES. The first cell height in wall units is $\Delta y^+/2 < 1$ for the whole length of the ramp (with the exception of a peak of this quantity slightly over 1 at $x/H = 0$). In the zone of interest ($0 < x/H < 5$, where the flow separates), the spanwise cell dimension is $5 < \Delta z^+ < 12$ and the streamwise cell dimension Δx^+ is below 12. On the upper wall the grid is much coarser. In fact, since the duct a large height relative to H , precursor studies have shown that the upper wall does not influence the separation region on the lower wall, and any loss of accuracy at the upper wall compensates with a saving of computational simulation time [13]. The unsteady physical time step used for LES and hybrid RANS/LES is equal to $\Delta t = 5 \cdot 10^{-4}$ s.

4.2.2 Inflow and boundary conditions

The Reynolds number of the problem is $Re = 13,700$, and it is based on the inlet velocity U_{in} outside the boundary layer and on the height of the step H . For the LES and hybrid RANS/LES presented in this chapter, a turbulent boundary layer has been imposed at the domain inlet ($x/H = -7.36$) on both the upper and lower wall. It is a collection of snapshots of a flow that evolves along a channel. This was generated by a precursor simulation performed by Lardeau *et al.* [66] that used a recycling method for generating the boundary layer. The recycling method consists of extracting a plane of data from a location several boundary-layer thickness downstream of the inflow, and rescaling the inner and outer layers of velocity profiles separately, to account for the different similarity laws that are observed in these two regions. The rescaled velocity profiles are then reintroduced at the inlet until a

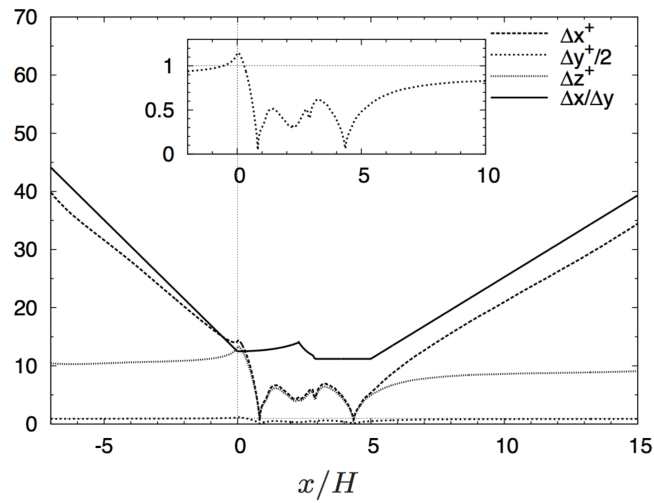


Fig. 4.3 Grid spacing in wall units and aspect ratio $\Delta x/\Delta y$ along the bottom wall [13].

statistically steady state is achieved. The flow-snapshots were collected at a position in the channel at which $Re_\theta = 1190$, for a boundary layer thickness equal to $\delta_{99} = 0.83H$. Some of the flow-snapshots are plotted in Figure 4.4, which shows contours of the instantaneous streamwise velocity. The profiles of mean velocity and the characteristics of the turbulent boundary layer are shown in figures 4.5 and 4.6, respectively.

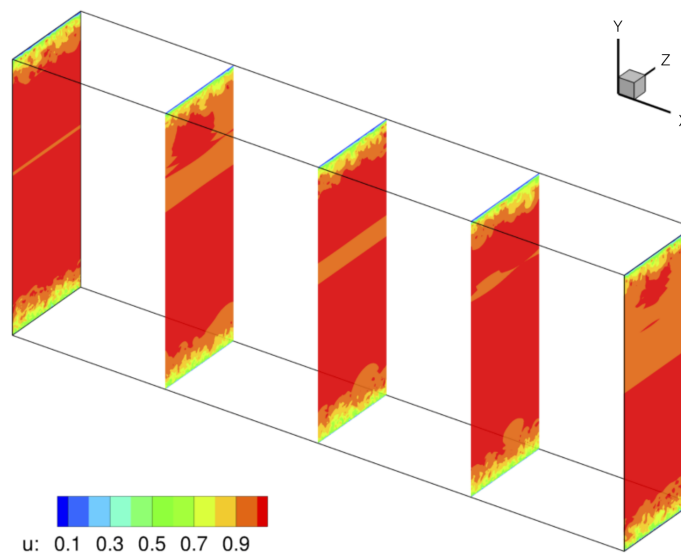


Fig. 4.4 Flow-snapshots of the inflow for the backward rounded map test case, organized in a turbulent box. Inflow data was received from Lardeau [57].

The outlet of the duct is a standard subsonic outlet. In this work, downstream of the duct, a buffer layer is introduced. This is meshed with a very coarse mesh in x -direction, in order

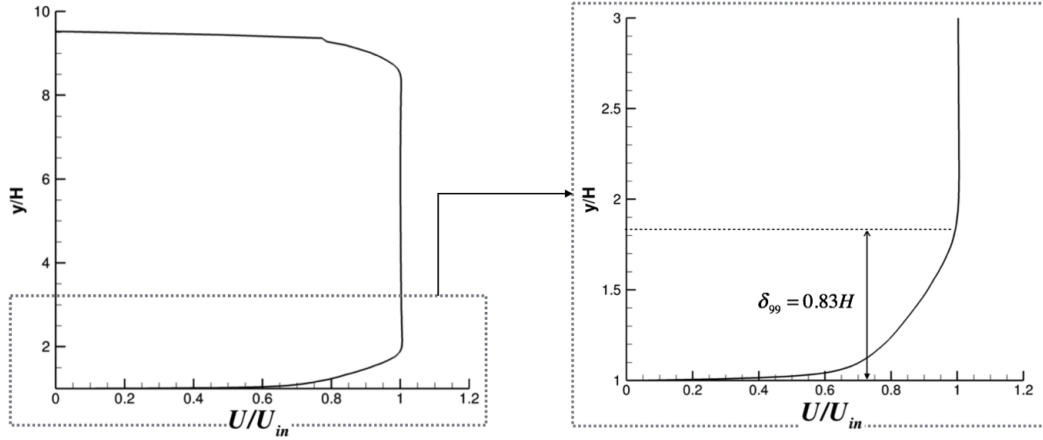


Fig. 4.5 Mean velocity in streamwise direction. Inflow data was received from Lardeau [57].

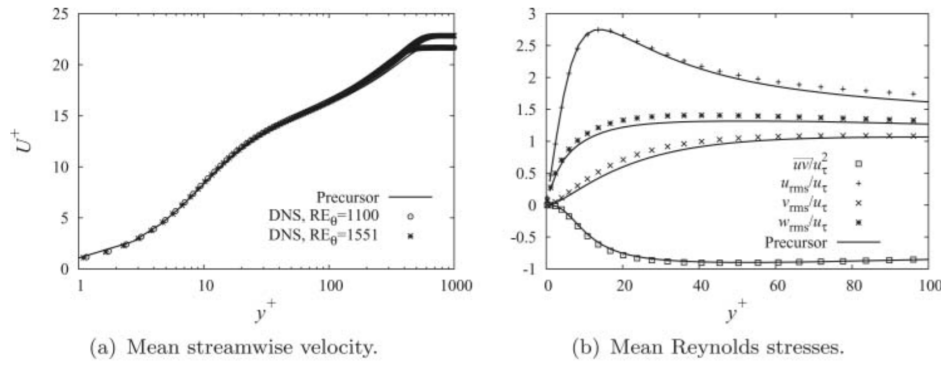


Fig. 4.6 Turbulent boundary (characteristic displacement thickness $Re_\theta \approx 1190$) of the inflow [13]. Comparison with DNS data [54].

to dump any reflections that might occur on the outlet surface. The lateral walls have been given periodic boundary conditions.

In this thesis, a source term in the z -momentum equation is introduced in order to sweep the flow along the span of the duct. If $NS_i(w) = 0$ represents the Navier-Stokes z -momentum equation for a volume Ω_i , then the equation is modified as:

$$NS_i(w) + f_{z,i}(x) = 0 \quad (4.3)$$

where $f_{z,i}$ is a ramp function of equation:

$$f_{z,i}(x) = \begin{cases} 0.01 (4/7x + 4) \cdot \Omega_i, & -7 < x/H < -21/4 \\ 0.01 \cdot \Omega_i, & -21/4 \leq x/H < 6. \end{cases} \quad (4.4)$$

Figure 4.7 shows the evolution of f_z along the ramp. This function increases gradually from 0 at the inlet of the ramp ($x/H = -7$), to $0.01 \cdot \Omega_i$ at $x/H = -21/4$, and then it is constant. This was chosen empirically, with the objective of skewing the boundary layer. In fact, the body force f_z generates a spanwise pressure gradient $\partial p/\partial z$ that skews the streamlines along the duct. This methodology was already used by Bentaleb *et al.* [14], who performed DNS of a boundary layer developing over a flat plate subjected to a spanwise pressure gradient. The DNS showed that the flow is skewed along the span, and the boundary layer becomes three-dimensional. Further results of the effect of the body force f_z are found in papers by Howard *et al.* [48] and Moin *et al.* [72]. In the latter, Moin explains that the skewed flow generated by a spanwise pressure gradient bears a strong resemblance to the infinite-swept wing flow. Both a channel flow subjected to spanwise pressure gradient and the flow over an infinite-swept wing experience turning of the streamlines as a result of $\partial p/\partial z$. In addition, the novelty of the study presented in this chapter consists of the presence of a streamwise pressure gradient, which leads to separation along the ramp. Evidences of the skewed flow generated by the forcing term f_z are reported in the next section.

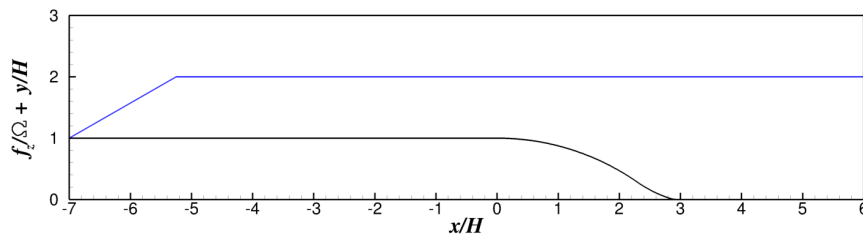


Fig. 4.7 Source term in the z -momentum equation.

Appendix C reports the LES validation study carried out on the same test case *without* crossflow. The simulation is needed to show that the case is set up correctly. Results are validated against experimental observations by Zhang & Zhong [126], and the simulation by Bentaleb *et al.* [13] (without crossflow).

4.3 Highly-resolved LES with crossflow

4.3.1 Overall view and major characteristics of skewed flow

This section treats the main characteristics of the skewed flow that develops along the ramp in the duct. The flow travels the duct for 20 times, and the solution is time-averaged

on the last 12 though-flows. Figure 4.8a shows that, for most of the duct, the flow travels at mean velocity¹ $\bar{U} = 1$ and, far enough from the lower wall, the flow is not affected by the ramp and the separation occurring along it. The flow interacts with a forcing term f_z and is skewed along the span of the duct. Figure 4.8b shows the flow streamlines over contours of the spanwise velocity w . The picture shows that the streamlines are not straight, but are effectively skewed along the duct.

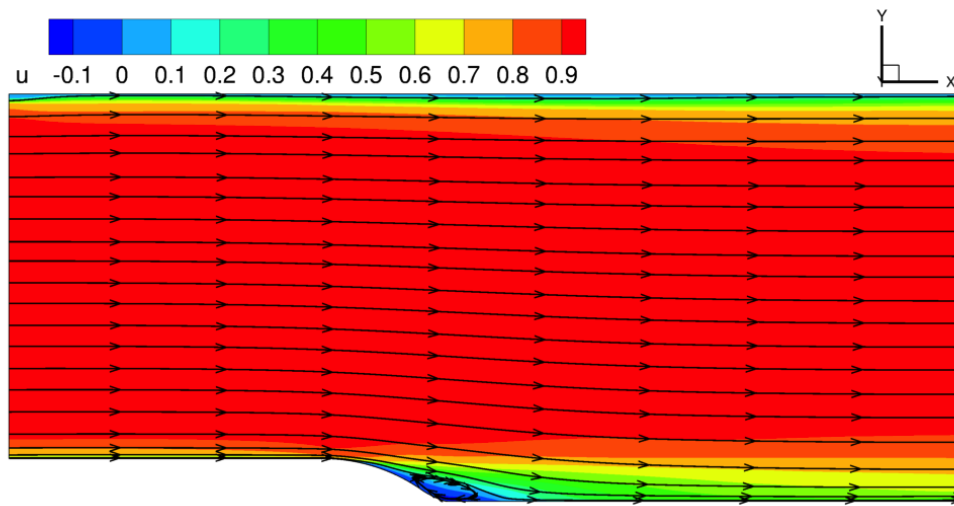
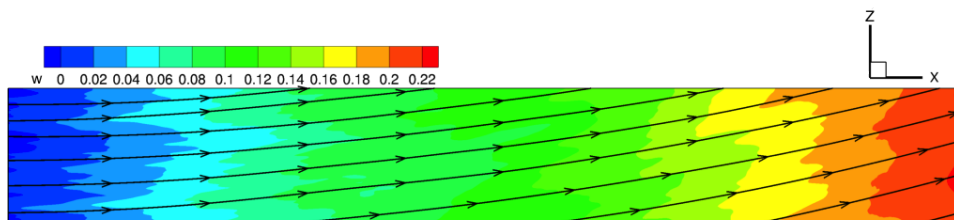
(a) $x - y$ plane.(b) $x - z$ plane.

Fig. 4.8 LES: Time-averaged flow along the duct.

On the lower wall, when the flow reaches the rounded step, separation occurs. Figure 4.9 shows the mean skin-friction lines at the wall of the ramp. The surface is coloured by streamwise velocity at $y^+ = 1$. The skin-friction lines converging in a single line are an indication of flow separation. On the other hand, skin-friction lines diverging from a single line show the location of flow reattachment. This picture also gives a qualitative feeling of

¹All variables are non-dimensionalized.

the skewness of the flow in the z -direction. The top view presented in Figure 4.10 shows the separation and reattachment lines clearly.

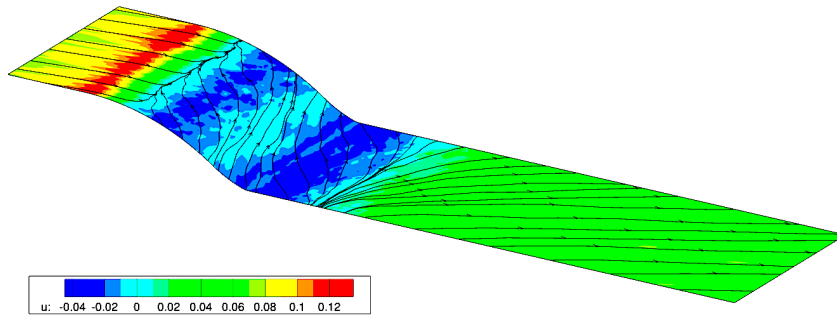


Fig. 4.9 Skin-friction lines on the wall of the backward ramp.

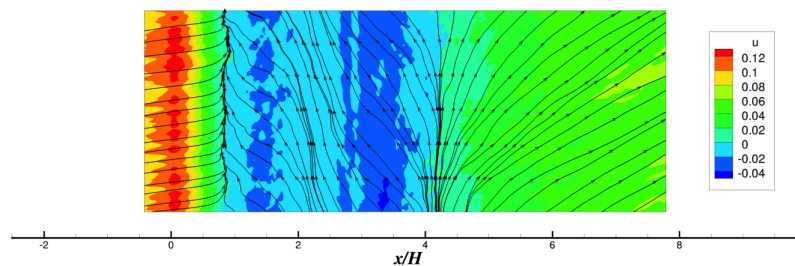
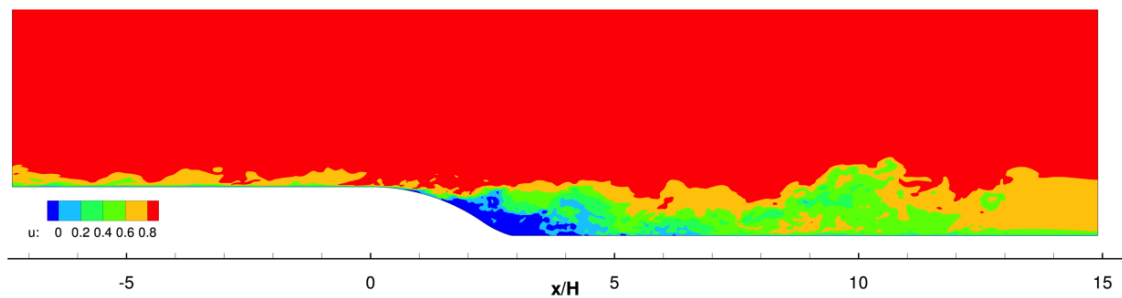


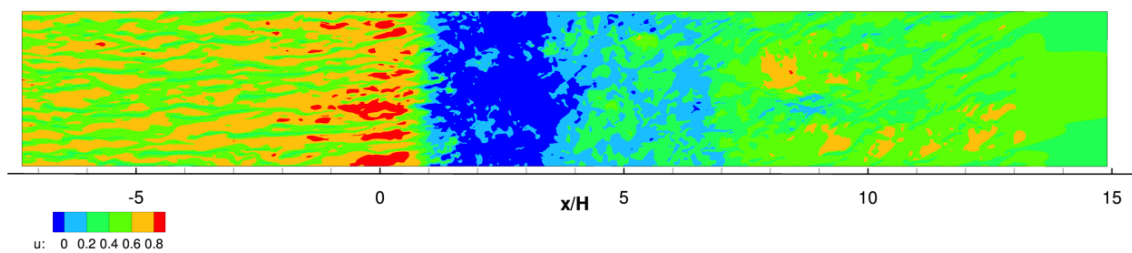
Fig. 4.10 Skin-friction lines on the wall of the backward ramp. Zoom on separation and reattachment lines.

In order to appreciate the turbulent character of the flow, instantaneous snapshots of the flow realization are plotted in figures 4.11a and 4.11b. The former shows the flow realization in the $x - y$ plane, the latter the flow in the $x - z$ plane. The two streamwise velocity representations highlight the turbulent characteristic of the flow. The velocity fluctuations become more and more important in the proximity of the lower wall. The dark blue region indicates the presence of a reversed flow, since the u velocity assumes negative values. However, the top view representation shows some patches of positive velocity enclosed in the blue area. These patches suggest that, for this particular instant in time, there are some areas in which the flow is attached within the recirculation region above the ramp. Moreover, the reattachment region is also quite patchy, indicating that the location of flow

reattachment is quite intermittent. Figure 4.12 shows isosurfaces of the Q -criterion coloured by the streamwise velocity. The biggest turbulent structures are located in the upper portion of the separated shear layer. They develop along the duct and are convected downstream, and at the same time they are skewed in the spanwise direction.



(a) Spanwise mid-plane.



(b) Top view at distance $y^+ = 15$.

Fig. 4.11 Instantaneous streamwise velocity.

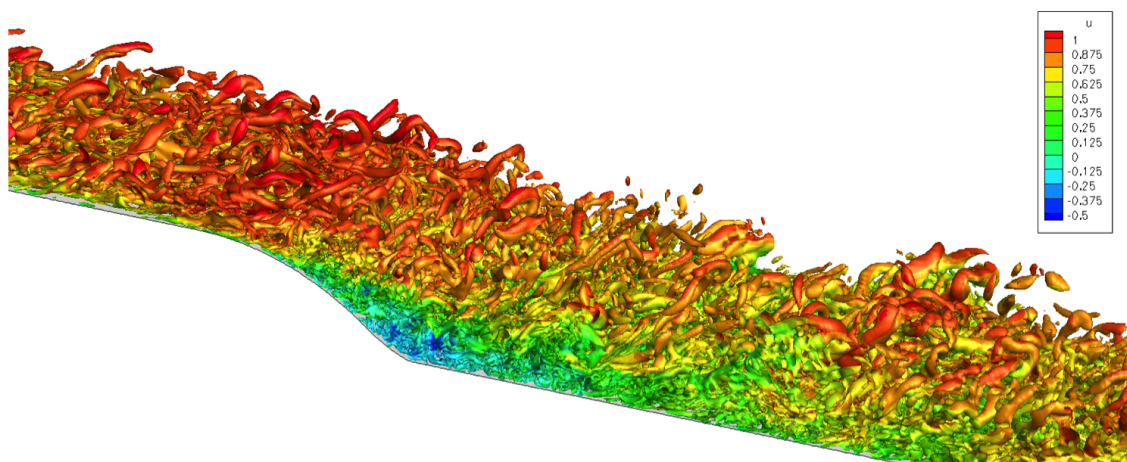


Fig. 4.12 Isosurface of the Q -criterion coloured by streamwise velocity.

The time-averaged and spanwise-averaged velocity fields are plotted in Figure 4.13 through use of streamlines in the $x - y$ plane. Figures 4.14a and 4.14b show the magnified views of the separation and reattachment locations, respectively. The detached flow is enclosed within a thin and elongated region (Figure 4.13 is not to scale). The time-averaged separation line is located at $x/H = 0.83$ and the time-averaged reattachment line is placed at $x/H = 4.25$. A comparison with the equivalent non-crossflow case (Appendix C) shows that the location of flow reattachment moves forward, and now the separation region is 10% bigger than in the case without crossflow (see Table C.1).

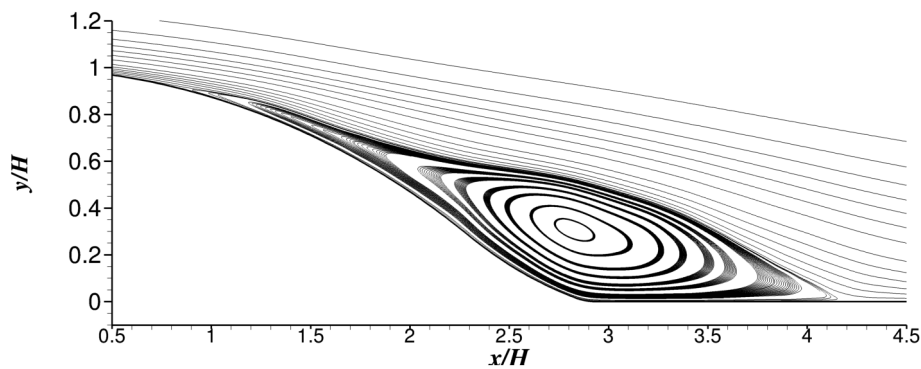
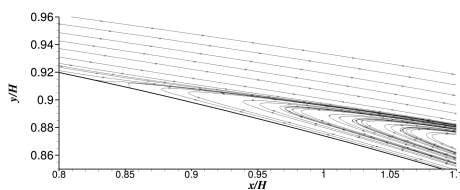
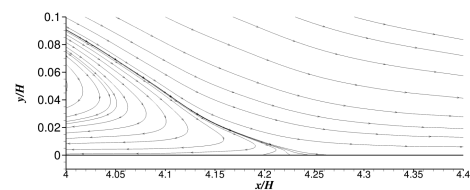


Fig. 4.13 Streamline contours of the time-averaged and spanwise-averaged flow field in the recirculation region.



(a) Zoom on separation location.



(b) Zoom on reattachment location.

Fig. 4.14 Streamline contours of the time-averaged and spanwise-averaged flow field in the recirculation region: magnified views at separation and attachment locations.

Figures 4.15a and 4.15b show the mean pressure C_p and the skin-friction coefficients C_f . Ahead of the ramp, the pressure drops significantly, causing a rapid acceleration of the boundary layer, and a sharp increase of the friction at the wall. Just beyond point $x/H = 0$, this trend is reversed. The streamwise pressure gradient acts against the boundary layer, slowing it down and causing an inflected velocity and flow detachment. The small hump in the C_p distribution at $x/H \approx 1$ reflects the thin initial separation region, as shown in Figure 4.14a, followed by larger hump and rapid growth of the recirculation zone from $x/H = 2$.

When the flow separates, as would be expected, the friction goes to zero suddenly, and then becomes negative. The point at which $C_f = 0$ and $dC_f/dx < 0$ indicates flow separation. After the separation point, the pressure increases until it reaches its maximum close to the reattachment point. Flow reattachment occurs when the skin-friction coefficient intersects the axis $x/H = 0$, this time with a positive gradient. Downstream of the recirculation zone, the pressure tends to reach a steady plateau. The boundary layer then develops along the flat plate until the outlet of the duct.

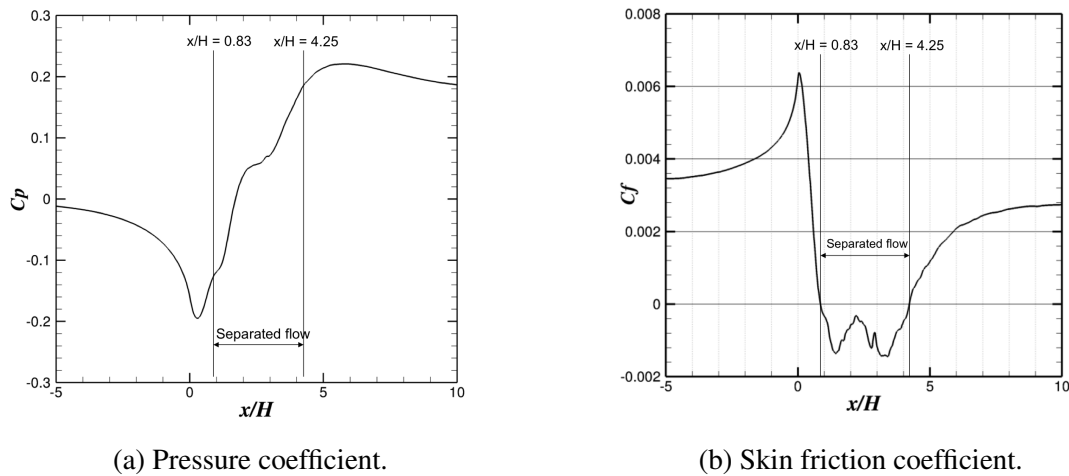


Fig. 4.15 Distributions of pressure and skin friction coefficients along the lower wall.

4.3.2 Velocity and Reynolds-stress profiles

Figure 4.16 shows profiles of the time-averaged velocity components for different locations along the ramp. Notably, Figure 4.16a shows the profiles of the mean streamwise velocity, which is the predominant velocity component in the flow; the profiles at $x/H = 0$ and $x/H = 0.5$ confirm the qualitative description given in the previous section. Hence, ahead of the ramp, the boundary layer accelerates owing to the drop of pressure on the ramp. For this reason, the velocity profiles are quite elongated. At the same time, the streamwise-adverse pressure gradient becomes more important, the flow undergoes deceleration over the ramp. At $x/H = 1$, the mean \bar{U} profile is reversed near the wall, indicating that the boundary layer is separated. Locations $x/H = 2$, $x/H = 3$ and $x/H = 4$ show that the flow is reversed, whereas the profile at location $x/H = 5$ shows that flow has reattached somewhere in the region $4 < x/H < 5$. For this reason, the mean velocity profile no longer shows reversed flow. The mean velocity \bar{V} in Figure 4.16b in the direction normal to the wall is negative for all the profiles, except for $x/H = 2$ and $x/H = 3$, where it assumes positive values. In fact, in the

recirculation region, the flow is reversed and forced to go up the ramp, until its velocity is again reversed and it accelerates downstream, forming the recirculation zone.

Figure 4.17 shows time-averaged Reynolds-stress profiles along the rump. For $0 < x/H < 1$ the streamwise Reynolds stresses $\overline{u'u'}$ are largely predominant over the other two normal components. This indicates an anisotropic character of the turbulence in the near-wall region before separation. By contrast, in the separated flow area, turbulent kinetic energy redistributes, feeding the other normal Reynolds-stress components until reattachment. The stresses $\overline{u'v'}$ are the most energetic Reynolds shear stresses, rising steeply after separation.

As standard practice for this kind of flow, Figure 4.18 shows the flatness parameter A introduced in Section 3.8.3. The map shows that $A \approx 0$ at the onset of flow separation, indicating that turbulence is anisotropic. This confirms what was observed in from the Reynolds stresses. In the separated region, A increases because turbulence tends to assume a more isotropic behaviour. This is confirmed by the Lumley triangles plotted for two different locations within the recirculation region: $x/H = 1$, and $x/H = 3$. Figure 4.19a shows that at $H = 1$ data is mostly distributed along the *axisymmetric expansion* edge, with a high concentration close to the top right vertex of the triangle. Such an expansion encourages the growth of the stream-wise normal stress and reduction in the cross-flow components. Therefore, at this location, turbulent structures tend to be elongated, assuming a rod-like shape. Moving away from the wall, the circles progress along the *axisymmetric expansion* edge, turbulence assuming the shape of a prolate spheroid. This is consistent with standard separated shear layers. As the triangle in Figure 4.19b shows, at $x/H = 3$, turbulent structures undergo *axisymmetric contraction*, involving a suppression of stream-wise normal stress, acquiring a ‘pancake’-like shape (oblate spheroid).

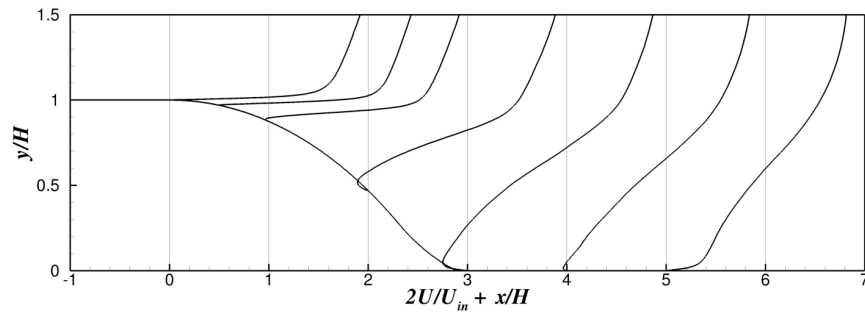
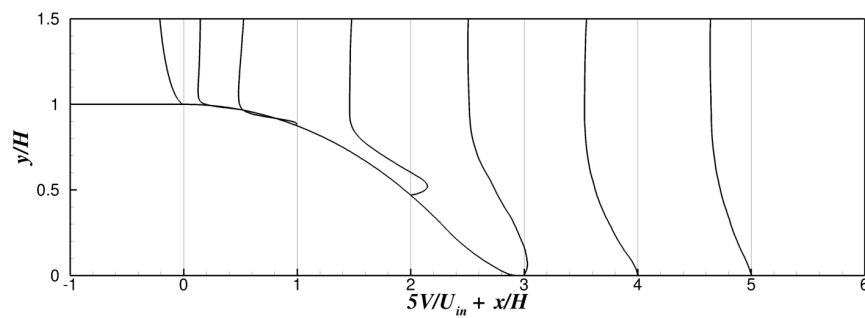
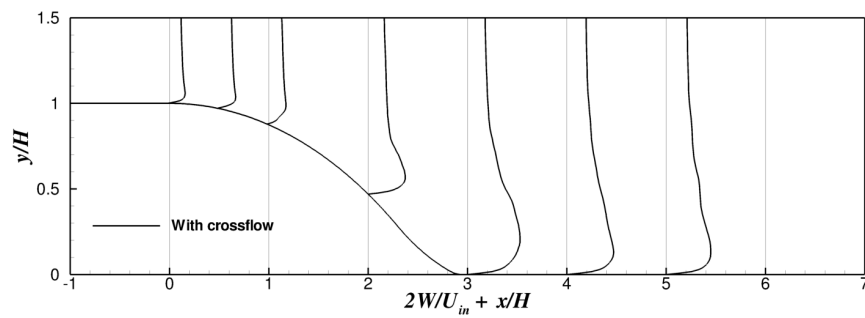
(a) \bar{U} profiles.(b) \bar{V} profiles.(c) \bar{W} profiles.

Fig. 4.16 LES with crossflow - Mean velocity profiles at various locations: $x/H = 0$; $x/H = 0.5$; $x/H = 1$; $x/H = 2$; $x/H = 3$; $x/H = 4$, and $x/H = 5$.

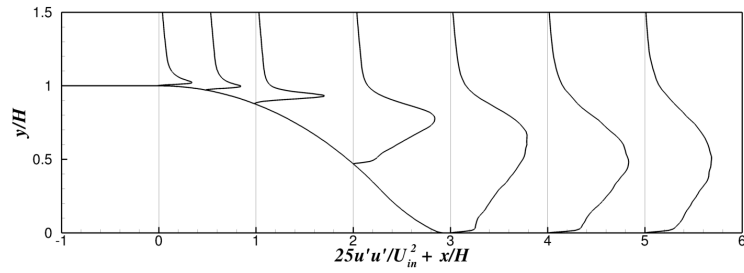
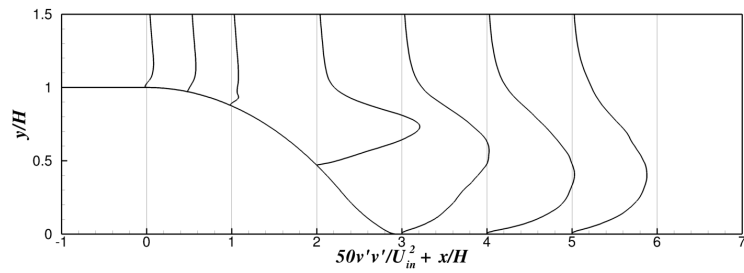
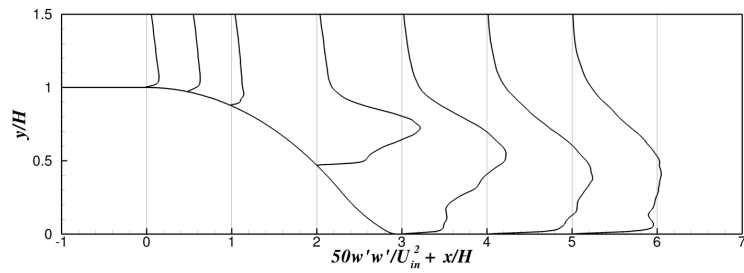
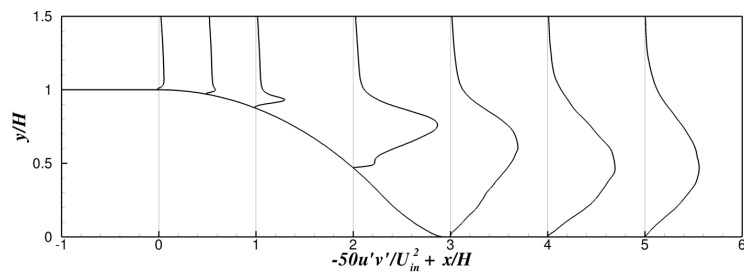
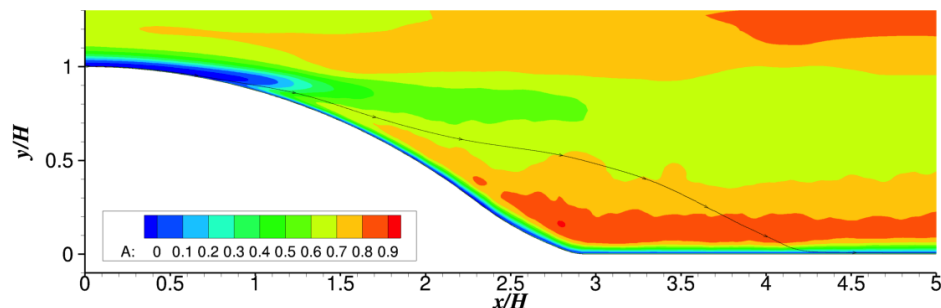
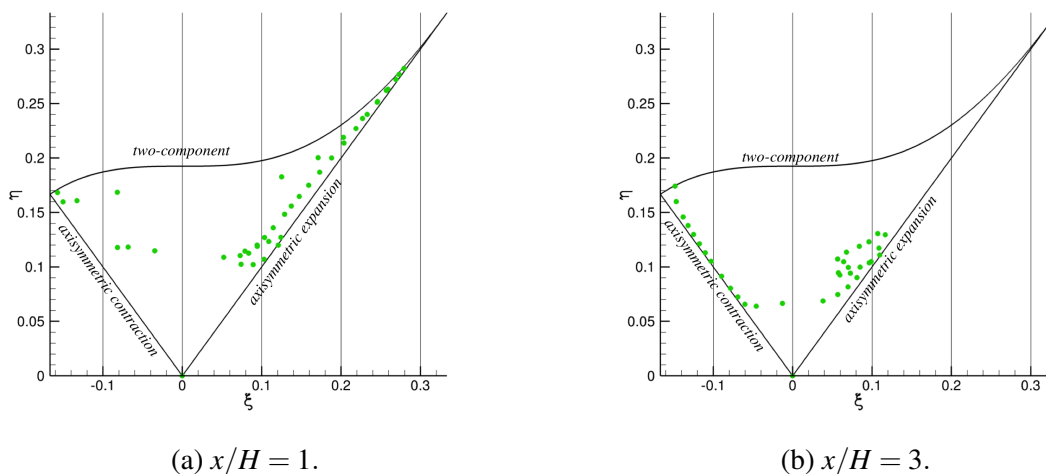
(a) $\overline{u'u'}$ profiles.(b) $\overline{v'v'}$ profiles.(c) $\overline{w'w'}$ profiles.(d) $\overline{u'v'}$ profiles.

Fig. 4.17 LES with crossflow - Mean Reynolds-stress profiles at various locations: $x/H = 0$; $x/H = 0.5$; $x/H = 1$; $x/H = 2$; $x/H = 3$; $x/H = 4$, and $x/H = 5$.

Fig. 4.18 Contour of the flatness parameter A .Fig. 4.19 Lumley triangles of the flow in the recirculation region, with $y/H < 1.5$.

4.4 RANS with crossflow

In order to understand the quality of their performance in predicting the separation of three-dimensional boundary layers, steady RANS studies are performed on the backwards rounded ramp. Three different turbulence models have been used to close the Reynolds-averaged NS equation: the Spalart-Allmaras (SA) model; the Menter-SST turbulence model, and the SSG/LRR- ω Reynolds-stress Model. Details of the three models are reported in Appendix B.

4.4.1 Overall view and major characteristics

RANS simulations are carried out with the same boundary conditions used for LES. The only difference consists of the inflow conditions, which, in this case, is a turbulent boundary layer profile gathered from the span-average and time-average of the LES inflow plane. The

RSM-RANS reads also the Reynolds stress profiles from the LES. For the eddy-viscosity models, at the inlet a turbulent intensity $I \approx u'/\overline{U_{in}} = 0.05$ (5%) has been specified. The minimum turbulent viscosity ratio was set to $\mu_t/\mu = 10$. To retrieve the turbulent kinetic energy k and the specific dissipation rate ω at the inlet, the following relations are used [11]:

$$k = \frac{3}{2} (\overline{U_{in} I})^2 \quad (4.5)$$

and

$$\omega = \rho \frac{k}{\mu} \left(\frac{\mu_t}{\mu} \right)^{-1}. \quad (4.6)$$

Simulations were carried out with $CFL = 1$.

The overall picture of the RANS results, shown in Figure 4.20, is similar to LES in the free-stream flow. However, over the ramp, the recirculation area is different from the mean flow obtained by the LES, and the results vary with respect to the turbulence model used. The locations of flow separation and reattachment computed by the three RANS methods are reported in Table 4.2.

Table 4.2 Comparison of separation and reattachment locations.

	SA-RANS	SST-RANS	RSM-RANS	LES
x/H separation	1.10	0.82	0.93	0.83
x/H reattachment	5.17	6.19	6.06	4.25
L_{sep}	4.07	5.37	5.13	3.42

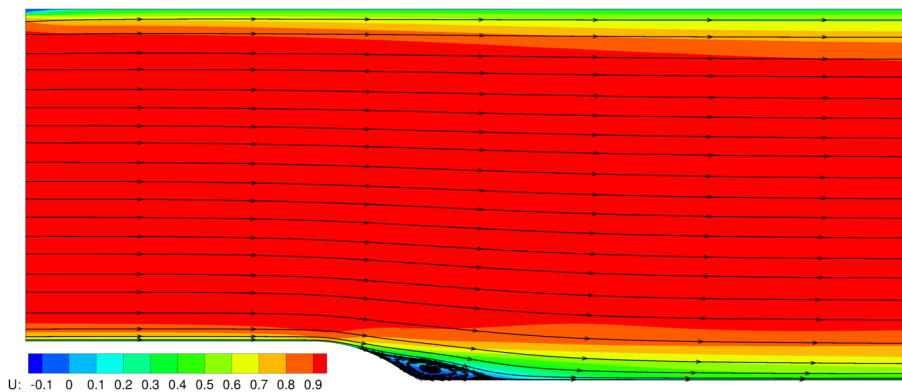


Fig. 4.20 RANS: flow along the duct.

SA and RSM over-predict the distance of the separation point from the start of the ramp by 32% and 12%, respectively. The SST model predicts the location of flow separation

almost perfectly. By contrast, the three models predict reattachment significantly further downstream than LES. SA has a relative error of 22% with respect to the LES reattachment distance from the start of the ramp. SST and RSM over-predict reattachment by around 45%. The length of the separation region predicted by SST and RSM exceeds the LES one by 57% and 50%, respectively. SA over-predicts this by 20%. However, this occurs because SA predicts separation later, hence the streamlines confine the recirculation region in a smaller area, with respect to the other two models. As commented in the Literature Review, the Menter-SST shows good capabilities in the prediction of the onset of flow separation, but then flow reattachment is delayed.

Figure 4.21 shows the pressure distribution calculated by RANS and LES over the lower wall of the duct. Only SA predicts the negative peak in the C_p , although this happens for the wrong reason. In fact, SA predicts a late separation, and, since the flow is attached for longer, it accelerates along the curved wall, and the pressure decreases. SST and RSM do not match the LES C_p trend either. Notably, even though SST predicts the onset of flow separation correctly, the long recirculation area influences the pressure field along the ramp. This shows clearly the limitations of RANS methods to compute detached flows correctly. In fact, both the negative peak seen for $0 < x/H < 1$ and the pressure plateau are under-estimated by 40% (in magnitude).

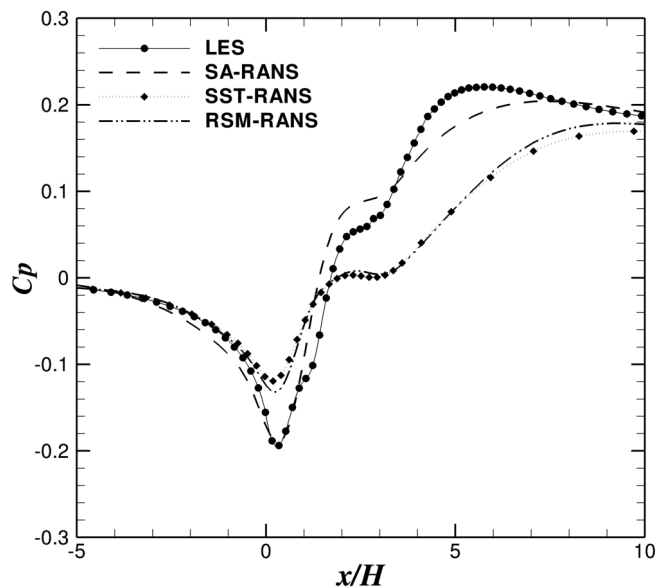


Fig. 4.21 Pressure coefficient over the lower wall of the duct computed by LES and RANS.

4.4.2 Velocity profiles

Figure 4.22 shows the velocity profiles obtained by RANS, compared to those obtained by the LES. Before separation, at $x/H = 0$ and $x/H = 0.5$, the \bar{U} velocity profiles computed by LES is fuller than the RANS ones, but it is in the separation region that the velocity profiles look quite different. In fact, at $x/H = 1$, at the wall the velocity profiles for all except SA are inflected and a very small reverse flow region near the wall can be observed. The reversed-flow depth for SST and RSM grows rapidly so that it grossly exceeds that seen for LES. This situation persists downstream, including through the delayed reattachment seen in RANS. SA detects flow separation much later but then the initial reversed-flow depth is quite close to LES, this continuing through $x/H \approx 3$ after which the delayed reattachment leads to strong differences in profiles (20-30% relative error).

Moreover, looking at the vertical velocity profiles \bar{V} at $x/H = 1$, it is notable that SA over-predicts the magnitude of the vertical component by 40% compared with LES. This results in changing the trajectory of the streamlines right above the separation bubble, forcing the flow to reattach earlier. At $x/H = 5$, the averaged flow should be completely attached, as predicted by LES. On the contrary, at this location RANS velocity profiles still show reversed flow.

Figure 4.22c shows that, in the boundary layer, the \bar{W} velocity predicted by RANS is much larger (100-150%) compared to that calculated using LES in the recirculation region. This is due to the fact that the crossflow is reaching a slower boundary layer, with respect to that predicted by LES. Far from the wall, on the contrary, the \bar{W} velocity profiles converge towards LES results.

As highlighted in the Literature Review, Reynolds-Stress transport equations include a pressure-strain term, which redistributes the energy among the normal stresses. The anisotropy maps and the Lumley triangles gathered from the LES study have shown instead that the separating boundary layer is characterised by a strong anisotropy. Figure 4.23 shows a comparison between the Reynolds stresses predicted by the RSM-RANS and those from the LES. At $x/H = 1$, it is notable that the modelled normal stresses are almost evenly distributed among the three components at the onset of flow separation. However, the LES predicts that here the streamwise component of the Reynolds normal stresses largely prevails over the other two. This was confirmed also by the streamwise normal Reynolds stresses $\overline{u'u'}$. Moreover, the modelled $\overline{v'v'}$ normal stresses are over-estimated by almost double, compared to the LES. Therefore, the more complex representation of the Reynolds stresses given by the RSM model does not result in good accuracy in the prediction of flow conditions around the onset of flow separation.

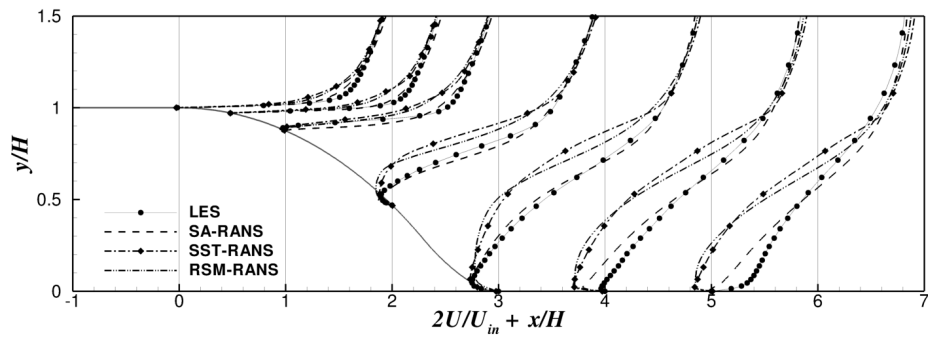
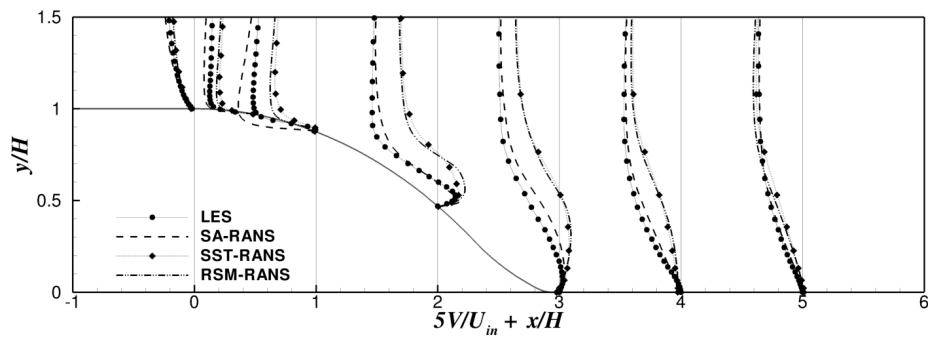
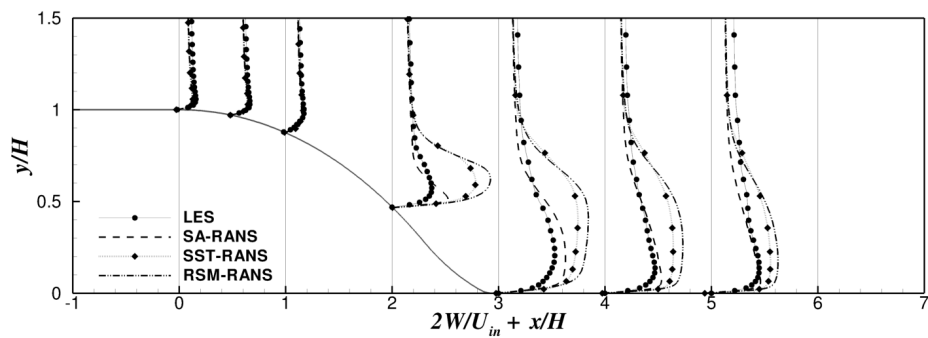
(a) \bar{U} profiles.(b) \bar{V} profiles.(c) \bar{W} profiles.

Fig. 4.22 RANS: mean velocity profiles at various locations: $x/H = 0$; $x/H = 0.5$; $x/H = 1$; $x/H = 2$; $x/H = 3$; $x/H = 4$, and $x/H = 5$.

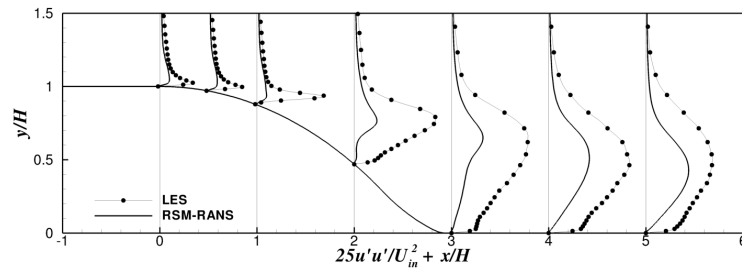
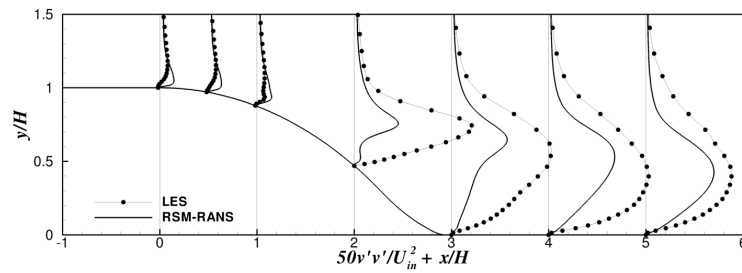
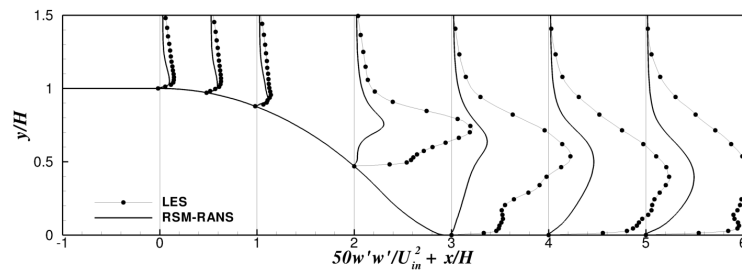
(a) $\overline{u'u'}$ profiles.(b) $\overline{v'v'}$ profiles.(c) $\overline{w'w'}$ profiles.

Fig. 4.23 Mean Reynolds-stress profiles at various locations: $x/H = 0$; $x/H = 0.5$; $x/H = 1$; $x/H = 2$; $x/H = 3$; $x/H = 4$, and $x/H = 5$. Comparison of LES with RSM-RANS.

In order to understand why RANS and LES present such major differences, notably in the prediction of the length of the recirculation zone, it is necessary to look deeper at the mechanisms that govern the Turbulent Kinetic Energy (TKE) balance in the flow. For this reason, the next section will look at the production and dissipation of TKE in the flow.

4.5 Production and dissipation of turbulent kinetic energy

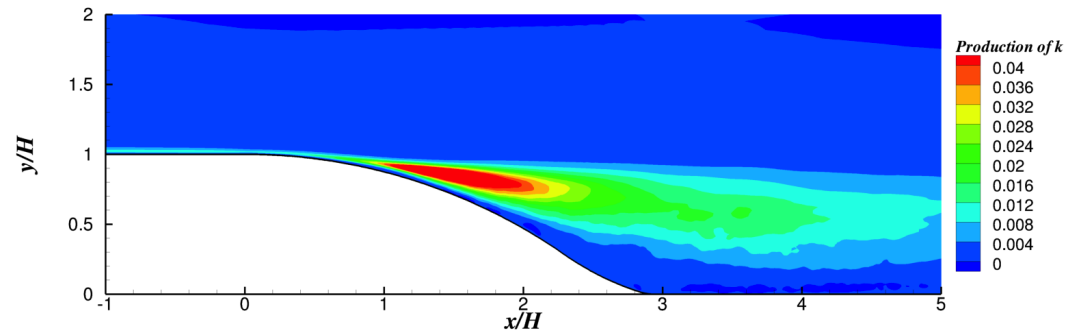
The separation occurring along the ramp results in the generation of intense turbulence. It is interesting to look at the TKE budgets to understand how it evolves within the recirculation region. The variation of turbulent kinetic energy in the flow is given by the equation [81]:

$$\frac{\partial k}{\partial t} + \bar{u}_j \frac{\partial k}{\partial x_j} = -\frac{1}{\rho} \frac{\partial \overline{u'_j p'}}{\partial x_j} - \frac{1}{2} \frac{\partial \overline{u'_i u'_i u'_j}}{\partial x_j} + 2\nu \frac{\partial \overline{u'_i s'_{ij}}}{\partial x_j} - \overline{u'_i u'_j \bar{s}_{ij}} - 2\nu \overline{s'_{ij} s'_{ij}}. \quad (4.7)$$

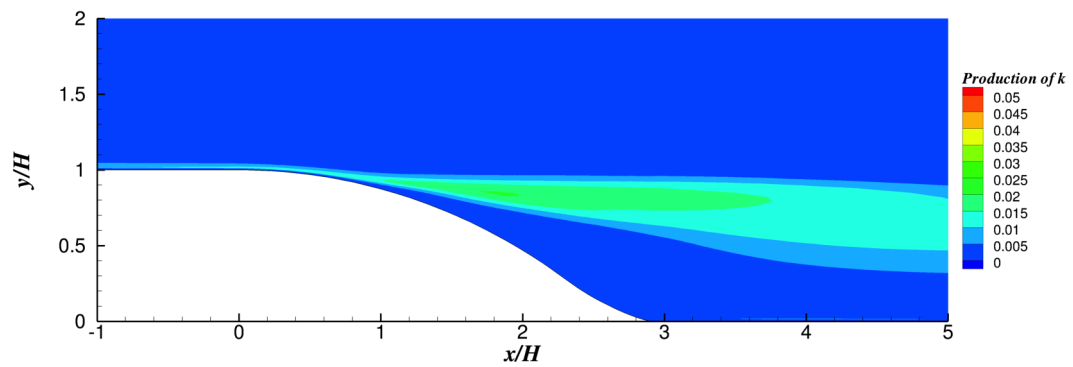
The terms on the right-hand side of the equation represent pressure diffusion, turbulent transport, molecular diffusion, production of turbulent kinetic energy (P_k), and dissipation of turbulent kinetic energy respectively. In this section, attention is paid to two of the TKE energy budgets - production and dissipation - for the SST and RSM turbulence models². For LES, production and dissipation rate are post-processed from the time-averaged Reynolds stresses and velocity gradients that are computed during the simulation (see Equation 3.48).

The production of TKE varies significantly with respect to the CFD method used to study the flow. In fact, Figure 4.24 shows contour maps of the production of TKE (P_k), from which it is possible to observe significant differences. The time-averaged P_k computed by the LES is presented in the top figure 4.24a, which shows that most of the turbulent kinetic energy is produced in the shear layer above the separation region. P_k is almost zero in the mean flow. The peak of P_k is achieved at the onset of flow separation; in the recirculation region P_k ranges between 0.02 and 0.03, dropping to zero near the lower wall. The LES P_k map differs from the RANS ones dramatically. In fact, the turbulence models are not able to produce as much turbulent kinetic energy as the LES does. SST and RSM can predict the rapid rise of TKE production at the onset of flow separation, but it does not reach the levels shown in the LES contour map. Figure 4.25 shows contour maps of the level of TKE dissipation. Dissipation is low and does not differ as significantly as the production term among the three methods. Figure 4.26 shows the production and dissipation profiles for $x/H = 1.5$, within the recirculation area. The figure shows that the peak in TKE production for RANS occurs much closer to the wall, in fact at only 20% of the wall distance of the LES peak; the RANS

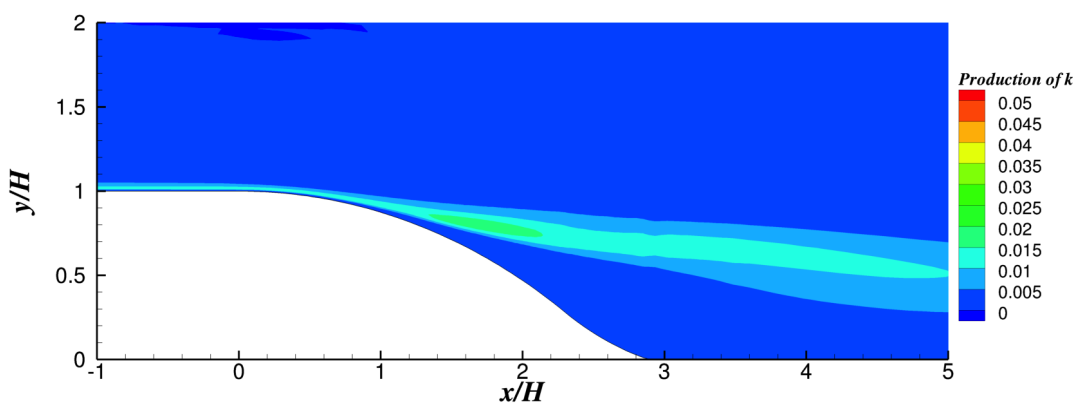
²The SA model does not have its own transport equation for the turbulent kinetic energy, hence it is not possible to extract the TKE budget from this model.



(a) LES



(b) SST-RANS



(c) RSM-RANS

Fig. 4.24 Production of turbulent kinetic energy contours.

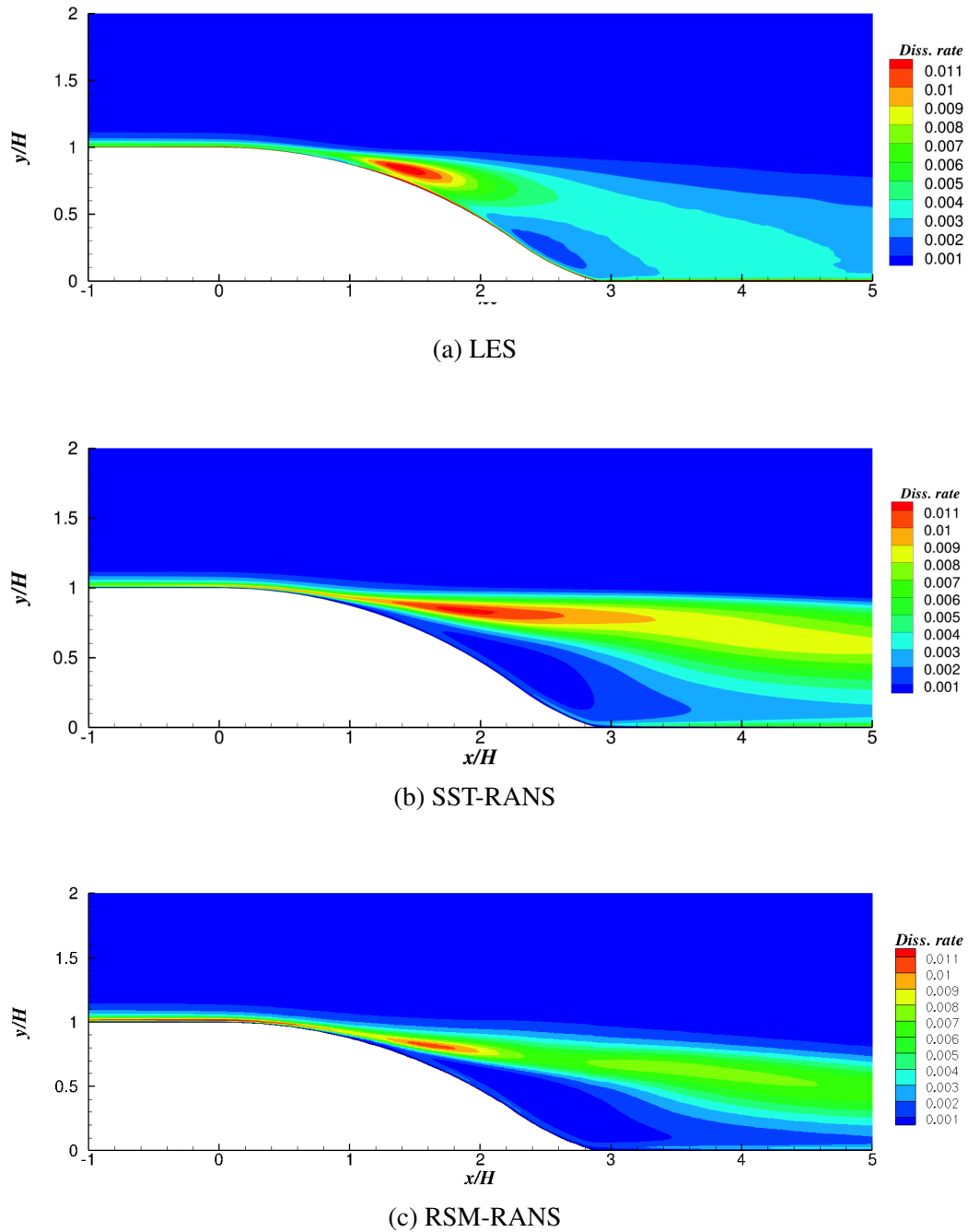


Fig. 4.25 Dissipation rate of turbulent kinetic energy contours.

peak is 30% lower and the area enclosed by the RANS curves is significantly smaller than the one under the LES curve. This results in a wrong computation of the turbulent kinetic energy profiles along the ramp, as shown in Figure 4.27.

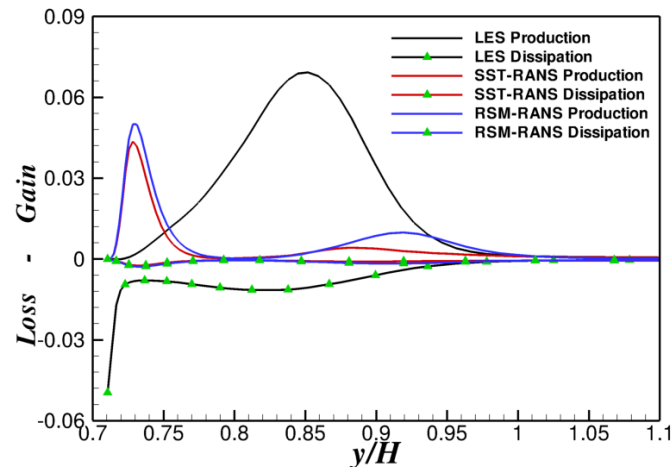


Fig. 4.26 Production and dissipation of TKE for $x/H = 1.5$.

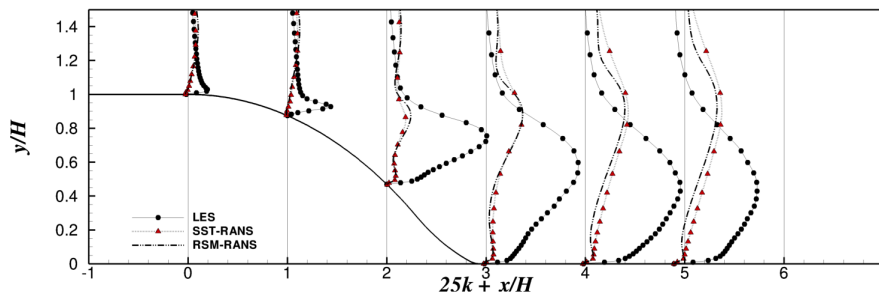


Fig. 4.27 TKE profiles along the ramp.

Turbulent kinetic energy encourages flow mixing in the shear layer. LES results show that the production of TKE promotes this mixing significantly. Consequently, high momentum drawn from the undisturbed free-stream flow re-energises the separated shear layer, promoting reattachment and rapid recovery along the lower wall downstream of the ramp. Since the levels of TKE observed in RANS is much lower compared to the LES, mixing is significantly less dynamic, resulting in a more extended separation region, hence the failure of reattaching the flow.

At this point, a hybrid RANS/LES is needed in order to investigate whether the RANS prediction can be enhanced through the use of an eddy-resolving simulation.

4.6 Hybrid RANS/LES with crossflow

The previous section has highlighted the fact that RANS methods fail to predict the separated flow along the ramp correctly. This is due to the lack of production of turbulent kinetic energy. Despite the fact that the Menter-SST model over-predicts the length of the recirculation area, its accuracy in predicting the onset of flow separation is still better than the one from the SA and RSM models. Therefore, the next step of the investigation consists of using a hybrid RANS/LES method with the Menter-SST turbulence model in order to look for an enhancement in the prediction of the reattachment and recovery point of the flow. To achieve this, the near-wall region is calculated in RANS mode, up to a dimensionless wall distance $\Delta y^+ \approx 100$ ($\Delta y \approx 0.2$). The rest of the flow domain is computed in LES mode. Time-averaging is performed on ten through-flows.

Figure 4.28 shows the time-averaged flow along the duct. As expected, the boundary layer separates along the ramp. Figure 4.29 shows a zoom into the recirculation region. The location of onset of flow separation has not changed with regards to the SST-RANS simulation. By contrast, flow reattachment occurs much earlier along the lower wall.

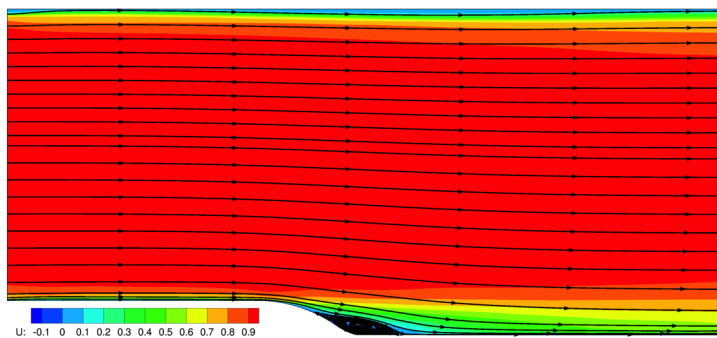


Fig. 4.28 Hybrid RANS/LES: flow along the duct.

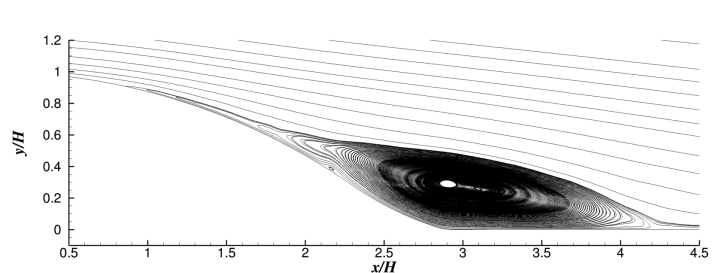


Fig. 4.29 Hybrid RANS/LES: flow recirculation region.

Table 4.3 gathers the separation and reattachment locations computed with the different approaches used in this chapter. This demonstrates that the hybrid simulation greatly enhances the prediction of flow reattachment, with only 0.7% error compared to the highly-resolved LES. The length of the separated region differs by only 0.8%. Figure 4.30 shows that also the prediction of the pressure coefficient is in a much more favourable agreement with the LES compared to the RANS.

Table 4.3 Comparison of separation and reattachment locations.

	SA-RANS	SST-RANS	RSM-RANS	Hybrid RANS/LES	LES
x/H separation	1.10	0.82	0.93	0.82	0.83
x/H reattachment	5.17	6.19	6.06	4.22	4.25
L_{sep}	4.07	5.37	5.13	3.39	3.42

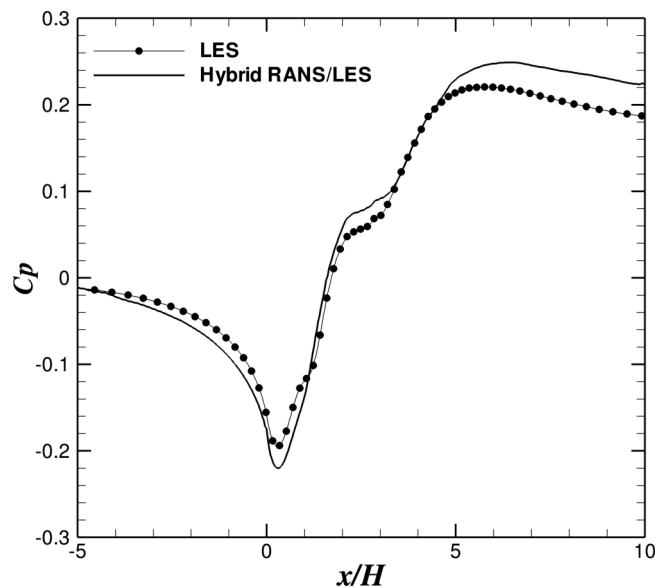


Fig. 4.30 Pressure coefficient over the lower wall of the duct computed by LES and hybrid RANS/LES.

Figure 4.31 shows the velocity profiles over the ramp. The RANS profiles are omitted for clarity reasons. Comparing this plot with the one in Figure 4.22, it is notable that the prediction of the velocity distribution has improved greatly. In fact, the hybrid RANS/LES trends follow the baseline LES along the whole length of the ramp. The relative error with respect to the LES is not larger than 5%, hence overall the results are in good agreement.

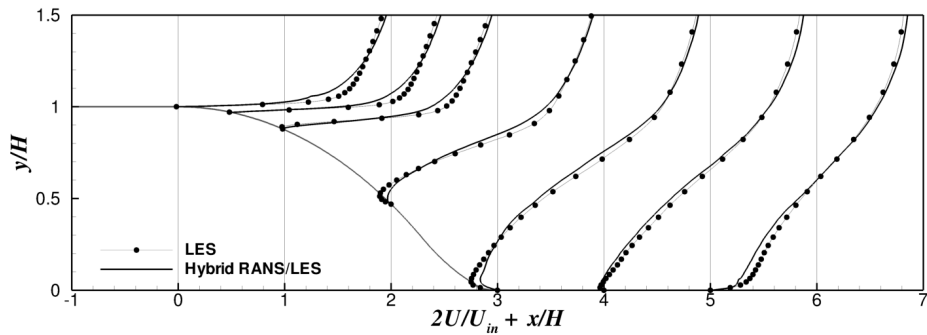
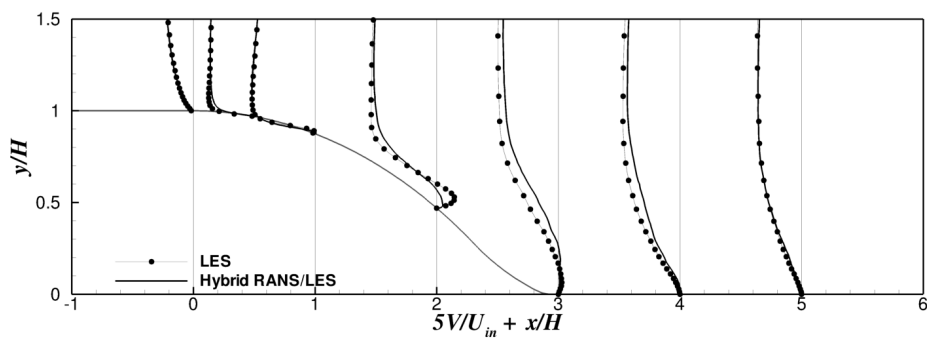
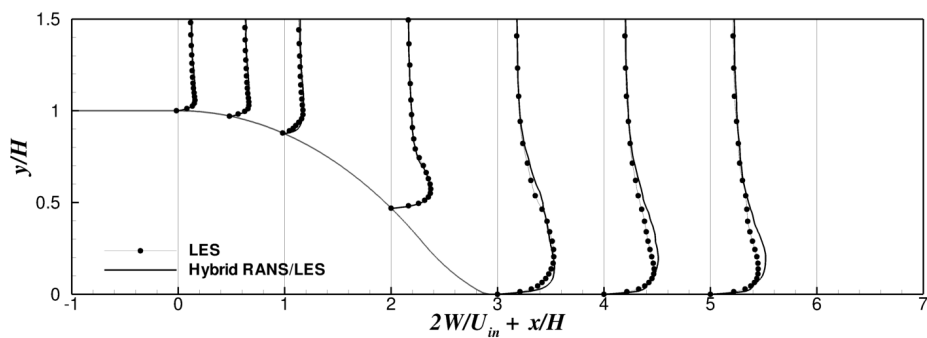
(a) \bar{U} profiles.(b) \bar{V} profiles.(c) \bar{W} profiles.

Fig. 4.31 Hybrid RANS/LES: mean velocity profiles at various locations: $x/H = 0$; $x/H = 0.5$; $x/H = 1$; $x/H = 2$; $x/H = 3$; $x/H = 4$, and $x/H = 5$.

The enhancement in the prediction of the flow along the ramp is achieved thanks to the LES of the separated flow along the ramp. The eddy-resolving simulation encourages production of turbulent kinetic energy, increasing flow mixing and promoting reattachment. This is confirmed by Figure 4.32, which shows that the level of production of TKE is comparable to the highly-resolved LES (Figure 4.24a). Therefore, the eddy-resolving

simulation is certainly beneficial to predict the correct flow features of a separating 3D boundary layer.

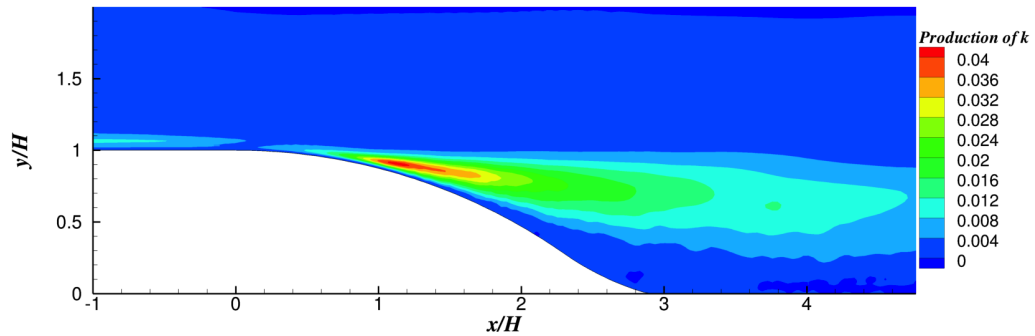


Fig. 4.32 Hybrid RANS/LES: production of turbulent kinetic energy contours.

4.7 Conclusions

This chapter focuses upon CFD methodologies to predict a three-dimensional boundary layer detaching from a backward rounded ramp with crossflow. Using a highly-resolved LES as the reference flow, the separation region is stretched by almost 10%, compared to the simulation without crossflow. The LES near-wall region at the onset of flow separation features a considerable turbulent anisotropy, as shown by the anisotropy maps and the Lumley triangles. This behaviour is not captured by the RSM simulation, since the Reynolds stresses distribute almost evenly among the three normal components, showing low levels of anisotropy. This is caused by the pressure-strain term in the transport equations of the Reynolds stresses. In the recirculation region, turbulent kinetic energy redistributes among the Reynolds stresses and turbulence assumes a more isotropic character.

The comparison between LES and RANS shows the limitations of RANS in predicting the detached flow accurately. The SST model is the best in capturing the location of onset of flow separation, though does not perform well in reattaching the flow downstream of the ramp. All RANS simulations completely miss the reattachment point defined by the LES, probably due to the fact that the models do not produce enough turbulence, as observed in the analysis of the production of, and profiles of, turbulent kinetic energy.

In order to enhance the capability of the SST simulation to predict flow reattachment, a hybrid RANS/LES simulation has been carried out. This shows a substantial improvement of the prediction of the length of the separation region, the reattachment location, and the velocity profiles including downstream recovery of the boundary layer. In fact, resolving

the detached shear layer in LES mode certainly encourages flow-mixing and reattachment downstream of the ramp. This implies also a better prediction of the pressure field along the ramp. Therefore, this study shows how important it is to resolve turbulence in the separated region of a flow.

These considerations are also valid for industrial applications, such as the flow around a VTP. In particular, the correct predictions of the separated region and of the location of reattachment, if present, is a key element in the computation of downstream pressure recovery and thus final aerodynamic loads. The flow around a VTP at high sideslip angle and/or deflected rudder is characterized by the presence of a three-dimensional boundary layer subject to separation. This chapter suggests that it is necessary to resolve turbulence to some extent in order to capture the real flow features.

Chapter 5

Steady and unsteady RANS simulations

5.1 Introduction

The first step of the investigation of the flow around a VTP consists of understanding for which conditions the RANS solution of a VTP is valid. As discussed earlier in the thesis, currently steady RANS simulations are the main tool used for the aerodynamic design of an aircraft, together with wind tunnel experiments and flight tests. However, in CFD there are still many open questions concerning the uncertainties of steady RANS performance for unsteady and highly turbulent flows. In particular, the literature review has shown that steady and unsteady RANS approaches are not capable to compute the separated flow over an aircraft geometry with accuracy. Furthermore, Chapter 4 has highlighted the reason why Reynolds-averaged methods fail.

The first objective of this chapter is to assess to what extent steady RANS simulations are valid for the flow around a VTP. To achieve this, three different turbulence models are used: the 1-equation SA turbulence model; the 2-equation $k - \omega$ SST turbulence model, and the Reynolds stress transport SSG/LRR- ω model. The simulations are carried out for different angles of incidence of the flow reaching the vertical stabilizer (sideslip angles), so that it is possible to determine for which sideslip angle the flow separates.

After the assessment of steady RANS performance, time accuracy is introduced through the use of URANS methods, with the aim of understanding whether URANS can predict an accurate flow solution for the cases in which RANS simulations fail. The same three turbulence models listed above are used also in URANS. This leads to the third objective of this chapter, that is to identify the best turbulence model for the computation of the separated flow over the VTP, helping to build the best possible methodology for the eddy-resolving simulations that are presented. The results illustrated in this chapter are computed using the TAU code.

5.2 The VTP model

The test case used in this work consists of a wind tunnel model tested at Airbus in 2011 [7]. The model is composed of fuselage and tail planes (horizontal tail and vertical tail), equipped with their control surfaces. When testing the behaviour of the tail surfaces, at Airbus it is usual not to use a complete geometry, but to adopt a wing-off model, which allows a larger model thus a higher Reynolds number for the experiment. VTP geometric characteristics are reported in Table 5.1¹.

Table 5.1 VTP geometry.

Leading edge sweep angle	44°
Quarter-chord line sweep	40°
t/c at root	0.1
t/c at tip	0.11
x/c of $(t/c)_{max}$	36%
x/c of hinge line	67%

The model was covered by pressure taps for pressure observations and was connected to a balance for the measurement of the forces and the moments that act on it. To simulate the incidence and the sideslip angles of the flow, the model can rotate around its support (as shown in Figure 5.1). The model has been tested for different sideslip angles β up to 20° and a set of different deflections of the rudder. When studying the local behaviour of the flow on the VTP, four sectional cuts of the geometry are considered. The sections are shown and named in Figure 5.2. They correspond to the locations of the pressure taps in the wind tunnel model. In this way, it will be possible to compare CFD results with wind tunnel data. Notably, calling η the non-dimensional coordinate along the span of the VTP, such that $\eta = 0$ is the location of the intersection between the VTP and the fuselage, and $\eta = 1$ represents the tip of the VTP, the four sections plotted in Figure 5.2 have the non-dimensional coordinates presented in Table 5.2.

Table 5.2 Sections of cut of the VTP.

Section	η
D-D	0.1
C-C	0.4
A-A	0.7
F-F	0.9

¹Sensitive data and the scale of the model cannot be given for confidentiality reasons.



Fig. 5.1 Assembly of the model in the wind tunnel. Photo courtesy of Airbus.

Experimental data collected in the wind tunnel need to be corrected before comparison with CFD data. In fact, the domain in which the physical wind tunnel model is tested is completely different from the computational domain used in this thesis, which aims to simulate operation in free air. Corrections have to take into account the wind tunnel working section, the presence of the walls of the wind tunnel, and the presence of the support of the model. Further information about wind tunnel corrections is reported in Appendix E. Moreover, in the geometry with deflected rudder, the gap between the fin and the rudder along the hinge was sealed with tape by the wind tunnel engineers, and this has to be taken into account in the virtual geometry.

CAD model and geometry repairing

The geometry of the model is designed in Catia v5[®], a CAD (Computer-Aided Design) software widely used in the industry. In order to realize a good quality mesh, it is necessary that the aircraft model is ‘watertight’, which means that no gaps would exist in the geometry surfaces. The CAD model is composed of NURBS (Non-uniform rational B-spline) surfaces,

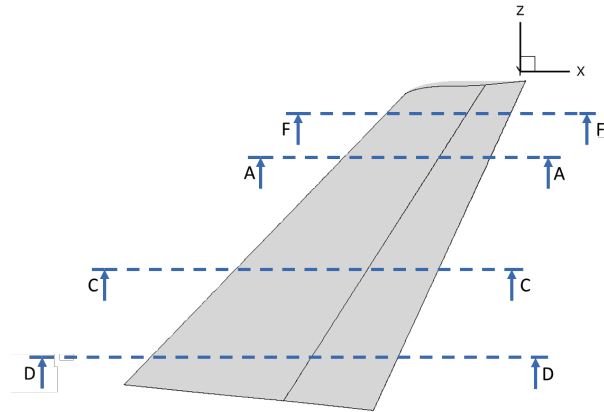
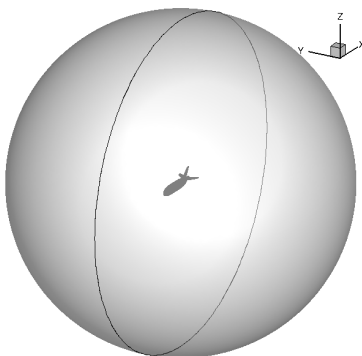


Fig. 5.2 Sections of cuts of the VTP.

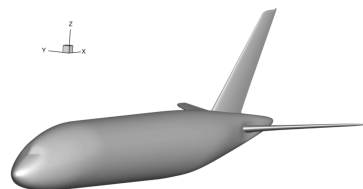
which are the surfaces that together constitute the shape of the aircraft model. Thus, before meshing it was necessary to make sure that each surface was closed.

The computational domain

The computational domain consists of a sphere with the aircraft model at the centre of it. The sphere has to be far enough from the model in order to prevent the flow from being disturbed at its boundaries. A sphere with a diameter equal to 50 times the Mean Aerodynamic Chord (MAC) of the VTP is chosen to define the farfield for this study (Figure 5.3a). The far-field is far enough to avoid reflections of the flow at the boundaries, so that the flow solution cannot be compromised by this, and can be considered an adequate representation of free-air conditions.



(a) Model and farfield.



(b) The aircraft surfaces (CAD model).

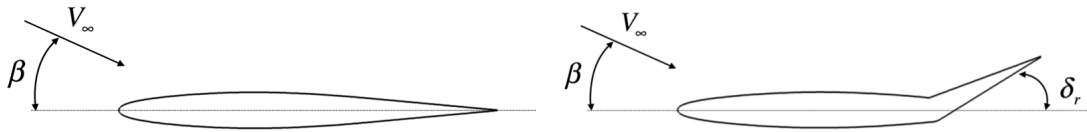
Fig. 5.3 The computational domain.

Boundary conditions

The boundary conditions are:

- farfield boundary conditions for the free stream flow:
 - $M_\infty = 0.2$,
 - Reynolds number based on the MAC of the VTP and on the free-stream velocity: $Re = 2.42 \times 10^6$, and
 - static pressure: $p_\infty = 1$ atm;
- viscous adiabatic wall for the surface of the wind tunnel model (Figure 5.3b).

Two different configuration of the wind tunnel model are taken into account throughout the thesis. The first configuration consists of the tail plane without rudder deflection (Figure 5.4a); in the second one, the rudder is deflected $\delta_r = 30^\circ$ (Figure 5.4b).



(a) Test case $\delta_r = 0^\circ$: no rudder deflection. (b) Test case $\delta_r = 30^\circ$ rudder deflection.

Fig. 5.4 2D sections of the VTP with a plane $z = const$.

The origin of the reference system is located at the notional centre of gravity of the wind tunnel model. Figure 5.5 shows a sketch of the axes and of the aerodynamic loads that are considered in this study. When the flow reaches the fin with a sideslip angle β , a side-force is generated over the tail plane. This is calculated as shown in Section 3.8.4. In this study, only the F_y component of the side-force along the y -axis is considered. Moreover, the tail generates a moment M_z about the z -axis. The force and moment coefficients are defined as follows:

- side-force coefficient:

$$Cf_y = \frac{F_y}{\frac{1}{2}\rho V_\infty^2 S_{ref}} \quad (5.1)$$

- yaw moment coefficient:

$$Cm_z = \frac{M_z}{\frac{1}{2}\rho V_\infty^2 S_{ref} \cdot MAC} \quad (5.2)$$

where ρ and V_∞ are the free stream flow density and velocity respectively, S_{ref} is the surface area of the VTP planform.

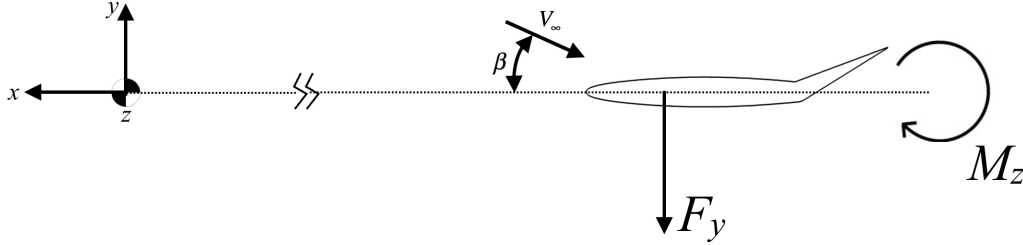


Fig. 5.5 Aerodynamic loads generated by the VTP.

Flow initialization

The flow is initialized through the following expressions:

$$\begin{aligned}
 \rho_{init} &= \rho_\infty \\
 p_{init} &= p_\infty \\
 u_{init} &= \cos(\alpha) \cdot \cos(\beta) \cdot V_\infty \\
 V_\infty &= M_\infty \cdot \sqrt{\gamma \frac{p_\infty}{\rho_\infty}} \\
 v_{init} &= \sin(\beta) \cdot M_\infty \cdot \sqrt{\gamma \frac{p_\infty}{\rho_\infty}} \\
 w_{init} &= \sin(\alpha) \cdot \cos(\beta) \cdot M_\infty \cdot \sqrt{\gamma \frac{p_\infty}{\rho_\infty}} \\
 \mu_{init} &= \frac{\rho_\infty V_\infty x_{MAC}}{Re_{MAC}} \\
 \mu_{t,init} &= \mu_{l,init} \cdot \mu_{t,ratio}
 \end{aligned} \tag{5.3}$$

where α is the incidence of the flow (which is zero), β is the sideslip angle, μ_{init} is the molecular viscosity of the flow, $\mu_{t,init}$ is the turbulent viscosity, and $\mu_{t,ratio}$ an input parameter defining the minimum turbulent viscosity.

Mesh for RANS simulations

The computational domain is meshed by a hybrid mesh, which has extensive structured regions in the near wall region and becomes unstructured in the farfield. In this thesis, the grid is generated using Solar, a mesher developed by the Aircraft Research Association, BAE Systems and Airbus. Details about the grid generator can be found in Reference [61]. Solar works in two steps:

1. generation of the surface mesh, and

2. generation of the volume mesh.

Details about the RANS mesh are reported in table 5.3.

Table 5.3 RANS mesh details.

No. of points	11,640,201
No. of tetrahedra	14,891,546
No. of prisms	44,544
No. of pyramids	282,625
No. of hexahedra	8,916,400
No. of surface triangles	5,480
No. of surface quadrilaterals	280,063

Figure 5.6 shows that the surface of the model is mainly discretized into quadrilateral patches, having as much structured character as possible, but triangular elements may also be found. The surface mesh is extruded into the volume, generating structured regions of hexahedra and also some columns of prisms. This semi-structured layer is made deep enough to contain the whole of an attached boundary layer at the flow conditions envisaged. At the wall the first cell height is targeted at $\Delta y^+ = 0.5$ as required for the proposed turbulence models.. The inner layer is composed of prismatic or hexahedral elements. In the outside layer, the grid becomes unstructured up to the farfield and is composed of tetrahedral elements. Between the structured and unstructured regions, there is the ‘buffer layer mesh’, which consists of pyramids. This layer assures a smooth transition between the structured and unstructured domains.

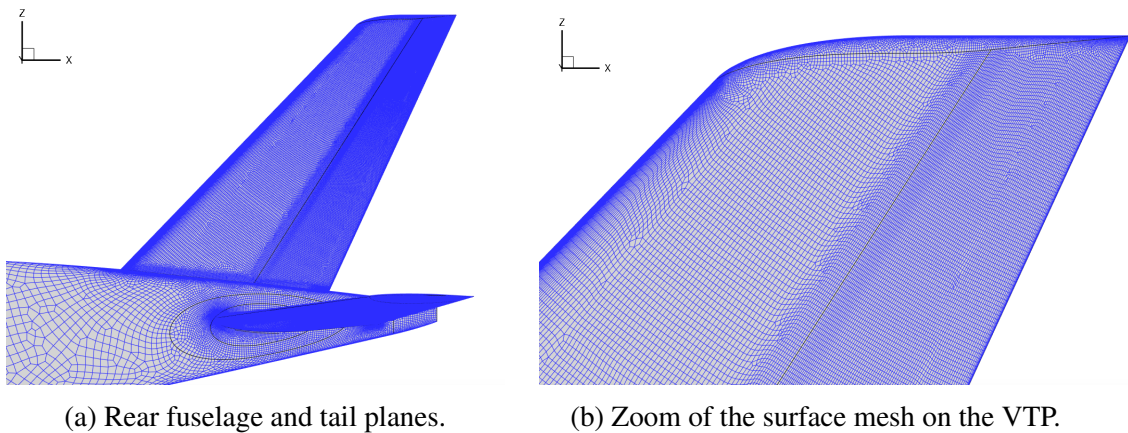


Fig. 5.6 Surface mesh of the wind tunnel model.

5.3 Steady RANS simulations

5.3.1 Steady results for VTP without rudder deflection

RANS simulations have been performed for zero rudder deflection, $\delta_r = 0^\circ$, and a set of different sideslip angles, for $\beta \simeq 0^\circ, \dots, 20^\circ$, with a step of $\Delta\beta \simeq 1^\circ$. These values match the sideslip angles measured in the wind tunnel. To study the convergence of the solution, the density residuals (Equation 3.46) and the side-force are considered.

Convergence of the density residuals and of the side-force coefficient are shown in Figure 5.7, where each portion of the graph represents a different sideslip angle. Throughout the thesis, residuals are always plotted using a logarithmic scale. The figure shows that residuals drop down 8-9 orders in the range of sideslip angles between 0.17° and 13° , whereas from $\beta = 14^\circ$ residuals drop by only three orders of magnitude. The convergence of the side force to a steady state is also reached up to $\beta = 13^\circ$. For higher values of β , the solver does not converge to a steady value of the side force, showing oscillations.

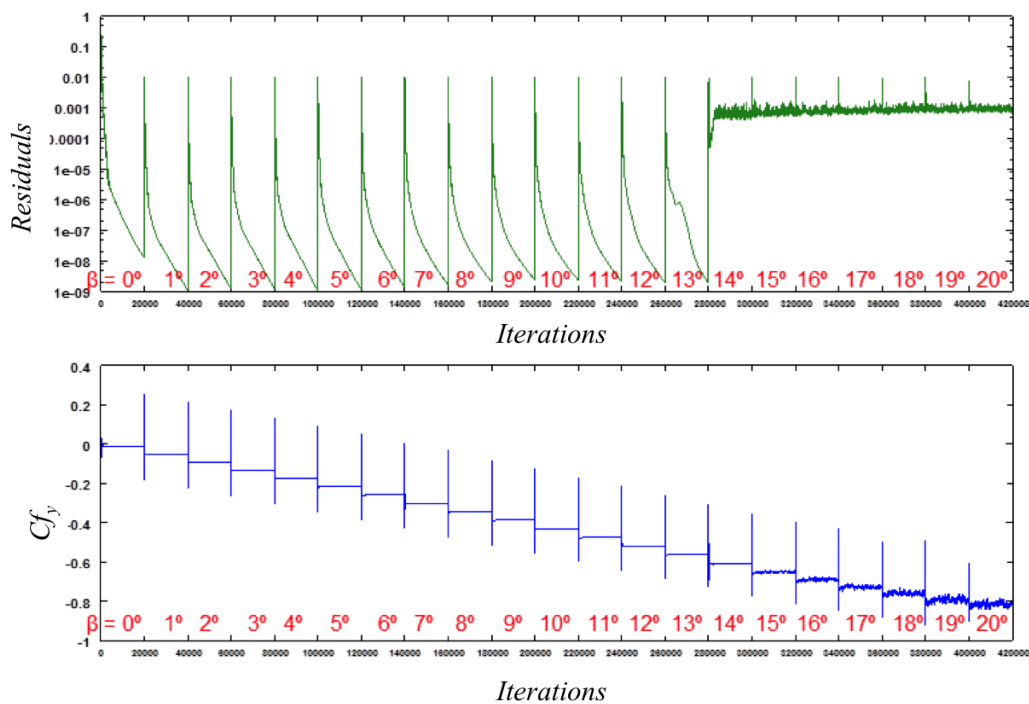


Fig. 5.7 RANS - Convergence of density residuals and sideforce: $\delta_r = 0^\circ$, $\beta = 0^\circ, \dots, 20^\circ$.

Figure 5.8 shows the skin-friction lines on both sides of the VTP coloured by contours of the pressure coefficient C_p . At low values of the sideslip angle, the flow is attached, as shown by the skin-friction lines. This is true up to $\beta = 13^\circ$. For $\beta = 14^\circ$, the skin friction lines diverge from a line near the tip and leading edge, indicating a reattachment here and implying

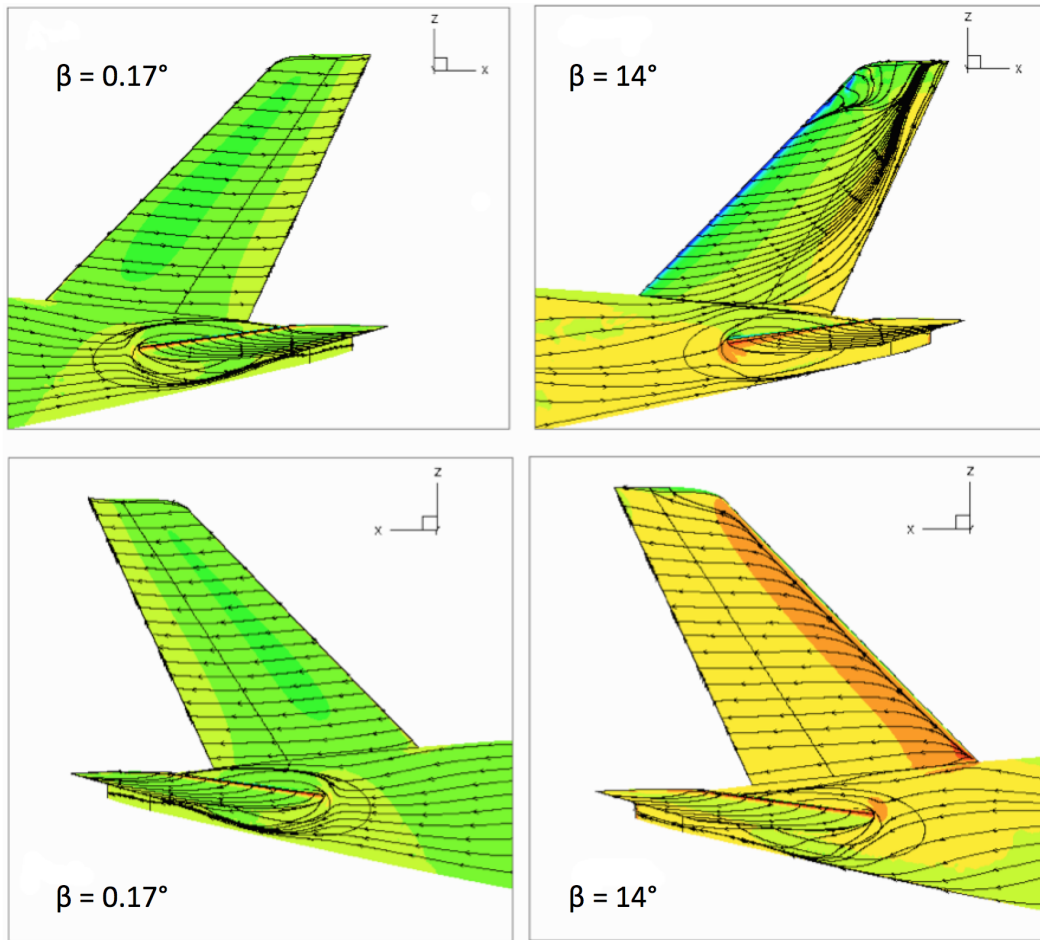


Fig. 5.8 RANS - Flow visualizations for $\delta_r = 0^\circ$. Top: suction side. Bottom: pressure side. Streamlines on C_p contours (RSM turbulence model).

a preceding separation at the leading edge. However, this flow representation cannot be assumed to be accurate. Firstly because the computation did not converge well in the residual, despite the unsteadiness in the side-force being only at a low level. Secondly there must always be uncertainty in the accuracy of even a well converged steady RANS result for a separated flow where unsteadiness may be a feature. Lacking time accuracy, such a solution may not even show properly the steady averaged property of a real unsteady flow.

Figure 5.9 shows the pressure distribution computed by RANS for $\beta = 0.17^\circ$ for four sections along the span of the VTP. The results compare favourably with wind tunnel data for these benign conditions.

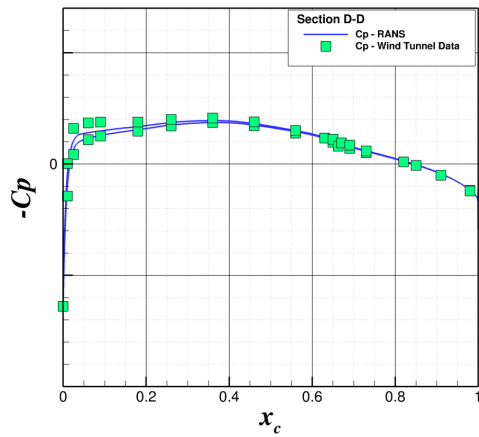
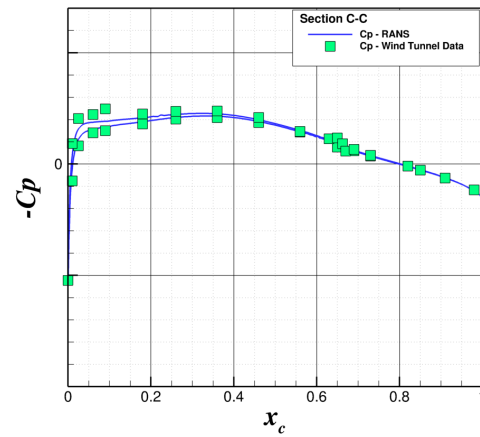
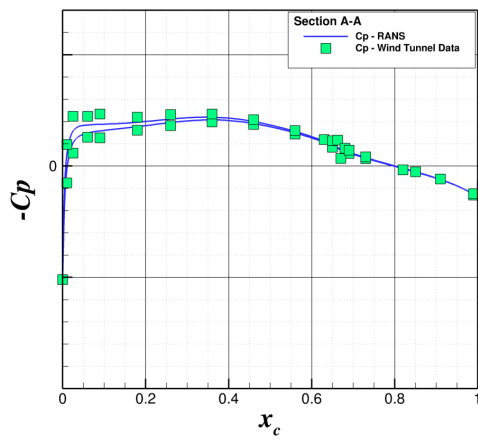
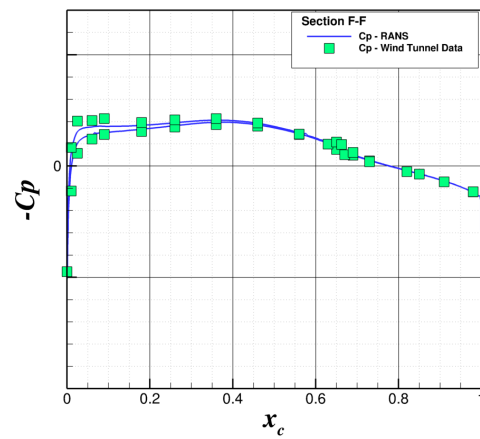
(a) Section D-D ($\eta = 0.1$)(b) Section C-C ($\eta = 0.4$)(c) Section A-A ($\eta = 0.7$)(d) Section F-F ($\eta = 0.9$)

Fig. 5.9 RANS - Pressure coefficient for four sections of cut obtained for $\delta_r = 0^\circ$ and $\beta = 0.17^\circ$ (RSM turbulence model).

5.3.2 Steady results for the VTP with rudder deflection

The results are shown for a rudder deflection equal to $\delta_r = 30^\circ$ and for a set of sideslip angles from $\beta \approx 0^\circ$ to $\beta \approx 20^\circ$. Figure 5.10 shows the convergence of the density residuals and the side force coefficient, reporting a worse convergence than that obtained for $\delta_r = 0^\circ$. In fact, the residuals drop down five-six orders of magnitude up to $\beta = 9^\circ$, whereas from $\beta = 10^\circ$, the density residuals drop down only three orders of magnitude. The side force does not show convergence to a steady value from $\beta = 10^\circ$ onward.

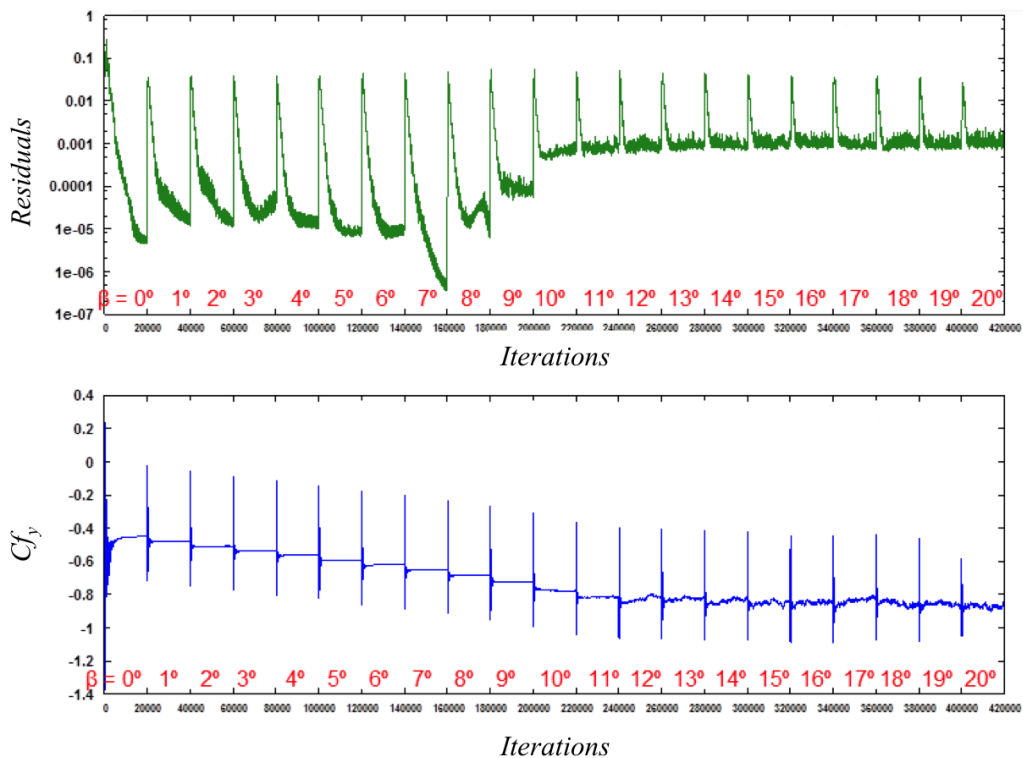


Fig. 5.10 RANS - Convergence of density residuals and sideforce: $\delta_r = 30^\circ$, $\beta \approx 0^\circ, \dots, 20^\circ$.

The flow on the VTP with deflected rudder is shown in Figure 5.11. Looking at the fin, for $\delta_r = 30^\circ$ the skin-friction lines show a reattachment on the suction side near the tip for $\beta = 10^\circ$. This is similar to the separation seen without deflected rudder, which appeared at a significantly higher $\beta = 14^\circ$. Moreover, the flow separates at the VTP hinge line for all β angles.

The flow topology along the deflected rudder presents clear separation lines that are skewed towards the tip. Such behaviour of the flow is consistent with what is observed in other experimental results, as pointed out in the Literature Review.

For $\beta = 0.17^\circ$, Figure 5.12 shows that the pressure distributions computed for different span sections compare favourably with the experiment. However, the negative peak in the

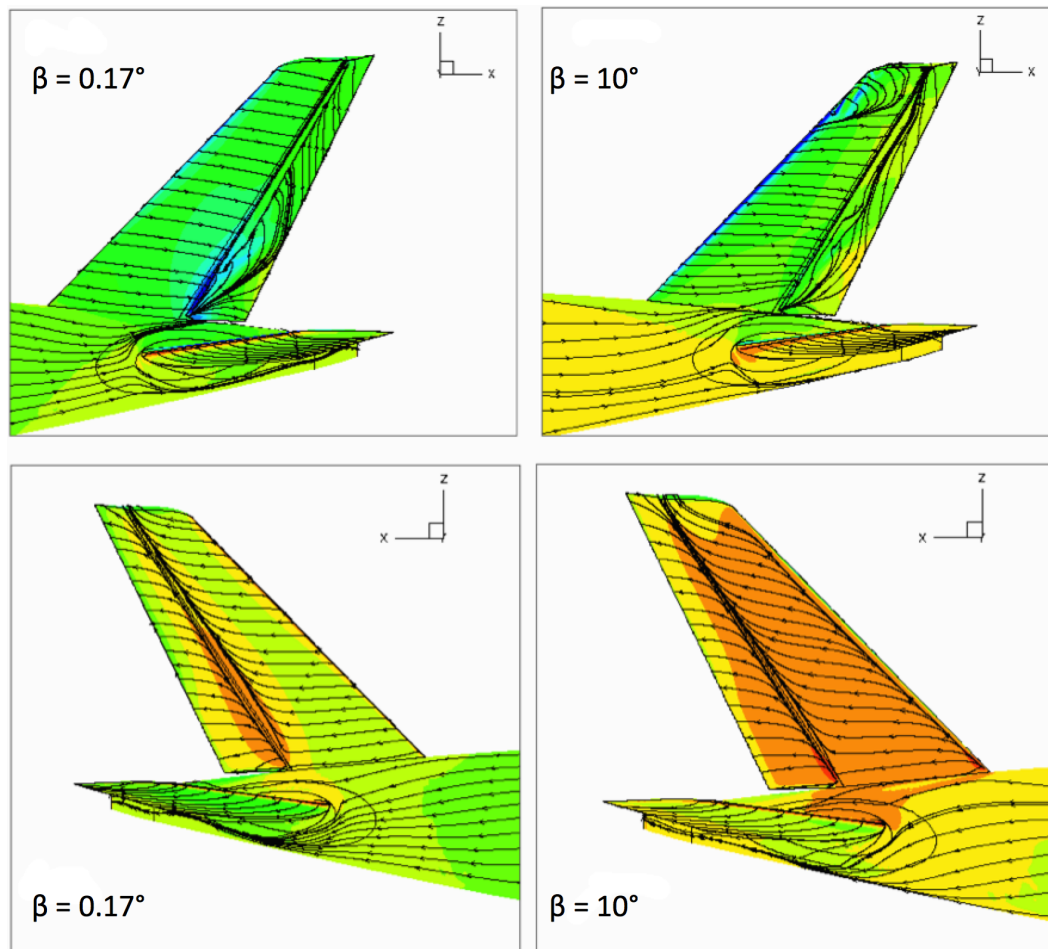


Fig. 5.11 RANS - Flow visualizations for $\delta_r = 30^\circ$. Top: suction side. Bottom: pressure side. Streamlines on C_p contours (RSM turbulence model).

C_p distribution near the hinge line is not well-predicted, since its location is aft of the tunnel results by about 5% of local chord. It is interesting to note that, even though flow separation occurs on the deflected rudder, the simulation still gives good results, which converge adequately. Due to the rudder deflection, a large side-force is generated by the VTP. Table 5.4 compares the integrated CFD aerodynamic loads to the experimental data. The computed results are quite close to experimental measurements, with a relative error ranging between 8% and 12% for the force coefficient C_{f_y} , and between 5% to 10% for the moment coefficient C_{m_z} . The SA and SST results are very close to each other, and these turbulence models seem to perform better than the RSM model.

The preliminary investigation obtained with steady RANS shows a flow that, for high sideslip angles separates massively on the fin and is unconverged, making it impossible to have confidence in these as steady results. At this point, this study has to investigate alterna-

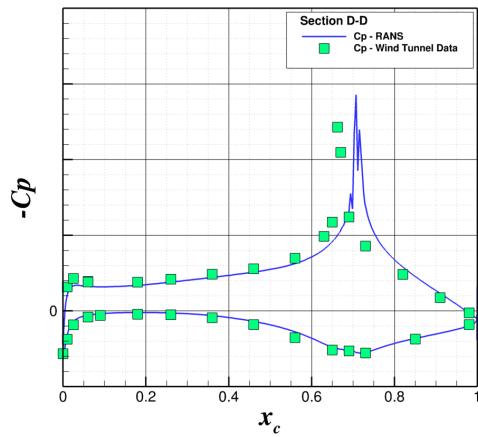
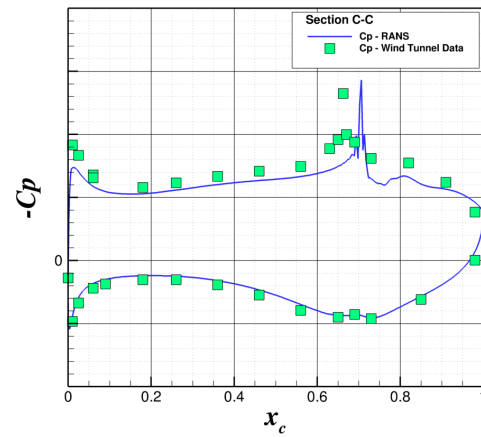
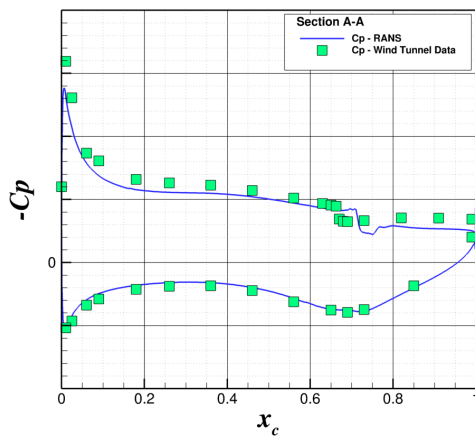
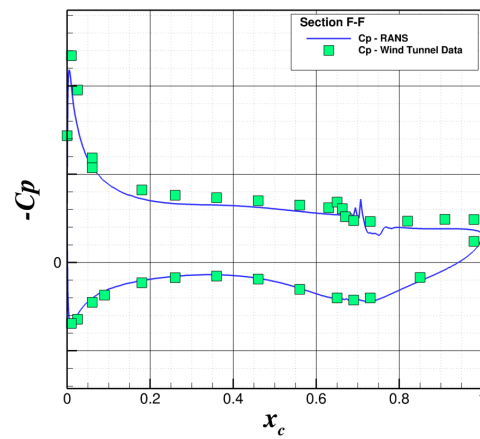
(a) Section D-D ($\eta = 0.1$)(b) Section C-C ($\eta = 0.4$)(c) Section A-A ($\eta = 0.7$)(d) Section F-F ($\eta = 0.9$)

Fig. 5.12 RANS - Pressure coefficient for four sections of cut obtained for $\delta_r = 30^\circ$ and $\beta = 0.17^\circ$ (RSM turbulence model).

Table 5.4 Loading on the VTP at $\beta = 0.17^\circ$ and $\delta_r = 30^\circ$

	SA-RANS	SST-RANS	RSM-RANS	Experiment
$ Cf_y $	0.47	0.46	0.45	0.51
$ Cm_z $	1.38	1.36	1.31	1.45

tive CFD approaches that would give a good solution and an answer to CFD uncertainties concerning the flow around a VTP.

The unsteady behaviour of the flow leads to a shift towards approaches that take into account the need for time accuracy. In a first step, unsteady RANS (URANS) techniques are used and results reported in the next sections.

5.4 Unsteady RANS simulations

As explained in Chapter 3, the main difference between steady and unsteady RANS simulations consists of the introduction of a physical time step in order to achieve time accuracy. The physical time Δt was chosen on the basis of the convective time t_c , which is the time taken by the free-stream flow at velocity V_∞ to travel a distance of one MAC. It is expressed as $t_c = MAC/V_\infty$. To define the time step Δt , an investigation of different fractions of t_c has been considered, resulting in setting the time step to the order of one-hundredth of the convective time step t_c : $\Delta t = t_c/100 \approx 5 \cdot 10^{-5}$ s. The convergence criterion of the inner iteration of the solver's dual time-stepping scheme has been set at a drop in the density residuals of two orders of magnitude. It is important to make sure that the convergence of the inner iterations of the side-force and yaw moment coefficients is reached. This has been checked for all the results reported in the thesis.

Unsteady simulations are run for two cases that do not converge when steady RANS is used, that is $\beta = 14^\circ$ for the non-deflected rudder, and $\beta = 10^\circ$ for the deflected rudder. Whilst the unsteady simulations are presented for these two particular case studies, the outcomes of the investigation should be relevant to any generic tail configuration with flow at high incidence.

The time-average of the unsteady flow solution is calculated following Equation 3.47. Averaging starts after any initial transients in the solution have largely disappeared. For this reason, monitoring of the solution is necessary. For URANS simulations, the solution is time-averaged for about 30 convective times.

5.4.1 Unsteady results for VTP without rudder deflection

The unsteady simulation carried out for $\delta_r = 0^\circ$ and $\beta = 14^\circ$ shows that the flow topology is completely different from that seen in the steady RANS simulations. Time-averaged flow visualizations are plotted in Figure 5.13. Only the suction side is represented, since it is the one where the most interesting aerodynamic features occur. The figure shows that there is a separation line that runs along the leading edge of the fin. The flow at high incidence reaches the fin on the pressure side, flows around the leading edge, and then separates from the fin. Comparing Figure 5.13 with the top-right plot in Figure 5.8, the reader can appreciate an important difference between the steady and the unsteady solution. In fact, the separation line is now predominant and runs along around three-quarters of the fin, whereas steady RANS cannot predict this.

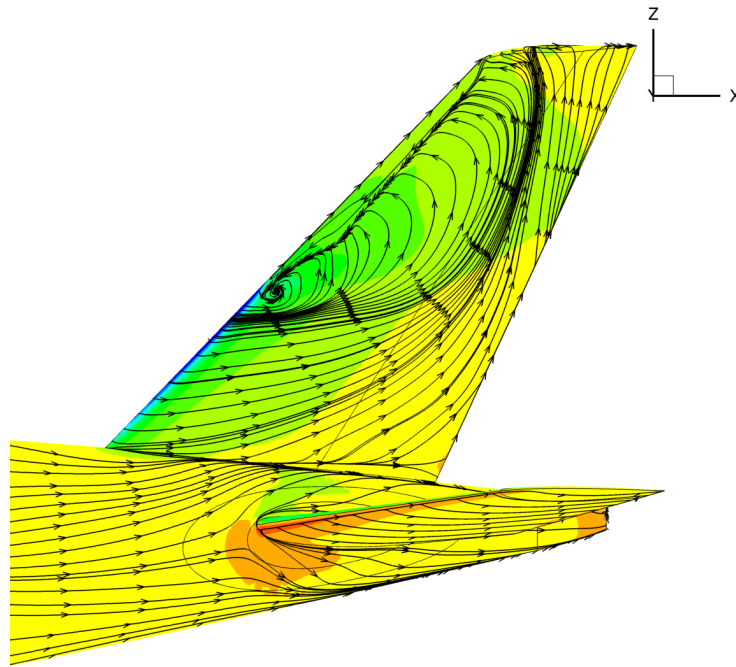


Fig. 5.13 URANS - Flow visualizations for $\delta_r = 0^\circ$ and $\beta = 14^\circ$ (averaged skin-friction lines, Menter SST turbulence model).

Figure 5.14a shows a good agreement between URANS results and the wind tunnel data at section D-D. All of the turbulence models line up with the wind tunnel observations. This is due to the fact that the flow is still attached at this location. At section C-C (Figure 5.14b), there is a disagreement between the results computed by the two eddy-viscosity models and the RSM one, the latter also being distant from experimental data. In fact, the RSM results show pressure distribution which is typical of a separated flow, i.e. the C_p curve tends to be flat. By contrast, experimental C_p data does not indicate separation occurring at this location.

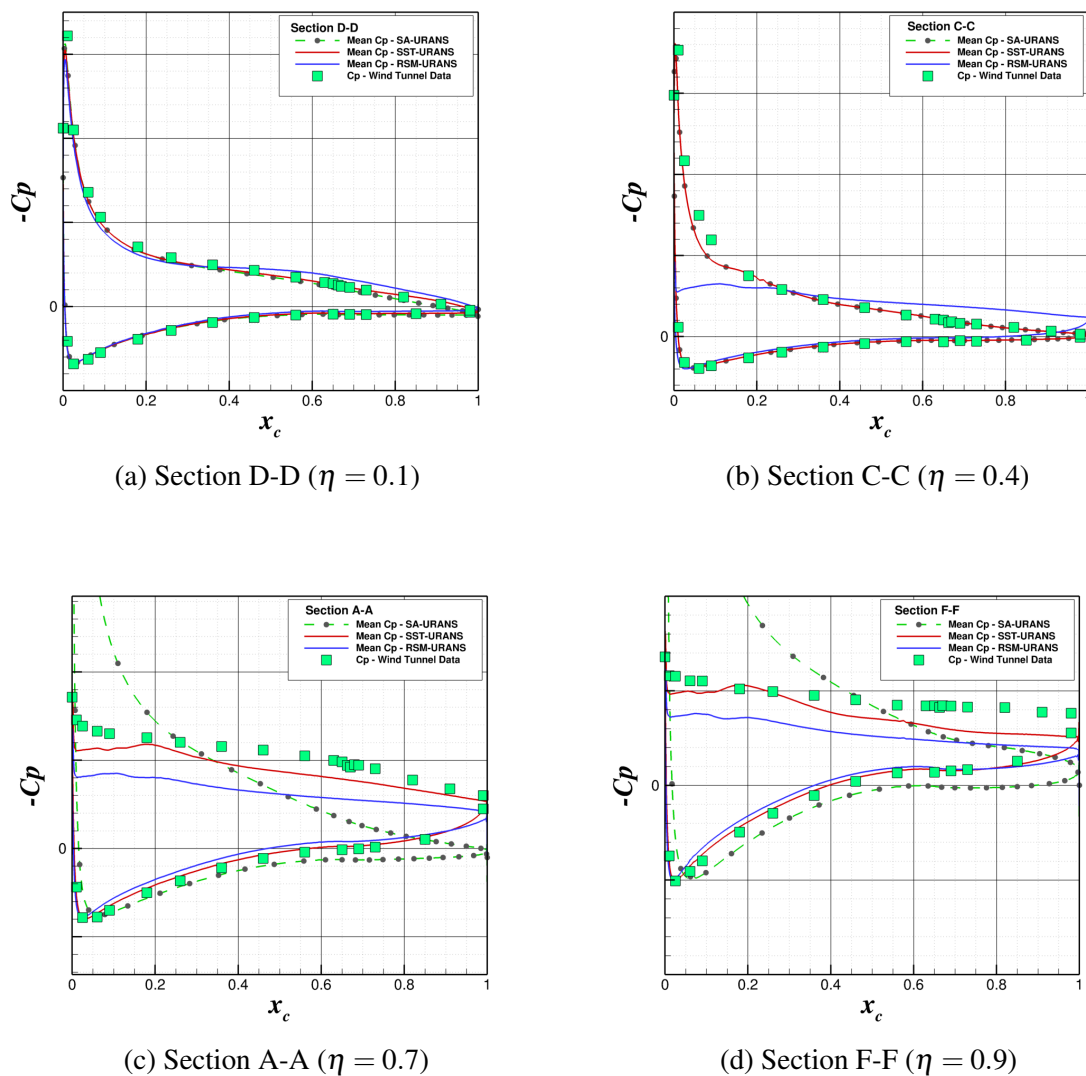


Fig. 5.14 URANS - Pressure coefficient for four sections of cut obtained for $\delta_r = 0^\circ$ and $\beta = 14^\circ$.

The pressure distributions computed for the locations closer to the VTP tip show some limitations of URANS methods in predicting highly separated flows. In fact, figures 5.14c and 5.14d show that none of the curves matches wind tunnel data on the suction side of the VTP. Menter SST results are more accurate than those obtained by the other two turbulence models, with an error of about 20% with respect to experimental data. For SA, the C_p is completely different from the experiment, having a form indicating an attached flow. The RSM shows a more sensible trend in the pressure distribution, similar to that seen for SST though somewhat further from the experimental points, but the error is around 40%.

Figure 5.15 shows a contour map of the Mach number field for section A-A, obtained by SST. The picture shows that the flow is almost undisturbed on the pressure side, accelerating along the surface of the VTP. By contrast, on the suction side, a separation region can be observed. This extends along one third of the chord of the VTP. The flow separates from the fin and slows down dramatically. Two vortical structures are observed in the detached region.

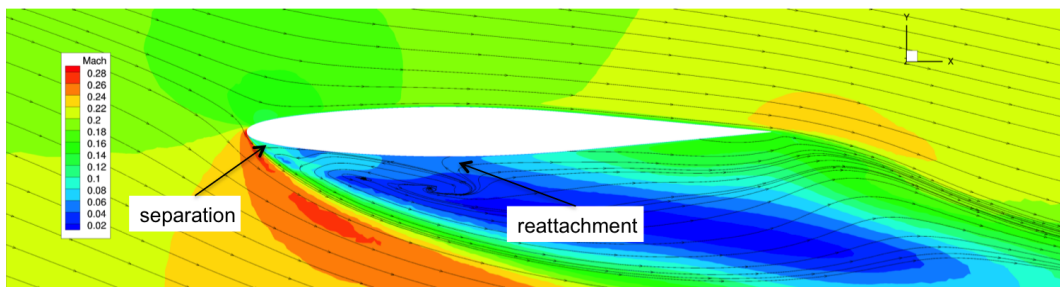


Fig. 5.15 URANS - Instantaneous Mach number contours with time-averaged streamlines, for $\delta_r = 0^\circ$ and $\beta = 14^\circ$. Section A-A (Menter SST).

The averaged side-force and yaw moment coefficients are reported in Table 5.5 for the three turbulence models used in this study. SA and SST simulations under-predict the integrated loads on the VTP by about 15%. This error is even higher for RSM, assessing around 50%. These result demonstrate the danger in relying only on integrated forces for assessing results quality in CFD. There is high potential for error cancellation in such a poor C_p distribution to result in reasonable integrated force values.

Table 5.5 Loading on the VTP for $\delta_r = 0^\circ$ at $\beta = 14^\circ$.

	SA-URANS	SST-URANS	RSM-URANS	Experiment
$ C_{f_y} $	0.59	0.55	0.51	0.66
$ C_{m_z} $	0.30	0.37	0.16	0.46

Spectral gap

One of the most complicated issues associated with URANS simulations consists of the so-called ‘turbulence double-counting’. When introducing time accuracy in the RANS equations, it is important to check the presence of a spectral gap, which indicates a net separation between turbulence modelling and turbulence resolving time scales. Tucker [110] explains that the key URANS requirement is $t_p \gg t_i$, where t_p is the unsteadiness period, and t_i is the turbulence timescale.

The period associated with the unsteady simulation t_p is of the order of one convective time step, $t_p \approx t_c$.

The turbulence timescale t_i is inversely proportional to the turbulent variable ω through the relation $t_i = (0.09\omega)^{-1}$ [70]. Table 5.6 shows that, for both the SST and the RSM models, $t_p \gg t_i$ by two-three orders of magnitude.

Table 5.6 Comparison between period and turbulent timescales in the SST and RSM URANS simulations.

t_p/t_c	$t_{i,SST}/t_c$	$t_{i,RSM}/t_c$
1	0.002 – 0.028	0.005 – 0.03

5.4.2 Unsteady results for VTP with rudder deflection

The unsteady simulation is carried out for $\beta = 10^\circ$ and $\delta_r = 30^\circ$. Figure 5.16 shows flow visualizations on the suction side of the VTP. The figure shows the presence of a separation line along the leading edge of the fin, and flow separation occurring over the hinge line of the rudder, which complicates the flow topology over the VTP.

The C_p distributions are plotted in Figure 5.17. The three turbulence models show C_p characteristics rather similar to what has been observed for the test case with no rudder deflection, and the SST generates the best results. The outer sections demonstrate that the flow is massively separated, both on the fin and the rudder. While the SST and RSM results show qualitatively reasonable capture of the experimental flow features, it can be seen that the introduction of time accuracy in the form of URANS is not enough to match experimental data exactly.

The Mach number contours are plotted in Figure 5.18, together with the time-averaged streamlines. On the suction side, the flow separates, but in this case the recirculation region on the fin is much smaller than for $\delta_r = 0^\circ$ and $\beta = 14^\circ$. By contrast, the flow is detached over the rudder, which features two counter-rotating vortices.

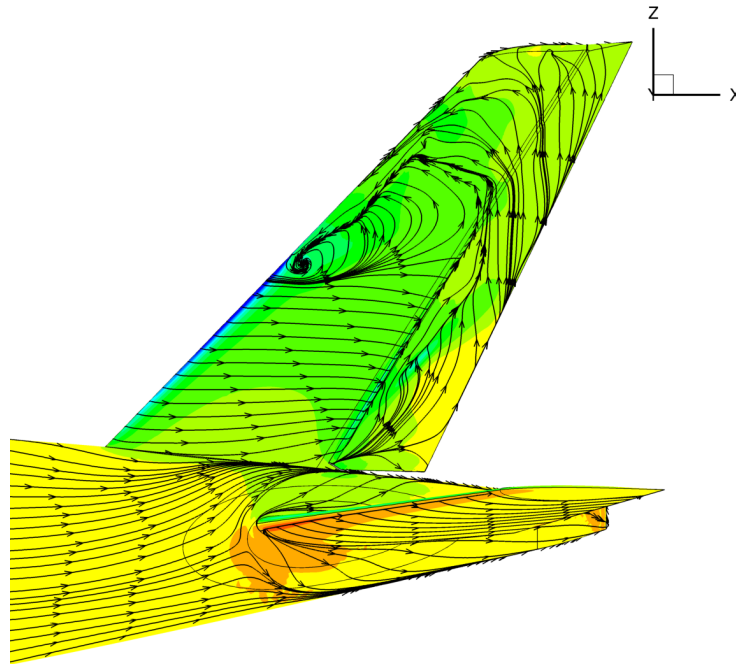


Fig. 5.16 URANS - Flow visualizations for $\delta_r = 30^\circ$ and $\beta = 10^\circ$ (averaged skin-friction lines, Menter SST turbulence model).

Isosurfaces of the Q -criterion are plotted in Figure 5.19. A turbulent structure detaches from the leading edge of the fin. The vortices convect downstream, and intersect one to another. The characteristic length of these eddies is comparable to the chord of the rudder. Not much more detail is captured in the unsteady RANS simulation, therefore it is not possible to observe the breakdown of the vortices from these results.

Two more vortices are detected by the simulation. One separates from the rudder and convects downstream, being slightly sucked towards the bigger separation region over the tip. The other is detected at the gap between the fuselage and the movable control surface, convecting undisturbed downstream. Moreover, it is possible to notice two more vortices generated at the tip of the horizontal tail plane, and a horse-shoe type vortex around its attachment to the fuselage.

Table 5.7 reports that the total aerodynamic load over the tail plane computed by URANS differs by about 5-8% from experimental data when an eddy-viscosity model is used. For RSM-URANS, this difference is higher.

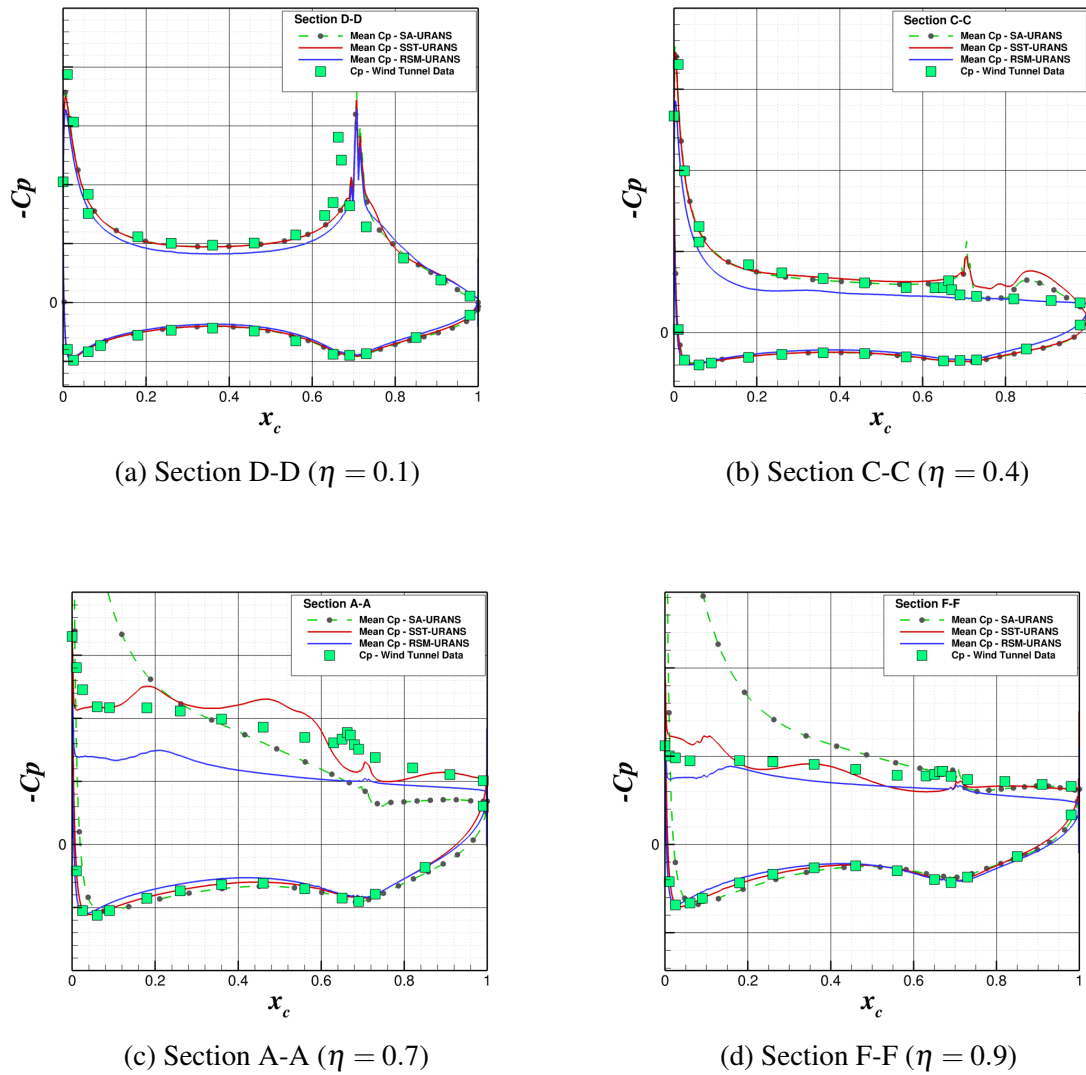


Fig. 5.17 URANS - Pressure coefficient for four sections of cut obtained for $\delta_r = 30^\circ$ and $\beta = 10^\circ$.

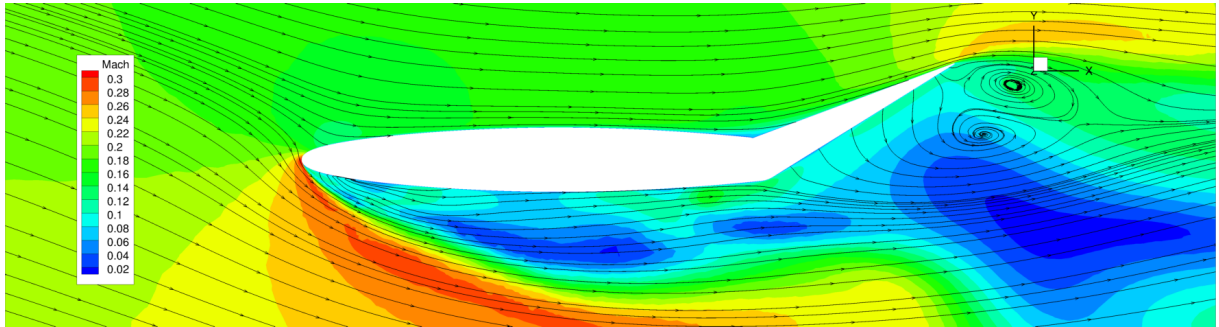


Fig. 5.18 URANS - Mach number contours with time-averaged streamlines for $\delta_r = 30^\circ$ and $\beta = 10^\circ$. Menter-SST turbulence model. Section A-A.

Table 5.7 Loading on the VTP at $\beta = 10^\circ$ and $\delta_r = 30^\circ$

	SA-URANS	SST-URANS	RSM-URANS	Experiment
$ C_{f_y} $	0.79	0.76	0.61	0.83
$ C_{m_z} $	1.58	1.57	1.06	1.46

5.4.3 Cost of the URANS simulations

Table 5.8 contrasts the accuracy of SST-URANS and RSM-URANS with the cost of the simulations for the two geometries studied in this chapter. SA-URANS are omitted from this analysis because their results cannot be reliable, due to the fact that separation is not predicted. The table shows that the cost of RSM simulations is 1.7 times higher than SST. However, there is no gain in the accuracy of the flow solution. In fact, the averaged error in the computation of the force and moment coefficient with the SST model is approximately three times lower than the RSM. Hence, the SST model is more suitable for such applications.

Table 5.8 Accuracy vs. costs of URANS.

	$\delta_r = 0^\circ$		$\delta_r = 30^\circ$	
	SST-URANS	RSM-URANS	SST-URANS	RSM-URANS
Accuracy (% err.)	18.5	44	8.5	25.5
Cost (CPU hours)	144,000	240,000	144,000	240,000

5.5 Conclusions

In this chapter, steady and unsteady RANS simulations on an aircraft wind tunnel model have been carried out with three different turbulence models, with the aim of understanding to what extent these techniques succeed in computing the flow around a VTP.

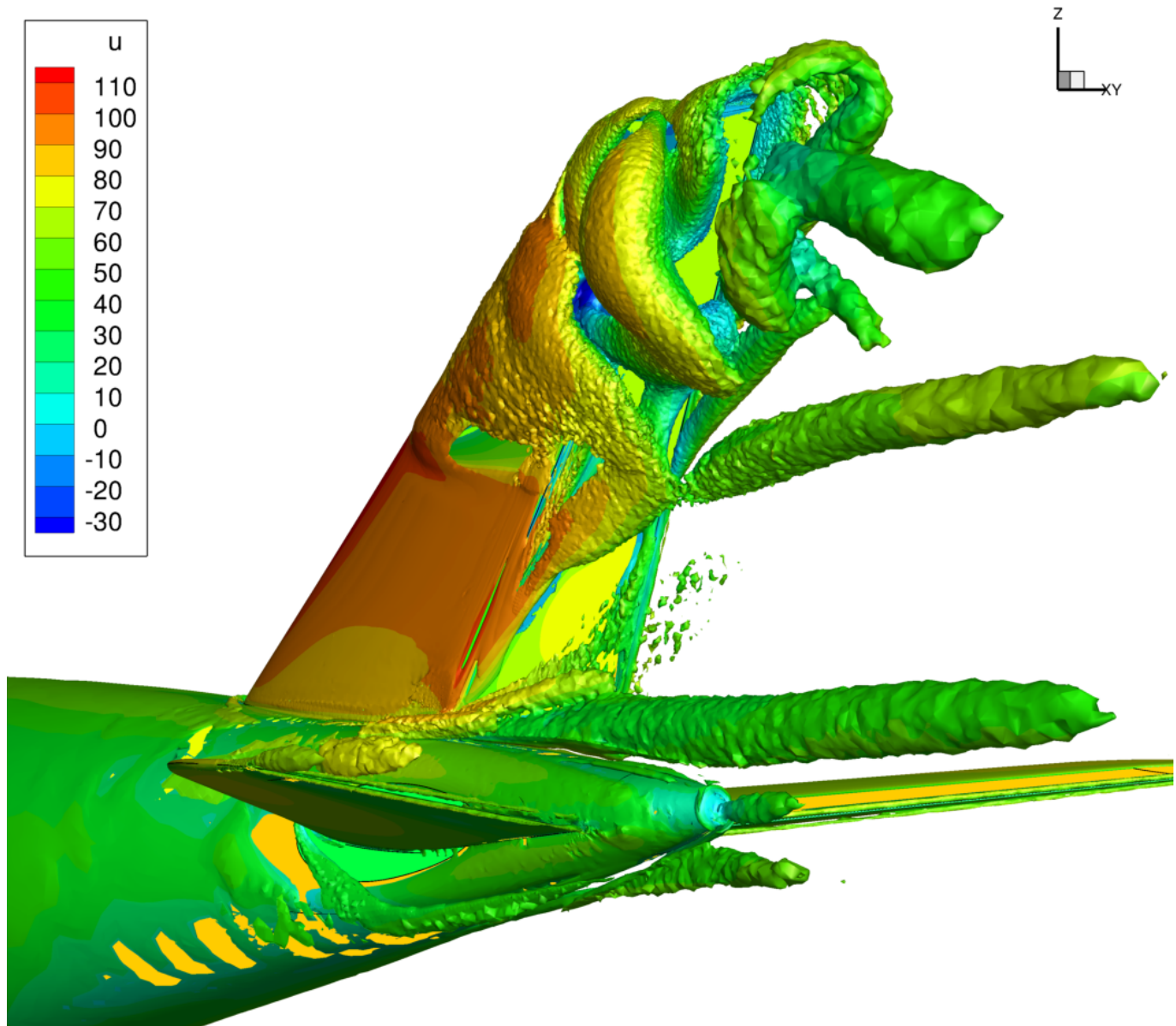


Fig. 5.19 URANS - Isosurface of the Q criterion for $\delta_r = 30^\circ$ and $\beta = 10^\circ$. Menter-SST turbulence model.

Steady RANS studies have been performed for a set of different sideslip angles, showing good convergence for low incidence values. However, when the flow reaches the tail plane with a sufficiently high sideslip angle, steady RANS simulations show poor convergence and inaccuracy in surface pressure. This is due to flow separation occurring on the suction side of the VTP. This is suggested by the skin-friction lines that converge and diverge to a single line, showing a singularity in the flow. When the flow separates, the level of convergence of the density residual is poor, thus not suitable for industrial applications. Similar results have been obtained with the three turbulence models. Therefore, under these circumstances, it is not possible to assess the aerodynamic loading on the VTP.

The strategy used for URANS studies aims to understand whether it is possible to achieve a good prediction of VTP aerodynamics by the introduction of time accuracy in the CFD methods. Flow visualizations show that separation occurs on the suction side of the VTP on the fin. Moreover, when the rudder is deflected, flow also detaches from the control surface along the hinge line. The computational simulations can provide us with an estimation of the VTP loading in the presence of massive flow separation, although an accurate matching with experimental data is not yet achieved. This is due to the fact that the flow is highly unsteady and turbulent, and URANS cannot capture its correct behaviour since turbulence is not resolved. Therefore, even though time accuracy is introduced in the RANS equations, this does not seem enough to provide a deeper understanding of the flow.

Nevertheless, the URANS study generates an important insight about the performance of turbulence models with such complicated flows. The simplest model, SA, has difficulty detecting the correct flow topology, as shown by plots of the pressure distribution. Therefore, whilst the total loads are closer to experimental data, the SA turbulence model does not encourage confidence in this particular industrial application. RSM-URANS is much more expensive than the other two eddy-viscosity models, due to the presence of more equations to be resolved, and for which it is generally harder to achieve solutions. However, this does not make the final solution more accurate, as expected from the analysis carried out in Chapter 4, where the pressure-strain term in the RSM formulation redistributes isotropy of the turbulence structures along the walls of the VTP. However, separation is characterised by marked anisotropy, hence turbulence is unlikely to be modelled correctly.

Performing URANS with the Menter-SST turbulence model is definitely the best choice for this particular flow. Results have shown the best trends among those presented in this chapter. The model captures the onset of flow separation and pressure distributions are closer to experiments, with respect to other turbulence models. Moreover, computation time is shorter than for RSM simulations.

Combining the lessons learnt from chapters 4 and 5, the next step in the current research consists of using hybrid RANS/LES methods, with the SST turbulence model functioning as a subgrid scale model. It will be interesting to see whether time-accuracy combined with resolved turbulence can improve the results and the prediction of the aerodynamic features of aircraft VTPs.

Chapter 6

Eddy-resolving simulations

6.1 Introduction

This chapter investigates the use of a hybrid RANS/LES method to predict the flow around a VTP at a high sideslip angle, with the objective of assessing whether eddy-resolving simulations can improve the flow solution obtained by URANS.

Hybrid RANS/LES methods combine the superior accuracy of large-eddy simulations in detached flow regions, with the efficiency of RANS turbulence modelling in attached boundary layers. As explained in Chapter 3, the hybrid RANS/LES method used in this thesis is the DDES. Hence, the boundary layer is still treated in RANS mode, whereas the detached flow is resolved using LES. This means that the prediction of the onset of flow separation is left to the turbulence model, and Chapter 5 has demonstrated that the SST model performs better for this task. For this reason, this is the model used for the hybrid simulations presented in this chapter. Moreover, Chapter 4 has highlighted the fact that an SST-RANS layer followed by LES gives a good prediction of the reattachment point, improving the prediction of the pressure distribution over the ramp. Therefore, this methodology is now used on the VTP.

The cases presented in this chapter follow the same boundary conditions presented in Chapter 5. The flow is initialised from the URANS simulations, for $\delta_r = 0^\circ$ and $\delta_r = 30^\circ$. Firstly, the chapter illustrates the mesh refinement required to design a grid for DDES; secondly the results will be presented in terms of overall flow features and predictions of the aerodynamic loads. Where appropriate, the DDES results will be contrasted to those from URANS. Finally, the assessment of the cost of the eddy-resolving simulations will be discussed. The results reported here are calculated using the TAU solver.

6.2 Mesh refinement

Hybrid eddy-resolving methods that use RANS and LES need to adapt the mesh for the use of both methodologies in the same computation, so that in the RANS zone the grid is relatively coarse compared with the LES zone. Therefore, for accomplishing hybrid RANS/LES studies presented in this thesis, the mesh has to be refined in a *target zone* in which it is desirable to perform LES. This will give more accuracy to the resolved turbulent structures. Mesh refinement is along the lines of the procedure described by Spalart [100]. Figure 6.1 shows a section of a VTP with deflected rudder.

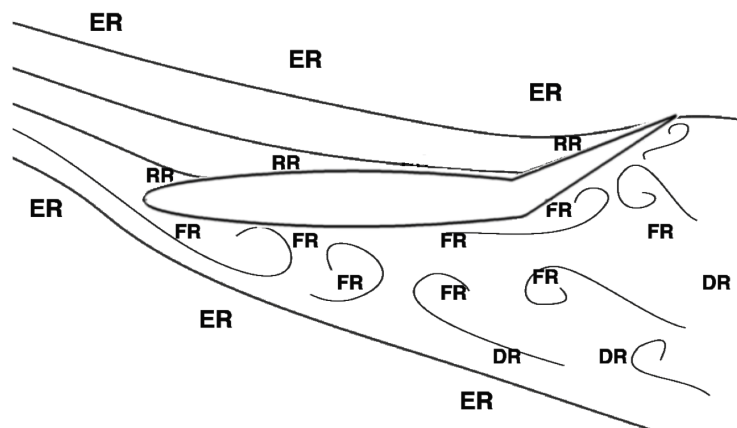


Fig. 6.1 Schematics of a section of VTP at high sideslip angle.

The flow reaches the fin at high sideslip angle, and the following zones can be identified:

- the Euler Region (ER), on the pressure side of the VTP. It is never entered by turbulence or by vorticity.
- the RANS Region (RR), which covers the boundary layer, including the location where flow separation starts. The grid follows the spacing discussed for RANS, targeting to $\Delta y^+ = 0.5$, with the variations over the surfaces shown in Figure 6.2. In streamwise and spanwise directions, the distribution of grid points is constant for most of the chord. Special refinement has been applied at the leading edge of the fin and along the hinge. The maximum grid spacing along the streamwise and spanwise directions are, respectively, $\Delta x_{max}^+ = 300$ and $\Delta z_{max}^+ = 400$. This satisfies near-wall grid requirements discussed by Davidson and Peng [28], and reported by Tucker [110];
- the LES Region (LR) is the actual target zone where eddies will be resolved. It consists of two further domains:

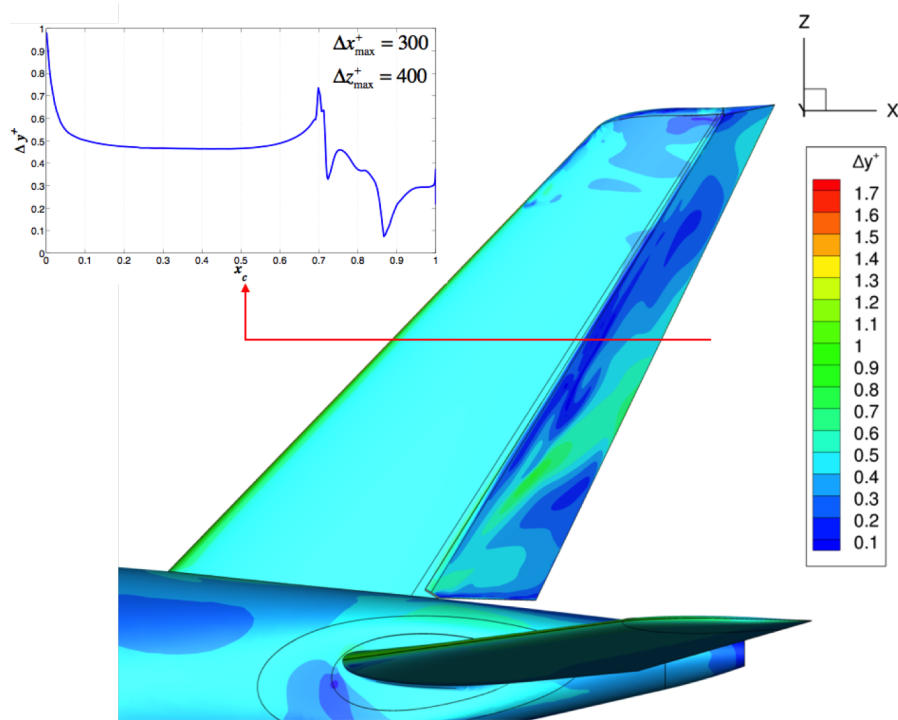


Fig. 6.2 Syrface contours showing Δy^+ for wall cell height.

- the Focus Region (FR), which is the region close to the body where the separated turbulence must be resolved, and
- the Departure Region (DR), which connects the FR to the ER downstream. Here the mesh can be slightly coarser than the mesh in the Focus Region.

For the LES region, grid spacing constraints are more weakly dependent upon the Reynolds number [107]. The grid elements are tetrahedral and spacing tends to be isotropic. The target grid spacing is set by the edge Δ_0 of a generic tetrahedron of the LR mesh. The ratio between δ (the boundary layer thickness), and the edge length Δ_0 is roughly equal to 1 in the LES region. This means that the mesh is well-refined in the target zone. The refinement of the volume mesh of the VTP was achieved through a mesh adaptation algorithm available in TAU (Reuss *et al.* [85]). The refinement involves the meshes outside of the boundary layer, where the elements are tetrahedral. The adaptation algorithm performs an isotropic refinement of each tetrahedron by bisecting each of its edges. Figure 6.3 shows a schematic representation of the adaptation procedure. The number of points and elements of the refined mesh is given in Table 6.1. Figure 6.4a shows the mesh refinement achieved on the suction side of the VTP. Notably, zooming in around the leading edge of the fin, the different sizes of the grid elements in the target zone is evident (Figure 6.4b). This picture shows also the

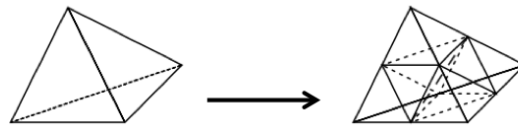
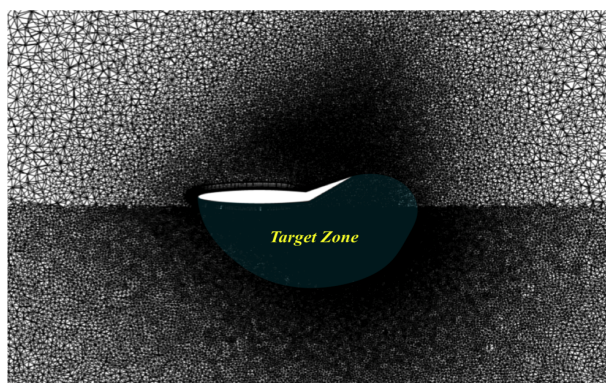


Fig. 6.3 Schematic of the grid refinement procedure [32].

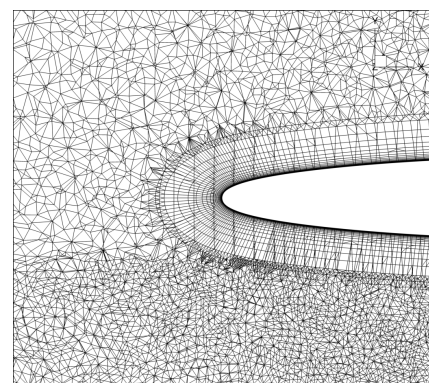
hybrid characteristic of the volume mesh: near the wall the extent of structured regions is maximized, whereas the mesh becomes fully unstructured further from the surface.

Table 6.1 DDES mesh details.

No. of points	33,336,836
No. of tetrahedra	115,872,202
No. of prisms	258,271
No. of pyramids	449,119
No. of hexahedra	13,590,426
No. of surface triangles	41,626
No. of surface quadrilaterals	443,672



(a) VTP mesh - section of cut at $z = 0.5$.



(b) Zoom over the VTP leading edge.

Fig. 6.4 Mesh refinement in the target zone.

6.3 Flow and numerical parameters

As for Chapter 5, the flow studied in this chapter has a free-stream Mach number $M_\infty = 0.2$ and the pressure at the farfield is equal to 1 atm. The Reynolds number based on the VTP MAC is equal to $Re = 2.42 \times 10^6$. The flow reaches the VTP at high sideslip angle. Notably, Table 6.2 reports that for $\delta_r = 0^\circ$ (no rudder deflection) the sideslip angle is equal

to $\beta = 14^\circ$, whereas for $\delta_r = 30^\circ$ the sideslip angle is equal to $\beta = 10^\circ$. These are the same flow conditions that were used for URANS studies in Chapter 5, having the steady RANS not shown convergence due to flow separation. For each case, the flow is initialised with the respective URANS solution discussed in Chapter 5.

Table 6.2 DDES test cases.

Rudder deflection	Sideslip angle
$\delta_r = 0^\circ$	$\beta = 14^\circ$
$\delta_r = 30^\circ$	$\beta = 10^\circ$

The choice of the physical time step is based upon the smallest grid edge in the LES region. To retrieve the edge length, it has been assumed that the mesh consists of regular tetrahedra, whose volume is given by:

$$\Omega_t = \frac{l^3}{6\sqrt{2}}, \quad (6.1)$$

where l is the edge of the tetrahedron. TAU can output the volume of the smallest grid element, from which it is possible to calculate the smallest edge element l_{min} . Hence, the physical time step has been evaluated from:

$$\Delta t = CFL \frac{l_{min}}{V_\infty} \quad (6.2)$$

where CFL is the Courant number. In this study CFL is set to 1, which means convective and pressure disturbances cannot travel more than the distance l_{min} during one time interval Δt . This is to avoid significant degradation of time accuracy due to too large a time step. This gives $\Delta t = 5 \cdot 10^{-6}$ s.

The time-average of the flow solutions takes place over 250 convective time steps, after a transient which allows the flow to develop from the URANS solution to the DDES one.

6.4 Results

6.4.1 Overall flow characteristics

No rudder deflection

The flow topology predicted by DDES is shown in Figure 6.5b. The skin-friction lines are similar to those observed by URANS (Figure 6.5a). The flow reaches the VTP at incidence

$\beta = 14^\circ$, forming a stagnation line on the pressure side of the surface. From the stagnation line, the flow bifurcates, that is, some streamlines develop along the pressure side and stay attached to the surfaces, and other streamlines flow around the leading edge and separate massively. The separation line is quite evident and extends from $\eta \approx 0.25$ all the way to the tip. In spanwise direction, the DDES predicts separation approximately 10% earlier than the URANS.

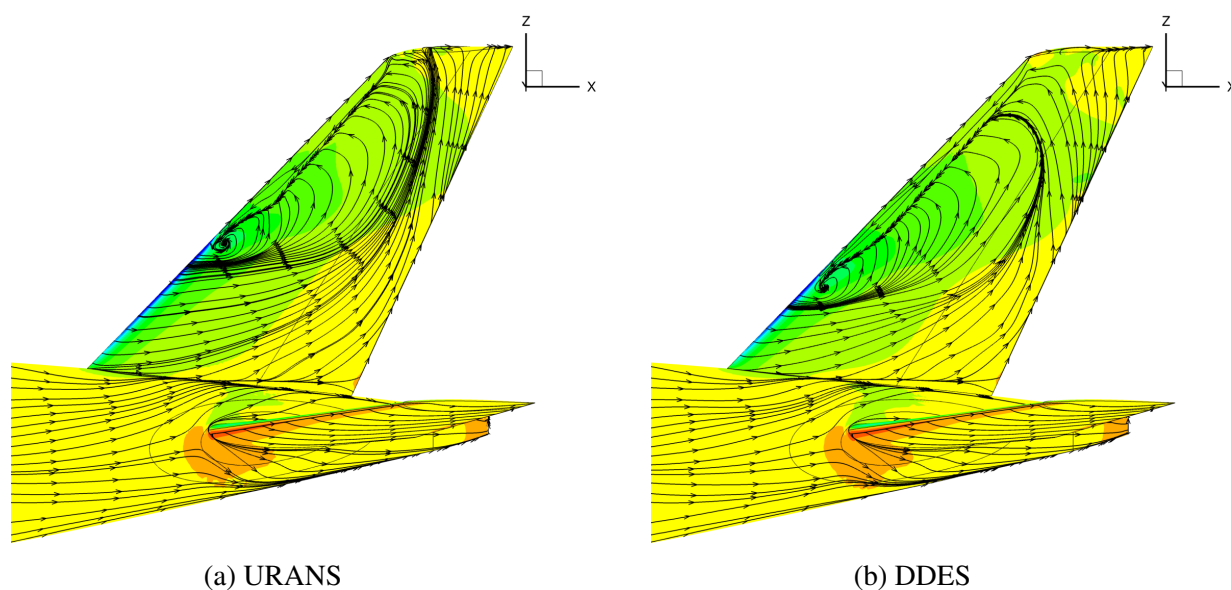


Fig. 6.5 Flow visualizations for $\delta_r = 0^\circ$ and $\beta = 14^\circ$ for the averaged flow, showing skin-friction lines and C_p colour contours. Comparison SST-URANS vs. SST-DDES.

Figure 6.6 shows a cut at constant z of the DDES volume solution, at $\eta = 0.7$. The flow on the pressure side is almost unperturbed, and the streamlines stay attached. The Mach number in these sections remains almost constant along the chord, increasing slightly towards the trailing edge. By contrast, the suction side presents a recirculation area along the whole chord of the VTP. The flow reattaches just before the trailing edge, where it detaches again. The time-averaged flow field is quite different from the URANS prediction. The latter (Figure 5.15) shows that the flow is separated only between $x_c = 0$ and $x_c = 0.5$. By contrast, Figure 6.6 shows that DDES predicts a reversed boundary layer along the whole chord of the VTP, with an off-surface recirculation region extending between $0 < x_c < 0.5$.

Figure 6.7 shows isosurfaces of the Q -criterion. The isosurfaces are coloured by streamwise velocity, so the blue regions indicate reversed flow in the streamwise sense. The surface of the model is coloured by a C_p contour map. This picture shows how turbulence develops on the suction side of the VTP due to a massive flow detachment taking place at the leading

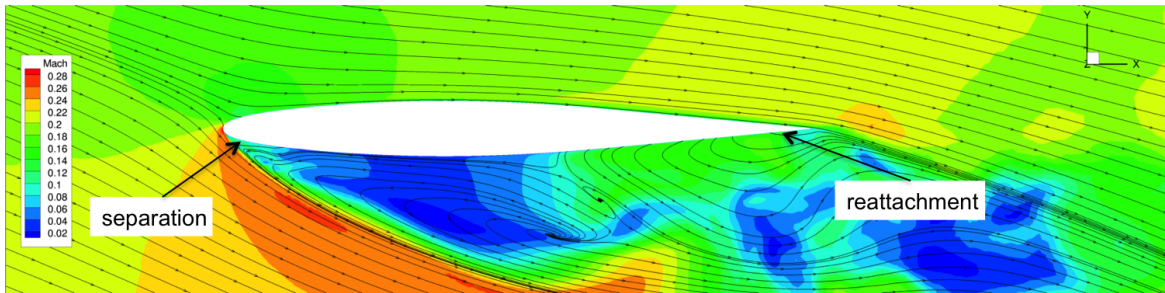


Fig. 6.6 DDES - Instantaneous Mach number contours with time-averaged streamlines, for $\delta_r = 0^\circ$ and $\beta = 14^\circ$. Section A-A $\eta = 0.7$.

edge. Vortical flow structures take off from the separation line, and break down into smaller eddies. The detached flow interacts with the separation occurring also at the tip of the VTP.

The turbulence models used for URANS were not able to predict all the flow features and turbulent structures discussed in this section. It will be interesting to see how much this increased accuracy with DDES influences the overall aerodynamic load prediction.

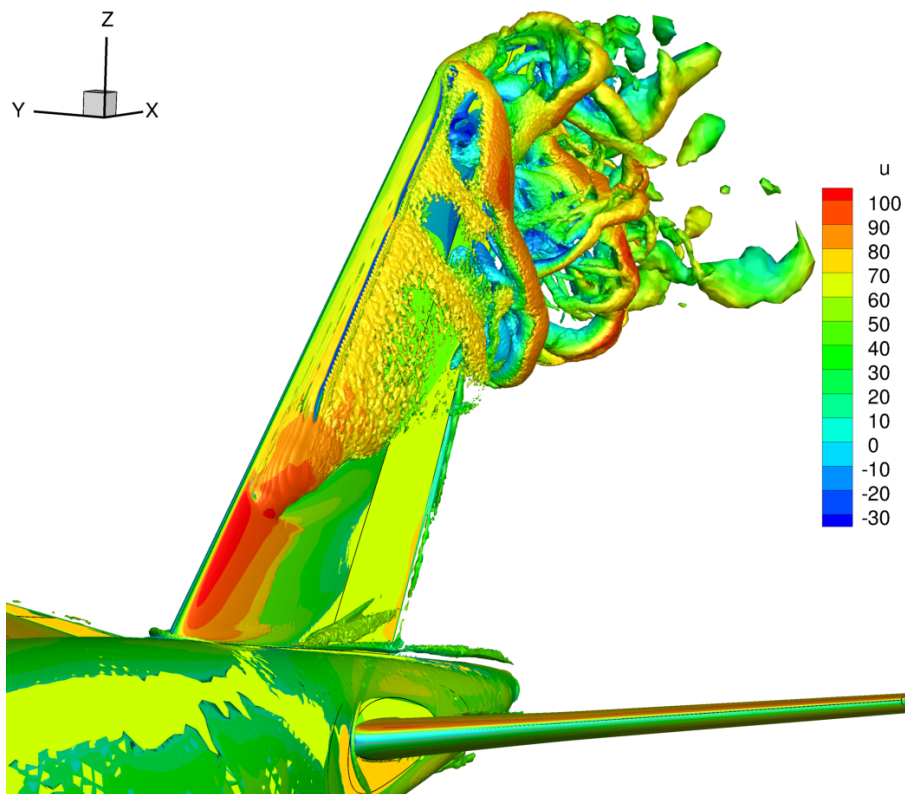


Fig. 6.7 DDES - Instantaneous isosurface of the Q -criterion for $\delta_r = 0^\circ$ and $\beta = 14^\circ$ coloured by streamwise velocity.

VTP with deflected rudder

In this section, the rudder is now deflected of 30° and the flow has a sideslip angle of 10° . As discussed previously, the VTP configuration with the deflected rudder is more challenging. This is due to the presence of flow separation on the leading edge of the fin and on the hinge line of the rudder. This is predicted by DDES, as shown in Figure 6.8b. In the lower part of the tail (from $\eta = 0$ to $\eta \approx 0.3$), the flow is attached along the fin and separates on the hinge line of the rudder. On the rest of the tail, from $\eta \approx 0.3$ to $\eta \approx 1$, the flow detaches much earlier, along the leading edge of the fin, similar to what observed for $\delta_r = 0^\circ$. Also in this case, in spanwise direction the DDES flow separates earlier (by approximately 20%) than the URANS.

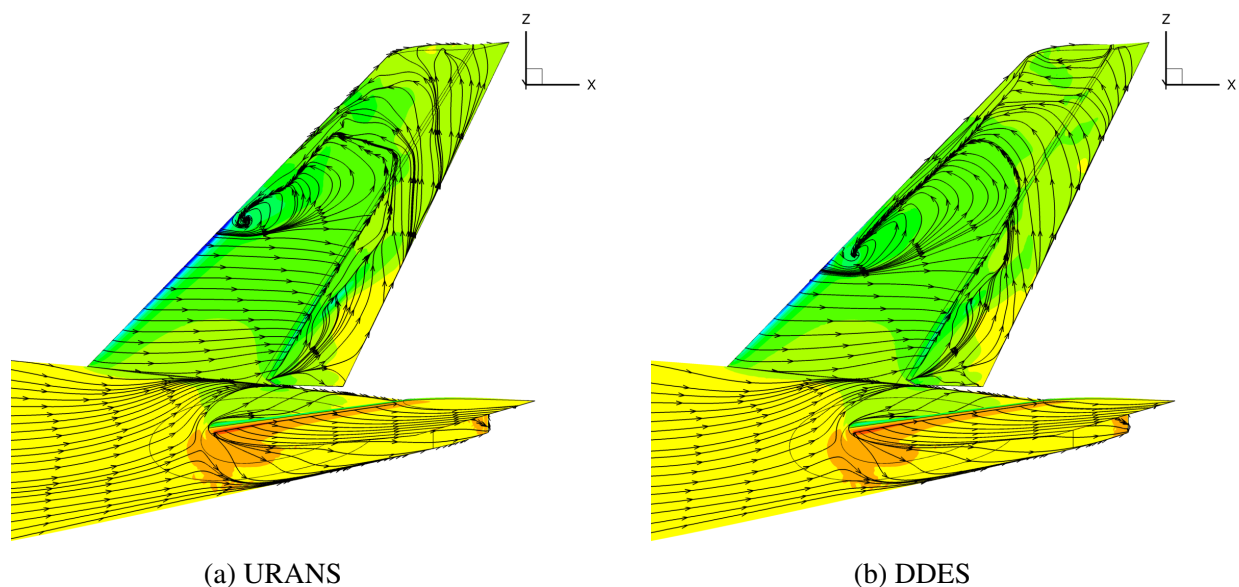


Fig. 6.8 Flow visualizations for $\delta_r = 30^\circ$ and $\beta = 10^\circ$ for the averaged flow, showing skin-friction lines and C_p colour contours. Comparison SST-URANS vs. SST-DDES.

Figure 6.9 shows a cut of the volume solution taken at $\eta = 0.7$. Comparing the streamlines obtained by DDES against the URANS ones (Figure 5.18), it is possible to observe that the flow topology looks quite different. In fact, the URANS simulation predicts only a mild flow separation on the leading edge of the fin, and the recirculation area predicted by DDES is almost absent. Furthermore, URANS results show two counter-rotating vortices along the suction side of the rudder, and this is quite different from the DDES result. By contrast, the DDES time-averaged streamlines highlight the fact that the flow is reversed along almost the whole length of the VTP chord. Moreover, another vortical structure is present over the deflected rudder. The size of this vortex is comparable to the chord of the deflected control surface.

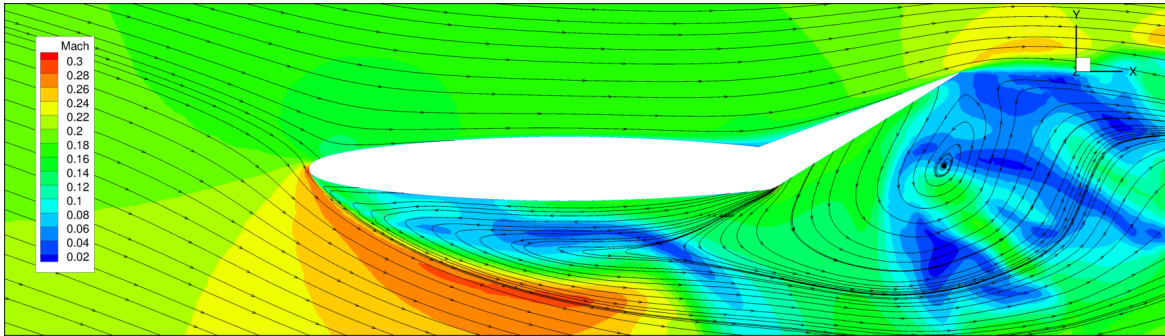
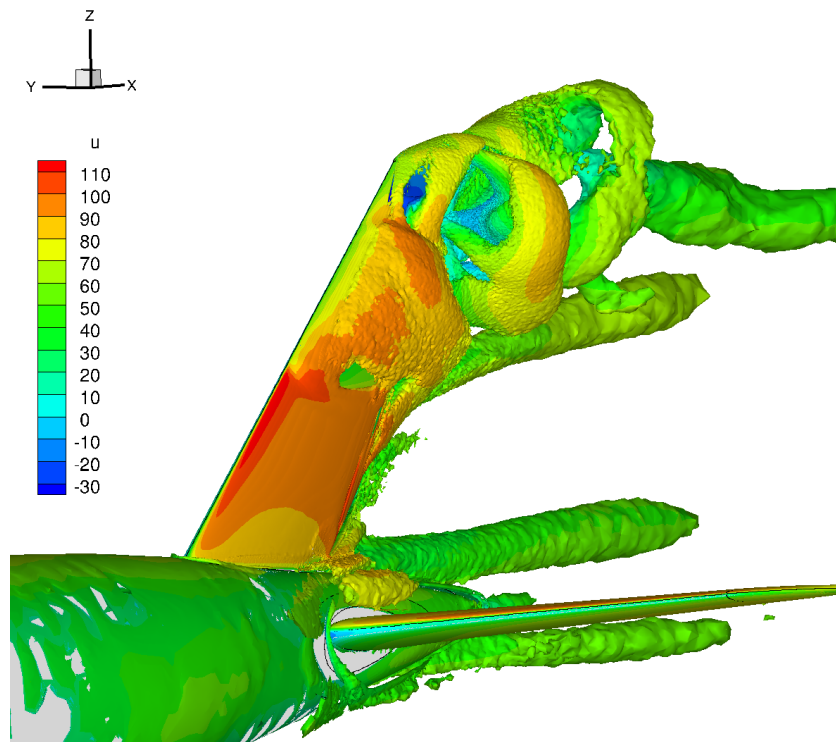
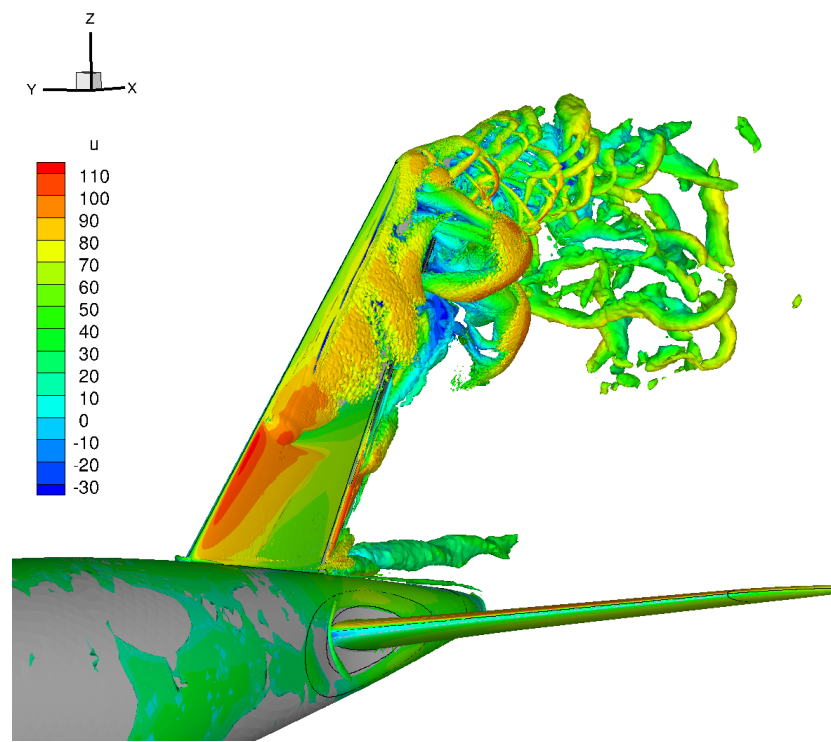


Fig. 6.9 DDES - Instantaneous Mach number contours with time-averaged streamlines for $\delta_r = 30^\circ$ and $\beta = 10^\circ$. Section A-A ($\eta = 0.7$).

Instantaneous flow realizations are plotted in figures 6.10, through the use of isosurfaces of the Q -criterion. Figure 6.10a shows the URANS solution that was presented in Chapter 5. The two figures show that, similarly to the case with no rudder deflection, the separation line is well distinguished along the leading edge of the fin. It can be seen that DDES is resolving vortical structures with significantly more detail than URANS, most importantly in the separated regions above the fin and rudder surfaces. The vortices convect downstream, but only the hybrid simulation is capable of capturing how the eddies break down into smaller vortical tubes downstream the separation. The gap between the fuselage and the deflected rudder is another location of flow separation. In fact, a streamwise vortex is formed between the deflected rudder and the fuselage, and this is well-predicted by both URANS and DDES. Overall, qualitatively, the isosurfaces computed by the eddy-resolving simulation have an improved resolution with respect to the URANS ones. Eddies are captured with more detail in the DDES, whereas the URANS solution does not have the same level of accuracy. In the next sections it will be interesting to understand whether this translates into a better prediction of the pressure distribution and aerodynamic loads over the VTP.



(a) URANS



(b) DDES

Fig. 6.10 Comparison of URANS and DDES turbulent structures for $\delta_r = 30^\circ$ and $\beta = 10^\circ$.

6.4.2 Predictions of the aerodynamic loads

Improving the CFD prediction of aerodynamic loads is of great interest for aircraft designers. The description of the flow captured by DDES highlights some differences with respect to unsteady RANS results. In this section, these differences will be quantified in terms of pressure distribution and integrated aerodynamic loads over the VTP.

VTP without deflected rudder

Analysis of the time-averaged pressure coefficient is conducted for the four sectional cuts of the VTP defined in Chapter 3. Figure 6.11 shows that, both URANS and DDES predict the pressure distribution correctly on the pressure side. On the suction side, as previously observed, the VTP with no rudder deflection does not present flow separation for $0 < \eta < 0.3$, hence Figure 6.11a shows that for $\eta = 0.1$ the results obtained by both URANS and DDES agree with the measurements. Further outboard, flow separation occurs. Figure 6.11b shows that section $\eta = 0.4$ corresponds to a type of grey area, where the flow is intermittent and not completely separated. In this region of uncertainty, the URANS solution is perhaps fortuitously more accurate than the hybrid RANS/LES solution.

The situation is different at $\eta = 0.7$ and $\eta = 0.9$, where the flow is completely detached. In fact, for $0.3 < x_c < 1$ DDES matches the experiment, whereas URANS still shows an error around 30% (especially for Section F-F). Closer to the leading edge, both URANS and DDES lack precision in determining the suction peak, which is missed by about 50%. This can be a source of error in the computation of the overall loading on the VTP. Overall, the pressure coefficient computed by DDES gives more reliability and robustness to the CFD results. The flat distribution of the C_p in the separation region is an indication of the fact that resolving turbulence indeed improves the flow solution, and the separation region is well-captured by the eddy-resolving simulation.

Through integrating the pressure over the VTP surface, aerodynamic loading is obtained. Figures 6.12 and 6.13 show the evolution in time of the side force and yaw moment coefficients, respectively. These plots reflect the fact that the VTP is excited unsteadily by the detached flow. The time-averaged loads are reported in Table 6.3. The loads prediction performed by DDES is significantly improved. In fact, the bar chart plotted in Figure 6.14 shows¹ that RSM-URANS is the least accurate method for resolving such flows. SST-URANS results produce an error ranging from 17% to 20%, whereas hybrid RANS/LES have a further improvement range, with the relative error ranging around 11-12%.

¹SA-URANS is omitted due to its failure to predict separation while the resultant forces do not reflect this failure. This is an example of the risk of error cancellation in surface integration, leading to an impression of spurious accuracy.

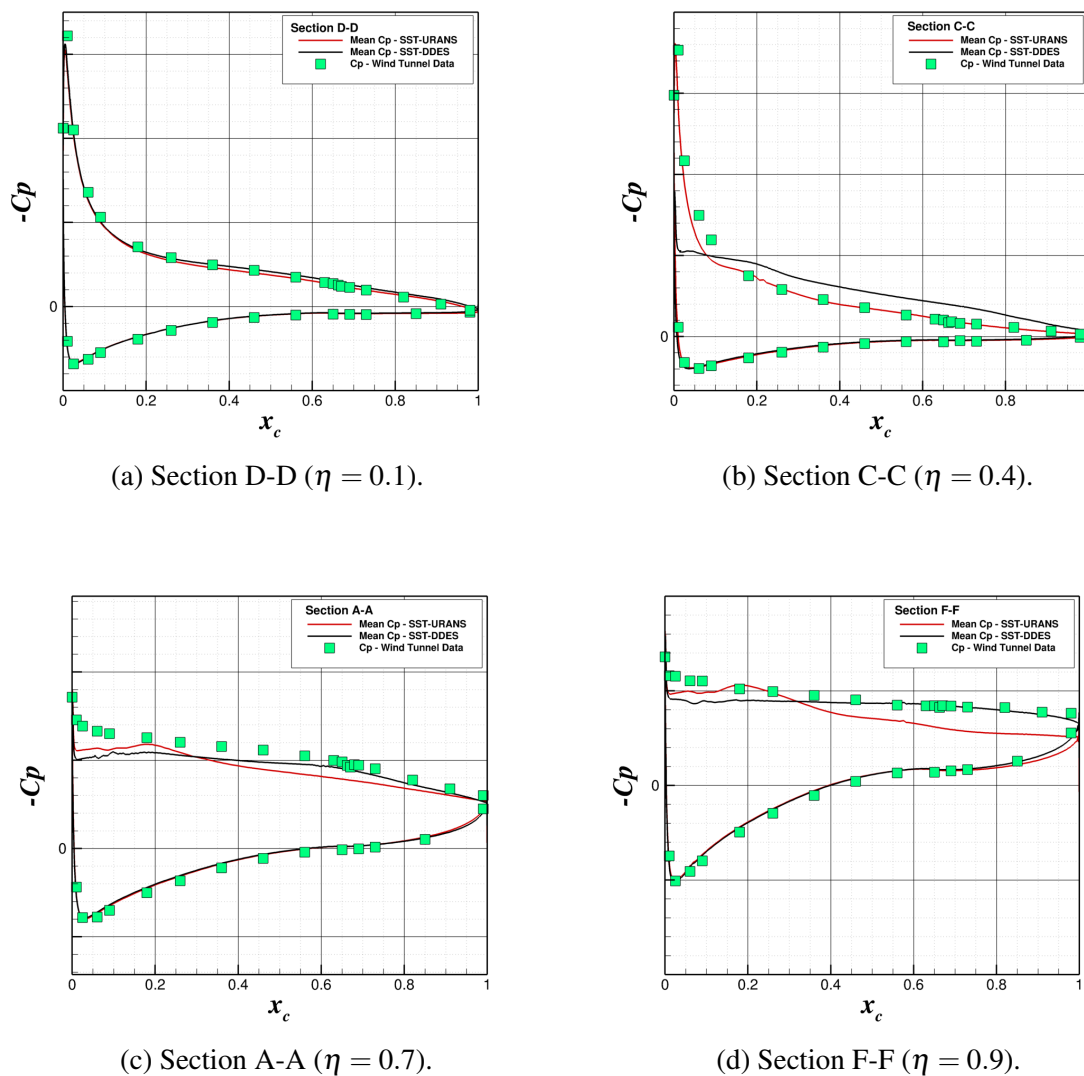


Fig. 6.11 DDES - Pressure coefficient for four sections of cut obtained for $\delta_r = 0^\circ$ and $\beta = 14^\circ$.

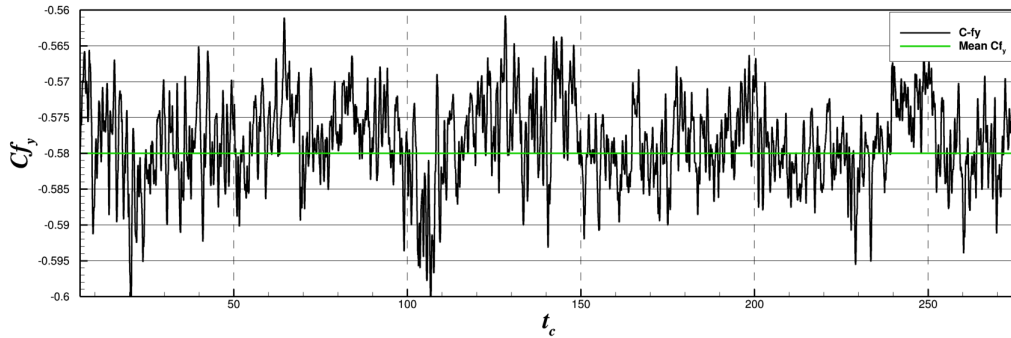


Fig. 6.12 DDES - Evolution of the side force coefficient with time, $\delta_r = 0^\circ$ and $\beta = 14^\circ$.

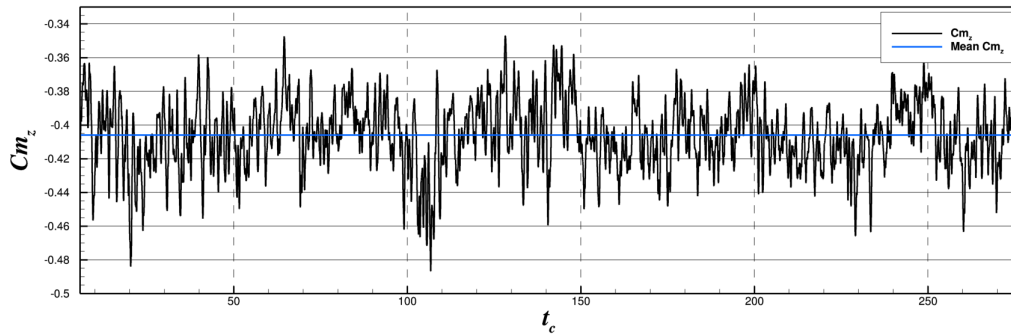


Fig. 6.13 DDES - Evolution of the yaw moment coefficient with time, $\delta_r = 0^\circ$ and $\beta = 14^\circ$.

Table 6.3 Loading on the VTP at $\beta = 14^\circ$ and $\delta_r = 0^\circ$

	SA-URANS	SST-URANS	RSM-URANS	SST-DDES	Experiment
$ Cf_y $	0.59	0.55	0.51	0.58	0.66
$ Cm_z $	0.30	0.37	0.16	0.41	0.46

VTP with rudder deflection

Figure 6.15 shows the distribution of pressure coefficient for the four sections of cuts along the tail plane. Overall, the DDES curve is in agreement with measurements for all sections of cut. An important improvement in the accuracy of C_p compared to URANS is achieved again where the flow is massively separated on the fin (sections A-A and F-F). In fact, the figures show that the DDES solution matches very closely the experimental data. A misplacement (by 5% of the chord) in the local peak near the rudder may be noticed, especially for section D-D. This could be due to a slight difference between the wind tunnel model and the computational one regarding the blending region between fin and rudder.

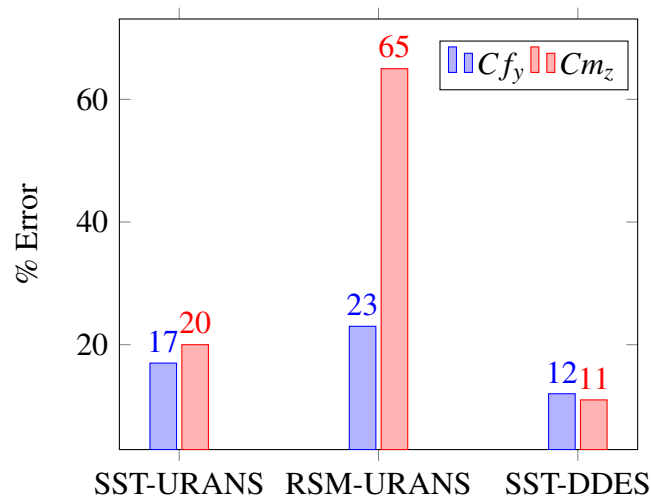


Fig. 6.14 Comparison of the accuracy of the three CFD methods ($\delta_r = 0^\circ$ and $\beta = 14^\circ$).

The trends of the side force coefficient and the yaw moment coefficient are similar to those observed for $\delta_r = 0^\circ$. However, in this case, the deflection of the rudder increases dramatically the force generated by the whole tail. The comparison with previous CFD computations and measurements is reported in Table 6.4.

Table 6.4 Loading on the VTP at $\beta = 10^\circ$ and $\delta_r = 30^\circ$

	SA-URANS	SST-URANS	RSM-URANS	SST-DDES	Experiment
$ C_{f_y} $	0.79	0.76	0.61	0.77	0.83
$ C_{m_z} $	1.58	1.57	1.06	1.42	1.46

As can be seen from the bar chart in Figure 6.16, the total side force coefficient computed by DDES differs by only 1% from SST-URANS, whereas the yaw moment differs by about 5%. Nevertheless, the trends of the pressure coefficients obtained by URANS are worse when the flow is detached, and this does not build much confidence in the computational result. By contrast, the results obtained by DDES look more reliable.

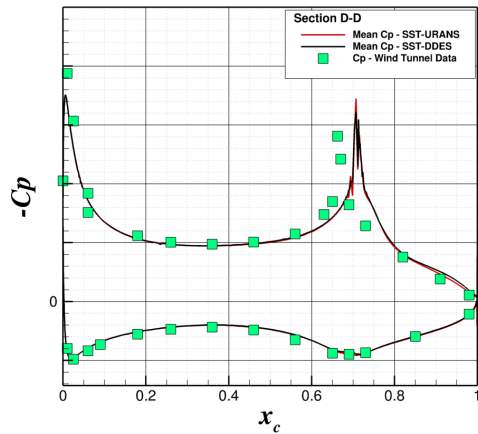
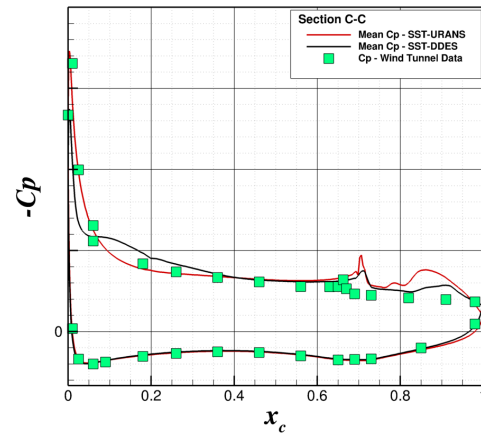
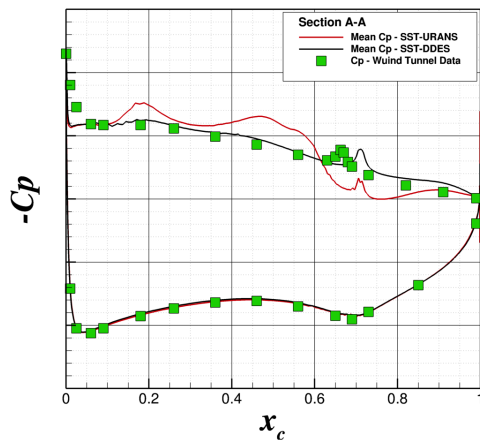
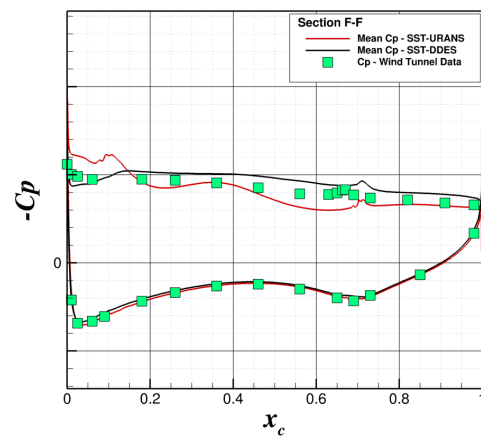
(a) Section D-D ($\eta = 0.1$).(b) Section C-C ($\eta = 0.4$).(c) Section A-A ($\eta = 0.7$).(d) Section F-F ($\eta = 0.9$).

Fig. 6.15 DDES - Pressure coefficient for four sections of cut obtained for $\delta_r = 30^\circ$ and $\beta = 10^\circ$.

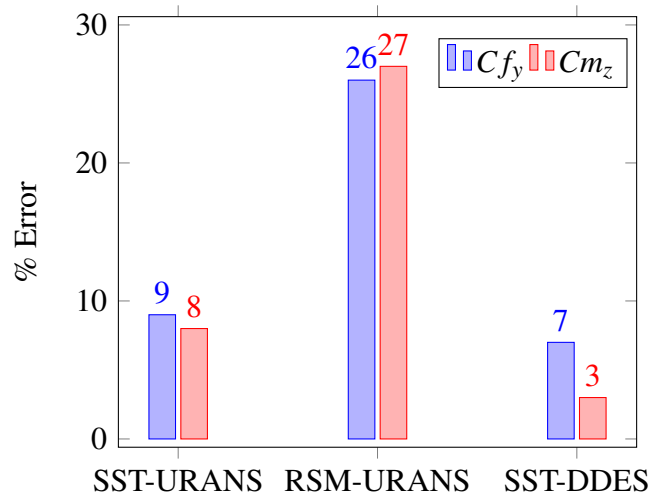


Fig. 6.16 Comparison of the accuracy of the three CFD methods ($\delta_r = 30^\circ$).

Spectral analysis

The trends of the force and moment coefficients plotted in the previous sections shows that the loads are quite unsteady, resulting in a signal that oscillates around a mean value by 5-10%. The Fourier Transform of this signal in the frequency domain offers more insights into the unsteady excitations of the flow around the VTP.

Figure 6.17 shows the trend of the amplitude P of the value of the side-force coefficient obtained for $\delta_r = 0^\circ$ with respect to frequency expressed as a Strouhal number St . The Strouhal number is defined as:

$$St = \frac{f \cdot MAC}{V_\infty}, \quad (6.3)$$

where f is the frequency gathered from the convective time series, and V_∞ is the free stream flow velocity. The x -axis is on logarithmic scale, in order to have a better visibility of the lower frequencies.

The figure shows that most harmonics concentrate for $0 < St < 0.5$ (i.e. low frequencies). In the detached flow region, on the suction side of the VTP, the flow is slowed down dramatically. Here the vortices travel a distance of approximately one MAC in 0.56 s. This translates into a frequency $f \approx 1.75$ Hz. Inputting this in the definition of the Strouhal number above, one obtains $St = 0.04$, which corresponds to the first harmonic of Figure 6.17. Figure 6.18 shows a downstream convection of vortices, suggesting the presence of vortex shedding, that is, the eddies created on the suction side of the VTP detach periodically from the fin (or the rudder). At least two other harmonics may be distinguished. They are likely to be linked to the vortex taking off from the tip and the wake of the whole model.

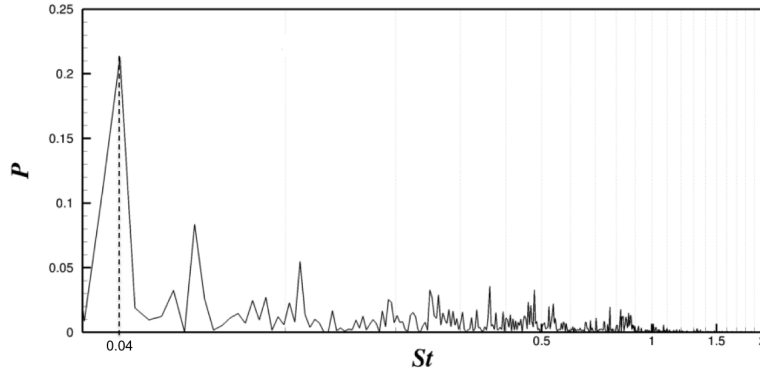


Fig. 6.17 Fourier Transform of the side force coefficient with respect to the Strouhal number.

High-frequency vortex structures cannot be observed from the spectrum of the side-force coefficient, since they are cancelled out in the integration of the side-force.

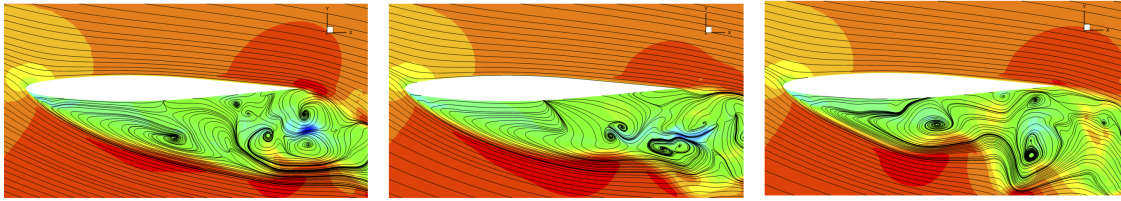


Fig. 6.18 Three snapshots of the flow solution for $\eta = 0.8$.

6.4.3 Shape of the turbulence and validity of turbulence modelling

Figure 6.19 shows isosurfaces of the Q -criterion coloured by the flatness parameter A introduced in Chapter 3. The figure shows that on the suction side, at the onset of flow separation the flow is characterised by a marked anisotropy, since the values of A are close to zero. In the separated flow region, A increases sharply, attaining values up to 0.8. This indicates that turbulence tends to redistribute the turbulent kinetic energy in the flow, and a return-to-isotropy is observed.

Figure 6.20 shows isosurfaces of the Q -criterion coloured by the misalignment angle α_{MA} between two turbulent shear stresses and the equivalent mean strain rate. For the pair $u'w'$ and $v'w'$, the misalignment angle has the form (Wang *et al.* [121]):

$$\alpha_{MA} = \left| \arctan \left(\frac{\frac{\partial u}{\partial z} + \frac{\partial w}{\partial x}}{\frac{\partial v}{\partial z} + \frac{\partial w}{\partial y}} \right) - \arctan \left(\frac{u'w'}{v'w'} \right) \right|. \quad (6.4)$$

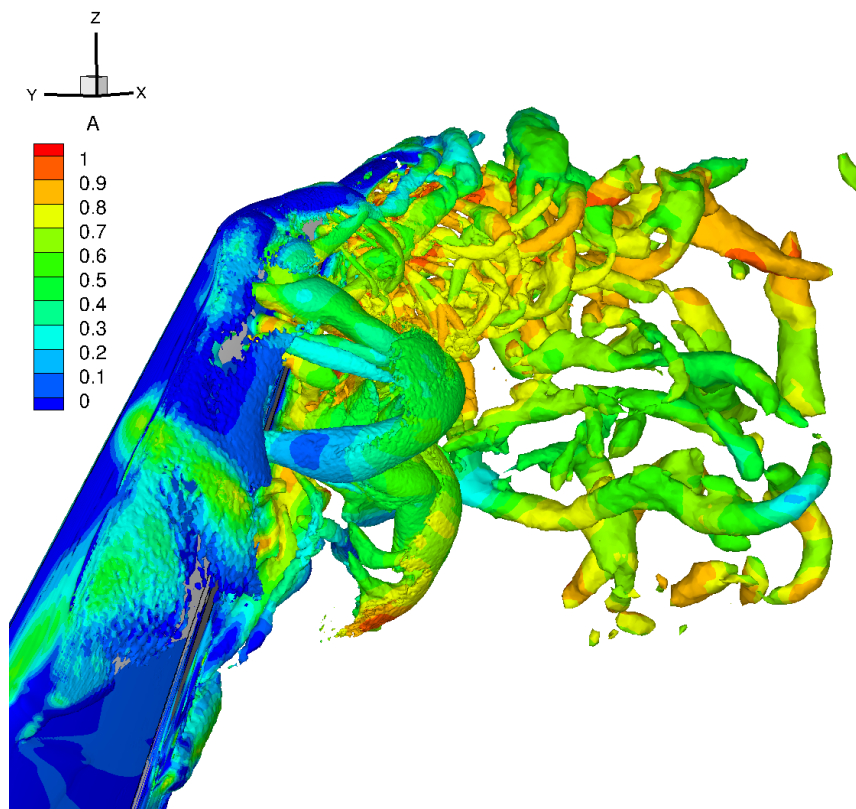


Fig. 6.19 Flatness parameter for a section of the flow field.

The values of α_{MA} range between 0° and 180° , differently from what hypothesised in eddy-viscosity models. In fact, as explained earlier, this kind of models relies upon the Boussinesq hypothesis, which expresses a proportionality and alignment between flow shear stresses and strains. However, Figure 6.20 shows that the flow around a VTP at high incidence is characterized by large regions of important misalignment between shear stresses and strains, hence the Boussinesq approximation is not valid. For this reason, future investigations of the flow around tail planes may include the use of the stress–strain lag eddy-viscosity model developed by Revell *et al.* [86], which takes into account the misalignment between stress and strain in unsteady turbulent flows. This approach could be used with the SST model, which gives better prediction of the separation point. The RSM model does naturally predict the lag but the poor prediction of the separation location appears to negate any benefits in this particular application.

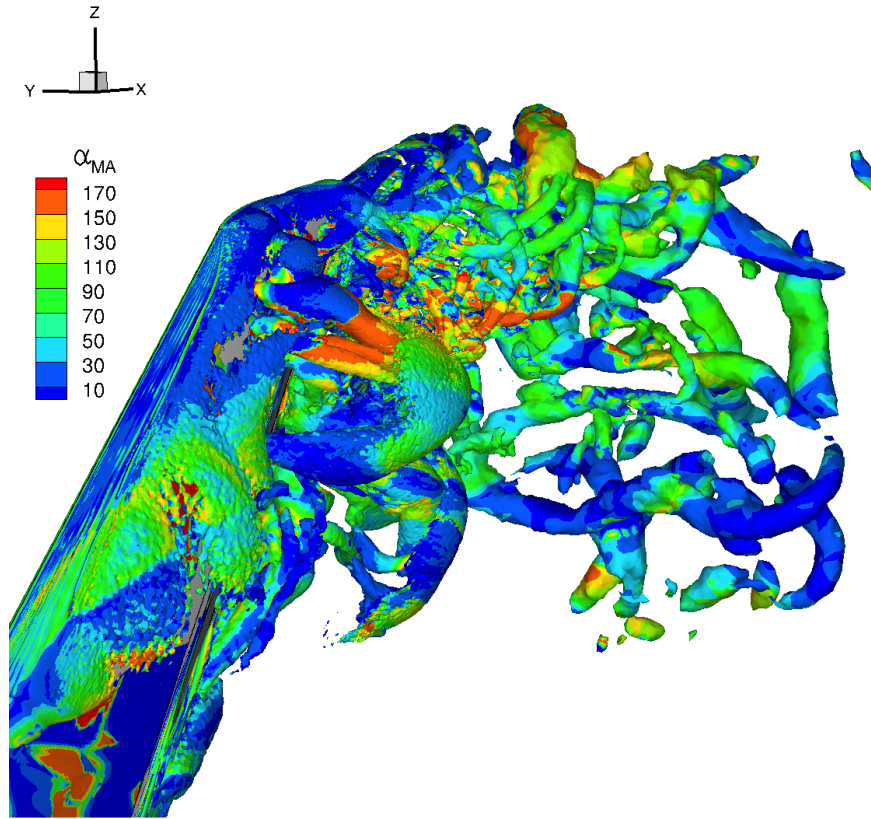


Fig. 6.20 Lag between shear stresses and strains for a section of the flow field.

6.4.4 Assessment of the behaviour of the DDES delay function

As discussed in Section 3.5, in DDES the integral turbulent length scale in the RANS model's dissipation term is replaced by a suitable, grid-dependent filter length:

$$l_{hyb} = l_{RANS} - f_d \cdot \max(0, l_{RANS} - l_{LES}).$$

It is worth writing again the expression of f_d , which is:

$$f_d = 1 - \tanh(8r_d^3)$$

with:

$$r_d = \frac{\mu + \mu_t}{\sqrt{S_{ij}S_{ij}}\kappa^2 d_w^2}.$$

The delay function controls the switch between RANS and LES, and delays the transition between the two methods. Notably, when $f_d = 0$, then $l_{hyb} = l_{RANS}$, therefore URANS mode is retained. On the contrary, when $f_d = 1$, LES behaviour is expected.

Figure 6.21 shows isosurfaces of the Q criterion coloured by the delay function f_d . The contours show that, in the separated flow region, f_d is predominantly equal to 1, as expected. The transition between 0 and 1 is gradual. This enables the shielding of the boundary layer, preventing it to be resolved in LES mode.

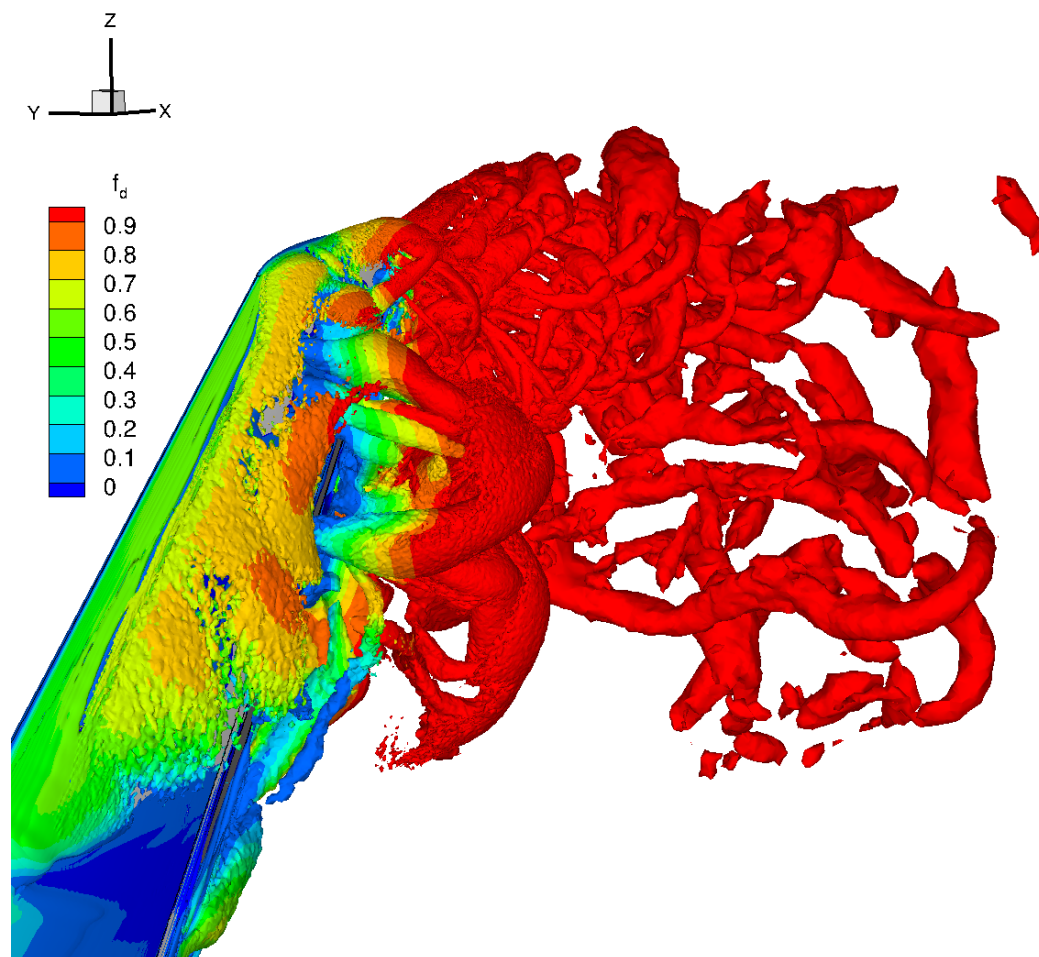


Fig. 6.21 Isosurfaces of the Q criterion coloured by the delay function f_d

Figure 6.22 shows a contour map of f_d for a horizontal cut of the flow field around the VTP. The figure shows that the delay function does not switch to 1 in some regions where the flow is detached, seeming to have a too conservative behaviour. Its formulation is based on the mixing length theory, which assumes a proportionality between the effective viscosity ($\mu + \mu_t$) and the strain-rate through the square of the wall distance d_w . This hypothesis is based on fundamental boundary layer theory, which is not adequate for the VTP boundary layer, which is characterised by three-dimensionality, recirculation and flow detachment. Moreover, according to the mixing length hypothesis, turbulence depends only upon the local

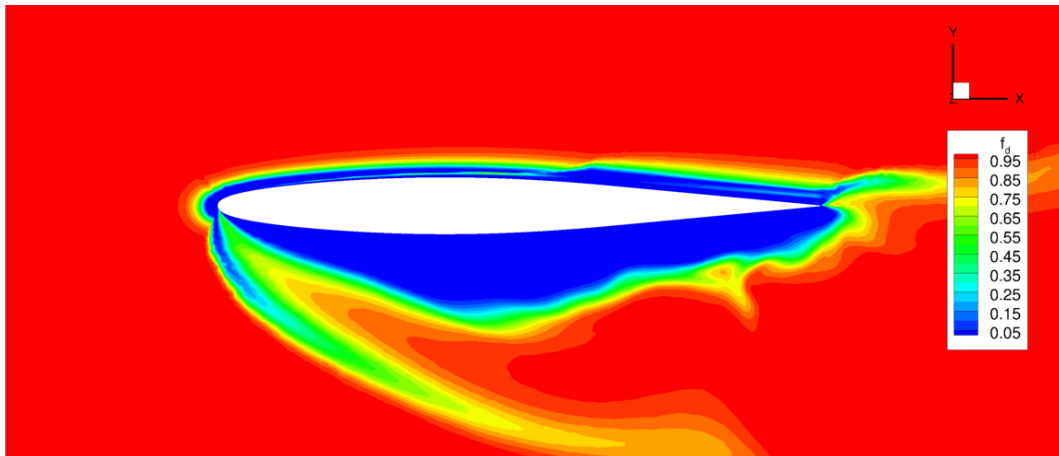


Fig. 6.22 Contour map of the delay function f_d for $\eta = 0.7$.

generation and dissipation rates. In reality, turbulence may be carried or diffused to locations where no turbulence is actually being generated at all.

Therefore, the formulation of the hybrid RANS/LES switch could be improved as part of future work. For instance, sensitivity studies on the calibrating coefficient (8 in the f_d equation) could be carried out, even though this would not discard the mixing length hypothesis. Moreover, instead of using the delay function, the interface for the differing models could be explicitly specified in terms of wall distance or fractions of the boundary layer thickness, as in Tucker and Davidson [112]. Another approach that could be tested in future work could be to adopt the use of a adaptive DES simulations, introduced by Durbin [33]. This technique enables to compute the DES constant C_{DES} locally within the flow, and it has shown promising results.

6.5 Cost of the simulations and overall considerations

Table 6.5 compares the performance of DDES with respect to URANS. Accuracy is given by the average of the relative errors obtained for the side force and yaw moment coefficients, whereas the cost is given by the number of CPU hours. The DDES of the VTP flow for $\delta_r = 0^\circ$ is more accurate than the URANS simulation by 38%, and, for $\delta_r = 30^\circ$, the relative URANS error is reduced by 41%.

It is important to consider how much improved accuracy costs. The number of CPU hours needed to achieve a fully-developed DDES solution is about four times the time required by URANS. If 480 cores are used in parallel for both methods, then 300 hours (almost two weeks) are needed for URANS, whereas 2500 hours (i.e. almost 3 months) are needed for DDES. However, at this ‘price’, the CFD practitioners buys:

Table 6.5 Accuracy vs. costs of URANS and DDES.

	$\delta_r = 0^\circ$		$\delta_r = 30^\circ$	
	SST-URANS	DDES	SST-URANS	DDES
Accuracy (% err.)	18.5	11.5	8.5	5.0
Cost (CPU hours)	144,000	600,000	144,000	600,000

- proven improved accuracy, and
- reliability of the flow solution.

These two factors are key to aircraft design. The introduction has highlighted how important it is to save weight in any aircraft installation, including the VTP. An improved and more reliable CFD prediction certainly helps with this task.

For these reasons, whilst hybrid RANS/LES are more costly, they should be certainly employed for VTP flows at high sideslip and/or rudder deflection angles. On the other hand, especially for industrial applications, reducing the cost of the simulation would be extremely helpful. To achieve this, a further zonalisation of the computational domain would be worth considering for future investigations. In fact, the results have shown that also on the suction side of the VTP attached flow regions may be found, and there is no need to refine the mesh in these areas, since the URANS resolution is acceptable. Conversely, in the areas where the flow is detached and highly turbulent and unsteady, the use of eddy-resolving methods has proved to be crucial and beneficial.

6.6 Conclusions

This chapter reports the study of two VTP configurations, one without rudder deflection and one with large deflection, at high sideslip angle, by the use of eddy-resolving simulations with the Menter SST turbulence model in a Delayed Detached-Eddy Simulation (DDES) scheme. Turbulence visualisations and stress anisotropy maps have shown that the detached flow over the VTP features three-dimensional vortical structures, characterised by large rotationality and anisotropy. Therefore, isotropic turbulence models have difficulties to assess the detached VTP flow correctly.

Results show an improvement in the prediction of the flow solution previously obtained by URANS simulations. This is obtained by resolving turbulence, rather than merely modelling it. In fact, the computation of the integrated aerodynamic loads is closer to the experimental observations, compared to the URANS. The relative error for the non-deflected rudder test

case ($\delta_r = 0^\circ$) drops to 11.5%, and for a rudder deflection $\delta_r = 30^\circ$ the error is about 5%. Not only are the integrated values of the side force and yaw moment improved, but also the local prediction of the pressure distributions for sectional cuts of the VTP. This gives much more reliability to the simulation and confidence in the results.

Nevertheless, DDES presents room for improvement. First of all, the behaviour of the delay function is not precise everywhere, since there are some areas in which the switch to LES mode is delayed too much, notably in the extensive separated region on the suction side of the VTP. Moreover, the cost of the simulation is another factor that may limit the application of DDES for the assessment of the VTP flow in industry. However, increased availability of powerful computing facilities in larger industrial organizations is also likely to happen. The cost of the simulation could be reduced using a more adapted mesh, along with a method which would zonally adapt the computational domain even further. In fact, keeping RANS mesh distribution in the areas where the flow is attached also on the suction side of the VTP would save computational time, and make the simulation more affordable for industrial simulations. This could be achieved, for example, by using mesh adaptation algorithms that would change the mesh density in the flow automatically, with respect to the physical flow feature.

Chapter 7

Concluding remarks and recommendations for future work

7.1 Conclusions

The aim of this thesis was to assess the flow around a vertical tail plane through CFD, investigating methods that can offer greater accuracy and thus confidence in the results. The air-flow around aircraft VTPs can involve flow separation at high sideslip angles and/or when the rudder is deflected. Eddy-resolving methods are certainly beneficial for a better assessment of detached turbulent flows, which are challenging to study using CFD. This thesis has shown that certainly eddy-resolving simulations are beneficial for the correct assessment of the flow around aircraft VTPs involving flow separation.

The study on a 3D boundary layer separating from a curved backward ramp indicates that, when dealing with separated flows, it is crucial to resolve turbulence to some extent. LES encourages turbulence production and flow-mixing, adjusting the flow features and promoting flow reattachment. This is shown contrasting the RANS results to the hybrid RANS/LES ones, the latter matching the reference highly resolved LES data favourably.

The study of the flow around the VTP was performed for different sideslip angles and two geometry deflection configurations (no rudder deflection and rudder deflected by 30°). Results were compared to wind tunnel measurements. The study was carried out in three steps:

1. study of the whole polar with steady RANS simulations and detection of the critical sideslip angle beyond which the RANS technique could not be converged;
2. study of the separation angle with unsteady RANS simulations, and

3. introduction of eddy-resolving simulations, in the form of Delayed Detached-Eddy Simulations (DDES) to seek improvements in the solution obtained by URANS.

The first step demonstrated that RANS studies perform acceptably until a critical sideslip angle, after which the steady method shows poor convergence. The associated inaccuracy is due to the fact that the flow separates massively on the suction side of the fin. This kind of flow cannot be predicted through steady RANS methods, and this translates into an erroneous prediction of the aerodynamic loads on the VTP.

The introduction of time-accuracy into the CFD method through URANS certainly helps. At high sideslip angles, URANS can detect the presence of a separation line running along almost three-quarters of the length of the fin. Moreover, in the case of a deflected rudder, flow separation is also detected at the hinge line of the VTP. Among the turbulence models used for the study, the Menter-SST has shown the best performance, better than that achieved with more advanced models based on the Reynolds stress closure. However, even though more accuracy was gained in the prediction of the loads on the VTP, locally the pressure distributions left room for improvement.

This improvement was achieved through eddy-resolving simulations, in the form of SST-DDES. This method combines the favourable capabilities of the Menter-SST model to predict flow separation with the necessity to resolve turbulence in the separated flow area. Detached flows over the VTP feature three-dimensional vortical structures, characterised by large rotation and anisotropy, and DDES is capable of capturing these effects. This results in a better prediction of the pressure distribution over the surfaces of the tails, leading to a more trustworthy prediction of the overall aerodynamic loads. Eddy-resolving simulations give much more reliability to the simulation and confidence in the results.

7.2 A strategy for the correct VTP flow assessment

Based on the forgoing discussion, the strategy illustrated in the flowchart in figure 7.1 is suggested. The process starts with the CAD model, which is meshed for RANS simulations. The first cell height of the grid aims at $y^+ = 0.5$. However $y^+ = 1$ would also be acceptable.

The first round of simulations is performed with RANS, and the Menter-SST turbulence model is suggested for the closure of the equations. Since VTP design conditions involve high values of sideslip angles, it is necessary to investigate what happens to the flow field for different values of β . As the sideslip angle increases, it becomes more and more challenging for steady simulations to converge. In fact, from a certain sideslip angle β_c the simulation does not converge, and it is not possible to determine the pressure distribution over the VTP, hence the aerodynamic loading. For $|\beta| < \beta_c$, if the solution is well-converged, it is possible

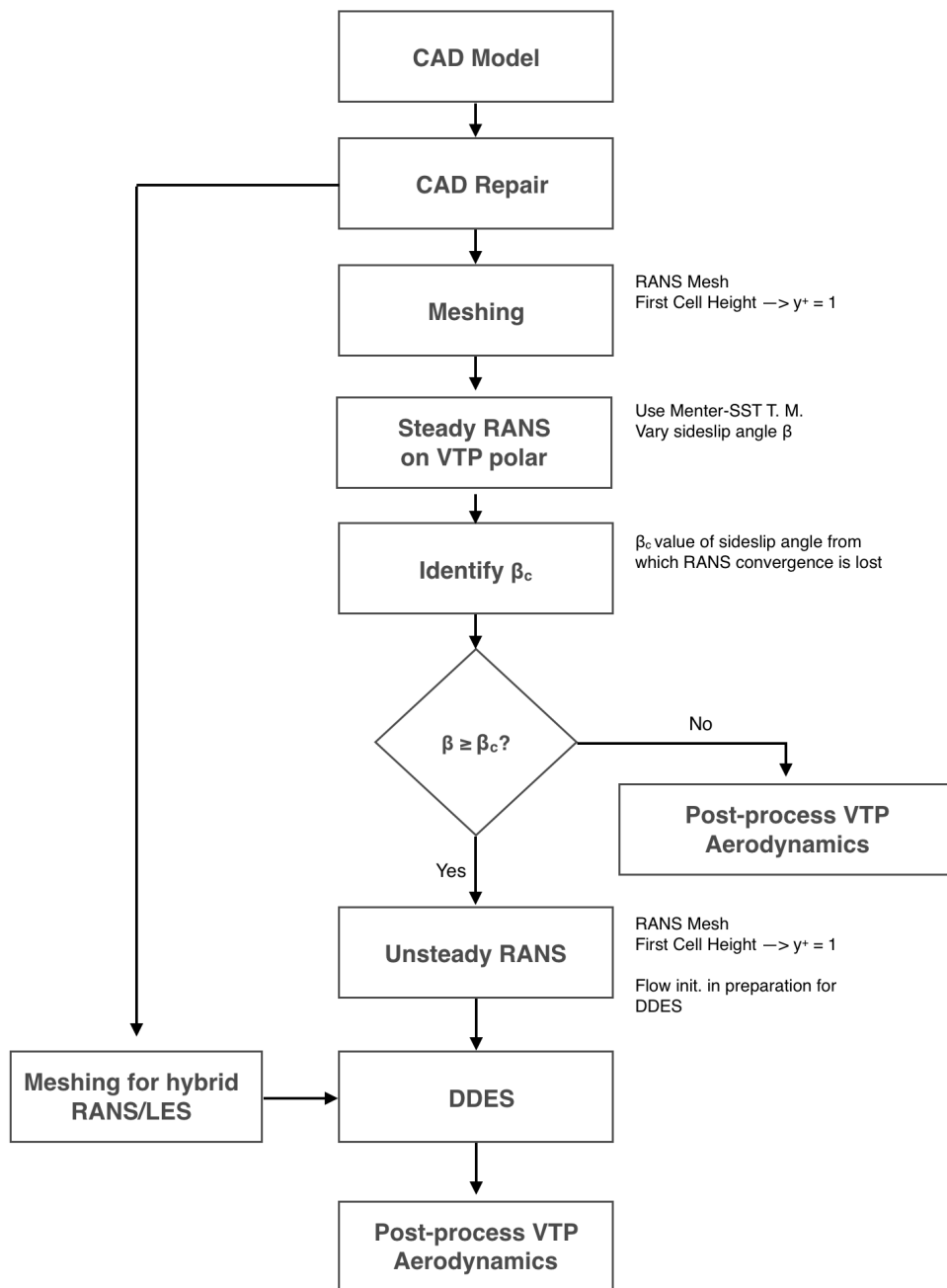


Fig. 7.1 Suggested strategy for VTP flow assessment.

to post-process the results of the simulation and ensure proper aerodynamic design. On the contrary, for $|\beta| \geq \beta_c$ this is not possible, since a non-converged flow solution is physically unacceptable.

For high sideslip angles, an accurate flow solution can be achieved with hybrid RANS/LES methods, in the form of DDES. However, two intermediate steps are necessary before using

DDES. The first consists of using unsteady RANS (URANS) simulations, the second one consists of adapting the mesh for eddy-resolving applications. URANS are restarted from the steady RANS simulation that does not converge (for $\beta = \beta_c$). The unsteady simulations can provide a good sense of the integral length scale of the turbulence, and can define the region in which the flow is separated. This enables us to understand the flow topology on the surface and detect the onset of flow separation.

The grid is refined in the regions where the flow is detached, such as the suction side of the fin and the region around the deflected rudder. This will enable resolution of smaller scales of turbulence, adding more accuracy to the flow solution. In order to save costs on the flow simulation, the mesh can be zonalised, that is, a RANS mesh can be retained over the regions where the flow is attached, whereas a refined grid spacing is encouraged in the detached-flow region. In future work, this can be left to automatic mesh adaptation algorithms that modify the grid density with respect to the flow features.

Finally, the hybrid RANS/LES can be performed. In order to know when to stop the simulation, the flow solution has to be constantly monitored. For example, the evolution of the side-force coefficient (or yaw moment) with time may be an efficient monitor for this simulation. After a transient, the value of the side-force (or yaw moment) should oscillate around a mean value, and the simulation can be stopped after about 150 convective times (1 convective time is the time for free-stream flow to travel one mean chord). Then the flow solution can be post-processed for time averaged and peak quantities, and aerodynamicists can extract all interesting quantities they need to perform the design of a VTP at high sideslip angle.

7.3 Recommendations for future work

Eddy-resolving simulations have been useful for studying the flow around a VTP at high incidence. A DDES method has been used to resolve this challenging flow, providing a solution for a flow that is unpredictable using RANS methods. Therefore, it would be interesting to perform more hybrid RANS/LES applications on this test case, trying different zonalisation methods (Zonal-DES or Improved DDES). It would be worth investigating also high-order methods, which can be able to propagate the large vortices generated on the separation region of the VTP. In fact, there is evidence that higher order schemes can be more accurate for scale-resolving simulations of unsteady turbulent flow, also saving computational time (Vermeire *et al.* [116], Wang *et al.* [120]).

The hybrid RANS/LES switch is controlled by the delay function, which needs improvement in future work. In fact, there are some flow areas in which LES mode is expected, but

the RANS/LES switch is delayed too much. The delay function used in this work relies on Prandtl's mixing length theory, which is not applicable to VTPs boundary layers. For future work, one strategy could be to discard the delay function, and the RANS/LES interface could be explicitly specified in terms of wall distance or fractions of the boundary layer thickness. Moreover, another approach that could be tested in future work could be to adopt the use of a adaptive DES simulations [33].

Furthermore, the aircraft geometry used in this thesis does not include the wing and engine. For future work, performing VTP simulations on a full wing-body-tail model might be effective, in order to study whether the vortex sheet shed off the wing creates disturbance in the tail planes.

This thesis might open new scenarios also for flow separation control studies. Accuracy in the prediction of flow separation over the VTP can certainly reap benefits in the design of devices that suppress flow separation, such as vortex generators.

This thesis seeks to break new boundaries of eddy-resolving simulations concerning aircraft VTP flows, demonstrating their important contribution to the definition of the aerodynamic characteristics of this particular aircraft component. This is one route in which the aviation industry can achieve benefits in aircraft performance and guarantee sustainable and reasonable growth of the aircraft industry.

Appendix A

Reynolds-Averaged Navier-Stokes Equations

A.1 Navier-Stokes Equations

The equations of fluid mechanics are known as Navier-Stokes (NS) equations and are based on three physical principles: conservation of mass, conservation of momentum and conservation of energy.

Navier-Stokes equations can be written in their conservation form, considering a finite control volume fixed in a flow, as in Figure A.1.

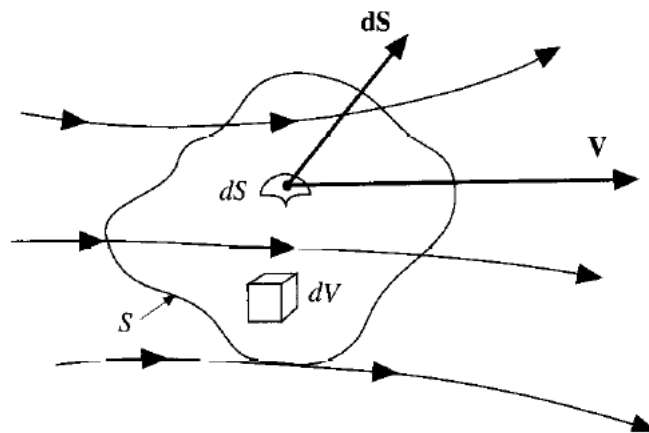


Fig. A.1 Control volume fixed in space, with the fluid flow moving through it [10].

The principle of conservation of mass leads to the continuity equation¹:

$$\frac{\partial \rho}{\partial t} + \nabla \cdot (\rho \mathbf{V}) = 0 \quad (\text{A.1})$$

where ρ is the density of the fluid, $\mathbf{V} = (u, v, w)^T$ is the velocity of the fluid (with its components), and t is the time. The system of reference is a Cartesian system $O(x, y, z)$.

The principle of conservation of momentum is derived from Newton's Second Law. The conservation form is:

$$\frac{\partial(\rho u)}{\partial t} + \nabla \cdot (\rho u \mathbf{V}) = -\frac{\partial p}{\partial x} + \frac{\partial \tau_{xx}}{\partial x} + \frac{\partial \tau_{yx}}{\partial y} + \frac{\partial \tau_{zx}}{\partial z} + \rho f_x \quad (\text{A.2})$$

$$\frac{\partial(\rho v)}{\partial t} + \nabla \cdot (\rho v \mathbf{V}) = -\frac{\partial p}{\partial y} + \frac{\partial \tau_{xy}}{\partial x} + \frac{\partial \tau_{yy}}{\partial y} + \frac{\partial \tau_{zy}}{\partial z} + \rho f_y \quad (\text{A.3})$$

$$\frac{\partial(\rho w)}{\partial t} + \nabla \cdot (\rho w \mathbf{V}) = -\frac{\partial p}{\partial z} + \frac{\partial \tau_{xz}}{\partial x} + \frac{\partial \tau_{yz}}{\partial y} + \frac{\partial \tau_{zz}}{\partial z} + \rho f_z \quad (\text{A.4})$$

where f_x , f_y and f_z are the components of a body force \mathbf{f} acting on the control volume per unit of mass (for example, due to gravity)², τ_{ij} are normal stresses when $i = j$ (related to the rate of change of the control volume), and τ_{ij} are shear stresses when $i \neq j$ (related to the time rate of change of the shearing deformation). For these stresses, Stokes obtains:

$$\tau_{xx} = \lambda \nabla \cdot \mathbf{V} + 2\mu \frac{\partial u}{\partial x} \quad (\text{A.5})$$

$$\tau_{yy} = \lambda \nabla \cdot \mathbf{V} + 2\mu \frac{\partial v}{\partial y} \quad (\text{A.6})$$

$$\tau_{zz} = \lambda \nabla \cdot \mathbf{V} + 2\mu \frac{\partial w}{\partial z} \quad (\text{A.7})$$

$$\tau_{xy} = \tau_{yx} = \mu \left(\frac{\partial v}{\partial x} + \frac{\partial u}{\partial y} \right) \quad (\text{A.8})$$

$$\tau_{xz} = \tau_{zx} = \mu \left(\frac{\partial u}{\partial z} + \frac{\partial w}{\partial x} \right) \quad (\text{A.9})$$

$$\tau_{yz} = \tau_{zy} = \mu \left(\frac{\partial w}{\partial y} + \frac{\partial v}{\partial z} \right). \quad (\text{A.10})$$

¹See Anderson [10] for the demonstration of NS equations.

²Body forces \mathbf{f} are neglected in all the work reported here.

The quantity μ is the molecular viscosity, which is a property of the fluid. It is strongly dependent upon temperature which can be represented using Sutherland's Law:

$$\mu = \mu_{ref} \left(\frac{T}{T_{ref}} \right)^{3/2} \frac{T_{ref} + S}{T + S} \quad (\text{A.11})$$

where T is the temperature of the fluid with viscosity μ , T_{ref} is the viscosity of a reference flow with viscosity μ_{ref} , and $S = 110.4$ K is a constant. The coefficient λ represents the bulk viscosity and is assumed to be equal to:

$$\lambda = -\frac{2}{3}\mu. \quad (\text{A.12})$$

The First Law of Thermodynamics applied to a fluid passing through a control volume yields the following form (neglecting the body forces):

$$\begin{aligned} \frac{\partial E_t}{\partial t} - \frac{\partial Q}{\partial t} + \frac{\partial}{\partial x} (E_t u + pu - u\tau_{xx} - v\tau_{xy} - w\tau_{xz} + q_x) \\ + \frac{\partial}{\partial y} (E_t v + pv - u\tau_{xy} - v\tau_{yy} - w\tau_{yz} + q_y) \\ + \frac{\partial}{\partial z} (E_t w + pw - u\tau_{xz} - v\tau_{yz} - w\tau_{zz} + q_z) = 0, \end{aligned} \quad (\text{A.13})$$

where:

$$E_t = \rho \left(e + \frac{V^2}{2} \right) \quad (\text{A.14})$$

is the total energy per unit volume and e is the internal energy. Q is the heat produced per unit volume by external agencies, and q is the rate of heat lost by conduction per unit of volume through the control surfaces given by Fourier's Law:

$$q_i = -k \frac{\partial T}{\partial x_i}, \quad (\text{A.15})$$

where k is the coefficient of thermal conductivity and T is the temperature.

Finally, to complete the set of equations, the equation of state that allows p to be calculated is needed:

$$p = (\gamma - 1) \rho \left(E_t - \frac{V^2}{2} \right). \quad (\text{A.16})$$

A.2 The Reynolds equations

Most aerospace flows are turbulent and one characteristic of turbulent flows is the randomness of the properties of the flow. Reynolds introduced a decomposition that enables superimposition of fluctuations of the flow variables until their steady state. Considering a generic quantity f , its time-average is defined as [81]:

$$\bar{f} = \frac{1}{\Delta t} \int_{t_0}^{t_0 + \Delta t} f dt, \quad (\text{A.17})$$

with Δt large compared to the period of the random fluctuations. In the conventional Reynolds decomposition, the flow variables are replaced by their time-averages plus the fluctuations:

$$f = \bar{f} + f'. \quad (\text{A.18})$$

For example, for the x-component of the velocity:

$$u = \bar{u} + u' \quad (\text{A.19})$$

A visual representation of the Reynolds decomposition for the x-component of the velocity can be seen in Figure A.2.

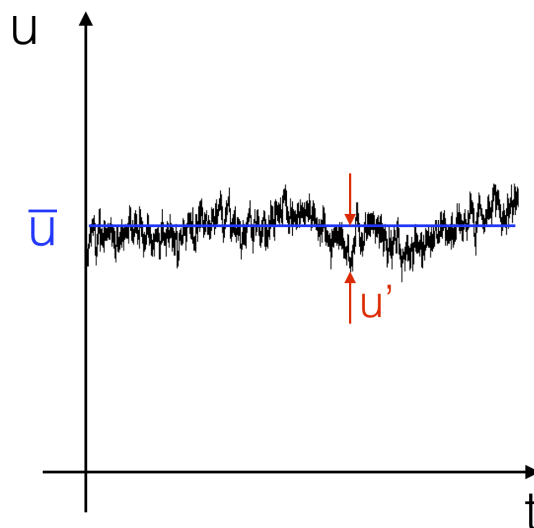


Fig. A.2 Reynolds decomposition.

The time-average of the fluctuations is zero:

$$\overline{f'} = \frac{1}{\Delta t} \int_{t_0}^{t_0+\Delta T} f' dt = 0 \quad (\text{A.20})$$

and the following relations hold:

$$\overline{\overline{f}g'} = 0, \quad (\text{A.21})$$

$$\overline{\overline{f}g} = \overline{f}\overline{g}, \quad (\text{A.22})$$

$$\overline{\overline{f+g}} = \overline{f} + \overline{g}. \quad (\text{A.23})$$

Usually, compressible flows are treated with the mass-weighted, or Favre, averaging procedure³:

$$\tilde{l} = \frac{\overline{\rho l}}{\overline{\rho}} \quad (\text{A.24})$$

where l stands for the velocity components and thermal variables (fluid properties such as pressure and density are not averaged). With this definition, new fluctuating quantities are defined by the Favre decomposition:

$$l = \tilde{l} + l''. \quad (\text{A.25})$$

For example, for the x-component of the velocity, the decomposition is:

$$u = \tilde{u} + u''. \quad (\text{A.26})$$

It is important to note that the time-averages of the fluctuating quantities $\overline{l''}$ are not zero (unless $\rho' = 0$). Rather, the time-average of the Favre fluctuations multiplied by the density is equal to zero:

$$\overline{\rho l''} = 0. \quad (\text{A.27})$$

A.2.1 The continuity equation in Reynolds form

Substituting the Reynolds decomposition A.19 in the continuity equation A.1 and time-averaging the equation, in tensor notation the continuity equation becomes:

$$\frac{\partial \overline{\rho}}{\partial t} + \frac{\partial}{\partial x_j} \left(\overline{\rho u_j} + \overline{\rho' u'_j} \right) = 0. \quad (\text{A.28})$$

³TAU, the CFD solver used for this project, uses RANS equations in Favre form.

The same equation written in Favre form is:

$$\frac{\partial \bar{\rho}}{\partial t} + \frac{\partial}{\partial x_j} (\bar{\rho} \tilde{u}_j) = 0. \quad (\text{A.29})$$

A.2.2 Momentum equations in Reynolds form

To obtain the RANS equations, the Reynolds decomposition and the time average are applied to the momentum equations A.2, A.3, and A.4, obtaining:

$$\frac{\partial}{\partial t} (\bar{\rho} \bar{u}_i + \overline{\rho' u'_i}) + \frac{\partial}{\partial x_j} (\bar{\rho} \bar{u}_i \bar{u}_j + \bar{u}_i \overline{\rho' u'_j}) = -\frac{\partial \bar{p}}{\partial x_i} + \frac{\partial}{\partial x_j} (\bar{\tau}_{ij} - \bar{u}_j \overline{\rho' u'_i} - \overline{\rho u'_i u'_j} - \overline{\rho' u'_i u'_j}). \quad (\text{A.30})$$

The Favre form of the averaged momentum equations is:

$$\frac{\partial}{\partial t} (\bar{\rho} \tilde{u}_i) + \frac{\partial}{\partial x_j} (\bar{\rho} \tilde{u}_i \tilde{u}_j) = -\frac{\partial \bar{p}}{\partial x_i} (\bar{\tau}_{ij} - \overline{\rho u'_i u'_j}) \quad (\text{A.31})$$

Comparing the Navier-Stokes equations with equations A.30 and A.31, apart from the observation that now the averaged quantities appear, we notice that some ‘apparent’ stresses $-\overline{\rho u'_i u'_j}$ or $-\overline{\rho u'_i u'_j}$ arise. They are called ‘Reynolds-stresses’ and are due to the fluctuating contribution (i.e. the turbulence) of the velocity of the flow.

A.2.3 The energy equation in Reynolds form

Using the total enthalpy H given by:

$$H = E_t + \frac{p}{\rho} \quad (\text{A.32})$$

and neglecting $\partial Q/\partial t$, equation A.13 can be re-written as:

$$\frac{\partial}{\partial t} \rho H + \frac{\partial}{\partial x_j} (\rho u_j H + q_j - u_i \tau_{ij}) = \frac{\partial p}{\partial t}. \quad (\text{A.33})$$

The Favre form of this equation⁴ is:

$$\frac{\partial}{\partial t} (\bar{\rho} \tilde{H}) + \frac{\partial}{\partial x_j} \left(\bar{\rho} \tilde{u}_j \tilde{H} + \overline{\rho u'_j H''} - k \frac{\partial \bar{T}}{\partial x_j} \right) = \frac{\partial \bar{p}}{\partial t} + \frac{\partial}{\partial x_j} (\tilde{u}_j \bar{\tau}_{ij} + \overline{u'_i \tau_{ij}}), \quad (\text{A.34})$$

in which the heat conduction law, equation A.15, has been used.

⁴The Reynolds form is not reported for the energy equation

A.3 The problem of the closure

Reynold-averaging the NS equations leads to have a system in which the number of unknowns is larger than the number of equations. Therefore, it is necessary to find a closure for the system of equations. There are two possible ways for achieving this. One consists of adopting the Boussinesq assumption [15], which reads:

$$-\overline{\rho u_i'' u_j''} = \mu_t \left(\frac{\partial \bar{u}_i}{\partial x_j} + \frac{\partial \bar{u}_j}{\partial x_i} - \frac{2}{3} \delta_{ij} \frac{\partial \bar{u}_k}{\partial x_k} \right) - \frac{2}{3} \delta_{ij} \bar{\rho} k \quad (\text{A.35})$$

where μ_t is the turbulent viscosity, and k is the turbulent kinetic energy. This assumption expresses the turbulent stresses as linear functions of mean flow gradients, therefore it is used in linear eddy-viscosity turbulence models.

The other way to close the RANS equations consists of using a Reynolds-Stress Transport model. In this case, transport equations are written for each of the turbulent Reynolds stresses, as explained in Appendix B.

A.4 Filtering the equation for Large-Eddy simulations

A turbulent flow is characterized by structures having different length scales, called *eddies* (or vortices). Physics drives the phenomenon of energy cascades, letting big vortices produce smaller and smaller eddies, which would eventually dissipate in thermal energy. Eddy-resolving techniques provide a numerical resolution of some eddies of the flow, which is different from turbulence modelling, which instead *models* the behaviour of the turbulent flow. With Large-Eddy Simulations, the larger 3D turbulent eddies are directly resolved, whereas the smaller scales are modelled.

The velocity field \mathbf{V} is decomposed into the sum of a *filtered* component $\widehat{\mathbf{V}}$ and a subgrid scale (SGS) component \mathbf{v}' . The former represents the motion of the largest eddies and is resolved, whilst the latter is modelled. Since:

$$\mathbf{V} = \widehat{\mathbf{V}} + \mathbf{v}', \quad (\text{A.36})$$

this process is analytically identical to that of Reynolds-averaging. Therefore, the incompressible filtered equations can be written as:

$$\frac{\widehat{D}(\widehat{u}_j)}{\widehat{D}t} = \frac{\partial}{\partial x_j} \left[\mu \left(\frac{\partial \widehat{u}_i}{\partial x_j} + \frac{\partial \widehat{u}_j}{\partial x_i} \right) - \frac{\widehat{p}}{\rho} \delta_{ij} - \tau_{ij} \right] \quad (\text{A.37})$$

where $\widehat{\cdot}$ represents a filtered variable, and:

$$\frac{\widehat{D}(\widehat{V}_j)}{\widehat{D}t} = \frac{\partial}{\partial t} + \widehat{\mathbf{V}} \cdot \nabla \quad (\text{A.38})$$

$$\tau_{ij} = \widehat{u_i u_j} - \widehat{u}_i \widehat{u}_j. \quad (\text{A.39})$$

Also, in this case a sort of modelling is needed to close the equations and solve the quantity $\widehat{u_i u_j}$, and a subgrid scale model (SGS) is required. However, in this thesis quasi-DNS-type simulations are performed over a backward ramp using a highly modified version of HYDRA [27], and no SGS models are used. Here the numerical dissipation does the job that a an SGS model would do. To ensure stability, a minimal smoothing is added to the numerical equations.

Appendix B

Turbulence models

In the thesis, the following turbulence models have been used:

- Spalart-Allmaras (SA) model;
- Menter-SST model, and
- SSG/LRR- ω model.

B.1 The Spalart-Allmaras turbulence model

The Spalart-Allmaras model [95] is a one-equation model which defines eddy-viscosity as:

$$\nu_t = \tilde{\nu} f_{v1}, \quad (\text{B.1})$$

with $f_{v1} = \frac{\chi^3}{\chi^3 + C_{v1}^3}$, and $\chi = \frac{\tilde{\nu}}{\nu}$. $\tilde{\nu}$ is called Spalart-Allmaras, and its transport equation reads:

$$\frac{\partial \tilde{\nu}}{\partial t} + u_j \frac{\partial \tilde{\nu}}{\partial x_j} = C_{b1} [1 - f_{t2}] \tilde{S} \tilde{\nu} + \frac{1}{\sigma} \{ \nabla \cdot [(\mathbf{v} + \tilde{\nu}) \nabla \tilde{\nu}] + C_{b2} |\nabla \mathbf{v}|^2 \} - \left[C_{w1} f_w - \frac{C_{b1}}{\kappa^2} f_{t2} \right] \left(\frac{\tilde{\nu}}{d} \right)^2 + f_{t1} \Delta U^2 \quad (\text{B.2})$$

with:

$$\tilde{S} \equiv S + \frac{\tilde{\nu}}{\kappa^2 d^2} f_{v2},$$

$$f_{v2} = 1 - \frac{\chi}{1 + \chi f_{v1}},$$

$$f_w = g \left[\frac{1 + C_{w3}^6}{g^6 + C_{w3}^6} \right]^{1/6},$$

$$g = r + C_{w2} (r^6 - r),$$

$$r \equiv \frac{\tilde{\nu}}{S \kappa^2 d^2},$$

$$f_{t1} = C_{t1} g_t \exp \left(-C_{t2} \frac{\omega_t^2}{\Delta U^2} [d^2 + g_t^2 d_t^2] \right),$$

$$f_{t2} = C_{t3} \exp(-C_{t4} \chi^2),$$

$$S = \sqrt{2\Omega_{ij}\Omega_{ij}},$$

where d is the distance from the closest surface and ΔU^2 is the norm of the difference between the velocity at the trip (usually zero) and that at the field point we are considering. The constants are reported in Table B.1.

Table B.1 Constants for the SA turbulence model.

σ	C_{b1}	C_{b2}	κ	C_{w1}	C_{w2}	C_{w3}	C_{v1}	C_{t1}	C_{t2}	C_{t3}	C_{t4}
0.667	0.1355	0.622	0.41	1.0764	0.3	2	7.1	1	2	1.1	2

B.2 The Menter-SST turbulence model

Menter's Shear-Stress Transport model combines Wilcox's $k - \omega$ turbulence model with the $k - \varepsilon$ model, with the additional ability to account for the transport of the shear stress in adverse pressure gradient boundary layers, which exist in the flows examined in this thesis. The model is based on the assumption that the shear-stress is proportional to the turbulent kinetic energy, which is introduced in the definition of eddy-viscosity.

In its conservation form, the two-equation turbulence model is written as:

$$\frac{D(\rho k)}{Dt} = \tau_{ij} \frac{\partial u_i}{\partial x_j} - \beta^* \rho \omega k + \frac{\partial}{\partial x_j} \left[(\mu + \sigma_k \mu_t) \frac{\partial k}{\partial x_j} \right] \quad (\text{B.3})$$

$$\frac{D(\rho \omega)}{Dt} = \frac{\gamma}{\mu_t} \tau_{ij} \frac{\partial u_i}{\partial x_j} - \beta \rho \omega^2 + \frac{\partial}{\partial x_j} \left[(\mu + \sigma_\omega \mu_t) \frac{\partial \omega}{\partial x_j} \right] + 2(1 - F_1) \frac{\rho \sigma_{\omega 2}}{\omega} \frac{\partial k}{\partial x_j} \frac{\partial \omega}{\partial x_j} \quad (\text{B.4})$$

with:

$$\tau_{ij} = \mu_t \left(2S_{ij} - \frac{2}{3} \frac{\partial u_k}{\partial x_k} \right) - \frac{2}{3} k \delta_{ij}. \quad (\text{B.5})$$

Two sets of constants are valid for the two blended models:

- Set 1 (SST-inner):

$$\sigma_{k1} = 0.85, \sigma_{\omega 1} = 0.5, \beta_1 = 0.075, a_1 = 0.31,$$

$$\beta^* = 0.09, \kappa = 0.41, \gamma_1 = \beta_1 / \beta^* - \sigma_{\omega 1} k^2 / \sqrt{\beta^*}, \text{ and}$$

- Set 2 (standard $k - \varepsilon$ constants):

$$\sigma_{k2} = 1.0, \sigma_{\omega 2} = 0.856, \beta_2 = 0.0828,$$

$$\beta^* = 0.09, \kappa = 0.41, \gamma_2 = \beta_2 / \beta^* - \sigma_{\omega 2} k^2 / \sqrt{\beta^*}.$$

Then the resultant constants of the SST model are given by the blending of the two sets of constants. Being ϕ_1 and ϕ_2 two generic constants of set 1 and set 2 respectively, the blended constant ϕ is given by:

$$\phi = F_1 \phi_1 + (1 - F_1) \phi_2. \quad (\text{B.6})$$

The function F_1 is calculated as follows:

$$F_1 = \tanh(\arg_1^4) \quad (\text{B.7})$$

with:

$$\arg_1 = \min \left[\max \left(\frac{\sqrt{k}}{\beta^* \omega y}, \frac{500\nu}{y^2 \omega} \right), \frac{4\rho\sigma_{\omega 2} k}{\text{CD}_{k\omega} y^2} \right] \quad (\text{B.8})$$

where y is the distance to the next surface and

$$\text{CD}_{k\omega} = \max \left(2\rho\sigma_{\omega 2} \frac{1}{\omega} \frac{\partial k}{\partial x_j} \frac{\partial \omega}{\partial x_j}, 10^{-20} \right) \quad (\text{B.9})$$

is the cross-diffusion term.

The turbulent eddy-viscosity is computed from¹:

$$\mu_t = \frac{\rho a_1 k}{\max(a_1 \omega, \Omega F_2)} \quad (\text{B.10})$$

where Ω is the absolute value of the vorticity given by $\Omega = \sqrt{2W_{ij}W_{ij}}$, W_{ij} , with

$$W_{ij} = \frac{1}{2} \left(\frac{\partial u_i}{\partial x_j} - \frac{\partial u_j}{\partial x_i} \right). \quad (\text{B.11})$$

and the function F_2 is defined as

$$F_2 = \tanh(\arg_2^2) \quad (\text{B.12})$$

with

$$\arg_2 = \max \left(2 \frac{\sqrt{k}}{\beta^* \omega y}, \frac{500\nu}{y^2 \omega} \right) \quad (\text{B.13})$$

If L is the approximate length of the computational domain, the boundary conditions recommended by Menter are:

$$\frac{U_\infty}{L} < w_{\text{farfield}} < 10 \frac{U_\infty}{L} \quad (\text{B.14})$$

¹Unlike the BSL model [81]

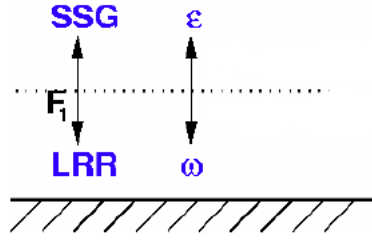


Fig. B.1 SSG/LRR- ω Reynolds stress scheme.

$$\mu_{\text{farfield}} = 10^{-3} \mu \quad (\text{B.15})$$

$$k_{\text{farfield}} = \mu_{\text{farfield}} \cdot w_{\text{farfield}} \quad (\text{B.16})$$

B.3 The SSG/LRR- ω turbulence model

The SSG/LRR- ω turbulence model is a Reynolds Stress Model that combines the LRR model [59] near the walls with the SSG model [102] in the farfield (Figure B.1). Both models are recast to use ω as the dissipation variable. The LRR- ω form was proposed by Wilcox as the stress- ω model. The combination of this with SSG- ω was an outcome of the European FLOMANIA project (Eisfeld [36]). The interchangeability between the two models is realized thanks to a blending function F_1 .

Adopting tensor notation, the Reynolds stresses can be written as:

$$\bar{\rho} \hat{R}_{ij} = -\tau_{ij} = \overline{\rho u'_i u'_j}, \quad (\text{B.17})$$

the Reynolds stress transport equation is:

$$\frac{\partial \bar{\rho} \hat{R}_{ij}}{\partial t} + \frac{\partial (\bar{\rho} \hat{R}_{ij} \hat{u}_k)}{\partial x_k} = \bar{\rho} P_{ij} + \bar{\rho} \Pi_{ij} - \bar{\rho} \epsilon_{ij} + \bar{\rho} D_{ij} + \bar{\rho} M_{ij}. \quad (\text{B.18})$$

The ω -equation in Menter's baseline form is:

$$\frac{\partial \bar{\rho} \omega}{\partial t} + \frac{\partial (\bar{\rho} u_k \omega)}{\partial x_k} = \frac{\alpha_\omega \omega}{\hat{k}} \bar{\rho} \frac{P_{kk}}{2} - \beta_\omega \bar{\rho} \omega^2 + \frac{\partial}{\partial x_k} \left[\left(\bar{\mu} + \sigma_\omega \bar{\rho} \frac{\hat{k}}{\omega} \right) \frac{\partial \omega}{\partial x_k} \right] + \sigma_d \frac{\bar{\rho}}{\omega} \max \left(\frac{\partial \hat{k}}{\partial x_j} \frac{\partial \omega}{\partial x_j}; 0 \right). \quad (\text{B.19})$$

On the right-hand side of equation B.18, the following terms appear:

- Production term, which is exact and does not need to be modelled:

$$\overline{\rho}P_{ij} = -\overline{\rho}\hat{R}_{ij}\frac{\partial\hat{u}_j}{\partial x_k} - \overline{\rho}\hat{R}_{jk}\frac{\partial\hat{u}_i}{\partial x_k}. \quad (\text{B.20})$$

- Dissipation term, modelled via:

$$\overline{\rho}\varepsilon_{ij} = \frac{2}{3}\rho\varepsilon\delta_{ij} \quad (\text{B.21})$$

with $\varepsilon = C_\mu\hat{k}\omega$, $C_\mu = 0.09$ and turbulent energy $\hat{k} = \hat{R}_{ii}/2$.

- Pressure-strain term, which reads:

$$\Pi_{ij} = \overline{\frac{p}{\rho} \left(\frac{\partial u''_i}{\partial x_j} + \frac{\partial u''_j}{\partial x_i} \right)}. \quad (\text{B.22})$$

This term is modelled as:

$$\begin{aligned} \overline{\rho}\Pi_{ij} = & - \left(C_1\overline{\rho}\varepsilon + \frac{1}{2}C_1^*\overline{\rho}P_{kk} \right) \hat{a}_{ij} + C_2\overline{\rho}\varepsilon \left(\hat{a}_{ik}\hat{a}_{kj} - \frac{1}{3}\hat{a}_{kl}\hat{a}_{kl}\delta_{ij} \right) \\ & + \left(C_3 - C_3^*\sqrt{\hat{a}_{kl}\hat{a}_{kl}} \right) \overline{\rho}\hat{k}S_{ij}^* + C_4\overline{\rho}\hat{k} \left(\hat{a}_{ik}\hat{S}_{jk} + \hat{a}_{jk}\hat{S}_{ik} - \frac{2}{3}\alpha_{kl}\hat{S}_{kl}\delta_{ij} \right) \\ & + C_5\overline{\rho}\hat{k} \left(\hat{a}_{ik}\hat{W}_{jk} + \hat{a}_{jk}\hat{W}_{ik} \right), \end{aligned} \quad (\text{B.23})$$

with:

$$\hat{a}_{ij} = \frac{\hat{R}_{ij}}{\hat{k}} - \frac{2}{3}\delta_{ij} \quad (\text{B.24})$$

$$\hat{S}_{ij} = \frac{1}{2} \left(\frac{\partial\hat{u}_i}{\partial x_j} + \frac{\partial\hat{u}_j}{\partial x_i} \right) \quad (\text{B.25})$$

$$S_{ij}^* = \hat{S}_{ij} - \frac{1}{3}\hat{S}_{kk}\delta_{ij} \quad (\text{B.26})$$

$$\hat{W}_{ij} = \frac{1}{2} \left(\frac{\partial\hat{u}_i}{\partial x_j} - \frac{\partial\hat{u}_j}{\partial x_i} \right). \quad (\text{B.27})$$

- Diffusion term, modelled as:

$$\overline{\rho}D_{ij} = \frac{\partial}{\partial x_k} \left[\left(\overline{\mu}\delta_{kl} + D\frac{\overline{\rho}\hat{k}\hat{R}_{kl}}{\varepsilon} \right) \frac{\partial\hat{R}_{ij}}{\partial x_l} \right]. \quad (\text{B.28})$$

- Fluctuating mass term $\overline{\rho}M_{ij}$, which is neglected.

All the coefficients are blended via the function F_1

$$\phi = F_1 \phi^{(LRR)} + (1 - F_1) \phi^{(SSG)}, \quad (\text{B.29})$$

where:

$$F_1 = \tanh(\zeta^4) \quad (\text{B.30})$$

$$\zeta = \min \left[\max \left(\frac{\sqrt{\hat{k}}}{C_\mu \omega d}; \frac{500 \hat{\mu}}{\bar{\rho} \omega d^2} \right); \frac{4 \sigma_\omega^{(\varepsilon)} \bar{\rho} \hat{k}}{C_D d^2} \right] \quad (\text{B.31})$$

$$C_D = \sigma_d^{(\varepsilon)} \frac{\rho}{\omega} \max \left(\frac{\partial \hat{k}}{\partial x_k} \frac{\partial \omega}{\partial x_k}; 0 \right). \quad (\text{B.32})$$

The constants are reported in Table B.2, where the superscripts (ω) or (ε) are omitted.

Table B.2 Constants for the SSG/LRR- ω RSM turbulence model ($C_2^{(LRR)} = 0.5556$).

	α_ω	β_ω	σ_ω	σ_d	C_1	C_1^*	C_2	C_3	C_3^*
LRR	0.556	0.075	0.5	0	1.8	0	0	0.8	0
SSG	0.44	0.0828	0.856	1.712	1.7	0.9	1.05	0.8	0.65
	C_4			C_5			D		
LRR	$0.5(18C_2^{(LRR)} + 12)/11$			$0.5(-14C_2^{(LRR)} + 20)/11$			$0.75C_\mu$		
SSG	0.625			0.2			0.22		

To set up the boundary conditions, the following equations are used:

- for the farfield (f.f.):

$$\hat{R}_{ij,f.f.} = \frac{2}{3} \hat{k}_{f.f.} \delta_{ij} \quad (\text{B.33})$$

$$\omega_{f.f.} = \frac{\bar{\rho} \hat{k}_{f.f.}}{\mu_{t,f.f.}} \quad (\text{B.34})$$

where $\hat{k}_{f.f.}$ and farfield turbulent viscosity $\mu_{t,f.f.}$ are set by the user:

- for the solid walls:

$$\hat{R}_{ij,wall} = 0 \quad (\text{B.35})$$

$$\omega_{wall} = 10 \frac{6\hat{\nu}}{\beta_\omega^{(\omega)} (\Delta d_1)^2} \quad (\text{B.36})$$

where (Δd_1) is the first cell height. The wall dissipation ω_{wall} is theoretically infinite; in the model its value is considered equal to 10 times the theoretical value at the first node off the wall.

Appendix C

Validation of LES on the backward ramp without crossflow

The incompressible version of HYDRA used in this thesis was validated by previous studies by Cui [27], and in Chapter 3 the HDT case has been illustrated. The purpose of this section is to demonstrate that the highly-resolved LES performed in this thesis has been set up correctly, and LES results are reliable. To achieve this, a simulation has been carried out on the test case run by Bentaleb *et al.* [13]. The test case consists of the same geometry described in Chapter 4, but the streamlines are not skewed by the presence of a crossflow. Hence the forcing term $f_{z,i}(x)$ is set to zero.

A turbulent boundary layer enters the channel and develops on the lower and upper walls. On the lower wall, the flow reaches a backward rounded ramp at $x/H = 0$, and separates and reattaches along the ramp. Table C.1 reports the locations of flow separation and reattachment calculated by the current LES. Results are compared against the analogous simulation by Bentaleb *et al.* [13] and the experiment by Zhang and Zhong [126]. The current LES predicts that the flow separates at $x/H = 0.83$, in agreement with the Bentaleb's results, and with 2% error with respect to the experiment. The recirculation bubble extends all over the ramp, and the boundary layer reattaches at $x/H = 4.0$. The reattachment location is very indistinct and intermittent. In fact, Bentaleb finds the reattachment point at $x/H = 4.36$, whereas Zhang and Zhong observe that reattachment occurs at $x/H = 4.15$. Overall, the length of the recirculation area calculated by the current LES differs by only 4% from the experimental results.

Figure C.1 shows the pressure coefficient distribution calculated along the ramp. The current LES and Bentaleb's study show a particular sensitivity of the wall pressure in the recirculation region, with a 5% difference between the two simulations.

Table C.1 Comparison of separation and reattachment locations.

	Current LES	Bentaleb <i>et al.</i> [13]	Zhang & Zhong [126]
x/H separation	0.83	0.83	0.85
x/H reattachment	4.0	4.36	4.15
L_{sep}	3.17	3.53	3.3

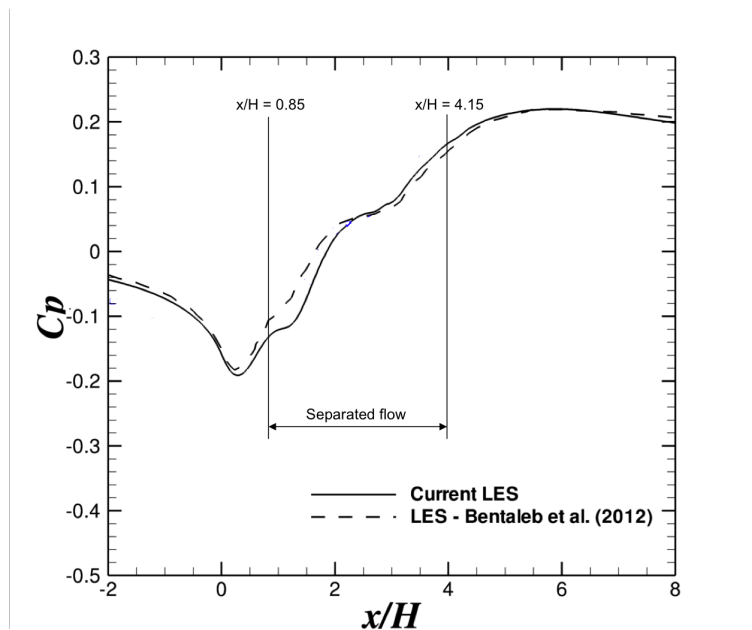
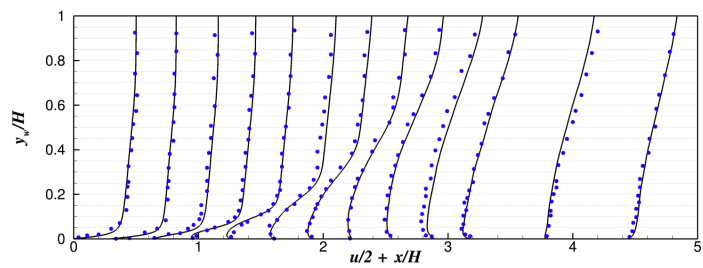


Fig. C.1 Pressure coefficient C_p obtained by LES without crossflow and comparison with reference data by Bentaleb *et al.*[13].

Looking at flow features in more detail, Figure C.2 compares the computation of the velocity, shear-stress and streamwise Reynolds stress profiles with experiment. Data is time-averaged and span-averaged¹. The y -axis represents the y_w coordinate, defined as $y_w = y - y_{wall}$. The curves compare favourably with the experimental observations, and the reversed flow in the separation region is well-captured. In the separation region, the shear-stress is slightly over-estimated by the LES by up to 5%, whereas the Reynolds stresses are under-estimated by about 7% next to the reattachment point.

Figure C.3 compares the velocity profiles and Reynolds stress profiles obtained by the current simulation and Bentaleb's one. The solid line represents the result obtained in this thesis. Figures C.3a and C.3b show profiles of mean streamwise velocity and normal-wall velocity respectively. There are only minor differences with respect to the reference data, therefore the mean flow topology is the same. The Reynolds stresses for this flow are plotted

¹The span-averaged data is the average of data in z -direction, i.e. along the span of the duct.



(a) Mean U velocity (x-direction).

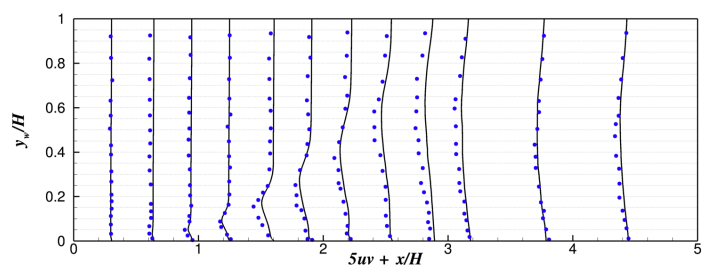
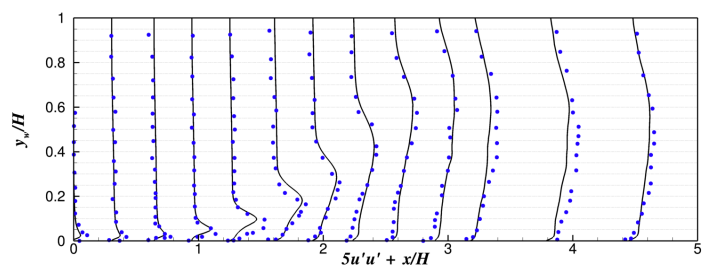
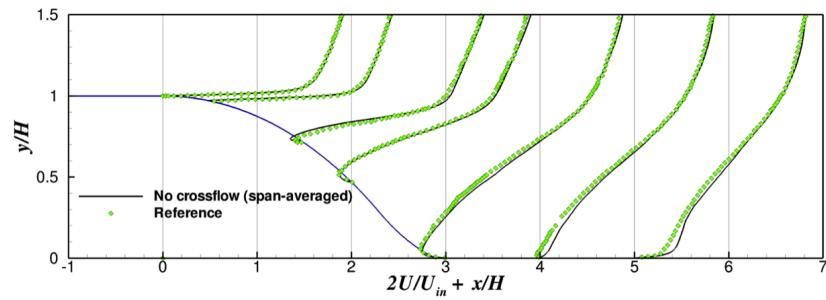
(b) Mean shear-stress uv .(c) Mean $u'u'$

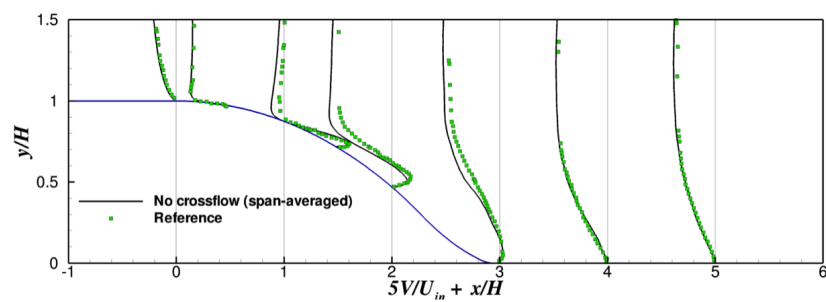
Fig. C.2 Velocity, shear-stress, and streamwise Reynolds stress profiles obtained by the current LES (solid lines) and comparison with experimental data by Zhang and Zhong [126] (circles).

in figures C.3c and C.3d. The former shows the normal stresses $\overline{u'u'}$, whereas the latter plots the shear stress $\overline{u'v'}$. Overall, agreement with the reference data is good, with only small differences within the separation region, at $x/H = 2$.

In conclusion, the results shown in this section demonstrate that the LES method used in this thesis is reliable. Overall the results compare favourably against the experimental observations for the scope of this study. Moreover, more confidence is given by the fact that the solver used hereby is able to replicate the same simulation reported performed by Bentaleb *et al.* [13].



(a) Mean U velocity (x-direction).



(b) Mean V velocity (y-direction).

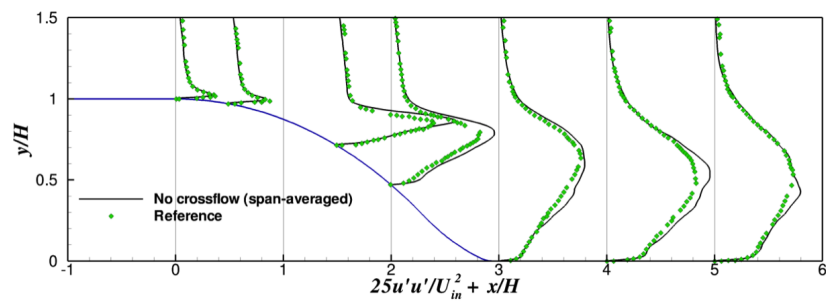
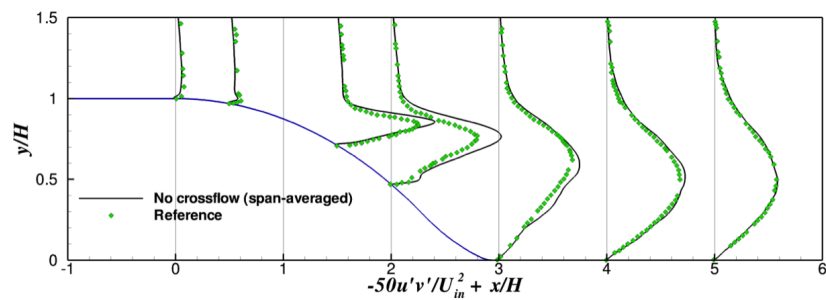
(c) Mean $u'u'$ (d) Mean $u'v'$

Fig. C.3 Velocity and Reynolds stress profiles obtained by LES without crossflow and comparison with reference data by Bentaleb *et al.*[13].

Appendix D

Grid convergence studies

To trust the RANS results obtained in the thesis, it is necessary to perform grid convergence studies on the meshes that has been used. Ideally, the results obtained on the two meshes should be the same. This section shows grid convergence studies on the backward ramp and on the VTP model used in the thesis.

D.1 Backward rounded step

The mesh of the backward rounded step is refined as shown in Table D.1. The total number of grid points is about 8 times the original mesh.

Table D.1 Backward rounded ramp grids comparison (no. of grid points).

	<i>x</i> -direction	<i>y</i> -direction	<i>z</i> -direction
Baseline RANS mesh	195	160	20
Refined RANS mesh	322	430	40

The flow-averaged solution obtained on the refined grid is plotted in Figure D.1, which shows a section of the backward ramp on the longitudinal plane with u velocity contours and streamlines. The results on the refined mesh are equivalent to those obtained on the baseline grid. In fact, even if the number of grid points has doubled in each direction, RANS is not capable to capture the separation and reattachment locations (for the same reasons explained in Chapter 4), with about 30% error with respect to the benchmark LES.

Finally, a comparison of the flow velocity profiles obtained on the two meshes is plotted in Figure D.2. The figures plot RANS results obtained with the Menter-SST turbulence model, in comparison with LES results. Despite small differences between the results on the baseline and the refined meshes, it is evident that, even though a grid refinement is performed,

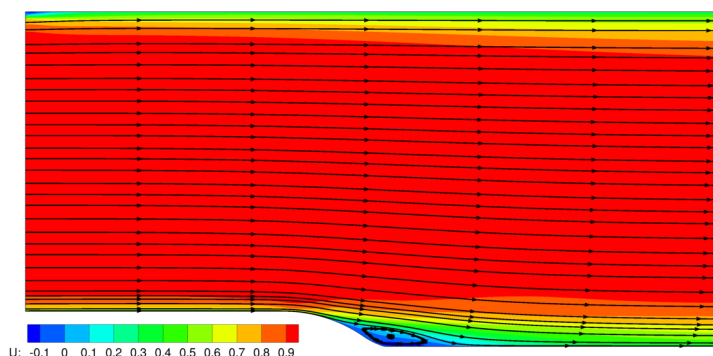


Fig. D.1 Grid independence study on RANS mesh for the backward rounded ramp. u velocity contours and streamlines.

the velocity profiles obtained by RANS are still far from the LES ones, especially in the recirculation region and around the reattachment point.

D.2 VTP model

Refining the mesh on the wind tunnel model is more complicated. In fact, the mesh is unstructured (except for the boundary layer), therefore it is more difficult to control the mesh density. Also, in this case a 1000% refinement has been performed on the mesh generated for RANS studies for $\delta_r = 0^\circ$. This is the baseline mesh, from which minor modifications are applied to take into account the deflection of the rudder. The characteristics of the baseline VTP mesh and the refined VTP mesh are summarized in Table D.2.

Table D.2 VTP grid comparison.

	Baseline mesh	Refined mesh
No. of points	11,640,201	87,433,594
No. of tetrahedra	14,891,546	229,927,340
No. of prisms	44,544	127,5824
No. of pyramids	282,625	177,5039
No. of hexahedra	8,916,400	47,885,101
No. of surface triangles	5,480	20,170
No. of surface quadrilaterals	280,063	1,774,033

Simulations have been performed for the refined mesh for $\beta = 0^\circ$, and the density residuals drop down by 6 orders of magnitude (Figure D.3). The flow solution is shown in Figure D.4 and can be compared to the top left frame of figure 5.11. The two images show the same C_p contours and streamlines.

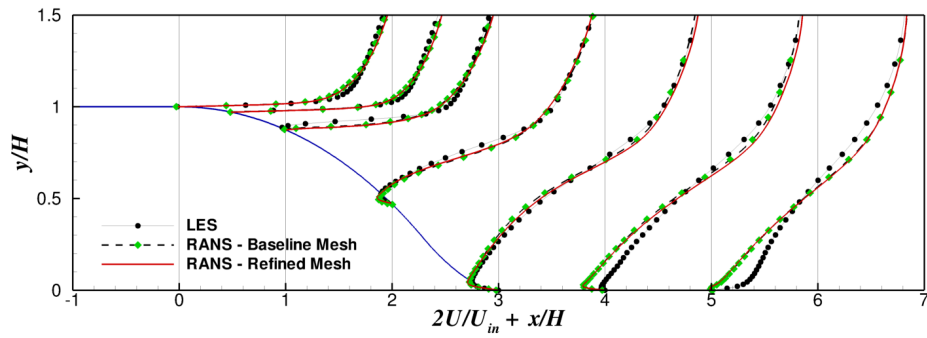
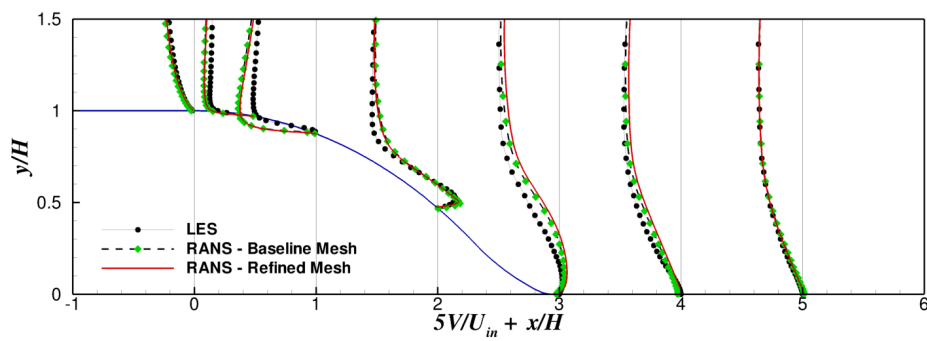
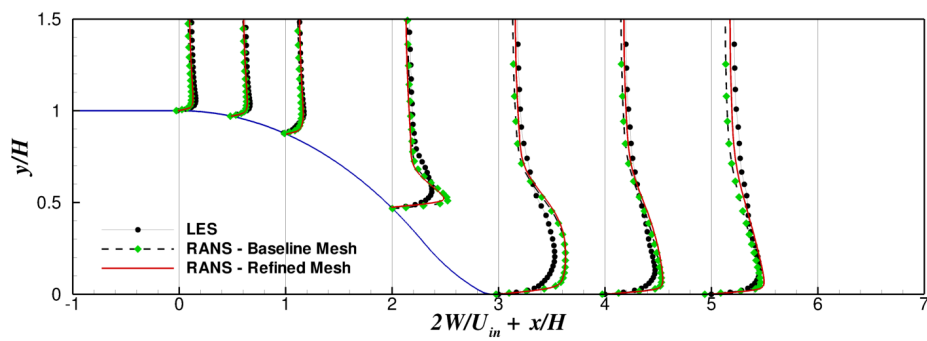
(a) \bar{U} profiles.(b) \bar{V} profiles.(c) \bar{W} profiles.

Fig. D.2 Comparison of the flow velocity profiles obtained on the baseline and refined grids.

A better understanding of the quality of the solution is given by the computation of the pressure coefficient C_p for sections of the VTP. This plot is given in Figure D.5 and shows the agreement of the C_p values along the chord of the VTP between the two meshes.

Therefore, it is possible to conclude that the baseline mesh has converged and is trustworthy.

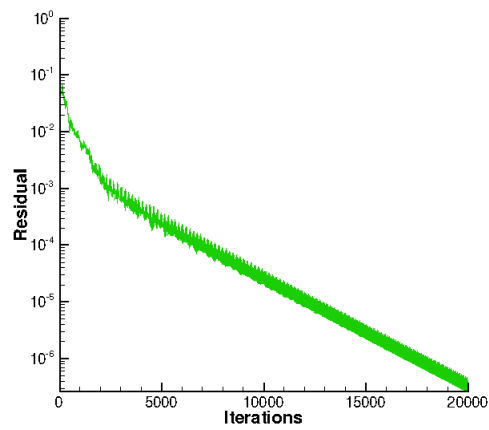


Fig. D.3 Density residual for the refined mesh for $\beta = 0^\circ$.

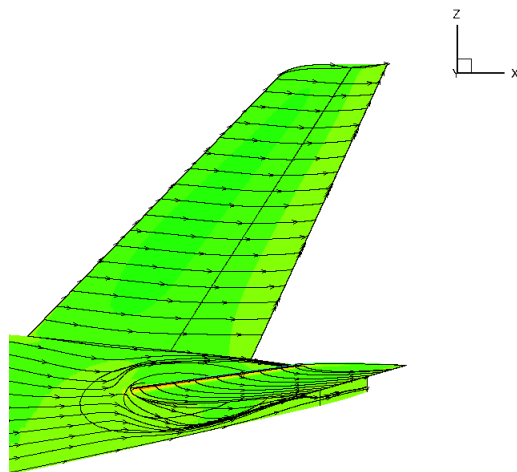
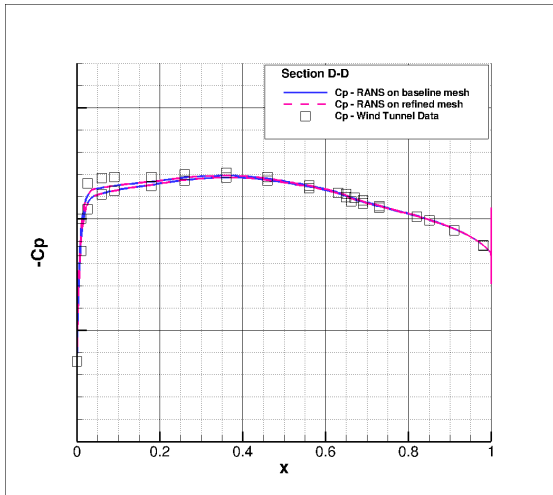
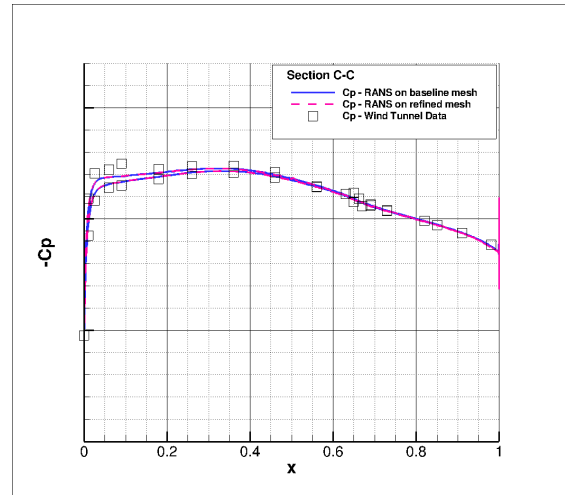
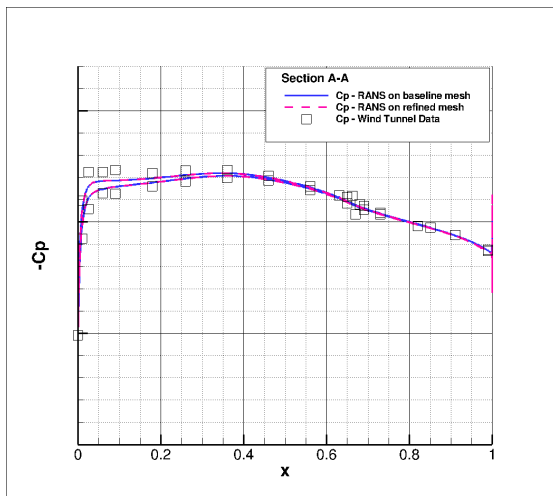
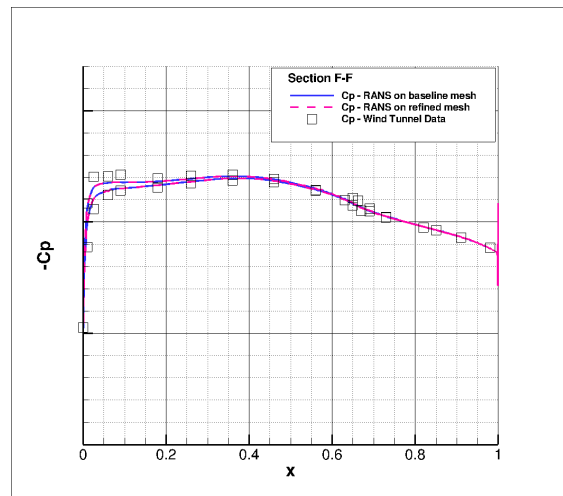


Fig. D.4 Flow visualization for the refined mesh for $\beta = 0^\circ$.

(a) Section D-D ($\eta = 0.1$).(b) Section C-C ($\eta = 0.4$).(c) Section A-A ($\eta = 0.7$).(d) Section F-F ($\eta = 0.9$).Fig. D.5 Grid convergence study: baseline mesh vs. refined mesh, $\delta_r = 0^\circ$ and $\beta = 0^\circ$.

Appendix E

Wind tunnel measurements

E.1 Data acquisition

For a standard wind tunnel test, whether a model representing an aircraft or a car or a building, there are some fundamental measures which need to be under-taken. Usually, the forces and moments exerted on the body due to the passage of fluid flow is measured. In addition, it is necessary to record the velocity of the fluid passing over the wind tunnel model and, if possible, make local measurements on the test piece itself.

The forces and the moments acting on the wind tunnel model are measured by load cell balances. They work with strain-gauges that convert the load acting on the test specimen into electrical signals. The gauges are bonded onto a beam or structural member that becomes deformed when the load is applied. In fact, the strain changes the electrical resistance of the gauges in proportion to the load.

The most usual method for obtaining surface pressure information on a wind tunnel model is through the installation of static pressure ports. Small-diameter holes are drilled into the surface of the model. Into this hole, a length of metallic hypodermic tubing is fitted and routed through the internal structure of the component. This tubing is ultimately enlarged by inserting the metallic tubing into a plastic tube which winds its way through the model to a pressure transducer. The quality of the hole in the surface of the model is very important. The main requirement is that the mouth of the hole is smooth and flush with the surface. It is essential that there are no burrs or other surface irregularities in the vicinity of the hole. The size of the hole also has some effect owing to the absence of a solid boundary. Fluid can be deflected into the hole and can cause the pressure acting in the hole to differ from the static pressure which would be measured by a hole of infinitely small diameter. The size of the error will depend not only on the diameter of the hole, but also the hole depth and

the internal arrangement of the pressure corrections. Model incidence is normally measured relative to gravity using an accelerometer device.

The measurement of the shape of the model at the exact time that the data is collected is becoming more important for the study of in-flight aircraft deformations. This is especially important for cruise, but deformation of slats and flaps is also gaining attention.

Several flow visualization techniques are available to visualize surface flow characteristics. Coloured or fluorescent oil painted onto the surface is a relatively simple way of visualizing surface flow features, such as separations and attachment points, shock positions, and surface streak lines. The pigment is painted onto the model surface under investigation and the tunnel is run at the required test conditions. The oil will then be subject to the flow and will indicate the features described. It is possible that the flow of oil will continue for some time therefore some judgement is required with respect to the duration of the test run so that the oil has flowed sufficiently to indicate features without disappearing completely.

A very common way of visualizing surface flow in low-speed tunnels is through the use of tufts. These fluorescent strands are attached to the surface of the model at one end and the other end is free. Once the flow is activated, the direction of the tufts is determined by the air flow. Aligned tufts represent attached airflow over the wing and scattered tufts represent flow separation from the wing. Smoke can also be used to trace streamlines.

E.2 Aerodynamic corrections

A wind tunnel model mounted in the test section is subject to constraints and modifications which are not experienced by the real model. Since in CFD flight conditions are simulated, it is necessary to understand the differences between the flow conditions measured in the tunnel and those that the aircraft would experience in flight, in order to apply relevant aerodynamic corrections. Figure E.1 shows an aircraft model in the working section of a wind tunnel.

First of all, the walls of the wind tunnel constrain the flow around the model. This is quite different from real flight conditions, where the section area is infinite. The model itself also creates a blockage effect, which further reduces the section area, causing an increase in flow velocity. In addition, the model is connected to a strut via a support. These physical elements modify the local flow around the model. Moreover, the incidence of the flow that reaches the aircraft model is modified by an upwash effect, which varies the direction of the lift and the drag. Furthermore, other sources of error may come from the calibration of the instruments, such as the balance, or of the tunnel flow itself. Therefore, the following calibrations or corrections are needed.

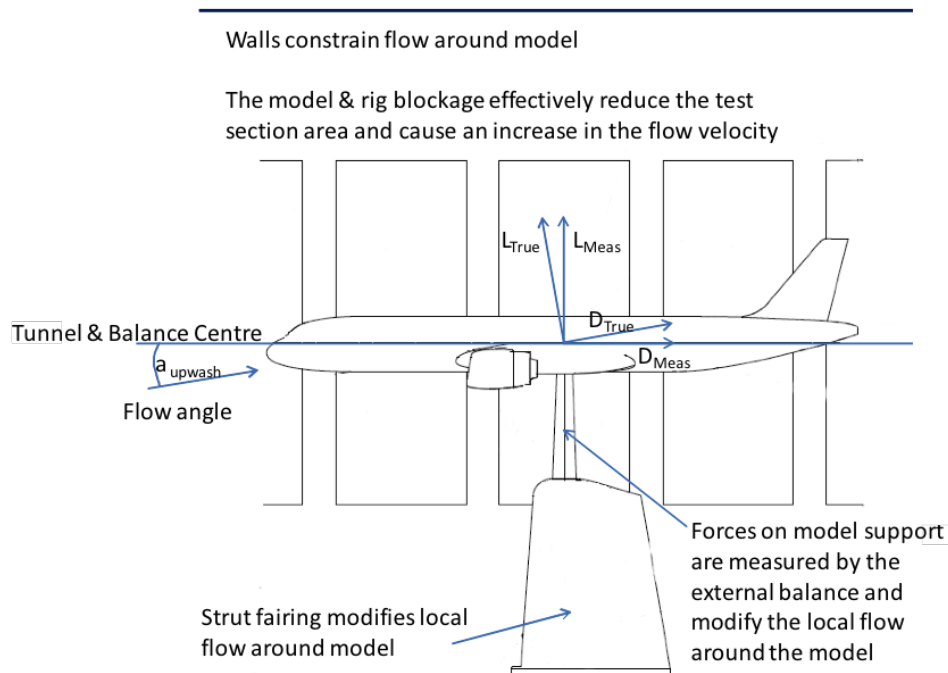


Fig. E.1 Wind tunnel constraints. Picture courtesy of Airbus.

Calibration of the balance. The calibration of the balance is performed using known loads. This is a relatively simple task, which can be repeated for different conditions, such as temperature.

Strut flexibility calibration. The forces acting on the model cause the strut rig supporting the model to deflect. This alters the position of the model which affects the moment terms. When an external balance is used, this has to be accounted for, and the deflection characteristics of each strut need to be assessed. The process involves loading the strut and strut-end assembly with known loads and measuring the displacements.

Dead-weight loading. The support can be located as accurately as possible so that the model attachment is as close as possible to the balance virtual centre. However, a correction can be introduced due to any offsets. This is done by loading at the strut pin centre and taking measurements from the balance.

Tunnel flow calibration. This is a dedicated set of measurements to calibrate the tunnel speed control and the flow angularity or jet pitch. This is performed with Pitot tube¹ measurements in the calculation of static and dynamic pressure. Flow angularity measurements

¹<https://www.grc.nasa.gov/www/k-12/airplane/pitot.html>

are carried out to define the effective angle of the flow in the working section, which can be disturbed by the presence of the model.

Support corrections. Any model has to be supported inside the test section. This modifies the flow locally around the model. Usually, the interference effects can be derived by testing the model on an alternative rig which enables the testing of a dummy representation of the test set-up (Figure E.2). The strut correction test will typically derive an increment between the dummy support present and absent. This increment can then be applied to the test set-up.

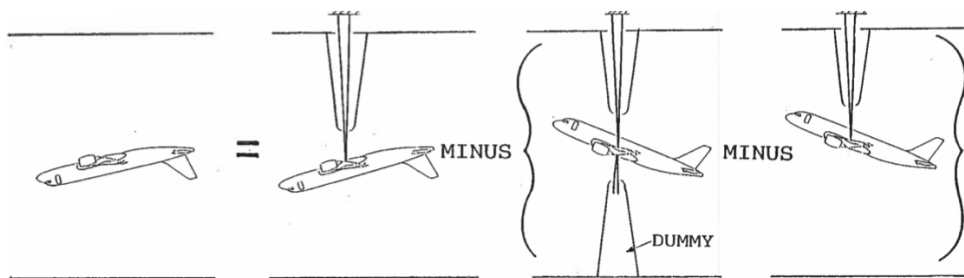


Fig. E.2 Wind tunnel support corrections. Picture courtesy of Airbus.

Blockage corrections. These are corrections for the flow-blocking effect of the model and mounting arrangement. The blockage of the model and support rig has the effect of accelerating the flow round the model, increasing the velocity hence the dynamic pressure at the model station. An empty-tunnel calibration test is performed in order to measure this disturbance.

References

- [1] Abbas, A., De Vicente, J., and Valero, E. (2013). Aerodynamic technologies to improve aircraft performance. *Aerospace Science and Technology*, 28(1):100–132.
- [2] Abbas-Bayoumi, A. and Becker, K. (2011). An industrial view on numerical simulation for aircraft aerodynamic design. *Journal of Mathematics in Industry*, 1(10):14.
- [3] ACARE (2010). *Beyond vision 2020 (Towards 2050)*. European Commission.
- [4] Agarwal, R. (1999). Computational fluid dynamics of whole-body aircraft. *Annual Review of Fluid Mechanics*, 31(1):125–169.
- [5] AIAA (1998). Guide for the Verification and Validation of Computational Fluid Dynamics Simulations. Technical report.
- [6] Airbus (2001). In-Flight Separation of Vertical Stabilizer - American Airlines Flight 587. Technical report.
- [7] Airbus (2011). Wind Tunnel Test Memorandum. Technical report.
- [8] Airbus (2013). Future Journeys (2013-2032). Technical report.
- [9] Alpman, E. and Long, L. (2005). Separated turbulent flow simulations using a Reynolds stress model and unstructured meshes. In *43rd Aerospace Sciences Meeting and Exhibit*. AIAA.
- [10] Anderson, J. D. (2011). *Fundamentals of Aerodynamics*. McGraw-Hill.
- [11] Ansys (2016). Fluent User’s Guide. Technical report.
- [12] Batten, P., Craft, T. J., Leschziner, M. A., and Loyau, H. (1999). Reynolds-Stress-Transport Modeling for Compressible Aerodynamic Applications. *AIAA Journal*, 37(7).
- [13] Bentaleb, Y., Lardeau, S., and Leschziner, M. (2012). Large-eddy simulation of turbulent boundary layer separation from a rounded step. *Journal of Turbulence*, 13(4):1–28.
- [14] Bentaleb, Y. and Leschziner, M. A. (2013). The structure of a three-dimensional boundary layer subjected to streamwise-varying spanwise-homogeneous pressure gradient. *International Journal of Heat and Fluid Flow*, 43:109–119.
- [15] Boussinesq, J. (1897). *Theory of tumultuous and whirling liquid flows*. Gauthier-Villars et fils.

- [16] Bower, D. R. and O'Callaghan, J. (2008). Utilization of CFD in the American Airlines Flight 587 Accident Investigation. In *26th AIAA Applied Aerodynamics Conference*.
- [17] Butcher, J. C. (1996). A history of Runge-Kutta methods. *Applied Numerical Mathematics*, 20:247–260.
- [18] Catalano, P. and Amato, M. (2003). An evaluation of RANS turbulence modelling for aerodynamic applications. *Aerospace Science and Technology*, 7(7):493–509.
- [19] Cecora, R.-D., Eisfield, B., Probst, A., Crippa, S., and Radespiel, R. (2012). Differential Reynolds Stress Modeling for Aeronautics. In *50th AIAA Aerospace Sciences Meeting and Exhibit*. AIAA.
- [20] Chapman, D. R. (1979). Computational aerodynamics development and outlook. *AIAA Journal*, 17(12):1293–1313.
- [21] Childs, R. E., Stremel, P. M., Kushner, L. K., Heineck, J. T., and Storms, B. L. (2016). Simulation of Sweep-Jet Flow Control, Single Jet and Full Vertical Tail. In *54th AIAA Aerospace Sciences Meeting and Exhibit*. AIAA.
- [22] Colin, Y., Deniau, H., and Boussuge, J. (2011). A robust low speed preconditioning formulation for viscous flow computations. *Computers and Fluids*, 47(1):1–15.
- [23] Comte-Bellot, G. and Corrsin, S. (1971). Simple Eulerian time correlation of full-and narrow-band velocity signals in grid-generated, 'isotropic' turbulence. *Journal of Fluid Mechanics*, 48(2):273–337.
- [24] Constantinescu, G. S. and Squires, K. D. (2000). LES and DES investigations of turbulent flow over a sphere. In *38th Aerospace Sciences Meeting and Exhibit*. AIAA.
- [25] Craft, T. J., Launder, B. E., and Suga, K. (1996). Development and application of a cubic eddy-viscosity model of turbulence. *International Journal of Heat and Fluid Flow*, 17(2):108–115.
- [26] Crumpton, P. I., Moinier, P., and Giles, M. B. (1997). An Unstructured Algorithm for High Reynolds Number Flows on Highly-Stretched Grids. In *10th international conference on numerical methods for laminar and turbulent flow*.
- [27] Cui, J. (2016). *Numerical Investigation of Disturbed Flow Environment Impact on Low Pressure Turbines*. PhD thesis.
- [28] Davidson, L. and Peng, S. H. (2003). Hybrid LES-RANS modelling: a one-equation SGS model combined with a k – epsilon model for predicting recirculating flows. *International Journal for Numerical Methods in Fluids*, 1018:1003–1018.
- [29] Deck, S. (2005). Zonal-Detached-Eddy Simulation of the Flow Around a High-Lift Configuration. *AIAA Journal*, 43(11):2372–2384.
- [30] Deck, S., Gand, F., Brunet, V., and Khelil, S. B. (2014). High-fidelity simulations of unsteady civil aircraft aerodynamics: stakes and perspectives. Application of zonal detached eddy simulation. *Phil.Trans.R.Soc.A*, 372(2022).

- [31] Delery, J. (2013). *Three-dimensional separated flow topology*. Wiley.
- [32] DLR Germany (2014). TAU-Code User Guide. Technical report.
- [33] Durbin, P., Yin, Z., and Jeyapaul, E. (2016). Adaptive Detached-Eddy Simulation of Three- Dimensional Diffusers. *Journal of Fluids Engineering*, 138.
- [34] Dwight, R. P. (2006). *RANS-based Analysis and Optimization using implicit and Adjoint Methods on Unstructured Grids*. PhD thesis.
- [35] Eisfeld, B. (2007). Numerical Simulation of Aerodynamic Problems with the SSG / LRR- ω Reynolds Stress Turbulence Model Using the Unstructured TAU Code. In *New Results in Numerical and Experimental Fluid Mechanics VI*, pages 356–363. Springer.
- [36] Eisfeld, B. and Brodersen, O. (2009). Advanced turbulence modelling and stress analysis for the dlr-f6 configuration. In *23rd Applied Aerodynamics Conference*. AIAA.
- [37] El-Askary, W. A. (2009). Turbulent boundary layer structure of flow over a smooth-curved ramp. *Computers and Fluids*, 38(9):1718–1730.
- [38] Evans, S., Lardeau, S., and Pettinelli, C. (2016). Validation of a Turbulence Methodology using the SST Model for Adjoint Calculation. In *AIAA SciTech*.
- [39] Forsythe, J. R., Squires, K. D., Wurtzler, K. E., and Spalart, P. R. (2004). Detached-Eddy Simulation of the F15-E at High Alpha. *Journal of Aircraft*, 41(2):193–200.
- [40] Fröhlich, J. and von Terzi, D. (2008). Hybrid LES/RANS methods for the simulation of turbulent flows. *Progress in Aerospace Sciences*, 44(5):349–377.
- [41] Furbo, E., Harju, J., and Nilsson, H. (2009). Evaluation of turbulence models for prediction of flow separation at a smooth surface. Technical report.
- [42] Fureby, C., Zhu, S., and Jones, D. (2015). Large Eddy Simulation of the Flow over a Contoured Ramp. In *Int. Symposium on Turbulence and Shear Flow Phenomena*.
- [43] Gand, F. (2013). Zonal Detached Eddy Simulation of a Civil Aircraft with a Deflected Spoiler. *AIAA Journal*, 51(3):697–706.
- [44] Gerhold, T. (2005). Overview of the Hybrid RANS Code TAU. In Kroll, N. and Fassbender, J. K., editors, *MEGAFLOW - Numerical Flow Simulation for Aircraft Design: Results of the second phase of the German CFD initiative MEGAFLOW, presented during its closing symposium at DLR, Braunschweig, Germany, December 10 and 11, 2002*, pages 81–92. Springer.
- [45] Hamilton, N. and Bayoán, R. (2015). Anisotropy of the Reynolds stress tensor in the wakes of wind turbine arrays in Cartesian arrangements with counter-rotating rotors. *Physics of Fluids*, 27.
- [46] Hedges, L. S., Travin, a. K., and Spalart, P. R. (2002). Detached-Eddy Simulations Over a Simplified Landing Gear. *Journal of Fluids Engineering*, 124(2):413.
- [47] Hitzel, S. M., Vila-Prat, A., and Sorensen, K. (2013). URANS-Simulations of Combat Aircraft Flight Maneuvers. In *31st Applied Aerodynamics Conference*. AIAA.

- [48] Howard, R. J. A. and Sandham, N. D. (2000). Simulation and Modelling of a Skewed Turbulent Channel Flow. *Flow, Turbulence and Combustion*, 65:83–109.
- [49] Hunt, J. C. R., Wray, A. A., and Moin, P. (1988). Eddies, Streams, and Convergence Zones in Turbulent Flows. In *Proceedings of the Summer Program*.
- [50] Iaccarino, G., Ooi, A., Durbin, P. A., and Behnia, M. (2003). Reynolds averaged simulation of unsteady separated flow. *International Journal of Heat and Fluid Flow*, 24(2):147–156.
- [51] Im, H.-S. and Zha, G.-C. (2014). Delayed Detached Eddy Simulation of Airfoil Stall Flows Using High-Order Schemes. *Journal of Fluids Engineering*, 136(11):111104–1 – 111104–12.
- [52] Jameson, A. (2015). The Origins and Further Development of the Jameson-Schmidt-Turkel (JST) Scheme. In *33rd AIAA Applied Aerodynamics Conference*.
- [53] Jeans, T. L., McDaniel, D. R., Cummings, R. M., and Mason, W. H. (2009). Aerodynamic Analysis of a Generic Fighter Using Delayed Detached-Eddy Simulation. *Journal of Aircraft*, 46(4):1326–1339.
- [54] Jimenez, J., Hoyas, S., and Siemens, M. P. (2010). Turbulent boundary layers and channels at moderate Reynolds numbers. *Journal of Fluid Mechanics*, pages 1–26.
- [55] Kalsi, H. S. and Tucker, P. G. (2016). A Novel Zonal RANS-DES Method for Prediction of Accelerated and Separated Flow. In *AIAA SciTech*.
- [56] Kraichnan, R. H. (1970). Diffusion by a Random Velocity Field. *Physics of Fluids*, 13(1970):22–31.
- [57] Lardeau, S. and Leschziner, M. (2011). The interaction of round synthetic jets with a turbulent boundary layer separating from a rounded ramp. *Journal of Fluid Mechanics*, 683:172–211.
- [58] Larsson, J. and Wang, Q. (2014). The prospect of using large eddy and detached eddy simulations in engineering design, and the research required to get there. *Philosophical Transactions of the Royal Society of London A: Mathematical, Physical and Engineering Sciences*, 372(2022).
- [59] Launder, B. E., Reece, G. J., and Rodi, W. (1975). Progress in the development of a Reynolds-stress turbulence closure. *Journal of Fluid Mechanics*, 68(03):537–566.
- [60] Launder, B. E. and Sharma, B. I. (1974). Application of the energy-dissipation model of turbulence to the calculation of flow near a spinning disc. *Letters in Heat and Mass Transfer*, 1(2):131–137.
- [61] Leatham, M., Stokes, S., Shaw, J. A., J., C., Appa, J., and Blaylock, T. A. (2000). Automatic Mesh Generation for Rapid-Response Navier-Stokes Calculations. In *Fluids 2000*.
- [62] Lele, S. and Nichols, J. W. (2014). A second golden age for aeroacoustics? *Philosophical Transactions of the Royal Society A: Mathematical, Physical and Engineering Sciences*, 372(2022).

- [63] Leschziner, M. A. (2004). Modelling turbulent separated flow in the context of aerodynamic applications. *Fluid Dynamics Research*, 38:174–210.
- [64] Leschziner, M. a. and Drikakis, D. (2002). Turbulence modelling and turbulent-flow computation in aeronautics. *Aeronautical Journal*, 106(1061):349–384.
- [65] Lumley, J. and Newman, G. (1977). The return to isotropy of homogeneous turbulence. *Journal of Fluid Mechanics*, 82:161–178.
- [66] Lund, T. S., Wu, X., and Squires, K. D. (1998). Generation of Turbulent Inflow Data for Spatially-Developing Boundary Layer Simulations. *Journal of Computational Physics*, 140(2):233–258.
- [67] Madugundi, D., Nagib, H., and Kiedaisch, J. (2008). Evaluation of Turbulence Models Through Prediction of Separated Flows with and without Flow Control and Circulation Effects. In *46th AIAA Aerospace Sciences Meeting and Exhibit*. AIAA.
- [68] Mary, I. (2007). ONERA strategy for LES of complex flows. In *LES for external aerodynamic flows: status and prospects*. Imperial College London.
- [69] Menter, F. R. (1992). Influence of Freestream Values on k-w Turbulence Model Predictions. *AIAA Journal*, 30(6):1657–1659.
- [70] Menter, F. R. (1993). Zonal Two Equation k-w Turbulence Models for Aerodynamic Flows. In *24th Fluid Dynamics Conference*. AIAA.
- [71] Menter, F. R., Kuntz, M., and Langtry, R. (2003). Ten Years of Industrial Experience with the SST Turbulence Model. *Turbulence Heat and Mass Transfer 4*, 4:625–632.
- [72] Moin, P., Shih, T. H., Driver, D., Mansour, N. N., Moina, P., and Shih, T. (1990). Direct numerical simulation of a threedimensional turbulent boundary layer. *Physics of Fluids*, 2:1846–1853.
- [73] Moinier, P. (1999). *Algorithm Developments for an Unstructured Viscous Flow Solver*. PhD thesis, University of Oxford.
- [74] Morkovin, M. V. (1970). Separation of Flow. *Science*, 170(3956):432–433.
- [75] Morton, S. A., Forsythe, J. R., Squires, K. D., and Cummings, R. M. (2003). Detached-eddy simulations of full aircraft experiencing massively separated flows. In *The 5th Asian CFD Conference*.
- [76] Nicolosi, F., Ciliberti, D., and Della Vecchia, P. (2016). Aerodynamic Design Guidelines of Aircraft Dorsal Fin. In *34th AIAA Applied Aerodynamics Conference*.
- [77] Nicolosi, F., Corcione, S., and Vecchia, P. D. (2014). Commuter Aircraft Aerodynamic Design : Wind-Tunnel Tests and CFD Analysis. In *29th Congress of the International Council of the Aeronautical Sciences*.
- [78] Oriji, U. R., Karimisani, S., and Tucker, P. G. (2015). RANS Modeling of Accelerating Boundary Layers. *Journal of Fluids Engineering*, 137(1).

- [79] Persson, T., Liefvendahl, M., Bensow, R. E., and Fureby, C. (2006). Numerical investigation of the flow over an axisymmetric hill using LES, DES, and RANS. *Journal of Turbulence*, 7:N4.
- [80] Piomelli, U. (2014). Large eddy simulations in 2030 and beyond. *Philosophical Transactions of the Royal Society A: Mathematical, Physical and Engineering Sciences*, 372:1–13.
- [81] Pope, S. B. (2000). *Turbulent Flows*. Cambridge University Press.
- [82] Probst, A., Radespiel, R., and Knopp, T. (2011). Detached-Eddy Simulation of Aerodynamic Flows Using a Reynolds-Stress Background Model and Algebraic RANS/LES Sensors. In *20th Computational Fluid Dynamics Conference*, pages 1–20. AIAA.
- [83] Probst, A. and Reuß, S. (2015). *Scale-Resolving Simulations of Wall-Bounded Flows with an Unstructured Compressible Flow Solver*, pages 481–491. Springer International Publishing, Cham.
- [84] Radespiel, R., Turkel, E., and Kroll, N. (1995). Assessment of Preconditioning methods. Technical report.
- [85] Reuss, S., Knopp, T., Probst, A., and Orlt, M. (2014). Assessment of Local LES-Resolution Sensors for Hybrid RANS/LES Simulations. In *Progress in Hybrid RANS-LES Modelling*.
- [86] Revell, A., Benhamadouche, S., Craft, T. J., and Laurence, D. R. P. (2006). A stress strain lag eddy viscosity model for unsteady mean flow. *Int. J. Heat Fluid Flow*, 27:821–830.
- [87] Rodi, W. and Scheuerer, G. (1986). Scrutinizing the k-epsilon Turbulence Model Under Adverse Pressure Gradient Conditions. *Journal of Fluids Engineering*, 108:174–179.
- [88] Rogers, S. E., Kwak, D., and Kiris, C. (1991). Steady and unsteady solutions of the incompressible navier-stokes equations. *AIAA Journal*, 29(4):603–610.
- [89] Sagaut, P. and Deck, S. (2009). Large eddy simulation for aerodynamics: status and perspectives. *Philosophical Transactions of the Royal Society A: Mathematical, Physical and Engineering Sciences*, 367(1899):2849–60.
- [90] Sartor, F. and Timme, S. (2015). Delayed Detached-Eddy Simulation of Shock Buffet on Half Wing-Body Configuration. In *22nd AIAA Computational Fluid Dynamics Conference*.
- [91] Seele, R., Graff, E., Lin, J., and Wygnanski, I. (2013). Performance Enhancement of a Vertical Tail Model with Sweeping Jet Actuators. In *SPACE Conference and Exposition*. AIAA.
- [92] Shur, M., Spalart, P. R., Strelets, M., and Travin, A. (1999). Detached-eddy Simulation of An Airfoil At High Angle of Attack. *Engineering Turbulence Modelling and Experiments*.

- [93] Simonsen, A. J. and Krogstad, P. Å. (2005). Turbulent stress invariant analysis: Clarification of existing terminology. *Physics of Fluids*, 17(8):1–4.
- [94] Spalart, P. R. (2009). RANS modelling into a second century. *International Journal of Computational Fluid Dynamics*, 23(4):291–293.
- [95] Spalart, P. R. and Allmaras, S. R. (1994). One-equation turbulence model for aerodynamic flows. *Recherche aerospaciale*, 1:5–21.
- [96] Spalart, P. R. and Bogue, D. R. (2003). The role of CFD in aerodynamics, off-design. *Aeronautical Journal*, 107(1072):323–330.
- [97] Spalart, P. R., Deck, S., Shur, M. L., Squires, K. D., Strelets, M. K., and Travin, A. (2006). A new version of detached-eddy simulation, resistant to ambiguous grid densities. *Theoretical and Computational Fluid Dynamics*, 20(3):181–195.
- [98] Spalart, P. R., Jou, W., Strelets, M., and Allmaras, S. R. (1997). Comments on the feasibility of LES for wings, and on a hybrid RANS/LES approach. In *Advances in DNS/LES*.
- [99] Spalart, P. R. and Venkatakrisnan, V. (2016). On the role and challenges of CFD in the aerospace industry. *Aeronautical Journal*, 120(1223):209–232.
- [100] Spalart, R. (2001). Young-Person’s Guide to Grids Detached-Eddy Simulation Grids. Technical report.
- [101] Speziale, C. G. (1987). On nonlinear K-1 and K - ϵ models of turbulence. *Journal of Fluid Mechanics*, 178:459–475.
- [102] Speziale, C. G., Sarkar, S., and Gatski, T. B. (1991). Modelling the pressure-strain correlation of turbulence: an invariant dynamical systems approach. *Journal of Fluid Mechanics*, 227:245–272.
- [103] Surana, a., Grunberg, O., and Haller, G. (2006). Exact theory of three-dimensional flow separation. Part 1. Steady separation. *Journal of fluid mechanics*, 564:57.
- [104] Torenbeek, E. (2013). *Advanced Aircraft Design*. Wiley.
- [105] Travin, A., Shur, M., Strelets, M., and Spalart, P. (2000). Detached-eddy simulations past a circular cylinder. *Flow, Turbulence and Combustion*, 63(1):293–313.
- [106] Travin, A., Shur, M., Strelets, M., and Spalart, P. R. (2002). *Physical and Numerical Upgrades in the Detached-Eddy Simulation of Complex Turbulent Flows*, pages 239–254. Springer, Dordrecht.
- [107] Tucker, P. (2006). Turbulence modelling of problem aerospace flows. *International journal for numerical methods in Fluids*, 51(3):261–283.
- [108] Tucker, P. G. (2007). Introduction. Computational aerodynamics. *Philosophical transactions. Series A, Mathematical, physical, and engineering sciences*, 365(1859):2379–88.

- [109] Tucker, P. G. (2011). Computation of unsteady turbomachinery flows: Part 2-LES and hybrids. *Progress in Aerospace Sciences*, 47(7):546–569.
- [110] Tucker, P. G. (2013). *Unsteady Computational Fluid Dynamics in Aeronautics*. Springer.
- [111] Tucker, P. G. (2016). *Advanced Computational Fluid and Aerodynamics*. Cambridge University Press.
- [112] Tucker, P. G. and Davidson, L. (2003). Zonal k-l based Large Eddy Simulations. In *41st Aerospace Sciences Meeting and Exhibit*.
- [113] Tucker, P. G. and Lardeau, S. (2009). Applied large eddy simulation. *Philosophical Transactions of the Royal Society A: Mathematical, Physical and Engineering Sciences*, 367(1899):2809–2818.
- [114] Turkel, E. L. I. (1987). Preconditioned Methods for Solving the Incompressible and Low Speed Compressible Equations. *Journal of Computational Physics*, 72:277–298.
- [115] Vassberg, J. C., DeHaan, M. A., Rivers, S. M., and Wahls, R. A. (2008). Development of a Common Research Model for Applied CFD Validation Studies. In *26th AIAA Applied Aerodynamics Conference*.
- [116] Vermeire, B. C., Witherden, F. D., and Vincent, P. E. (2017). On the Utility of GPU Accelerated High-Order Methods for Unsteady Flow Simulations : A Comparison with Industry-Standard Tools. *Journal of Computational Physics*, 334:497–521.
- [117] Vos, J., Rizzi, a., Darracq, D., and Hirschel, E. (2002). Navier–Stokes solvers in European aircraft design. *Progress in Aerospace Sciences*, 38(8):601–697.
- [118] Wagner, C., Hüttl, T., and Sagaut, P. (2007). *Large-Eddy Simulation for Acoustics*. Cambridge University Press.
- [119] Waldmann, A., Gansel, P. P., and Lutz, T. (2015). Unsteady Wake Flow of an Aircraft under Low-Speed Stall Conditions in DES and PIV. In *53rd AIAA Aerospace Sciences Meeting*.
- [120] Wang, Z. J., Fidkowski, K., Bassi, F., Caraeni, D., Cary, A., Deconinck, H., Hartmann, R., Hillewaert, K., Huynh, H. T., Kroll, N., May, G., Persson, P.-o., Leer, B. V., and Visbal, M. (2012). High-Order CFD Methods : Current Status and Perspective. *Int. J. Numer. Meth. Fluids*, 00:1–42.
- [121] Wang, Z.-N. and Yuan, X. (2013). Unsteady Mechanisms of Compressor Corner Separation Over a Range of Incidences Based on Hybrid LES/RANS. In *ASME Turbo Expo 2013: Turbine Technical Conference and Exposition*.
- [122] Wilcox, D. C. (1988). Multiscale model for turbulent flows. *AIAA journal*, 26(11):1311–1320.
- [123] Wilcox, D. C. (2006). *Turbulence Modeling for CFD (Third Edition)*. DCW Industries.
- [124] Xiao, Z.-X. and Luo, K.-Y. (2015). Improved delayed detached-eddy simulation of massive separation around triple cylinders. *Acta Mechanica Sinica*, 31(6):799–816.

-
- [125] Yoon, S. and Jamesont, A. (1988). Lower-Upper Symmetric-Gauss-Seidel Method for the Euler and Navier-Stokes Equations. *AIAA Journal*, 26(9).
- [126] Zhang, S. and Zhong, S. (2010). Experimental Investigation of Flow Separation Control Using an Array of Synthetic Jets. *AIAA Journal*, 48(3):611–623.
- [127] Zhu, F. (2014). *Geometric Parameterisation and Aerodynamic Shape Optimisation Name*. PhD thesis, University of Sheffield.

